

**TURBULENT FLOW CONTROL USING
SPANWISE TRAVELLING WAVE VIA
LORENTZ FORCING**

Peng Xu, MEng. BEng.

THESIS SUBMITTED TO THE UNIVERSITY OF NOTTINGHAM

FOR THE DEGREE OF DOCTOR OF PHILOSOPHY

March 2009

Abstract

Lorentz-forcing spanwise travelling wave actuation in the turbulent boundary layer has been studied in a water channel at various experimental conditions ($St = 139.2, 186$ and 232 ; $T^+ = 17, 42$ and 82). At the Reynolds number of $Re_\tau = 388$, a maximum skin friction drag reduction of 30% is achieved in some cases, while up to 22.8% of viscous drag increase is also observed.

The results of the turbulent boundary layer profiles show that the turbulence intensities for both the drag-reducing and the drag-increasing cases are reduced. The higher moments of turbulence statistics such as the skewness and the kurtosis increase near the wall when $T^+ = 42, St = 232$ in the drag-reducing case. For the drag-increasing case ($T^+ = 17, St = 232$), the skewness and the kurtosis are decreased when very close to the wall ($y^+ < 6$), while they are increased for $y^+ > 6$, similar to the drag-reducing case. The reduction in the turbulent intensities as well as the changes in VITA velocity profiles suggest that the drag changes are due to the modified near-wall activities by the Lorentz forcing.

Flow visualisation shows that the low-speed streaks are twisted into the spanwise directions in both the drag-reducing and the drag-increasing cases. For the drag-reducing case, the low-speed streaks are clustered together to form a wide low-speed region similar to what Du et al (2002) have found. This low-speed region seems to act as the ‘storage’ of low-speed fluid to help reduce the skin friction drag. To achieve the drag reduction, the spanwise displacement of low-speed streaks must be greater than 115 wall units in the

present configuration, which compares well with the average spacing of low-speed streaks in the turbulent boundary layer.

When the drag increase occurs, only pseudo-local spanwise oscillation is observed without a formation of a wide low-speed region. The pseudo-local spanwise oscillation appears to produce converging and diverging motions around the forcing-activation area. The induced streamwise vorticity layers are believed to enhance the effect of the sweep motion, which results in the increasing skin-friction drag.

Acknowledgements

First of all, I would like to thank my supervisor, Prof. Kwing-So Choi, for his academic and financial supports, helpful suggestions, encouragement and patience during the course of my study. He has shown me what a scientist should do and how to become a researcher. Appreciation is also given to the University of Nottingham for the award of 'Postgraduate Scholarship for China' and the School of Mechanical, Materials and Manufacturing Engineering of University of Nottingham for the award of 'Research Scholarship'.

Thanks must go to my colleagues Dr. Timothy N. Jukes, Richard Walle, Yong-Duck Kang and Dr. Faycal Bahri for their support and suggestions over the years. Also, thanks are extended to the technicians for their technical supports, especially Andy Matthew and Brian Foster.

I would like to show my greatest appreciation to my family, my Mum, Yuqiu Zhang; my Dad, Zujia Xu and my dear wife, Yiyun Ling, in particular for their patience and support over these years.

Contents

Abstract	i
Acknowledgements	iii
Nomenclature	vii
List of Figures	x
Chapter 1. Introduction	1
Chapter 2. Literature Review	4
2.1. Introduction	4
2.2. Outline of Turbulent Boundary-layer Theory	5
2.2.1. The Reynolds Equations	6
2.2.2. The Law of the Wall in Turbulence	8
2.2.3. Some Statistical Quantities in the Study of Turbulence	9
2.3. Coherent Structures in Turbulent Boundary Layers	11
2.3.1. Low and high-speed Streaks	12
2.3.2. Ejections and Sweeps	15
2.3.3. Vortical Structures	18
2.3.4. Outer Region	22
2.3.5. Shallow Water Waves	23
2.4. Turbulence Regeneration Cycle	25
2.5. Skin-friction Reduction In Turbulent Flow	32
2.5.1. Skin-friction Drag Reduction Strategies	32
2.5.2. Several Skin Friction Drag Reduction Approaches	35
2.6. Electro-Magnetic Turbulence Control (EMTC)	41
Chapter 3. Experimental Setup	85

3.1. Introduction	85
3.2. Open Water Channel and Test Section	85
3.3. Improvement of The Water Channel	86
3.3.1. Free Surface Effects and Flap Setting	86
3.3.2. Screens And Diffuser	87
3.3.3. Supporting Frame For Hot-film Anemometry	89
3.3.4. Temperature Controlling And Monitoring	90
3.4. Flow Visualisation Experimental Setup	90
3.4.1. Design of The Injection Slot	91
3.4.2. Water Treatment	92
3.5. The Design of Electro-magnetic Actuators	93
3.5.1. Introduction	93
3.5.2. The Geometry of The Electrode Sheet	94
3.5.3. The Phasing Strategy For Spanwise Travelling Wave	95
3.5.4. Mylar Sheet Surface Measurement	95
3.6. Velocity Measurement System	97
3.6.1. Hot-Film Anemometry	97
3.6.2. Velocity Calibration	99
3.6.3. Lorentz Forcing Effects On The Hot-film Sensors	100
3.7. Error Analysis Of Velocity Measurements	101
3.8. Traversing System, Data Acquisition And Power Unit	105
Chapter 4. Effects of Lorentz Forcing Spanwise Travelling Wave On Near-wall Turbulence Structures	134
4.1. Introduction	134
4.2. Turbulent Boundary Layer Without Control	136

4.3. Turbulent Boundary Layer With Lorentz Forcing Spanwise Oscillation	138
4.4. Turbulent Boundary Layer With Lorentz Forcing Spanwise Travelling Wave	140
4.4.1. Flow Visualisation Without Flow	140
4.4.2. Flow Visualisation With Flow	142
4.5. Conclusions	148
Chapter 5. Effects of Travelling Wave On Turbulent Boundary Layers	170
5.1. Introduction	170
5.2. Skin Friction Measurement And Wall Positioning	171
5.3. Boundary Layer Velocity Profiles	174
5.4. Energy Spectra and PDF	177
5.5. VITA Analysis	179
5.6. Spanwise Two-point Correlation of u Velocity	183
5.7. Phase-Averaged Drag, Momentum and Correlations	184
5.8. Summary	190
Chapter 6. Conclusions and Future work	225
6.1. Conclusions	225
6.2. Future Work	228
Reference	230
Appendices	262
Attached CD	

Nomenclature

A	calibration constant
a	electrode spacing and magnet spacing
B	calibration constant
B_0	magnetic field strength at wall
C	calibration constant
C_{Lv}	correlation coefficient
c	wave velocity
c_f	skin-friction coefficient ($c_f = \frac{\tau_w}{\frac{1}{2}\rho U_\infty^2} = 2\left(\frac{u_\tau}{U_\infty}\right)^2$)
D	calibration constant
DR	Drag Reduction ratio ($D.R. = \frac{c_f - c_{f0}}{c_{f0}}$)
$D(t)$	detector function used in VITA
d	water depth
E	voltage
F	calibration constant
Fr	Froude number ($Fr = \frac{U_\infty}{\sqrt{gd}}$)
g	gravitational acceleration
I	current
J_0	current density
k	VITA detector threshold
l	reference length
L_{ij}	a factor used in the correlation of low-speed streaks and velocities
M	momentum of fluids
\tilde{p}	hydrodynamic pressure
R_{MCf}	correlation coefficient between momentum and friction
	$(R_{MCf} = \int_0^{T^+} \frac{M'(t^+) \bullet C_f'(t^+)}{\sqrt{(M'(t^+))^2} \sqrt{(C_f'(t^+))^2}} dt^+)$
Re_τ	friction velocity Reynolds number ($Re_\tau = u_\tau \delta / \nu$)

R_{uu}	spanwise two-point correlation ($C_{ij} = \overline{u'_i u'_j} / ((\overline{u'^2})_i \cdot \overline{u'^2})^{1/2}$)
SR	sample rate
St	Stuart number ($St = J_0 B_0 \delta / \rho u_\tau^2$)
\tilde{s}_{ij}	the rate of strain ($\tilde{s}_{ij} = \frac{1}{2} (\frac{\partial \tilde{u}_i}{\partial x_j} + \frac{\partial \tilde{u}_j}{\partial x_i})$)
T	excitation period or sample time
t	time
u	streamwise velocity
U_∞	free-stream velocity
U	mean streamwise velocity
\hat{U}	an unbiased estimated true mean value of velocity u
u_τ	friction velocity ($u_\tau = \sqrt{\frac{\tau_w}{\rho}} = \sqrt{v \frac{dU}{dy}}$)
u'	streamwise velocity fluctuation
ξ	the coordination i (x, y or z in my study)
X, x	streamwise direction
Y, y	wall-normal direction
Z, z	spanwise direction
Δ^+	non-dimensional penetration depth ($\Delta^+ = au_\tau / \nu$)
Δt	time interval
δ	boundary layer thickness
δ_{ij}	Kronecker factor
λ	wavelength
μ	dynamic viscosity
ν	kinematic viscosity (μ/ρ)
ρ	density; spectral reflectance
τ_w	mean wall shear stress (skin-friction, $\tau_w = \mu \frac{\partial U}{\partial y} \Big _0$)
$\tilde{\sigma}_{ij}$	stress tensor ($\tilde{\sigma}_{ij} = -\tilde{p} \delta_{ij} + 2\mu \tilde{s}_{ij}$)
σ^2	mean square error
ε	normalised rms error
η	dimensionless wall normal position ($\eta = y / \delta$)

Subscripts and Superscripts

- + indicates viscous scaling, also referred to as inner-scaling. Viscous time, length and velocity scales are $t^+ = tu_\tau^2/\nu$, $l^+ = lu_\tau/\nu$, $u^+ = u/u_\tau$
- ' rms value
- ∞ free-stream condition
- ~ a tilde denotes the instantaneous value at (x_i, t) of a variable

List of Figures

2.1.1	Flow visualisation by Reynolds	47
2.2.1	Law of the Wall in the turbulent boundary layer	47
2.2.2	Probability density	48
2.2.3	A function with positive skewness	48
2.2.4	Kurtosis profiles	49
2.2.5	Sketch of a spanwise correlation	49
2.3.1	Low-speed streaks visualised by hydrogen bubbles	50
2.3.2	Low-speed streaks visualised by fluorescent dye	50
2.3.3	Side view of low-speed streaks	51
2.3.4	Correlation between low-speed streaks and velocity	51
2.3.5	Near wall streaks and formation mechanism	52
2.3.6	Mechanism of low-speed streak movement	53
2.3.7	Concept of low-speed streak formation	54
2.3.8	VITA from Blackwelder and Kaplan (1976)	55
2.3.9	Primary structure from Theodorsen (1952)	56
2.3.10	Hairpin vortices from Head & Bandyopadhyay (1981)	57
2.3.11	Effect of Reynolds number on hairpin structures	58
2.3.12	Horse shoe vortex from Robinson (1991b)	58
2.3.13	Conceptual model of Robinson (1991b)	59
2.3.14	Probability map of the positive eddy and streaks	60
2.3.15	Turbulent boundary layer outer edge	61
2.3.16	Flow visualisation of outer layer	62
2.3.17	Outer layer sketch from Falco (1977)	63
2.4.1	The self-sustaining process. From Waleffe and Kim (1997)	64
2.4.2	Redistribution of streamwise velocity U by streamwise vortices	65
2.4.3	Hairpin formation from Zhou <i>et al.</i> (1999)	67
2.4.4	Hairpin concept from Adrian <i>et al.</i> (2000)	68
2.4.5	Hairpin packet form Adrian <i>et al.</i> (2000)	69
2.4.6	Eruption follows a merging event of near-wall structures	70
2.4.7	Structure supporting cycle	71
2.4.8	The role of hairpins	71
2.4.9	Kim (2005)'s self-sustaining process	72
2.5.1	Suction control	72
2.5.2	Results from Kerho (2002)	73
2.5.3	Flow structure with oscillation	74
2.5.4	Choi (1998)'s model	75
2.6.1	Thibault and Rossi (2003)'s EM actuator	76
2.6.2	Spanwise velocity due to oscillation	76
2.6.3	Du (2002)'s Lorentz forces	77
2.6.4	Different forms used by Du <i>et al.</i> (2002)	77
2.6.5	Actuators used in the DNS of Du <i>et al.</i> (2002)	78
2.6.6	Phasing strategy used by Du <i>et al.</i> (2002)	78
2.6.7	Lorentz forces from Du <i>et al.</i> (2002)	79
2.6.8	Some results from Du <i>et al.</i> (2002)	80
2.6.9	Drag history from Du <i>et al.</i> (2002)	81
2.6.10	Phase averaged velocity from Du <i>et al.</i> (2002)	82

2.6.11	Lorentz forcing actuator from Breuer et al (2004)	83
2.6.12	Results from Breuer et al (2004)	84
3.2.1	Water channel setup	108
3.3.1	Setup for trailing flap angle adjustment	109
3.3.2	Flow visualisation	110
3.3.3	Diffuser	112
3.3.4	Supporting frame	114
3.3.5	PSD results before and after the supporting frame	115
3.3.6	Heat exchanger to control the injection solution temperature	116
3.4.1	Injection slot	117
3.4.2	Arrangement of the injection system	118
3.4.3	Check of the injection effects	119
3.4.4	Contaminated water	120
3.5.1	Configuration of the electro-magnetic units	121
3.5.2	Top view of the electrode sheet	122
3.5.3	Upper frame of the magnet holder	123
3.5.4	Force form and voltage	123
3.5.5	Phasing strategy	124
3.5.6	Laser gauge	124
3.5.7	Surface measurement result	125
3.6.1	Top view of the test plate	126
3.6.2	Boundary type hot-film probe	126
3.6.3	Dimensions for the hot-film sensor	127
3.6.4	Constant Temperature Anemometer sketch	127
3.6.5	A CTA unit	128
3.6.6	Signal used for low-speed calibration	128
3.6.7	Calibration curve	129
3.8.1	Control unit	129
3.8.2	Required signal output	130
3.8.3	Sample control signal	131
3.8.4	Illustration of the simultaneous samples of velocity & voltage	131
3.8.5	Comparison of the mean velocity profile with DNS	132
3.8.6	Comparison of the skewness profile with DNS	132
3.8.7	Comparison of the kurtosis profile with DNS	133
4.1.1	Correlation between the dye stripe and streak	150
4.2.1	Flow visualisation of the turbulent boundary layer	153
4.2.2	Sweeps	155
4.3.1	Mean velocity profiles with Lorentz force spanwise oscillation	156
4.3.2	Turbulent intensity with Lorentz force spanwise oscillation	156
4.3.3	Skewness with Lorentz force spanwise oscillation	157
4.3.4	Kurtosis with Lorentz force spanwise oscillation	157
4.3.5	Structure comparison	158
4.4.1	Flow visualisation setup without flow	159
4.4.2	Flow visualisation without flow in the drag reducing case	160
4.4.3	Flow visualisation without flow in the drag increasing case	161
4.4.4	Flow field for visualisation with flow	161
4.4.5	Flow visualisation with flow in the drag reducing case	167
4.4.6	Summary of the effects in drag reducing case	168
4.4.7	Flow visualisation with flow in the drag increasing case	169
4.4.8	Velocity distribution in the drag increasing case	168

5.2.1	Near wall velocity gradient	196
5.2.2	Skin-friction drag reduction at different T^+	196
5.2.3	Skin-friction drag reduction at different St	197
5.3.1	Mean velocity profiles for cases without and with control	197
5.3.2	inner scale profiles for cases without and with control	198
5.3.3	Turbulent intensity profiles	198
5.3.4	Inner-scaled mean velocity profiles at $T^+ = 42$; $St = 232$	199
5.3.5	Turbulent intensity profiles for $T^+ = 42$; $St = 232$. DR = 28.9%	199
5.3.6	Skewness profiles for $T^+ = 42$; $St = 232$. DR = 28.9%	200
5.3.7	Kurtosis profiles for $T^+ = 42$; $St = 232$. DR = 28.9%	200
5.3.8	Inner-scaled mean velocity profiles for $T^+ = 17$; $St = 232$	201
5.3.9	Turbulent intensity profiles for $T^+ = 17$; $St = 232$. DR = -22.8%	201
5.3.10	Skewness profiles for $T^+ = 17$; $St = 232$. DR = -22.8%	202
5.3.11	Kurtosis profiles for $T^+ = 17$; $St = 232$. DR = -22.8%	202
5.4.1	Energy spectra for $T^+ = 42$; $St = 232$. DR = 28.9%	204
5.4.2	Energy spectra for $T^+ = 17$; $St = 232$. DR = -22.8%	205
5.4.3	PDF for $T^+ = 42$; $St = 232$. DR = 28.9%	207
5.4.4	PDF for $T^+ = 17$; $St = 232$. DR = -22.8%	208
5.5.1	VITA detection scheme	209
5.5.2	Ensemble averaging VITA events	209
5.5.3	VITA for $T^+ = 42$; $St = 232$. DR = 28.9%	210
5.5.4	VITA for $T^+ = 17$; $St = 232$. DR = -22.8%	211
5.6.1	Spanwise correlation of u for $T^+ = 42$; $St = 232$. DR = 28.9%	213
5.6.2	Spanwise correlation of u for $T^+ = 17$; $St = 232$. DR = -22.8%	214
5.7.1	Lorentz forces with timing	215
5.7.2	Drag reduction with timing for $T^+ = 17$; $St = 232$. DR = -22.8%	215
5.7.3	Drag reduction with timing for $T^+ = 42$; $St = 232$. DR = 28.9%	215
5.7.4	Lorentz forcing effects in the drag increasing case	216
5.7.5	Correlation profiles for $T^+ = 17$; $St = 232$. DR = -22.8%	217
5.7.6	Correlation profiles for $T^+ = 42$; $St = 232$. DR = 28.9%	217
5.7.7	Drag ratio for $T^+ = 17$; $St = 232$. DR = -22.8%	218
5.7.8	Drag ratio for $T^+ = 42$; $St = 232$. DR = 28.9%	218
5.7.9	Phase averaged momentum in the drag reducing case	219
5.7.10	Phase averaged momentum in the drag increasing case	219
5.7.11	Mechanism of travelling wave in the drag increasing case	221
5.7.12	Mechanism of spanwise oscillation	221
5.7.13	Streamwise vorticity layers induced in drag increasing case	222
5.8.1	Conceptual model for drag-reducing case	223
5.8.2	Conceptual model for drag-increasing case	224

Chapter 1

Introduction

Research has shown that the turbulence regeneration cycle is associated with the near-wall region (Jimenez & Pinelli 1999) and coherent structures seem to play an important role in the production of turbulence (Schlichting 1979; Murlis et al. 1982; Hussain 1986), which suggests near-wall structures are potential targets for the application of turbulent flow control. One of the strategies for drag reduction is to modify or disturb any part of the near-wall activities (Karniadakis & Choi 2003). A lot of research has been performed with this aim to achieve drag reduction. For example, active control using blowing and suction (Choi et al. 1994; Lee & Kim 1998; Meng et al. 1998), a large-scale control strategy applied to the turbulent flow with the aim of stabilising the low-speed streaks (Schoppa & Hussain 1998) and the transverse motions used to weaken the streamwise vortices (such as Du et al. 2002). Of interest are the near-wall low-speed streaks that play a crucial part in determining the skin friction and producing the turbulent kinetic energy (Adrian 2007), with Adrian et al. (2000) observing the low-speed streaks in the outer layer, as well. It is commonly accepted that the low-speed streaks are the collection of slow fluid motions (Kim et al. 1971) and considered to be associated with the quasi-streamwise vortices (Kline et al. 1991).

During the studies on flow control, the electro-magnetic (Lorentz) force attracts some researchers' attention. Generated when an electrically conducting fluid flows through an electromagnetic field, the Lorentz force is a body force that is non-intrusive to the flow. It allows many different types of

control to be introduced, for instance, streamwise force control (Henoeh & Stace 1995), wall-normal blowing or suction (Nosenchuck & Brown, 1996), spanwise oscillation (Berger et al 2000; Pang & Choi 2004; Breuer et al 2004) and spanwise travelling wave (Du et al. 2000 and 2002). Due to these benefits, the flow control by Lorentz forcing (called Electro-Magnetic Turbulence Control) has been extensively studied in the past decade.

In this thesis, the Lorentz-forcing spanwise travelling wave is studied through experiments. It is the first experimental study of the turbulent flow control by spanwise travelling wave actuation via Lorentz forcing. The aim is to find the effects of the spanwise travelling wave actuation and to better understand its mechanisms. To achieve this, the velocity profiles and turbulent statistics with and without Lorentz forcing are obtained using hot-film anemometry. Flow visualisations are performed to help the understanding of the functions of the low-speed streaks in this flow control technique.

Chapter 2 provides a brief literature review on turbulent boundary theory, coherent structures and turbulence regeneration cycles. It is followed by a discussion of drag reduction strategies. Finally, a general description of drag reduction techniques is presented, with an emphasis on Electro-Magnetic Turbulence Control.

In Chapter 3, an experimental arrangement is introduced with a focus of on the author's contributions.

Chapter 4 introduces the spanwise motion induced by the Lorentz-forcing spanwise travelling wave excitation with flow visualisation and velocity profiles. The flow visualisation and statistical data of the spanwise oscillation

are presented to verify the electrode pattern and show the differences between spanwise oscillation and spanwise travelling wave.

Chapter 5 shows the velocity measurements of a turbulent boundary layer with and without spanwise travelling wave actuation. Both drag reduction and drag increase are observed and the mechanisms are proposed.

In Chapter 6 the conclusions and future work are presented. Finally, Appendix 1 shows the IUTAM paper published in 2008 and Appendix 2 shows the calibration curves from the manufacturer of the flow meter.

Chapter 2

Literature Review

2.1. Introduction

The study of turbulence has been carried out since Osborne Reynolds in 1883 according to record (Kline 1991). Figure 2.1.1 shows the differences between laminar and turbulent flows. By showing the study of flows over solid surfaces (Prandtl, 1905), Ludwig Prandtl might have been the first person to document the study of the boundary layer.

Due to the fact that the turbulent boundary layer produces significantly higher skin-friction drag than the laminar boundary layer and due to the flow being turbulent in most practical situations because of high Reynolds numbers, it is obvious that the turbulent boundary layers attract much more attention and efforts of researchers who have tried to understand the fluid motions (George and Castillo 1997) to achieve their flow-control objectives.

However, in turbulence, the theoretical equations do not give the entire theory (Tennekes and Lumley 1997). Large-scale three-dimensional turbulence is still a big challenge to researchers and one of the most complicated aspects of turbulence studies (Branover et al. 2004). One must be willing to use (and be capable of using) simple physical concepts based on experience to bridge the gap between the equations and the actual flows (Tennekes and Lumley 1997).

2.2. Outline of Turbulent Boundary-Layer Theory

It is very difficult to precisely define turbulence. But turbulence can be described by the characteristics of turbulent flows (Tennekes and Lumley 1997), which is shown below.

Irregularity or randomness is one characteristic of all turbulent flows. This makes the approach to turbulence problems count on statistical methods.

The diffusivity of the turbulence, which causes the increasing rates of momentum, heat and mass transfers, is the second important feature of all turbulent flows. If a flow pattern does not exhibit spreading of velocity fluctuations through the surrounding fluid, it surely is not turbulent.

Thirdly, large Reynolds number always accompanies turbulent flows. The turbulence often originates as instability in laminar flows if the Reynolds number becomes large enough. The instability is related to the interaction of viscous terms and nonlinear inertia terms in the equations of motion. This interaction is very complex. One cannot rely on the equations alone to obtain the answers, because the theoretical approaches to problems in turbulence research are still at a trial-and-error stage. Turbulence research is still one of today's major unsolved myths in physics (Tennekes and Lumley, 1997).

The three-dimensional vorticity fluctuations are the fourth characteristic of turbulent flows (Tennekes and Lumley, 1997). Turbulence is rotational and three dimensional and is characterised by high levels of fluctuating vorticity. The random vorticity fluctuations that characterise the turbulence could not maintain themselves if the velocity fluctuations are two dimensional, since an important vorticity maintenance mechanism, known as vortex stretching, is absent in two-dimensional flow.

Fifth, turbulent flows are always dissipative. Viscous shear stresses increase the internal energy of the fluid at the expense of the kinetic energy of turbulence. The turbulence needs a continuous supply of energy to make up for these viscous losses. If no energy is supplied, the turbulence decays rapidly. In other words, the major distinction between random waves and turbulence is that waves are essentially nondissipative (though they often are dispersive), while the turbulence is essentially dissipative.

The continuum phenomenon is another feature of turbulence that is governed by the equations of fluid mechanics.

Last but not least, turbulent flows are flows and turbulence is not a feature of fluids but of fluid flows. The major characteristics of turbulent flows are not controlled by the molecular properties of the fluid in which the turbulence occurs. Since the equations of motion are nonlinear, each individual flow pattern has unique characteristics that are associated with its initial and boundary conditions.

2.2.1 The Reynolds Equations

In turbulence, a description of the flow at all points in time and space is not feasible (Tennekes and Lumley 1997). Instead, following Reynolds (1895), scientists have developed equations governing mean quantities, such as the mean velocity (Tennekes and Lumley, 1997). The equations of motion of an incompressible fluid are:

$$\frac{\partial \tilde{u}_i}{\partial t} + \tilde{u}_j \frac{\partial \tilde{u}_i}{\partial x_j} = \frac{1}{\rho} \frac{\partial}{\partial x_j} \tilde{\sigma}_{ij} \quad (2.2.1)$$

$$\frac{\partial \tilde{u}_i}{\partial x_i} = 0 \quad (2.2.2)$$

Here, $\tilde{\sigma}_{ij}$ is the stress tensor. Repeated indices in any term indicate a summation over all three values of the index; a tilde denotes the instantaneous value at (x_i, t) of a variable.

If the fluid is Newtonian, the stress tensor $\tilde{\sigma}_{ij}$ is given by

$$\tilde{\sigma}_{ij} = -\tilde{p}\delta_{ij} + 2\mu\tilde{s}_{ij} \quad (2.2.3)$$

In equation (2.2.3), δ_{ij} is the Kronecker delta, which is equal to one if $i = j$ or zero otherwise; \tilde{p} is the hydrodynamic pressure and μ is the dynamic viscosity. The rate of strain \tilde{s}_{ij} is defined by

$$\tilde{s}_{ij} = \frac{1}{2} \left(\frac{\partial \tilde{u}_i}{\partial x_j} + \frac{\partial \tilde{u}_j}{\partial x_i} \right) \quad (2.2.4)$$

If equation (2.2.3) is substituted into equation (2.2.1) and if the continuity equation (2.2.2) is invoked, the Navier-Stokes equations are obtained:

$$\frac{\partial \tilde{u}_i}{\partial t} + \tilde{u}_j \frac{\partial \tilde{u}_i}{\partial x_j} = \frac{1}{\rho} \frac{\partial \tilde{p}}{\partial x_i} + \nu \frac{\partial^2 \tilde{u}_i}{\partial x_j \partial x_j} \quad (2.2.5)$$

Here, ν is the kinematic viscosity ($\nu = \mu/\rho$)

For a statistically steady and isothermal flow of a Newtonian fluid the continuity equation (2.2.2) and Navier-Stokes (momentum) equation (2.2.5) can be written into the related time-mean governing equations (2.2.6) and (2.2.7), (Bruun 1995)

$$\frac{\partial U_i}{\partial x_i} = 0 \quad (2.2.6)$$

$$U_j \frac{\partial U_i}{\partial x_j} = \frac{1}{\rho} \frac{\partial P}{\partial x_i} + \nu \frac{\partial}{\partial x_j} \left(\frac{\partial^2 U_i}{\partial x_j \partial x_j} - \overline{u'_i u'_j} \right) \quad (2.2.7)$$

Here, the capitalised U denotes the time-mean value; u' is the velocity fluctuation; $\tilde{u} = U + u'$.

2.2.2 The Law of the Wall in Turbulence

Turbulence cannot sustain itself and cannot generate Reynolds stresses if y^+ is small, $y^+ = y \times \nu / u_\tau$, where y is the wall normal distance and u_τ is the friction velocity. The details are explained in Chapter 5. Experimental evidence has confirmed this and shown that this region is up to about $y^+ = 5$, which is called the viscous sublayer. In the viscous sublayer, the velocity fluctuations do not contribute much to the total stress because of the overwhelming effects of viscosity. The velocity profile must be linear ($u^+ = U/u_\tau = y^+$) when the Reynolds stress is neglected (Balachandar and Ramachandran 1999).

Meanwhile the velocity profile in the log layer must satisfy the logarithmic law at large y^+ (Tennekes and Lumley, 1997), whose relationship is commonly

$$u^+ = \frac{1}{k} \ln(y^+) + A \quad (2.2.8)$$

Here, $k = 0.41$ is the von-Karman constant and $A = 5.0$ (Nezu, I., and Nakagawa, H., 1993).

Figure 2.2.1 shows the experimentally obtained velocity profiles. The region where neither the viscous nor Reynolds stresses can be neglected is called the buffer layer. The turbulent production rate reaches the maximum in this layer around $y^+ = 12$.

In summary,

Viscous sublayer: $0 \leq y^+ < 5$ $u^+ = y^+$

Buffer layer: $5 < y^+ < 30$

Log layer: $y^+ \geq 30$ $u^+ = 1/k \cdot \ln y^+ + A$

2.2.3 Some Statistical Quantities in the Study of Turbulence

In figure 2.2.2 the levels of velocity $\tilde{u}(t)$ are scanned by an electronic “window” of Δt . The output signal is shown below $\tilde{u}(t)$. By adjusting the electronic “window” successively to different heights, a function similar to the one shown to the right of $\tilde{u}(t)$ is obtained, and this function is called the probability density, denoted as $B(u)$ here (Tennekes and Lumley 1997).

The mean square departure σ^2 from the mean value U is called the variance, or second (central) moment (Tennekes and Lumley 1997). It is defined by

$$\sigma^2 \equiv \overline{(u')^2} \quad (2.2.8)$$

The square root of the variance is called the standard deviation or root-mean-square (rms) amplitude. The standard deviation is the most convenient measure of the width of $B(u)$.

The third moment, however, $(u')^3$ only depends on the lack of symmetry in $B(u)$. If $B(u)$ is symmetric about the origin, $\Sigma(u')^3 = 0$. Nondimensionlising $(u')^3$ by σ^3 gives a dimensionless measure of the asymmetry, which is called the skewness (S):

$$S \equiv \overline{(u')^3} / \sigma^3 \quad (2.2.9)$$

Figure 2.2.3 shows a function with a positive value of S . The skewness is positive because the large negative values of $(u')^3$ are not as frequent as large positive values.

The fourth moment, nondimensionlised by σ^4 , is called the kurtosis factor; it is represented by the symbol K :

$$K \equiv \overline{(u')^4} / \sigma^4 \quad (2.2.10)$$

Two functions, one with a relatively small and the other with a relatively large kurtosis, are sketched in figure 2.2.4. The value of the kurtosis is large if the values of $B(u)$ in the tails of the probability density are relatively large. The peaky function in figure 2.2.4 frequently takes on values far away from the axis, therefore its kurtosis is large. Kurtosis is also called a flatness factor due to its shape. For normal distribution $K = 3$ and $S = 0$.

The transport in real flows generally is inhomogeneous and nonstationary (Tennekes and Lumley 1997). This is the heart of the turbulence problem. Unfortunately, it is impossible to describe the details of the fluid transport in other than very simple cases.

Averages of products are computed in the following way.

$$\overline{\tilde{u}_i \tilde{u}_j} = \overline{(U_i + u'_i)(U_j + u'_j)} = U_i U_j + \overline{u'_i u'_j} \quad (2.2.11)$$

The terms consist of a product of mean values and fluctuations respectively. The mean value is a coefficient as far as the averaging is concerned and the average of a fluctuating quantity is zero.

If $\overline{u'_i u'_j} \neq 0$, u_i and u_j are said to be correlated; if $\overline{u'_i u'_j} = 0$, the two are uncorrelated. A measure for the degree of correlation between the two variables u_i' and u_j' is obtained by dividing $\overline{u'_i u'_j}$ with the square root of the product of the variances $(\overline{u'^2})_i$ and $(\overline{u'^2})_j$. This gives a correlation coefficient C_{ij} , which is defined by

$$C_{ij} = \overline{u'_i u'_j} / ((\overline{u'^2})_i \cdot (\overline{u'^2})_j)^{1/2} \quad (2.2.12)$$

If $C_{ij} = \pm 1$, the correlation is said to be perfect. Each variable, of course, is perfectly correlated with itself. A transverse correlation is shown in figure 2.2.5.

The energy exchange between the mean flow and the turbulence is governed by the dynamics of the large eddies according to Tennekes and Lumley (1997). “Large eddies contribute most to the turbulence production because turbulence production increases with eddy size. The energy extracted by the turbulence from the mean flow thus enters the turbulence mainly at scales comparable to the integral scale.”

The viscous dissipation of turbulent energy, on the other hand, occurs mainly at small scales, which implies that the internal dynamics of turbulence must transfer energy from large scales to small scales. Of course, turbulence can maintain itself only if it receives a continuous supply of energy.

2.3. Coherent Structures in Turbulent Boundary Layers

The descriptions of coherent structures were initially found from flow visualisation studies. More attention has been paid to coherent structures recently and their importance has been well recognised (Schlichting 1979; Murlis et al. 1982; Hussain 1986; Babiano & Provenzale 2007; Guala, M. et al. 2007; Mans et al. 2007).

Coherent structures are the small regions within the turbulent boundary layer with correlation either in space or time or both and have their own properties. The shapes and sizes of the regions are as diverse as the methods used to find them. Robinson (1991a) described it as a three-dimensional region of flows that exhibits significant correlation with itself or with other flow variables over a range of space and time, which is significantly larger than the smallest local scales of the flow. Babiano and Dubos (2005) found that the strongly energetic regions where the energy transfer occurs are mostly localised around

the coherent structures. This again suggests the importance of coherent structures in sustaining turbulence within boundary layers because the turbulence needs to be maintained with continuous energy input.

Generally, coherent structures consist of low/high speed streaks, ejections and sweeps, and vortical structures etc. The coherent structure details are discussed in the following sections. Please note it does not mean each structure is independent from others although they are discussed in separate sections.

2.3.1 Low and High-speed Streaks

When talking about near-wall coherent structures, one of the most observable features has to be mentioned, which are low-speed streaks. These were found by Kline et al. (1967) via flow visualisation of hydrogen bubbles in the near-wall region of a water channel, as shown in Figure 2.3.1. The white bubble areas correspond to the low-speed streaks (Smith and Metzler, 1983). A similar result is shown in Figure 2.3.2 that demonstrates the visualisation of the low-speed streaks with a laser sheet and fluorescent dye. A photograph showing smoke flow visualisation of low-speed streak structures in a turbulent boundary layer (Mathieu and Scott, 2002) is shown in Figure 2.3.3 from cross-section views where the low-speed streaks are divided by smoke wires along the flow direction.

The streaks are recognised as the collection of near-wall low-speed fluid, which has been verified by experimental measurements and numerical calculations (Chernyshenko and Baig, 2005). Results obtained with the combined PIV and dye visualisation technique (Mans et al. 2007) clearly illustrate that the low-speed streaks consist of slow motion fluids (negative

velocity fluctuations) as shown in Fig. 2.3.4, which also provides direct connection between the dye stripe and the low-speed streak.

According to Kline et al. (1976), these ‘low-speed streaks’ occur from very close to the wall ($y^+ < 1$) to around $y^+ = 50$ and extend for a streamwise distance of up to $x^+ = xu_\tau/\nu \approx 1000$. Although these low-speed streaks occur randomly in space and time, the average spanwise streak spacing is $z^+ = zu_\tau/\nu \approx 100$. These dimensions have been confirmed by many researchers (such as Blackwelder, 1997). Furthermore, an average interval between bursts of $T^+ = 300(\nu/u_\tau^2)$ is observed by Blackwelder and Kaplan (1976).

These elongated flow features are noticed to move along the wall, migrate slowly and lift upwards. They begin to oscillate at around $y^+ \approx 8 \sim 12$ and this oscillation amplifies as it moves outward further into the faster flow zone, often experiencing a violent oscillation or break-up and moving rapidly away from the surface. When these rapid outward movements occur, the lifted low-speed streaks are believed to become involved in large-scale fluctuations (Kline et al., 1976; Blackwelder, 1997; Kerho, 2002). Furthermore, it is clear that vortices are present in the high shear region in between the high and low-speed streaks (Mans et al., 2007).

Because the viscous shear stress causes the kinetic energy of the turbulence to dissipate, the turbulence needs a continuous supply of energy to make up the losses. Klebanoff (1954) found that the majority of the turbulent energy production occurs just outside the viscous sublayer. Kline *et al.* (1967) pointed out that the lifting and break-up of low-speed streaks possibly play an important role in the production of Reynolds stress and turbulent kinetic energy. A number of researchers have confirmed the existence of the

low/high-speed streaks and, furthermore, the interactions of the low-speed streaks with the flow of the outer layer is a prominent feature in the process of transferring energy between the inner and outer regions of the boundary layer (Corino and Brodkey 1969; Clark and Markland 1971; Hanratty 1956; Grass 1971; Kim et al. 1971; Blackwelder 1997; Meng 1997; Kerho 2002).

Although it is generally agreed that streaks contribute to the generation of turbulent energy, there is no generally accepted view on the mechanism of the streak formation and numerous competing theories and conceptual models exist (Chernyshenko and Baig 2005).

Generally, the existence of the pattern of slow longitudinal motion regions is explained by assuming the existence of a pattern of the wall-normal motion.

One of the oldest (Stuart 1965) patterns is longitudinal vortices as illustrated in figure 2.3.5 (b). “Rows of vortices elongated in the direction of the mean flow and rotating in alternating directions capture the fluid and transport it from the wall and to the wall in alternating stripes. The fluid transported from the wall is moving slower than on average at this distance from the wall, while fluid advected to the wall is moving faster. This creates the wavy longitudinal velocity profile at a fixed distance from the wall.” (Chernyshenko and Baig, 2005).

Similarly, Kline et al (1967) proposed a mechanism of the formation and breakup of the streaks as seen in figure 2.3.6, which is that the streaks form from the result of vortex stretching due to large fluctuations acting on the flow near a smooth wall in the presence of a strong mean strain. The production of the turbulence near the wall in such a flow arises primarily from a local, short-duration, intermittent dynamic instability of the instantaneous velocity profile.

A hairpin vortex is thought as another candidate for the pattern of wall-normal motions responsible for the streaks (Smith & Metzler, 1983), whose definition is discussed in the following section 2.3.3. In this case, the low speed regions directed away from the wall are not necessarily elongated itself, but when moving downstream with the hairpin vortex, this region leaves behind a trace in the form of an elongated streak. Kerho, M., (2002) provides a conceptual model of a low-speed streak formation and burst adapted from Kim et al. (1971) and Smith & Walker (1997) as seen in figure 2.3.7. Other patterns of wall normal motions generating streaks are also proposed (Jang, Benney & Gran 1986; Sreenivasan 1988; Brooke & Hanratty 1993; Waleffe, Kim & Hamilton 1993; Hamilton, Kim & Waleffe 1995; Schoppa & Hussain 1998 and Waleffe 2003).

Joshi and Rempfer (2007) found there is a significant correlation between the magnitude of the velocity vectors and the magnitude of nonlinear energy. Therefore, the low and high-speed streaks can be located at various scales and correlated with the energy transfer in the near-wall region. Generally, there is a positive energy transfer when the fluid moves away from the wall (ejections) and negative energy transfer when the fluid is moving towards the wall (sweeps), which is discussed in the next section.

2.3.2 Ejections and Sweeps

The word ‘ejection’ was used by Kline et al. (1967) to describe the motion of low-speed streaks being oscillated and moved outwards away from the wall. This movement of the low-speed fluid is thought to have a contribution to the production of the Reynolds stress in the turbulent boundary layer in the region beyond $y^+ = 12$. Ejections have been treated by many dynamical models as an

instability mechanism in the early stages of coherent studies (Kline et al. 1967; Kim et al. 1971; Meng 1997; Corino et al. 1969).

Corino and Brodkey (1969), however, emphasised the importance of large-scale motions of accelerated flow towards the wall which are called 'sweeps'. The sweep seems to lead to an increase in the velocity gradient by transferring high momentum fluid towards the wall and increases the local wall-shear stress. Following their results, Corino and Brodkey (1969) proposed an early model for the regeneration cycle of the near-wall turbulence: a lift-up of the low-speed fluid from the wall, with distinct eruptions or ejections of the fluid into the outer-region, leading to a regeneration cycle and generating a large percentage of the Reynolds stresses.

Grass (1971) also delineated the importance of "sweeps" (+u, -v motions) in the near wall region. By using the hydrogen bubble technique combined with the time-streak marker, Kim et al. (1971) demonstrated that the turbulence production during the lifting of the low-speed streak is very high. Wallace et al. (1972) showed that the contribution to the Reynolds stress by sweeps and ejections are nearly 70% each at $y^+ \approx 15$, giving a total of 140% production. However, the wall-ward and outward interactions give negative contributions of 20% each (40% total deduction), balancing the Reynolds stress production (140% - 40% = 100%). In addition, the sweep events are found to contribute more to the turbulent production in the near wall region. Similar results are found by Willmarth and Lu (1972) and Lu and Willmarth (1973), with the frequencies and durations of ejections and sweeps being about the same.

A 'bursting cycle' was proposed by Offen and Kline (1975). They observed that the sweeps act to induce an adverse pressure gradient above a low-speed

streak. This would initiate the ‘bursting cycle’ by lifting the low-speed streak away from the wall. However, following the ‘ejection’, they observed an inrush of high momentum fluid to splash against the wall to replace the ejected low momentum fluid. This ‘sweep’ forms the new low-speed streaks at the location between the old streaks, which thus closes the chain of turbulence energy producing events.

Blackwelder and Kaplan (1976) applied the conditional sampling technique of Variable Interval Time Averaging (VITA) to turbulence research. The VITA technique is based on the correlations between the rapidly changing quantities (e.g. velocity) and the turbulent events, such as sweeps. Figure 2.3.8a shows the conditionally averaged velocity profiles and the corresponding time-averaged mean velocity profiles. By tracking typical sweep events, Blackwelder and Kaplan (1976) observed that before the sweep ($-3.1\text{ms} < \tau < 0\text{ms}$, $\tau = 0$ corresponds to the time of detection) there is an inflectional velocity profile, similar to the observation by Kline et al. (1967). Blackwelder and Kaplan (1976) also found that the events seem to affect a large region of the boundary layer, as seen in figure 2.3.8b that shows the magnitude of the burst event throughout the boundary layer and the signals are highly correlated along the wall normal direction.

According to the discussions above, the majority of the turbulent production in the entire boundary layer occurs in the buffer layer through the events of ‘ejections’ and ‘sweeps’. The ejection and the turbulent bursting process are responsible for 80% of the total shear stress generated in the boundary layer (Coustols, E., 1996). Additionally, Orlandi and Jimenez (1994) showed that the transport of high momentum fluid towards the wall (‘sweeps’) is more

important than the low momentum fluid moving away from the wall ('ejection') for the induction of high skin-friction in the turbulent boundary layer.

These features will be discussed throughout the following sections especially when the turbulent regeneration cycle is discussed.

2.3.3 Vortical Structures

Much research and effort has been made to study dominant vortical structures throughout the whole boundary layer (Kovasznay 1970; Willmarth and Lu 1972; Lu and Willmarth 1973; Blackwelder and Kaplan 1976 and Sherman 1990). These vortical structures have many varieties in shapes and functions.

Theodorsen (1952) suggested that those responsible for the transfer of momentum and heat are three-dimensional flow patterns, shown as horseshoe or ring-shaped structures (refer to figure 2.3.9). These structures are proposed to be everywhere in wall-bounded turbulent flows but with different scales.

With the correlation measurement, Townsend (Townsend 1956) found that the dominant structures near the wall are tilted vortices and he pointed out that these vortices are initially streamwise but are tilted upward in the downstream direction. Townsend (1956) also proposed eddies' Reynolds-number similarity hypothesis that is confirmed by Kunkel, G. J. and Marusic, I., (2006).

Early observations by Kline *et al.* (1967) suggested that streamwise vortices are responsible for the streaky structures. Basing on his DNS study in the near-wall region of the turbulent boundary layer, Robinson (1991) showed that the near-wall region contains counter-rotating vortices oriented and tilted downstream, much like the structures suggested by Townsend (1956). He

pointed out the quasi-streamwise vortices are the fundamental feature of the near-wall turbulence. Jeong, J. et al. (1997) showed that the dominant near-wall educed coherent structures are highly elongated quasi-streamwise vortices and the vortices are inclined 9° in the vertical (x, y) plane and tilted 4° in the horizontal (x, z) plane. The vortices of alternating sign overlap in x as a staggered array. In particular, the vortices tilting (in the (x, z) plane) are found to be responsible for sustaining the coherent structures through the redistribution of streamwise turbulent kinetic energy to normal and spanwise components via coherent pressure (strain effects).

The importance of the quasi-streamwise vortices has also been recognised by other researchers (such as Corino and Brodkey 1968; Smith and Schwartz 1983; Kline and Robinson 1988).

While the buffer layer contains tilted streamwise vortices, Robinson observed the outer layer consists of transverse vortices and the log layer holds possibly both. Hutchins and Marusic (2007) found a regime of very long meandering positive and negative streamwise velocity fluctuations in the log and lower wake regions of turbulent boundary layers. The length of these structures can commonly exceed 20δ . They argued that this ‘superstructure’ maintains a presence or footprint in the near-wall region, seeming to modulate or influence the near-wall cycle. This input of low-wave-number outer-scaled energy into the near-wall region is consistent with the rise in near-wall streamwise intensities.

Hairpin structures were observed by Head and Bandyopadhyay (1981) experimentally with the smoke flow visualisation. They provided images obtained with various light-sheet configurations which appeared to cut, or not,

the axis of the vortex tubes depending on the orientation of the light sheet. The selected configurations are a longitudinal plane normal to the wall and two transverse planes inclined, respectively, at an angle of 45° upstream and 45° downstream (see figure 2.3.10). They concluded that the hairpin vortices are the major components of a turbulent boundary layer at all Reynolds numbers and the shapes are as seen in figure 2.3.11.

Robinson (1991a and 1991b), defined the hairpin structures with three parts, the legs, neck and head as shown in figure. 2.3.12. He figured that these structures commonly appear more asymmetrically rather than symmetrically. This was recognised by Moin and Kim (1985) as well. Robinson (1991a and 1991b) also proposed a possible relation among quasi-streamwise vortices, hairpin vortices and low-speed streaks, as shown in figure. 2.3.13.

With the more advanced Particle Image Velocimetry (PIV), Liu et al. (1991) observed the length of the hairpins seems to be limited only by the boundary layer thickness, δ , regardless of Reynolds number. Carlier and Stanislas (2005) studied the coherent structures taking part in the generation and preservation of wall turbulence with PIV as well. The eddy structures are identified in instantaneous velocity maps in order to determine their mean characteristics and possible relationships amongst these structures. In the logarithmic region, the results show that the observed eddy structures appear to organise like elongated vortices, tilted downstream, mainly at an angle of about 45° and having a 'cane' shape. They seem to originate at 25 wall units away from the wall as quasi-streamwise vortices and migrate away from the wall while tilting to form the head and legs of a hairpin. Away from the wall their circulation is nearly constant resulting from the increased radius and the decreased vorticity

(Carlier and Stanislas 2005). Figure 2.3.14(a) gives the probability of finding a positive eddy structure in the velocity field when a high-speed streak is located at $y^+ = 15$ in the (y, t) plane. A peak is clearly observable in the immediate vicinity of the high-speed streak, showing that the eddy structures are relatively often associated with these streaks. This also is true for the low-speed streaks, as illustrated by figure 2.3.14(b). The level and the size of the regions of the highest probability indicate that the possibilities that the plane cuts these two types of coherent structure (vortices and streaks) simultaneously are fairly high (Carlier and Stanislas 2005).

Adrian et al. (2000) observed that the hairpin structures expand from $y^+ \approx 50$ to the edge of the turbulent boundary layer. A concept of hairpin ‘packets’, an alignment of many such vortices, is employed to explain most of the observed behaviour in a turbulent boundary layer, owing to the fact that the low-speed streaks associated with individual vortices are only a few hundred viscous wall units long (Zhou et al. 1999). Adrian et al. (2000) found greater coherence in the streamwise components than in the wall-normal and spanwise components because of the streamwise alignments of the vortices. Hence, the correlation length of the streamwise velocities is much longer than the correlation lengths of the other two components. The individual vortex member contributes to the Reynolds stress and the wall-normal turbulence locally, owing to the limited spatial coherences of the vortical components. They interpreted this as smaller-scale active or universal motions. The nesting of smaller packets within larger ones, which are within even larger ones, and so on, creates the appearance of multiple zones of the uniform streamwise momentum, which is an observed characteristic of the logarithmic layer (Meinhart & Adrian 1995).

Kline and Robinson (1989a and 1989b) attempted to class the coherent motions. Apart from the structures mentioned in the previous sections, they proposed strong near-wall shear layers and large δ -scale bulges in the outer region of the boundary layer. Of those structures, the vortical structure is thought one of the most important (Kline and Robinson, 1989a and 1989b). It is argued that these vortical structures induce the Reynolds shear stress motions (and thus turbulent kinetic energy production) at their peripheries, while dissipating the energy in their interiors (Diorio et al. 2007).

2.3.4. Outer Region

The outer region of the turbulent boundary layer is usually defined as the region $y/\delta > 0.15$, whereby the action of viscosity becomes less and less dominant. In this region the 'large-scale motions' are known to appear in the form of turbulent bulges (Laufer & Narayanan 1971) whose mean height is $\sim \delta$, mean streamwise length is $\sim 2\delta$, and mean spanwise width is $\sim 1\delta$ – 1.5δ (Kovaszny, Kibens & Blackwelder 1970; Brown & Thomas 1977; Cantwell 1981; Murlis, Tsai & Bradshaw 1982). Figure 2.3.15a shows a side view of a turbulent boundary layer. Because this picture is taken when a flat plate is towed in water and fluorescent dye is used, both layers are shown above and below the plate. However, the upper dye image is the study objective and the edge of the dye indicates the interaction between the turbulence and the outer flow. Figure 2.3.15b illustrates the relationships between the outer edge and the boundary layer thickness.

Figure 2.3.16 presents an example of the smoke wire visualisation taken from the work of Lekakis (1988). In the x - z plane (upper image), the smoke wavers sinuously with a wavelength somewhat greater than $2R$ (where R is $\sim \delta$). The

side view in the middle image shows the smoke extending up to about $0.2R$ in the (x, y) plane, e.g. filling the logarithmic layer. The regions enclosed by boxes (a) and (b) contain patterns of groups of thin, 45° inclined structures consistent with the patterns expected from hairpins (Guala, M. et al. 2006).

Flow visualisation studies by Falco (1977) showed ‘typical eddies’ or ‘Falco eddies’ on the upstream sides of the turbulent bulges, which move towards the wall and are possibly responsible for the ‘sweep’ type motions near the wall (Fig. 2.3.17).

Furthermore, Guala, M. et al. (2006) found the very large-scale motions are energetic, typically containing half of the turbulent kinetic energy of the streamwise component in the outer region of fully developed turbulent flow.

2.3.5 Shallow water waves

Because this study is carried out in an open water channel, the surface wave effects are listed here as background knowledge. Although the water depth and velocity are carefully selected and the flow in this experiment isn’t a shallow water flow, shallow water waves are cited to show the surface wave effects. For shallow water waves, as for instance tidal waves and the hydraulic jump, the characteristic velocity V is the average flow velocity, averaged over the cross-section perpendicular to the flow direction. The wave velocity, c , is equal to the square root of gravitational acceleration g , times cross-sectional area A , divided by free-surface width B :

$$c = \sqrt{g \frac{A}{B}} \quad (2.3.1)$$

For rectangular cross-sections with a uniform depth d , the Froude number can be simplified to:

$$Fr = \frac{U_{\infty}}{\sqrt{gd}} \quad (2.3.2)$$

The Froude number directly relates to the speed of a surface disturbance, and because the increase of the Froude number causes the surface disturbance to increase (Henderson 1966), the effect of the Froude number can be viewed as a perturbation applied to a canonical boundary layer (Balachandar et al. 2001). For $Fr < 1$ the flow is called a subcritical flow, for $Fr > 1$ the flow is characterised as a supercritical flow, and when $Fr \approx 1$ the flow is denoted as a critical flow.

The Froude number is generally assumed to have no effect on the friction characteristic of the open turbulent boundary layer (Chow, 1988). This agrees well with Keulegan's (1938) suggestion that pipe flow formulations could probably be adopted in an open channel flow.

Recently, Balachandar et al. (2001) investigated the characteristics of turbulent boundary layers developing on a smooth flat plate in an open water channel at moderately high Froude numbers ($0.25 < Fr < 1.1$) and low Reynolds numbers ($100 < Re_{\tau} < 2900$) with LDA. They confirmed the skin friction factor is not dependent on the Froude number. They present results that show that the viscous sublayer is insensitive to the imposed disturbance, being more rapid closer to the wall than the overlap region (Tachie, et al., 2001(a) and (b)). There is no apparent Froude number effects on the skewness and kurtosis distributions in the near-wall region either. The log-law is valid, but the turbulent intensity peak value is increased when the Fr number is increased (Balachandar et al. 2001). Balachandar et al (2001) also concluded that the large changes in skewness between the edge of the boundary layer and the free

surface is a unique characteristic of open channel flows and is not reported in zero-pressure gradient flat plate flows.

2.4 Turbulence Regeneration Cycle

The understanding of the near-wall turbulence regeneration cycle is very important for the study of turbulence control and drag reduction strategies. Although many models have been proposed, they can be categorised into parent-offspring or instability based mechanisms (Schoppa and Hussain 2002). One obvious idea implies that certain primary structures appear directly from an unstructured background. They can produce other structures and so on until the last structure in the chain is dissipated by viscosity or destroyed by chaotic motions (Chernyshenko and Baig 2005). So far no general agreement has been reached on what plays the role of the primary structure. Another possibility is the existence of a closed cycle of regeneration of structures (Chernyshenko and Baig, 2005), in which, say, the streamwise vortices produce the streaks and the streaks instability in turn produce the streamwise vortices and so on. The cycle may include more types of structures than these two. In this concept, none of the structures is primary. The details are discussed below.

Although the energy transfer within the turbulent boundary layer is little known, nothing stops the scientists going ahead. Klebanoff (1954) had already shown that the majority of turbulence energy production occurs just outside the viscous sublayer. Kline et al. (1967) explained that the violent ‘ejection’ process seems to play an important part in transferring momentum and energy between inner and outer regions of the boundary layer. Corino and Brodkey (1969) suggested a ‘chain of events’, or ‘bursting cycle’, plays a key role in generating and maintaining the turbulence cycle. The first stage is the lifting-

up of the low-speed streaks from the innermost layer to form an unstable local inflectional velocity profile (Kim et al. 1971). Then a rapid oscillation occurs in the downstream of the inflectional zone. This oscillation leads to a 'break-up'. Following the 'break-up', the oscillatory motions turn into more chaotic modes, accompanied by more quiescent flows and return in the form of the low-speed streaks. Thus the cycle of production and dissipation of the turbulence continues. This process occurs most in the region of $0 < y^+ < 100$. Landahl (1975) suggested that the streak breakdown ('break-up') triggers another breakdown, forming a self-sustaining cycle within the boundary layer. Moreover, Kim, et al. (1971) seemed to have recognised the importance of streamwise vortices to the 'burst' cycle. Investigations of the relationship between the low-speed streaks near the wall and the outer flow field were undertaken by Offen and Kline (1973) with dye injection, where results show that the lift-ups are associated with disturbances caused at the wall by motions towards the wall and such disturbances originate in the logarithmic region as results of the interactions of earlier bursts from upstream.

In 1982, Smith and Schwartz (1982) described a model of the regeneration cycle in which the low-speed streaks are explained as the trailing parts of the interacting hairpin vortices. They believed that when the vortex moves progressively closer to the wall, the adverse pressure gradient is intensified, leading to a local flow separation and ejection. The subsequent displacement of the ejected fluid is counteracted by an inflow of high momentum fluid from the immediate upstream (sweep events). Thus, the cycle is completed.

Falco (1991) concluded in his study that the predominant lifted structure is in fact a ring-like vortex. He proposed that the formation of these ring-like

structures is a result of the pinch-off and the reconnection of the lifted hairpin structures.

Jeong, Hussain et al. (1997) presented a near-wall vortical model by a conditional sampling technique. Their results review an ensemble averaged coherent structure that consists of a train or array of alternating signed quasi-streamwise vortices.

Waleffe and Kim (1997) proposed a self-sustaining process by extracting the mechanisms that maintain the turbulence as seen in figure 2.4.1. The self-sustaining process consists of three distinct phases. First, the weak streamwise rolls redistribute the streamwise momentum to create large spanwise fluctuations shown in figure 2.4.2. The spanwise inflections then lead to a wake-like instability in which a three-dimensional disturbance develops. The primary nonlinear effect resulting from the development of the instability forms the streamwise vortices, closing the self-sustaining process.

Jimenez et al. (1999) also found the dominant regeneration mechanism is that the vortices extract energy from the mean shear flow through inflectional instabilities. They pointed out that the near-wall turbulent cycle is self-regenerating and absent of any outer flow.

Similarly, Schoppa and Hussain (2000) pointed out that the shear layers alongside the vortices are generated by the streak instabilities. They found that the roll-up at the tip of these inclined shear layers, is associated with a tilting of the downstream end of the newly formed streamwise vortex to form a new streamwise hairpin structure.

Asai et al. (2002) investigated the instability of the three-dimensional high-shear layer associated with a near-wall low-speed streak experimentally and

concluded that the near-wall flow is highly disturbed in turbulent flows, so that the streak instability can be excited by the existing or the developing turbulent fluctuations. They also demonstrated that the growth of the symmetric mode of the low-speed streak leads to the formation of the hairpin vortex with a pair of counter-rotating streamwise vortices, while the anti-symmetric mode evolves into a train of quasi-streamwise vortices with the vorticity of alternate signs. The results also show that the phenomenon of the wall turbulence generation occurs in the late stage of high-frequency secondary instability, i.e. the breakdown of the thin internal shear layers (formed away from the wall) into the high-frequency vortices. Nevertheless, the streak instability can lead to the occurrence of coherent quasi-streamwise vortices and therefore the regeneration cycle is completed. Besides, Asai et al. (2002) emphasise the occurrence of low-speed streaks and the associated generation of hairpin vortices and/or quasi-streamwise vortices are the phenomena dominating the near-wall turbulence.

Some researchers propose the concept of 'hairpin packets'. Zhou et al. (1999) advised a conceptual regeneration model with the formation of coherent hairpin packets in the wall turbulence. It shows that the initial hairpin vortex persists in time and induces upstream, downstream and other hairpin vortices associated with ejections. This system of hairpin vortices generates progressively a low-speed streak. The envelope of this vortical system is tilted at an angle to the wall of 10° to 15° on its upstream side and 7° to 15° on its downstream side. They concluded that the single hairpin has the capability to develop a 'hairpin packet' if strong enough. As explained in figure 2.4.3, several hairpins form either upstream or downstream of the original one. By

application of the results from both PIV and numerical simulations, they argued most of the flow features observed earlier such as the shear layer, the ejections, the low-speed streaks, the lift-up, the oscillation and the burst are evolved from the hairpin vortex packets. The entire boundary layer is populated with hairpin and streamwise vortices.

Figure 2.4.4 is used by Adrian et al. (2000) to illustrate the link between a single hairpin and the low-speed streak. This model is based on the notion of 'hairpin packets' as well. The head together with the neck introduce a 'Q2' motion (ejection) that is defined as an event of negative u and positive v (low-speed fluid moving upwards). The vortex head and necks pump the low-speed fluid away from the wall at approximately 45° . The legs of the counter-rotation are quasi-streamwise and lift up the low-speed fluid between them. A 'Q4' event (sweep, positive u and negative v) interacts with the 'Q2' event and forms a 'stagnation zone'. Adrian et al. (2000) also found low-speed streaks in the outer layer as well as in the buffer layer and the time delayed u -autocorrelation function is known to possess a long tail, indicating the structure is very long (of the order of δ or more) in the streamwise direction (Grant 1958; Townsend 1958). These structures are confirmed by Adrian et al. (2000) to be Townsend's (1956) large-scale inactive motions and are interpreted to be consequences of the coherent inductions of the hairpins in a 'packet'. These 'packets' often occur with more than 10 individual hairpins and can be as long as 2δ in the streamwise direction. There seems to be some smaller and younger packets lying close to the wall within larger and older packets as shown in Fig. 2.4.5. Green, Rowley and Haller (2007) also studied the evolution of a single hairpin vortex into a packet of similar structures and

showed that the birth of a secondary vortex corresponds to a loss of hyperbolicity of the Lagrangian coherent structures.

Ganapathisubramani, et al. (2005) identified the packets of hairpin vortices by a feature-detection algorithm appearing in the log region, but did not find them in the outer wake region with PIV measurement in a turbulent boundary layer at moderate Reynolds number ($Re_\tau \sim 1100$). The two-point spatial velocity correlations computed using the PIV data reveal that the long streamwise correlations of u component velocities are dominated by slower streamwise structures.

The turbulent layers cannot be separated. The interaction between the wall and the core regions of the turbulent channels has been studied by many researchers (Flores and Jiménez 2006). Marie, L. and Daviaud, F. (2004) provided the evidence proving that the turbulent drag is dominantly generated by coherent structures at the largest scales of the flow.

The dynamics of the large-scale structures and the near-wall structures in the streamwise minimal channel may be described as follows (Toh, and Itano, 2005). Immature near-wall structures are continually generated through a local instability near a watershed between two adjacent large-scale circulations and slowly move towards either of the two. Moreover, a dominant near-wall structure continually attracts and merges weaker structures into itself, beneath the low-speed region of a large-scale structure. These facts suggest a tight coupling between a large-scale structure and the near-wall structures as described in figure 2.4.6(a). A large-scale structure induces the near-wall structures to move in the spanwise direction toward the area under the low-speed region of the large-scale structure. Generally, when two near-wall

structures merge, a concentrated eruption occurs and this causes an influx of fluid from the near-wall region into the outer region. Such a merging event is seen in figures 2.4.6(b) and (c). The spanwise location of these eruptions tends to be reasonably immobile. In their simulations, a concentrated eruption appears to be stronger than a burst which occurs as part of the self-sustaining process. The coupling with the near-wall structures through the three processes above probably enables the large-scale structure to survive (see figure 2.4.7). The whole cycle is denoted as a ‘co-supporting cycle’ of a large-scale structure and near-wall structures, to distinguish this from the self-sustaining process of a single near-wall structure.

Natrajan and Christensen (2006) demonstrated that the hairpin vortices and their formation of large-scale packets are important contributors to the inner-scale energy transfer in the log layer of wall turbulence. A composite conceptual scenario that accounts for all of the energy transfer behaviour observed is presented in Fig. 2.4.8. Their analysis reveals that the strong ‘forward and backward-scatter’ events occur spatially coincident to individual hairpin vortices and their large-scale organisation (vortex packets). Large-scale regions of forward scatter are coincident with strong ejections induced by the individual vortices. The most intense forward-scatter events are found to occur when these ejections are opposed by the sweep motions. The strong backward scatter of energy is observed at the trailing edge of the vortex packets and the weaker backscatter is also noted locally around the individual heads of the hairpin structures. While the hairpin vortices generate significant localised forward scatter of energy, they form into larger-scale entities, coincident with the inclined interface of the vortex packets. In contrast, while

the vortices generate somewhat weaker backscatter, the possible coherent alignment of hairpin vortex packets in the streamwise direction, as proposed by Adrian (2000), may account for the generation of significant backscatter between the trailing edge of one packet and the leading edge of another. In particular, this backward scatter of energy may represent a net energy transferring from the smallest hairpin in the downstream packet to the largest hairpin of the upstream packet (Natrajan and Christensen 2006).

Kim (2005) summarised the self-sustaining turbulence process in the turbulent boundary layer through various studies of the drag reduction as seen in figure 2.4.9. A common feature of drag reducing flows, regardless of what method, is the weakening of the near-wall streamwise vortices strength and the increased spacing. This implies the streamwise vortices and the associated streaks play an important role in the turbulence regeneration process (Chernyshenko and Baig, 2005).

2.5. Skin-friction Reduction In Turbulent Flow

In this section we shall summarise the strategies for skin-friction drag reduction and review some successful approaches.

2.5.1 Skin-Friction Drag Reduction Strategies

Research of the turbulent boundary layer not only provides understanding for the causative physics behind the remarkable effects of turbulent drag reduction, but can also lead to the logical design of a technology capable of producing novel viscous drag reduction (Frohanpfel et al. 2007).

Turbulence cannot maintain itself but depends on its environment to obtain energy (Tennekes and Lumley 1997). A common source of energy for

turbulent velocity fluctuations is the shear in the mean flow; other sources, such as buoyancy, exist too (Tennekes and Lumley 1997). Therefore, if the turbulence regeneration cycle is disturbed, the turbulence cannot obtain energy from the mean flow and the turbulence will decay. Recent research showed that the turbulence regeneration cycle is associated with the near-wall region (Jimenez & Pinelli 1999) and accordingly one of the strategies for drag reduction is to modify or disturb any part of the near-wall activities (Karniadakis & Choi, 2003). Furthermore coherent structures play an important role in the production of turbulence, suggesting that targeting these structures can achieve the objective of turbulent flow control. Much research has been done to achieve this aim and have achieved a lower drag regime (such as Jung and Mangiavachi 1992; Choi and Moin *et al.* 1994; Hamilton and Kim *et al.* 1995; Choi 1996; Berger and Kim *et al.* 2000; Du *et al.* 2002).

For instance, an active control targeting sweep and ejection events was described by Lee and Kim (1998) using out-of-phase blowing and suction. The results showed that the out-of-phase blowing prevents the formation of high vorticity regions on the wall by pushing these regions far away from the surface, and the strength of the vorticity is reduced, resulting in a reduction of the surface viscous drag. Choi *et al.* (1994) showed that significant drag reduction is achieved when the dynamically significant coherent structures are suppressed in the near-wall region. They also suggested a possibility of efficient wall skin-friction reduction methodologies by reducing the activities of sweeps only. Two drag reduction mechanisms were proposed: first, deterring the sweep motion towards the wall and second, stabilising and preventing lifting of the spanwise vorticity near the wall. Meng *et al.* (1998)

argued that a prediction strategy is necessary to capture the targeted events for active turbulence control. Results also showed that the onset of the instability of the flat Stokes layers can be suppressed by wall suction and enhanced by wall injection (Gao and Lu 2005).

Studies indicate that the growing streamwise perturbations driven by streamwise vortices and the resulting Reynolds stresses play a significant role in both the transition to turbulence and the near-wall turbulent flow (Renardy, M., 1995). Illuminated by these, Schoppa and Hussain (1998) applied a large-scale control strategy to the turbulent flow with the aim of stabilising low-speed streaks and arresting the production of new streamwise vortices. Results show that it could lead to skin friction reduction by suppressing the underlying streak instability mechanism.

Jiménez (1999) also suggested any measures to reduce the near-wall turbulence should be focused on the near-wall streamwise vortices. The weakening of streamwise vortices has been successful and in doing so, skin friction drag has been reduced (Du et al. 2002).

An overview of drag-reduction techniques is presented in the following sections. The drag reduction in this thesis mainly focuses on the skin friction reduction. The techniques for other drag forms such as form drag and pressure drag are reviewed by Bushnell (2003) et al. Bushnell (2003) also described several emerging drag-reduction approaches, either active or reactive/interactive, and claimed “the drag reduction potentially available from synergistic combinations of advanced configuration aerodynamics, viscous drag-reduction approaches, revolutionary structural concepts and propulsion integration.”

2.5.2 Several Skin Friction Drag Reduction Approaches

Many successful applications of drag-reducing techniques can be seen in the world, for example, polymer additives used in oil-pipelines and riblets used on the hull of the racing yacht.

A maximum drag reduction has been achieved when polymer or surfactant additives are fed into water where 70% of drag reduction has been found (Berman 1978; Hoyt 1989; Yang S.-Q & Dou, G. 2005; Paschkewitz, et al. 2005; Liberzon, et al. 2006). Surfactant is more mechanically stable than a polymer, hence has been widely used in heat transfer system etc (Tiederman 1989; Hoyt 1989; Itoh et al. 2005). Benzi, R et al. (2006) tried to derive a theoretical approach to drag reduction with dilute polymer solution in wall-bounded turbulence. They obtain a universal maximum drag reduction (MDR) asymptote, and complement that theory with a discussion of the cross-over from the MDR to the Newtonian plug when the drag reduction saturates. Similar approaches are also applied by Casciola and Angelis (2007) to find out the energy transfer mechanics in the dilute polymer solution. Basically, it is believed that the additives form long chain-like or net-like structures and suppress the turbulence (Tiederman 1989; Hoyt 1989; Gyr and Bewersdorff 1989; Virk 1975). The streamwise flow driven by the streamwise vortex would have the effect of diminishing the vortex due to the viscoelasticity introducing a negative feedback (Renardy, M., 1995).

Riblets, one of the successful techniques, are passive devices consisting of longitudinal grooves, whose concept comes from the nature of shark's skin (Raschi and Elsom 1986). The depth and spacing are commonly in the region 10 – 30 wall units and are critical to achieve drag reduction (Walsh 1990;

Bandyopadhyay 1986; Choi et al. 1993; Choi 2001). 10% of drag reduction has been observed for practical riblets. Choi (1987, 1989) deduced that the riblets act as small fences to restrict the spanwise movement of vortices near the wall. Jiménez and Pinelli (1999) also proposed that the quasi-streamwise vortices are weakened by the riblets.

Another idea that comes from nature is the use of compliant coatings, which is from the observation of the dolphin's skin in a laminar flow (Kramer, 1961). The compliant coating responds to the pressure pulse generated during a sweep event, thereby modifying the turbulence (Choi et al. 1997). Riley et al. (1988, 2000) and Bushnell and Hefner (1977) gave reviews on this topic, explaining that a flexible surface can comply with the flow and modify the boundary layer to delay transition and reduce turbulent skin friction. Tamilarasan (2000) has found up to 10% drag reduction could be achieved using a silicone rubber coating on the inside of a water pipe flow. Bandyopadhyay et al. (2005) developed the low-molecular weight rubber-like silicone coatings based on a linear interference theory of the interaction between the turbulence pressure fluctuation and the viscoelastic coating. By matching the natural frequency of the coating to the turbulent boundary layer region of the maximum Reynolds stress production, they achieved the drag reduction although they found the ability to reduce the drag generally decreases with the aging of the coatings.

Drag reduction by micro-bubble injection in liquid boundary layers has also been studied by many researchers from the 1980's (Legner 1984; Merkle and Deutsch 1989; Meng and Uhlman 1998). In nature, penguins have already learned to expel air bubbles into their slipstreams during high-speed

manoeuvres (Bechert 1997). In our world, 1~4% net drag reduction has been reported with an experiment carried out in a full-scale ship by Kodama et al. (2003). However, the drag-reducing mechanism is still not concluded. Basically, one scenario is that the effect of the bubbles is to reduce the fluid density and hence increase the kinematic viscosity leading to a damping of turbulent fluctuations (Legner 1984). Meng and Uhlman (1998) suggested that the break-down of bubble scales extracts energy away from the turbulence production, which is responsible for the drag reduction.

The opposite control is a method to achieve turbulence control and drag reduction by producing a feed-back actuation to the flow when detecting spatial and temporal signatures of the near-wall events such as sweeps (Gavarini et al. 2005) This has been widely used as an effective way to control the flow (Gao and LU, 2005). By suppressing the ejection and bursting process, the selective suction can reduce the Reynolds stress, leading to a reduction in turbulent skin friction (Kerho, 2002). Choi, Moin et al. (1994) and Hammond, Bewley et al. (1998) found a 'virtual wall' is established when the drag reduction is achieved in this method. Gavarini et al. (2005) also targeted the asymptotically elongated (in the streamwise direction) flow structure to reduce the disturbance energy in the form of blowing and suction at the wall in a pipe flow. A considerable reduction, as compared to the uncontrolled case, is obtained in the case of the control laws operating over a long section of the pipe. Kerho (2002) used a selective active sensor/suction technique to identify and remove low-speed streaks from a turbulent boundary layer in order to reduce the skin friction with a MEMS (Micro-Electro-Mechanical-Systems) based micro-valve due to the small streak areas and the high burst frequencies

involved. The selective suction can reduce the mass flow required as compared to the continuous uniform suction. Figure 2.5.1 shows the sensor, the suction port and the valve arrangement. The first picture in figure 2.5.2 shows the initial streaky structure development over the sensor. When the valve opens, the majority of the structure can be seen to be removed by the suction port in the subsequent pictures in figure 2.5.2. “By the time the valves closes at $t = 1.27s$, the majority of the structure has been removed from the boundary layer (Kerho, 2002)”. Kerho (2002) has demonstrated that the low-speed streaks can be identified and selectively removed from a naturally growing turbulent boundary layer and that the removal of these streaks can lead to a net skin friction reduction.

Near-wall streaks are targeted in several control strategies. A lower amplitude standing wave type of excitation has been applied throughout the flow domain by Schoppa & Hussain (1998) with the aim of stabilising the near-wall streaks. They found out that the normal vorticity ω_y is a key indicator of the formation of new streamwise vortices near the wall by streak instability. Specifically the growth rate of the streak’s sinuous instability mode grows with the magnitude of ω_y , so if it falls below a threshold no such instability occurs, which leads to a drag reduction (Schoppa & Hussain, 1998).

Spanwise wall oscillation is also a hot topic in turbulent flow control for drag reduction. It was originally carried out by Jung *et al.* (1992) via a DNS study, which showed that a drag reduction of up to 40% could be achieved after five wall oscillation periods. This research also showed that the wall oscillation damps the turbulent coherent structures, as can be seen in figure 2.5.3. This investigation was later confirmed by Laadhari *et al.* (1994) experimentally and

Baron and Quadrio (1996) in their DNS study. Experimental investigations have also been carried out by many researchers (such as Choi *et al.* 1998; Choi and Clayton 2001; Cicca *et al.* 2002 and Choi 2002, 2005). Laadhari *et al.* (1994) and Baron and Quadrio (1996) found the spatial coherence between the longitudinal vortices and the low-speed streaks can be disrupted by oscillating a wall in the spanwise direction. Choi *et al.* (1998) found that the wall surface displaced by more than 50 wall units in the spanwise direction would disturb the sequence of near-wall events in the turbulent boundary layer and reduce the production of turbulence energy. Akhavan *et al.* (1993) showed that any change in the mean strain disturbs the semi-equilibrium state between the turbulence and the mean flow, leading to a reduction in the ability of turbulence to extract the energy from the mean flow and resulting in a reduction in skin-friction drag. Choi *et al.* (1998) suggested that the tilting of streamwise vortices into the spanwise direction is responsible for reducing the drag and the spanwise wall velocity. Similar results were obtained with an oscillating pipe section (Choi and Graham 1998). Furthermore, Choi and Clayton (2001) proposed that a negative spanwise vorticity created by the spanwise-wall oscillation hampers the stretching of the longitudinal vortices in the viscous sublayer as shown in figure 2.5.4.; consequently, the near-wall burst activity is weakened, leading to a reduction on turbulent skin-friction drag. Dhanak and Si (1999) also found that the rate of the turbulent kinetic energy production is significantly reduced by the interaction between the quasi-streamwise vortices and the modified Stokes layer (Blennerhassett and Basson, 2006) on an oscillating wall, leading to a rapid viscous annihilation of the coherent structure. Baron and Quadrio (1996) found there is a 10% net

energy saving by spanwise-wall oscillation when the velocity is a quarter of the free-stream velocity.

Zhao et al (2004) used the spanwise travelling waves of a flexible wall to control the turbulent flow. They found such an on-wall open-loop vorticity creation control can effectively reduce the friction drag for any incompressible Newtonian fluid. The control effect is similar to that of the transverse wave controls by the spanwise near-wall oscillating flow/wall oscillation and the travelling wave excitation. They propose the main physical mechanism is the change of boundary vorticity flux due to the wall acceleration. The change forces the streamwise vorticity generated at the wall to be confined in a thin generalised Stokes layer. And hence it alleviates the low-speed streaks, suppresses the streamwise vortices in the viscous sublayer, associated with a regularised wall skin-friction pattern. The control effect is due to wall acceleration while the input energy is proportional to the wall velocity. Thus, the optimal wave pattern should be minimising wall velocity, but maximising wall acceleration in a certain averaged sense over a period (Zhao et al, 2004).

A new technique giving significant drag reduction in turbulent shear flows has been proposed by using a buoyancy effect to generate periodic spanwise motion (Yoon et al., 2006). An optimum strip size of about 250 wall units gives drag reduction of about 35%. The greater the buoyancy forces, the smaller the strip size which attains the maximum drag reduction. It is highlighted that the induced lateral motions by the buoyancy forces are similar to those induced by spanwise wall oscillations.

Other techniques of turbulent drag reduction include Large-Eddy-Break-Up devices (LEBUs) (Yajnik and Acharya 1977; Badyopadhyay 1986; Anders

1989 and Saville 1989), drag reduction by dimples (Choi et al., 2006) and Micro-Electro-Mechanical-Systems (MEMS) (Rathnasingham and Breuer 2003; Warsop 2004) technology for active turbulence control.

2.6 Electro-Magnetic Turbulence Control (EMTC)

The Lorentz (Electro-Magnetic) force is generated when an electrically conducting fluid flows through an electromagnetic field. It is a body force which is non-intrusive to the flow and allows many different types of control to be introduced such as streamwise force control (Henoach & Stace 1995), wall-normal blowing or suction (Nosenchuck & Brown 1993), spanwise oscillation (Berger et al 2000; Pang & Choi 2004; Breuer et al 2004) and other Magnetohydrodynamic control (Ristenpart, Aksay and Saville 2007; Shatrov, V. and Gerbeth, G. 2007; Kassinosa, Knaepen and Carati 2007). Close to the boundary wall, these Lorentz forces can act directly on the velocity and the vorticity (Thibault and Rossi 2003). Due to its benefits, the flow control by Lorentz forcing (or Electro-Magnetic Turbulence Control) has attracted many researchers' attention and has been extensively studied in the past decades.

Gailitis and Lielausis (1961) might be the pioneers to apply the Lorentz force to flow control, where a streamwise Lorentz force was applied to prevent the thickness of the laminar boundary layer profile from increasing. Tsinober (1967) showed that a Blasius boundary layer profile becomes more stable when the Lorentz force is applied to the flow. Nosenchuck (1992) and his group explored the possibility of achieving viscous drag reduction in the turbulent boundary layer with Lorentz forces. In these experiments, the Lorentz force is created along the wall-normal (perpendicular to the flow) direction so that it can interact with the near-wall turbulence structures

responsible for the turbulence production. Some of the results indicate that turbulence is significantly affected by the wall-normal Lorentz force and reports showed a reduction of skin-friction drag of up to 50% (Nosenchuck and Brown, 1996).

Henoch and Stace (1995) performed the experiments using a one-dimensional, streamwise Lorentz force acting in either upstream or downstream directions. They found the force generates a near-wall jet, decreasing the thickness of the boundary layer and suppressing the turbulence intensities. With the increased forces in the downstream direction, the effects on the flow are more significant (Henoch and Stace, 1995). When the force is moderate, the mean flow is unaffected but the wall-shear stress fluctuations and the turbulence intensity are suppressed by up to 30%. However, when the force reaches the maximum in their experiment, the skin-friction and the turbulence intensity are increased. Crawford and Karniadakis (1997) confirmed Henoch and Stace's results that the skin-friction increases whereas the turbulence intensity is reduced in their study. Lim et al. (1998) carried out a numerical simulation to investigate the effects of Lorentz forces on streamwise vortices. They found that the Lorentz force induced from either the wall-normal or the spanwise direction inhibits the induced motions by streamwise vortices and reduces their strength. Whereas, the streamwise magnetic flux doesn't affect the flow in their configuration. They also found the spanwise magnetic flux is more effective than the wall-normal one in reducing the strength of streamwise vortices.

Bandyopadhyay and Castano (1996) have developed a number of Lorentz force actuators which are similar to the design of Nosenchuck (1995). Their new design produces a three dimensional Lorentz force whose penetration

depth can be adjusted by the distance between the electrodes. The actuators can produce forces with pulsed phases as well. With a number of EMTC actuators of miniature electrodes and magnets, Bandyopadhyay and Castano (1996) carried out the flow control experimentally and numerically. With the pulsed Lorentz force generated by an array consisting of five micro-tiles, they found the narrow hairpin vortices are superimposed into the mean flow. It was postulated that the pulsed force creates a resonance condition similar to that produced by an oscillating Stokes layer. However, they found no drag reduction.

O'Sullivan and Biringen (1997) and O'Sullivan (1998) repeated the experiment of Bandyopadhyay and Castano (1996) with numerical simulations. They found that the Lorentz force is too weak to have any effect on a turbulent flow field. They also carried out some other arrangements. One was to try to produce a resonance relationship between the force frequency and either the average burst frequency or the Stokes layer frequency with both static and pulsed-in-time forces at two frequencies. Approximately 5% and 10% drag reductions are found in the vicinity of the actuators for the static and the pulsed force fields, respectively. They also set up a condition of local spanwise oscillation and only found 1% drag reduction.

Kral and Donovan (1996) performed a very interesting numerical simulation. A Lorentz force distribution is employed, which acts as a source of vorticity but with zero net circulation. The Lorentz force varies both spatially and temporally. A maximum of 35% drag reduction is observed. They argued that the drag reduction occurs because roll-cell structures are formed that transport vorticity away from the wall. Posdziech and Grundmann (2001) investigated

numerically the effects of a Lorentz force over an infinitely long circular cylinder. The induced Lorentz force stabilises the flow, delays flow separation, reduces the drag and lift, and suppresses the von Karman vortex street. Their results also showed that the drag strongly depends on the geometry of the electromagnetic actuator and on its location at the cylinder surface. They suggested that the effect of flow control increases with larger Reynolds numbers, since the boundary layer thickness and the penetration depth of the Lorentz force are closely connected.

Weier et al. (1998) also utilised Lorentz force in the streamwise direction for separation control, but no drag reduction has been reported.

The Lorentz forces in the wall-normal direction were investigated by Rossi and Thibault (2002), and Thibault and Rossi (2003). It demonstrates that the wall jet could be achieved with their configuration as shown in figure 2.6.1.

The Lorentz forcing spanwise oscillation has been investigated by many researchers numerically and experimentally (Berger et al, 2000 and Pang & Choi, 2004; Xu & Choi, 2008). The spanwise velocity profiles induced by the spanwise Lorentz forces are shown in figure 2.6.2. More than a 40% drag reduction was obtained in all the studies.

Du et al. (2000, 2002) introduced a force pattern of a spanwise travelling wave. Due to the fact that no ideal travelling wave (sinuous) forces can be obtained in the real world, the forces are of the 'two-pump' form (see figure 2.6.3) instead of the sinusoidal shape forces. The results show that travelling wave actuation has to sweep faster along the spanwise direction to obtain drag reduction compared with the ideal sinusoidal waveform (Du et al. 2002). Other forms of forces are also discussed (see figure 2.6.4) and a drag increase

is found when only a one directional force (as shown in figure 2.6.4b) is used to travel across the wall. The electromagnetic tiles used by Du et al. (2002) are similar to that used by Nosenchuck (1992). The tile arrangement is shown in Figure 2.6.5. Their pulsing strategy includes 16 phases that are classified into two categories, each having eight phases (Du et al. 2002). In the first class (class I), all negative electrodes are aligned in the streamwise x-direction. In the second class (class II), all positive electrodes are aligned in the streamwise x-direction. The first phase of class I is shown in figure 2.6.6(a). Each subsequent phase in this class shifts the entire pattern one electrode over in the positive spanwise z-direction. The first phase in Class II is shown in figure 2.6.6(b). Again, each subsequent phase in this class shifts the entire pattern one electrode over in the positive spanwise z-direction. The 16-phase pulsing pattern is formed by taking two consecutive phases in each class alternately. First, take the first two phases in Class 1 (i.e. 1 and 2), followed by the first two phases in Class 2 (3 and 4); then, take the next two phases in Class 1, and so on.

The generated forces are 3-D as seen in figure 2.6.7. There is no jet produced, which depends on the force strength and the distance between the two electrodes (Du et al., 2002). Moreover, the simulation results show that the large values of the amplitude I are not necessary to obtain the drag reduction, where the value of the interaction parameter I (denoting the force strength) is in global units and thus depends on the Reynolds numbers. In particular, the spanwise velocity has a travelling wave form similar to the excitation force, which results in the 'regularisation' of the streamwise vorticity (Du et al., 2002), as shown in figure 2.6.8. The effect of the travelling wave, when it is

effective in reducing the skin-friction, is to weaken and in many cases to eliminate most of the wall streaks (Du et al., 2002). A wide 'ribbon' of low-speed velocity is formed in the study of Du et al. (2002). They argued this is a significant new finding, because the streaks and streak spacing are usually difficult to alter even in cases where a very large amount of drag reduction has been obtained. Figure 2.6.9 shows the drag history, where a maximum of 30% drag reduction is observed. In order to compare the corresponding flow structures, figure 2.6.10 shows the first Fourier mode of the streamwise velocity at $y^+ = 4$ along the span. Figure 2.6.10a plots a local (in time) drag decrease and the corresponding streaks (streamwise velocity stripes). A similar plot is shown in figure 2.6.10b. By comparing the phases between the maximum of the external force and the maximum of the filtered streak curve, Du et al. (2002) observed the maximum of the first mode of the streaks and the maximum of the Lorentz force always appear at a phase difference in the interval $[\pi/2, \pi]$. In addition, there is a slight phase difference (4 viscous time units for $T^+ = 50$) between the drag force and the excitation force.

Breuer et al (2004) designed the new electromagnetic actuators with a conductive polymer coating to avoid the electrode loss as shown in figure 2.6.11. A maximum of 10% drag reduction is measured with a spanwise oscillating Lorentz force. They also succeeded in generating a travelling wave pattern with this setup and obtained a velocity profile with PIV in the still water as shown in figure 2.6.12.

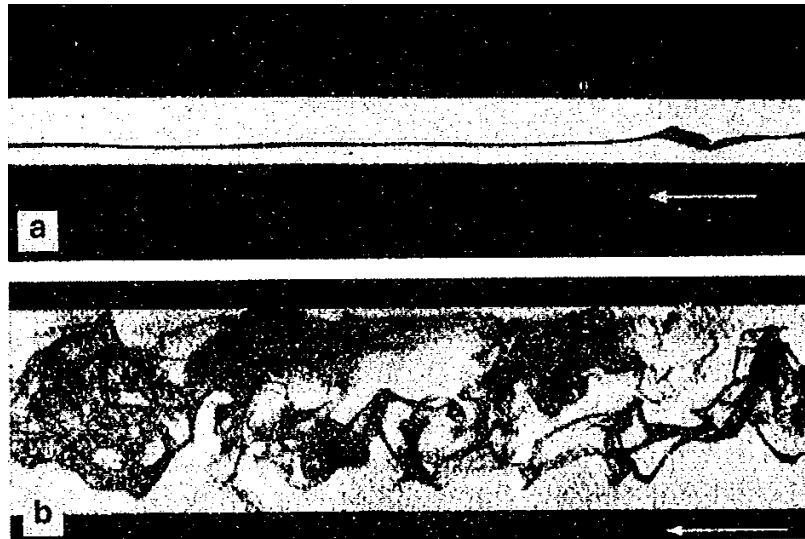


Figure 2.1.1 Flow visualisation experiment by O. Reynolds (1883). Flow in water made visible by dye, W. Dubs (1939). (a) laminar flow; (b) turbulent flow. From Schlichting (1951).

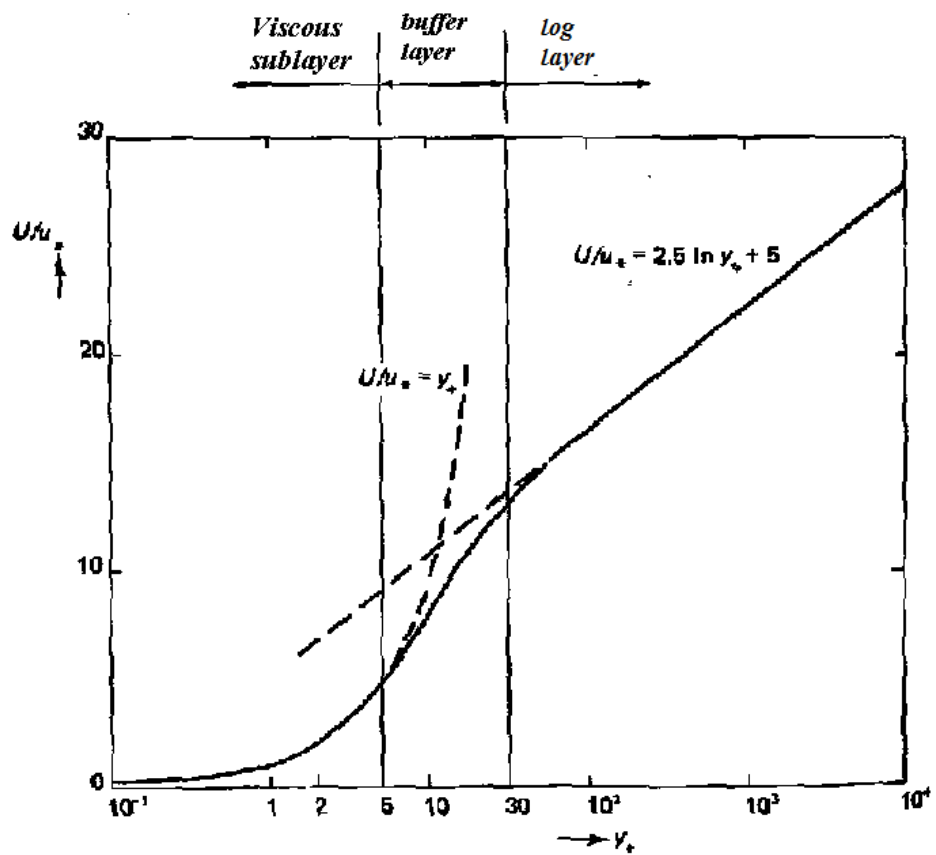


Figure 2.2.1 Wall law in the turbulent boundary layer. From (Tennekes and Lumley, 1997)

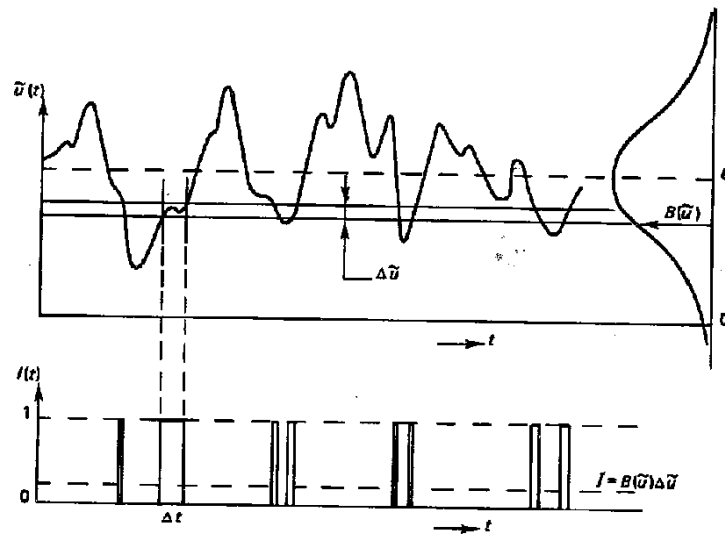


Figure 2.2.2 Measurement of the probability density of a stationary function.

The function $I(t)$ is the discriminator output. From Tennekes and Lumley (1997).

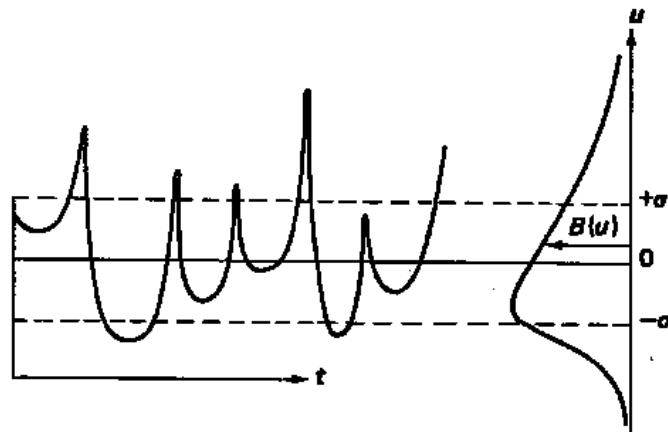


Figure 2.2.3. A function with positive skewness. From Tennekes and Lumley

(1997).

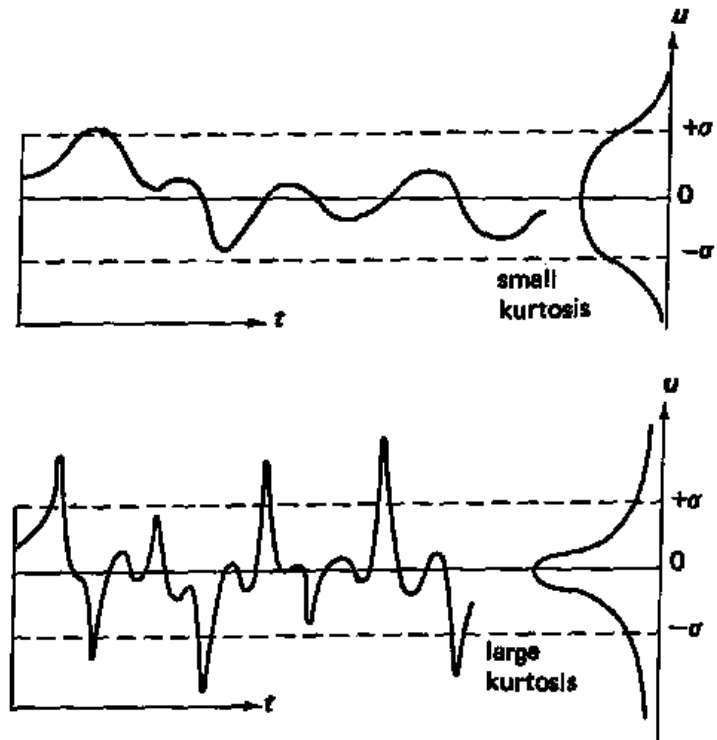


Figure 2.2.4. Functions with small and large kurtosis. From Tennekes and Lumley (1997).

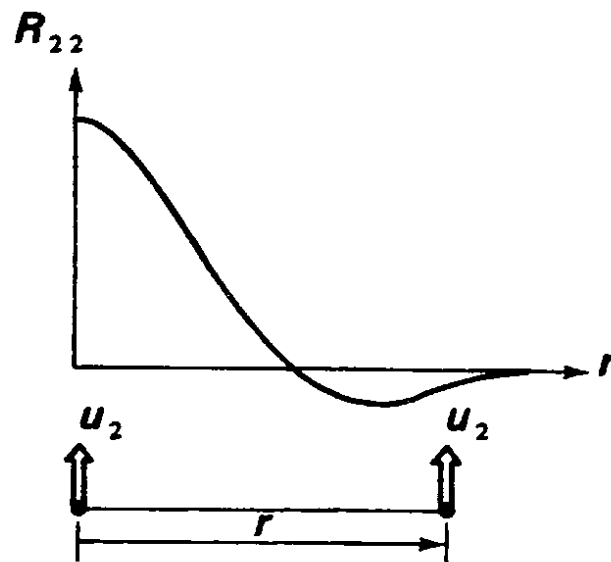


Figure 2.2.5. Sketch of a transverse correlation. R_{22} is the correlation coefficient of two u_2 velocities with a spanwise distance of r . From Tennekes and Lumley (1997).

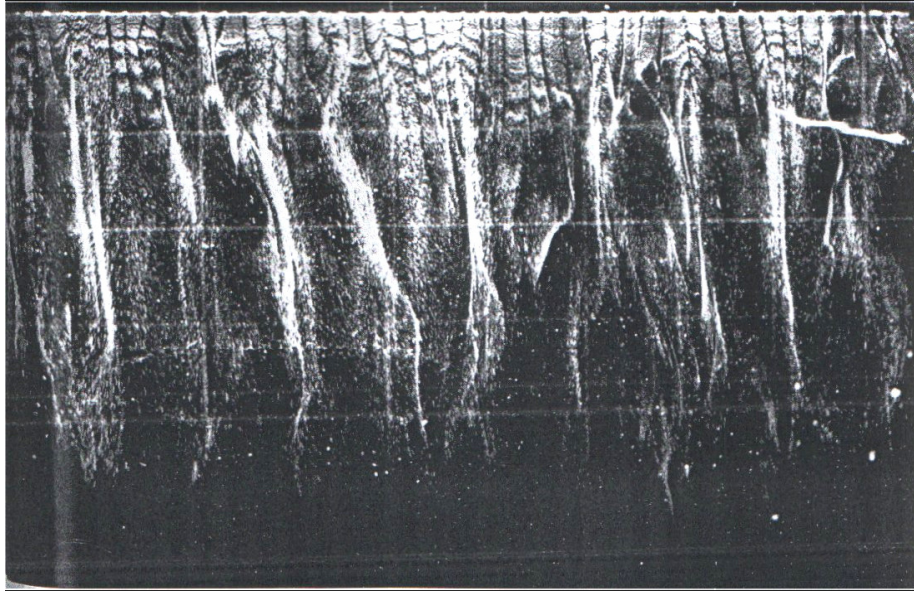


Figure 2.3.1. Low-speed streaky structures of the turbulent boundary layer visualised by the hydrogen bubble technique at $y^+ = 4.5$. Flow direction is from top to bottom. From Kline et al. (1967).

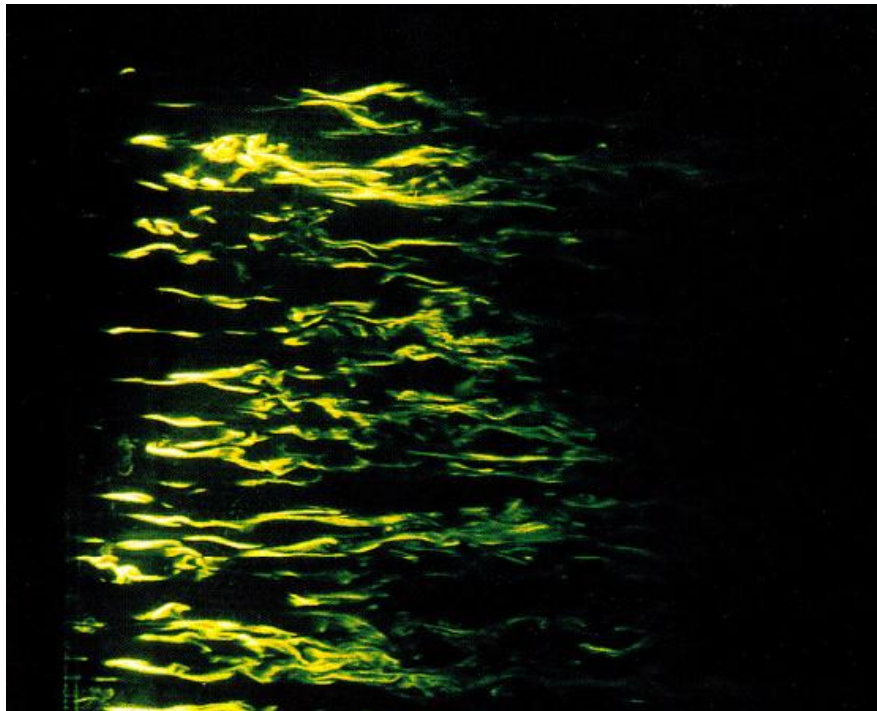


Figure 2.3.2. Plan view of low-speed streaks that are visualised using a laser sheet and fluorescent dye. Flow direction is from the left to the right. From Gad-el-Hak, Blackwelder and Riley (1984).

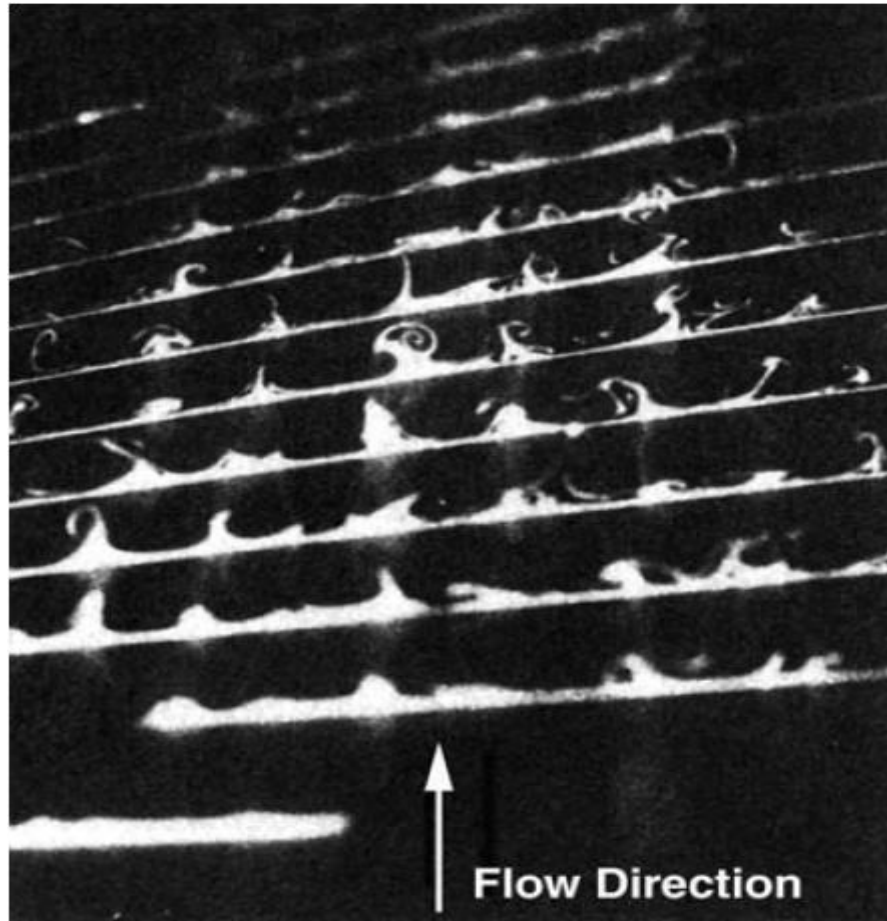


Figure 2.3.3 Smoke flow visualisation of low-speed streak structures in the turbulent boundary layer on a flat plate. From Mathieu and Scott (2002)

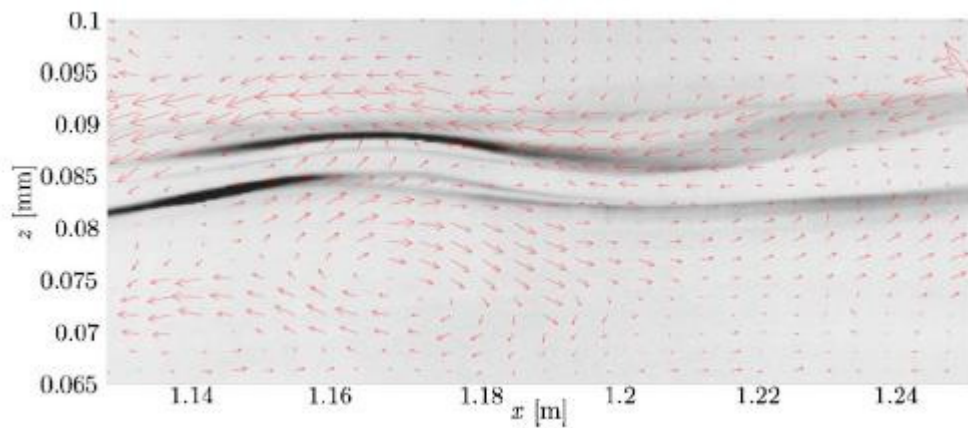


Figure 2.3.4. A typical combined PIV-LIF result, $U = 0.125$ m/s. The vector plot presents the fluctuating velocity field (u' , w') while the gray scale indicates the dye intensity. Flow is from the left to the right. From Mans et al.

(2007)

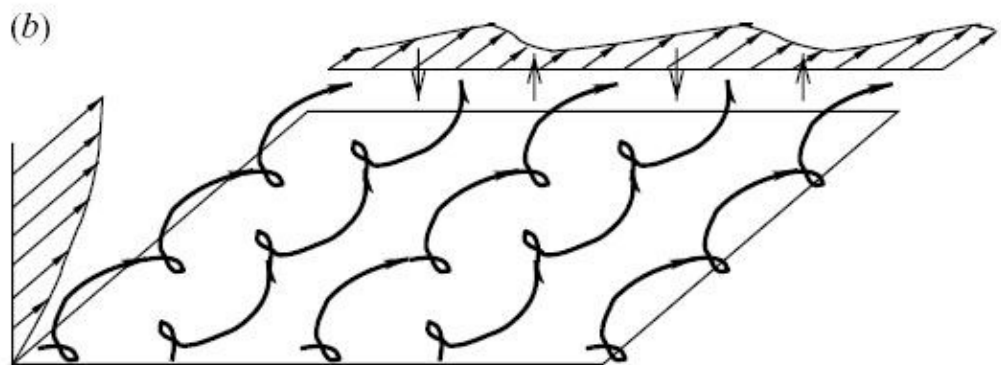
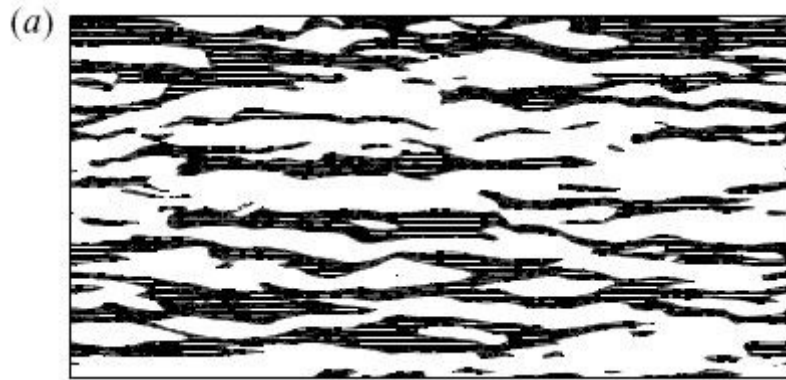
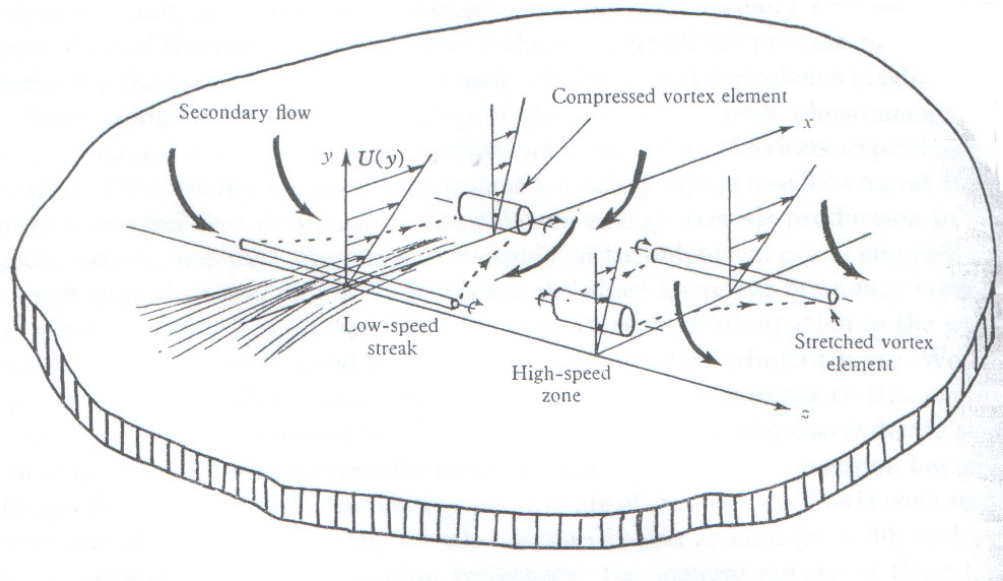
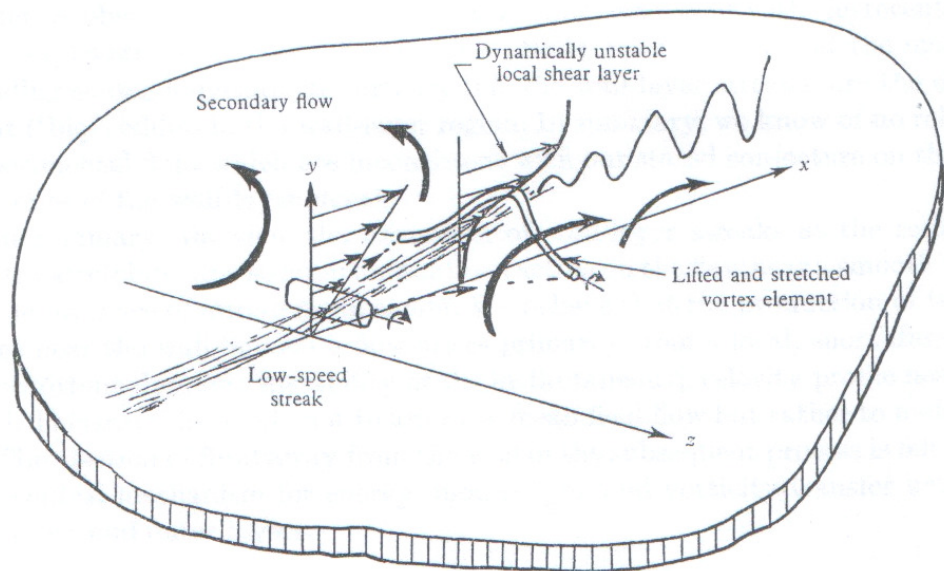


Figure 2.3.5. (a) Streaks in the near-wall turbulent flow at $y^+ = 5.6$ from the wall and (b) the hypothetical mechanism of streak formation by longitudinal vortices. From Chernyshenko and Baig (2005)



(a)



(b)

Figure 2.3.6 a) Mechanism of a low-speed streak created from the vortex lines due to the inherent three-dimensionality of the outer boundary layer turbulence.

b) Mechanism of a low-speed streak lift up and breakdown. From Kline *et*

al.(1967).

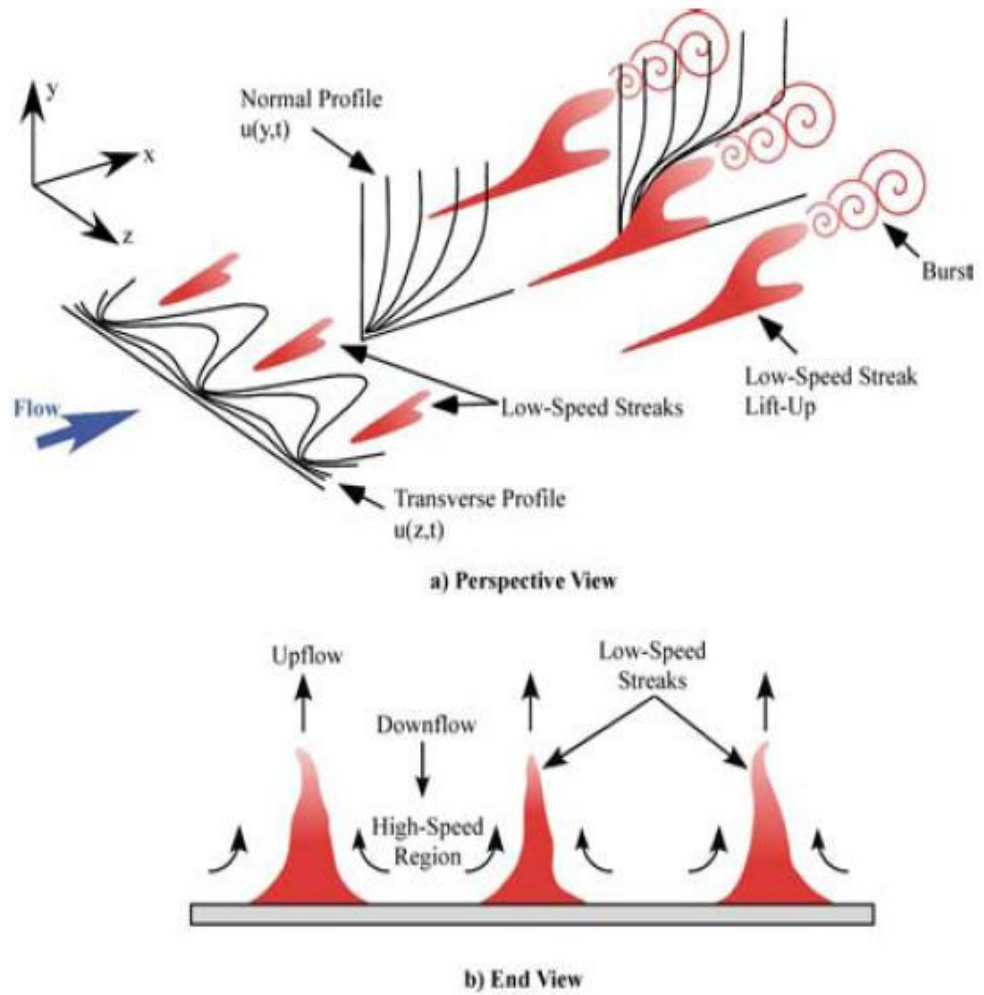
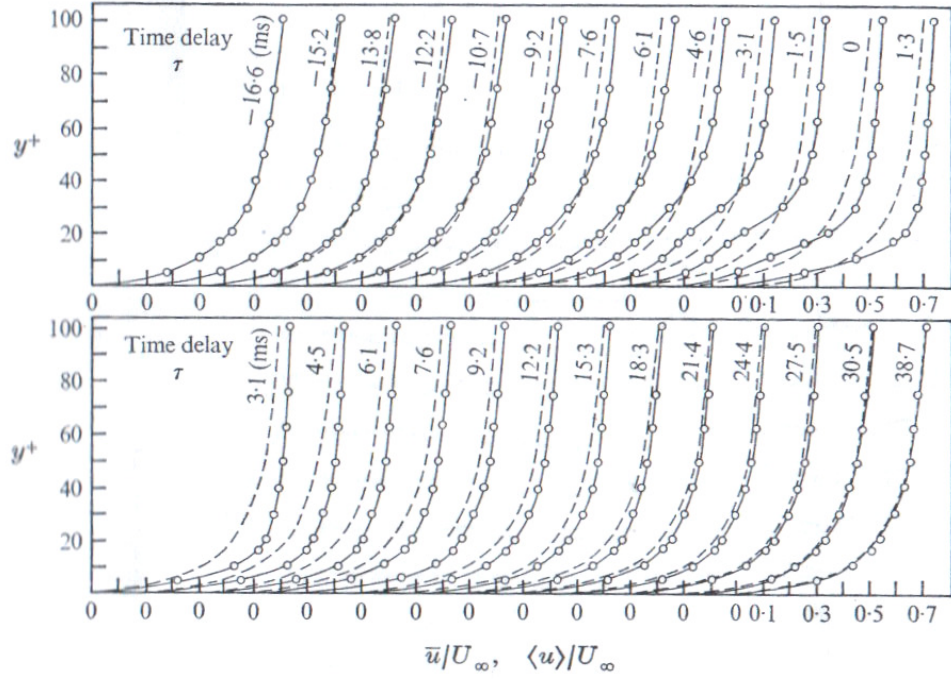
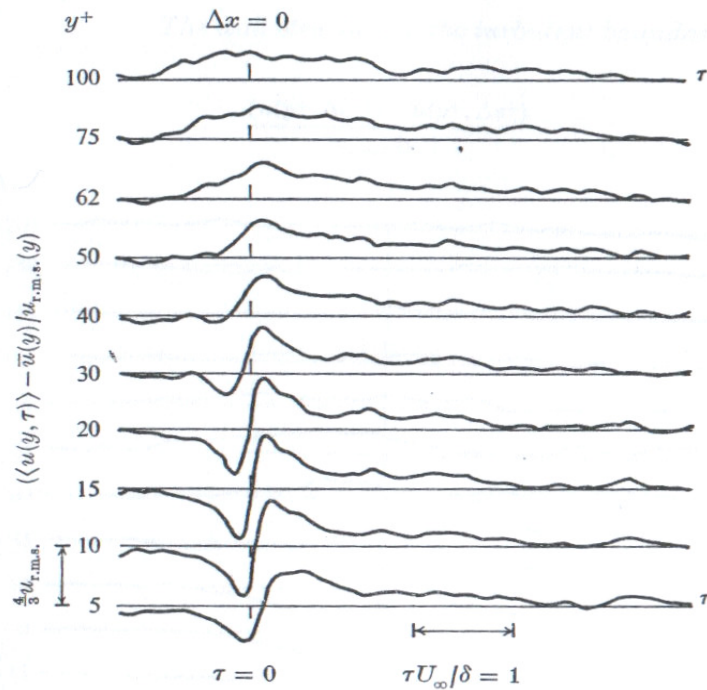


Figure 2.3.7 Conceptual model of a low-speed streak formation and burst adapted from Kim et al. (1971) and Smith & Walker (1997) and Kerho (2002).



(a)



(b)

Figure 2.3.8 a) Conditionally averaged velocity profiles of an event and the time averaged mean velocity profiles at various time delays, τ , relative to the point of detection ($\tau = 0$). b). Conditionally averaged hot-wire signal at several wall normal locations. From Blackwelder and Kaplan (1976).

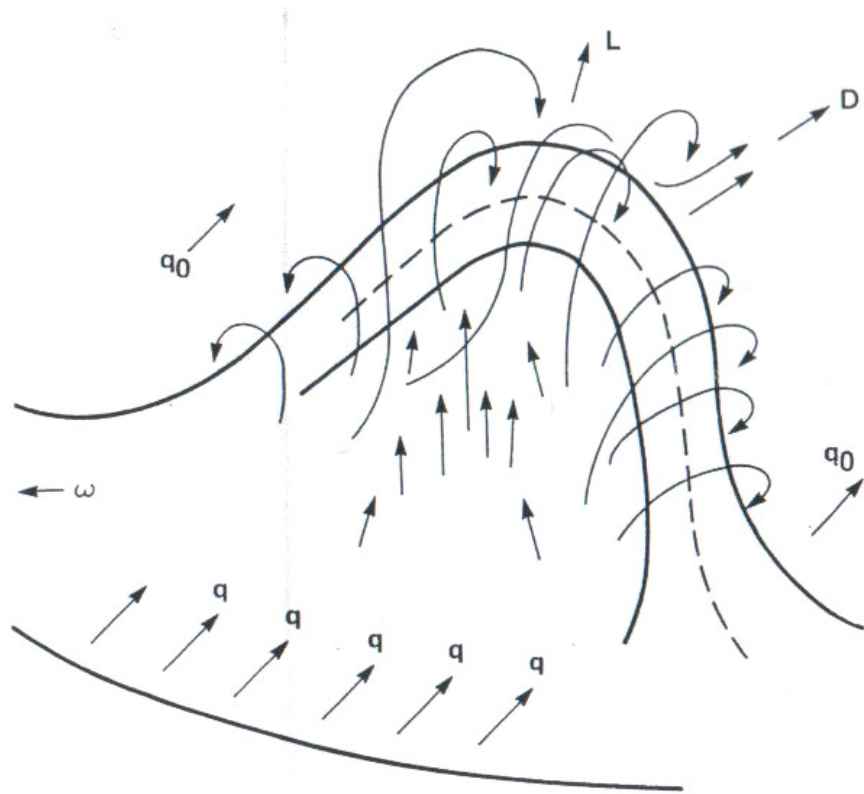


Figure 2.3.9. Primary structure of wall-bound turbulence. From Theodorsen (1952).

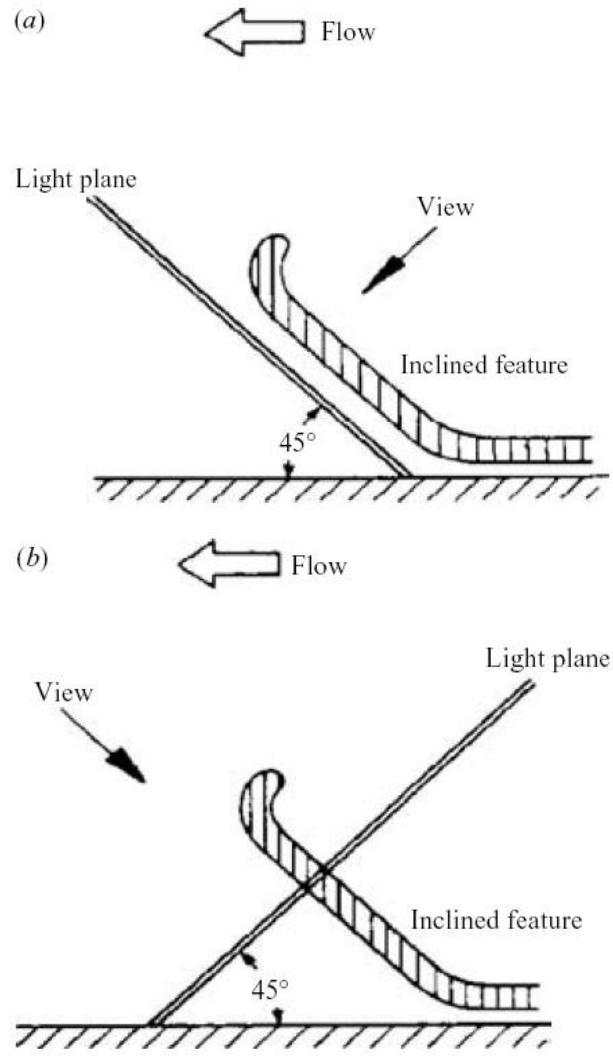


Figure 2.3.10 Hairpin vortices and inclined planes by Head & Bandyopadhyay (1981) (a) Downstream tilted plane, (b) Upstream tilted plane.

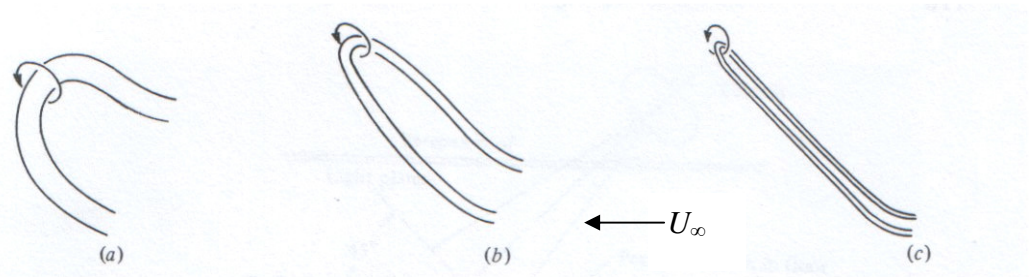


Figure 2.3.11. Effect of Reynolds number on hairpin structures in the outer boundary layer. a) Very low Re. b) Moderate Re. c) High Re. From Head and Bandyopadhyay (1981).

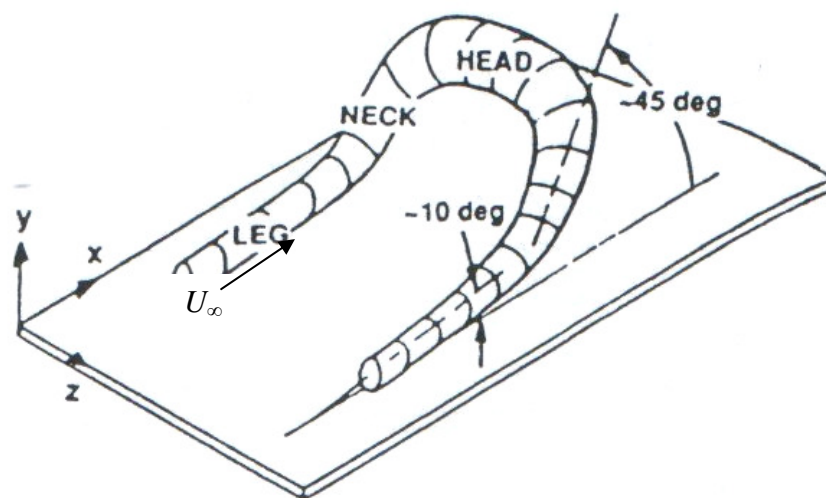


Figure 2.3.12. Horse shoe vortex. From Robinson (1991b).

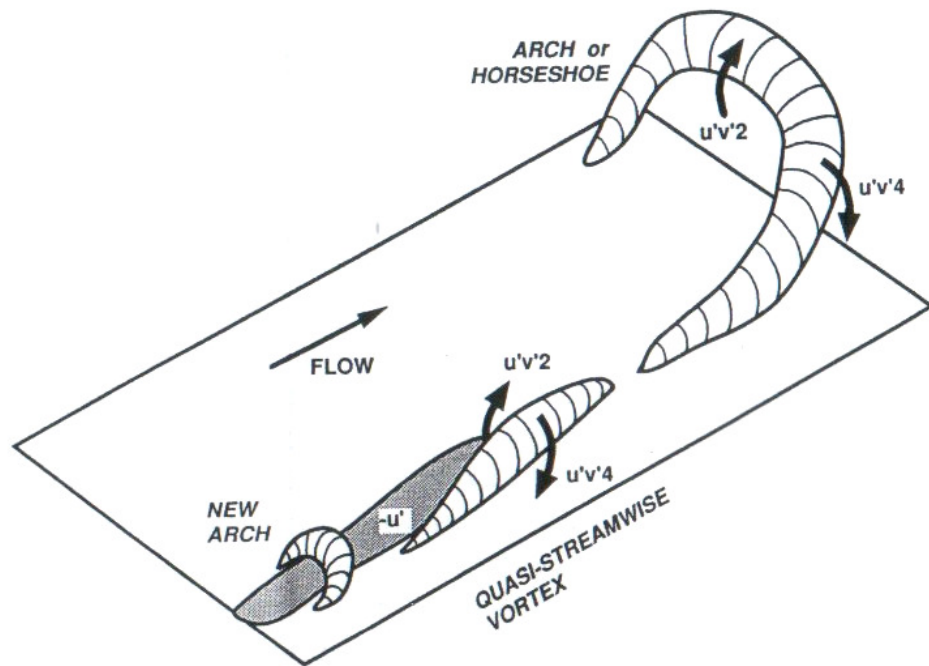


Figure 2.3.13. Conceptual model of the relationships between ejections/sweeps and quasi-streamwise vortices in the near-wall region and the relationship between ejections/sweeps and arch-shaped vortices in the outer region. From Robinson (1991b).

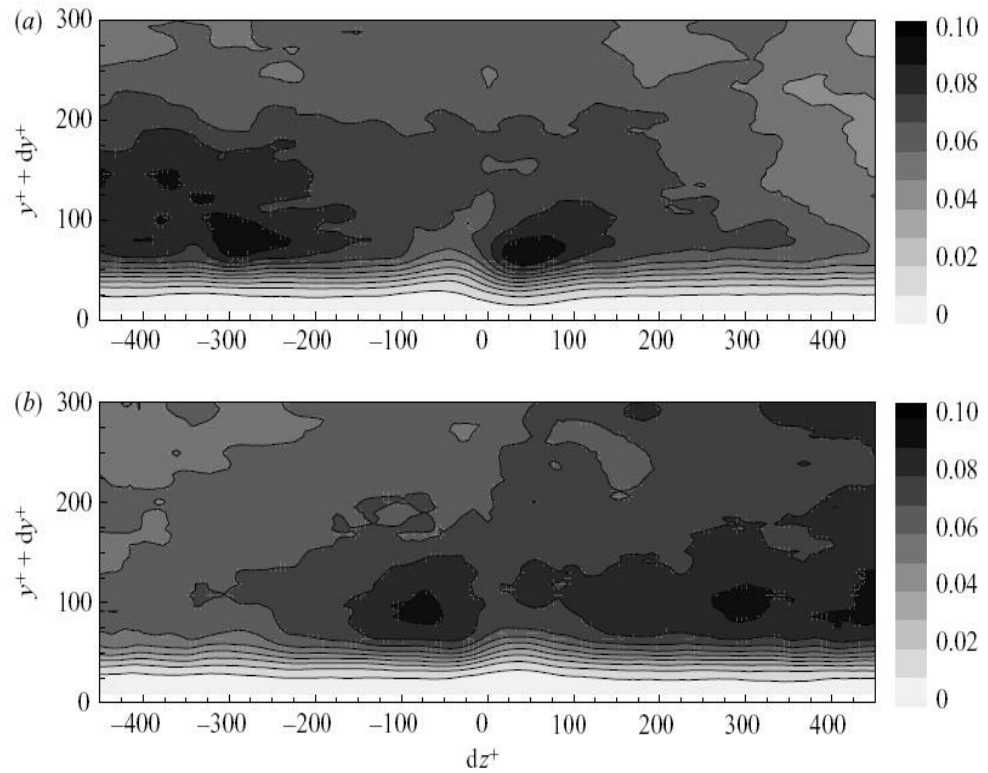
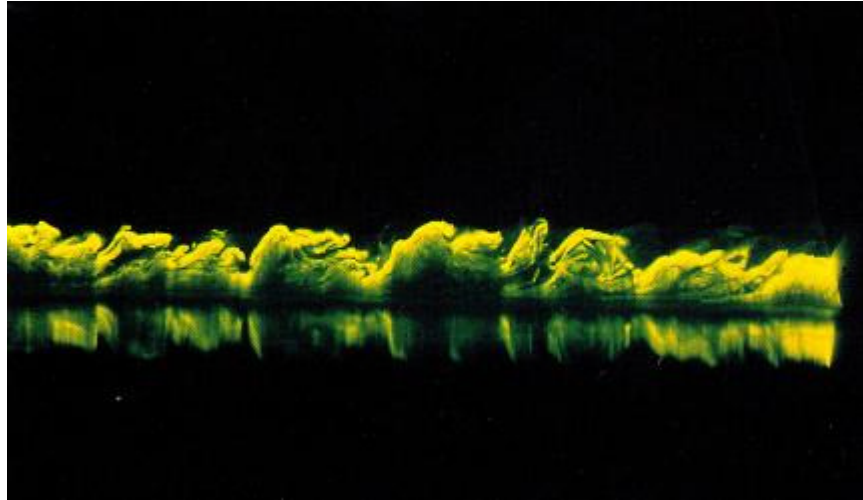
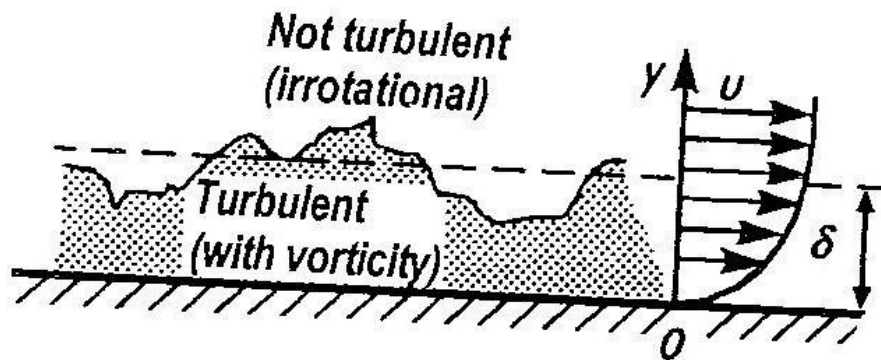


Figure 2.3.14. Probability map of the location of positive eddy structures compared to high-speed streaks and low-speed streaks at $y^+ = 15$ and $R_\theta = 7500$ in the (dz, dy) -plane. (a) Fixed point, high-speed streak; moving point, positive eddy structure. (b) Fixed point, low-speed streak; moving point, positive eddy structure. From Carlier and Stanislas (2005).



(a)



(b)

Figure 2.3.15. (a) Side view of a turbulent boundary layer. Flat plate towed in a water tank. Large eddies are visualised using a sheet of laser and fluorescent dye. From Gad-el-Hak, Blackwelder, and Riley, 1984); (b) Sketch of the outer edge of a turbulent boundary layer, From Tennekes and Lumley (1997).

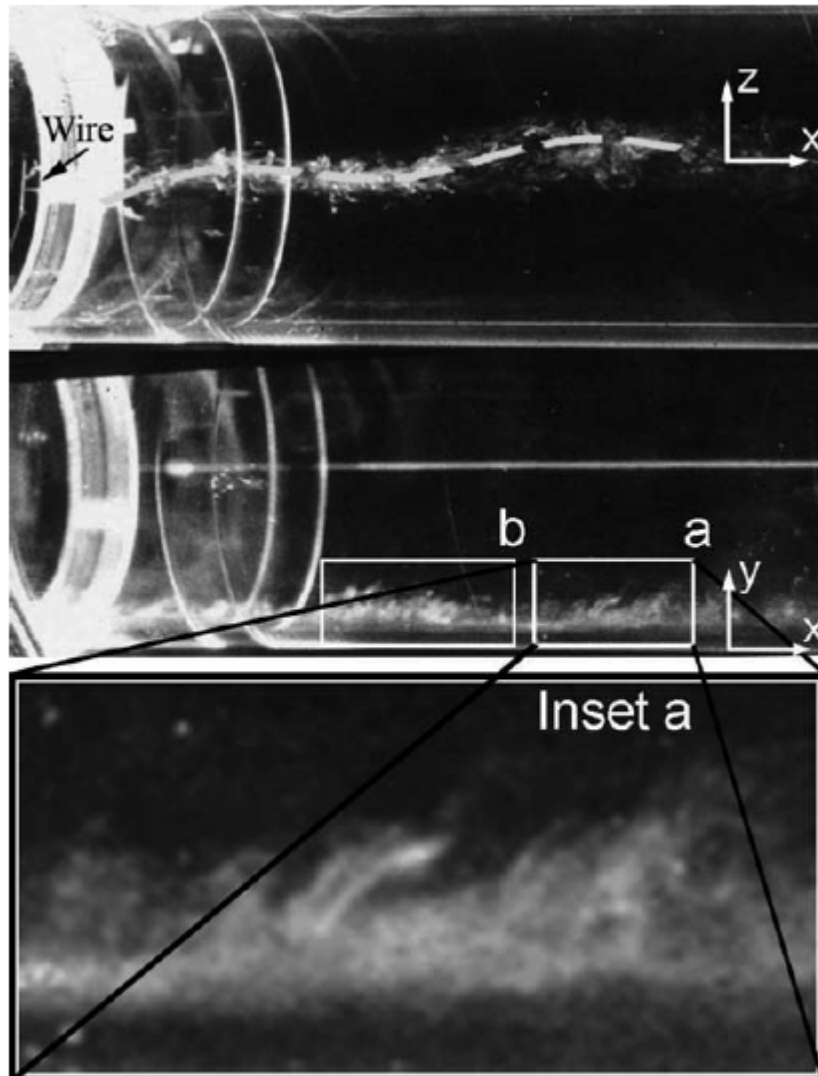


Figure 2.3.16. Smoke visualisation in the streamwise wall-normal (x, z)-plane (upper image, plane view) and (x, y)-plane (section view). Note the large-scale oscillation of the turbulent bulge, consisting of smaller-scale structures aligned in the streamwise direction. Insets (a) and (b) enclose groups of inclined structures that may be a packet of hairpins. The flow is left to right and the smoke wire is location at $y/R = 0.021$. From Lekakis (1988).

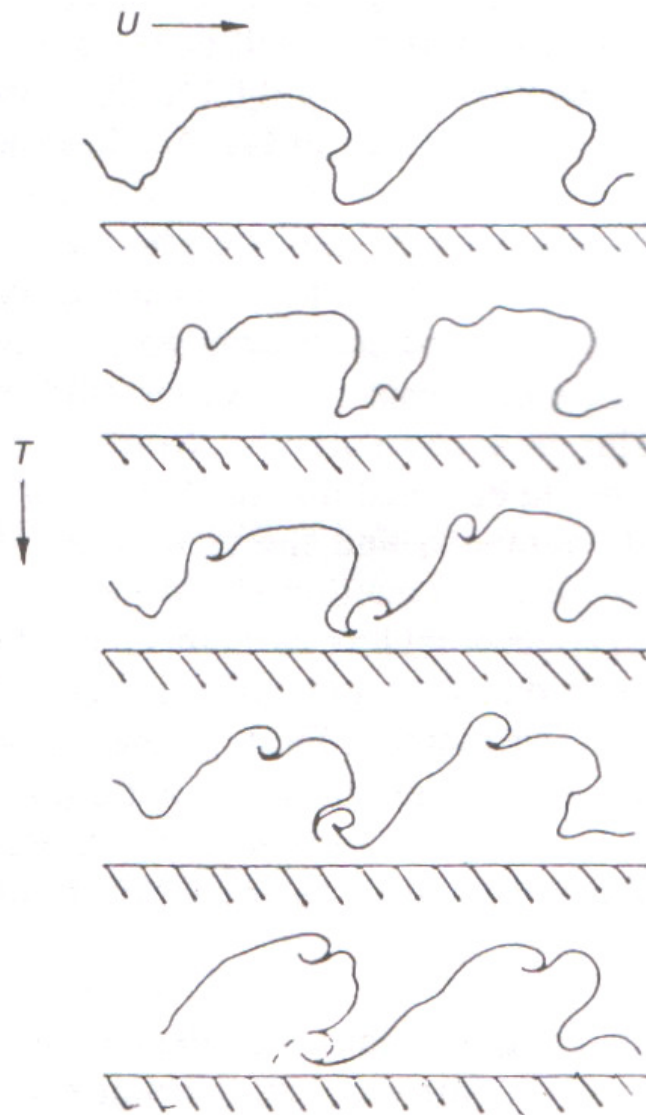


Figure 2.3.17. The outer boundary layer structure showing a sharp interface between rotational turbulent flow within the boundary layer and irrotational free-stream flow. 'Typical (Falco) eddies' are formed on the back interfaces of the turbulent bulges. From Falco (1977).

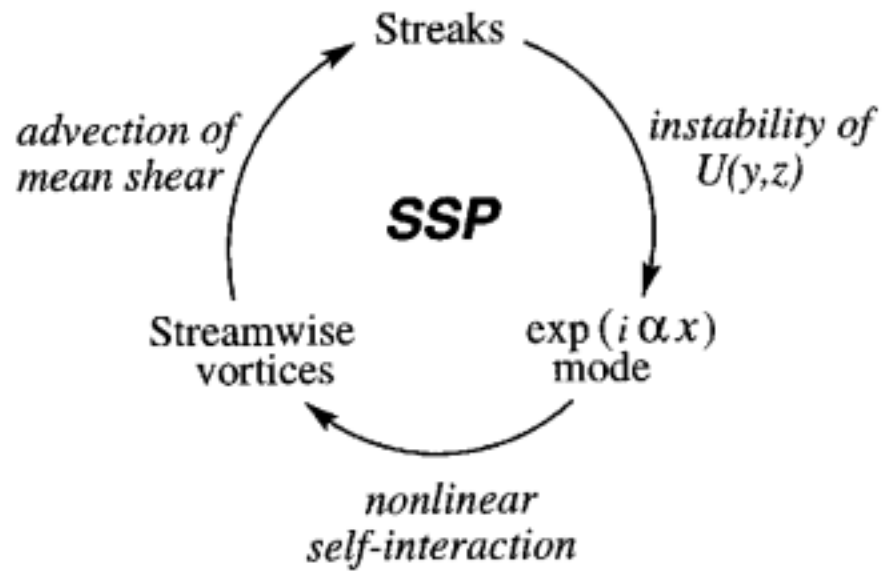
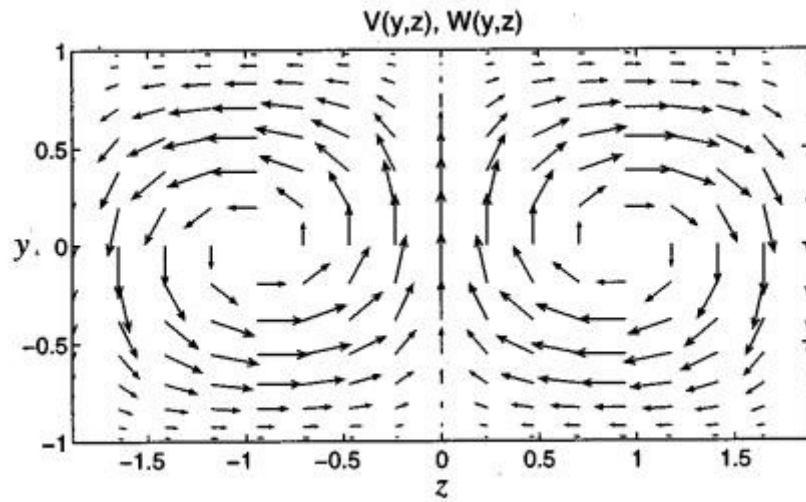
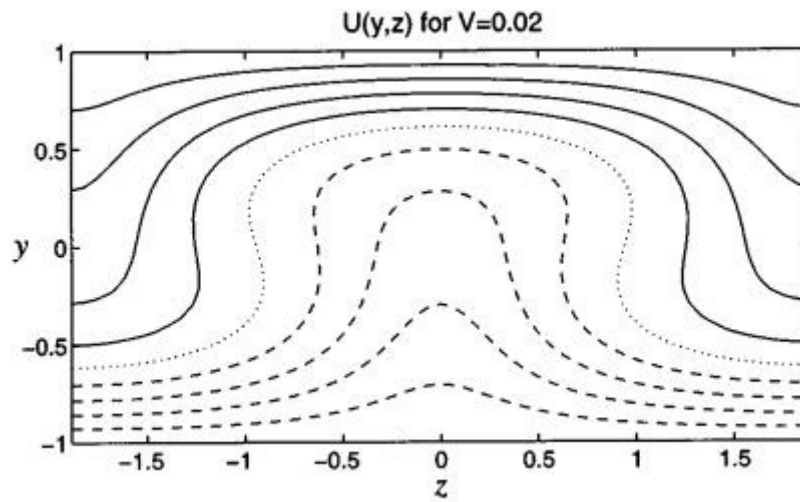


Figure 2.4.1. The self-sustaining process. From Waleffe and Kim (1997)



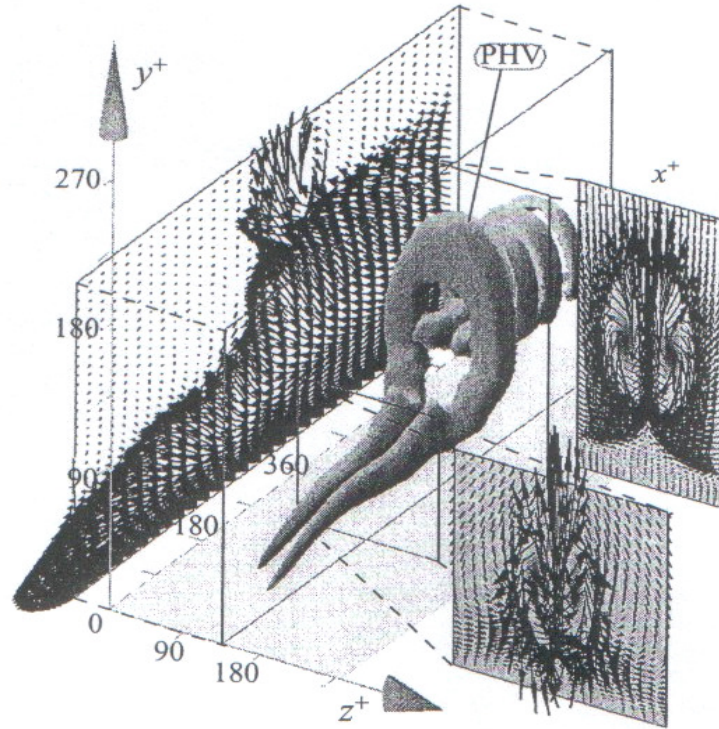
(a)



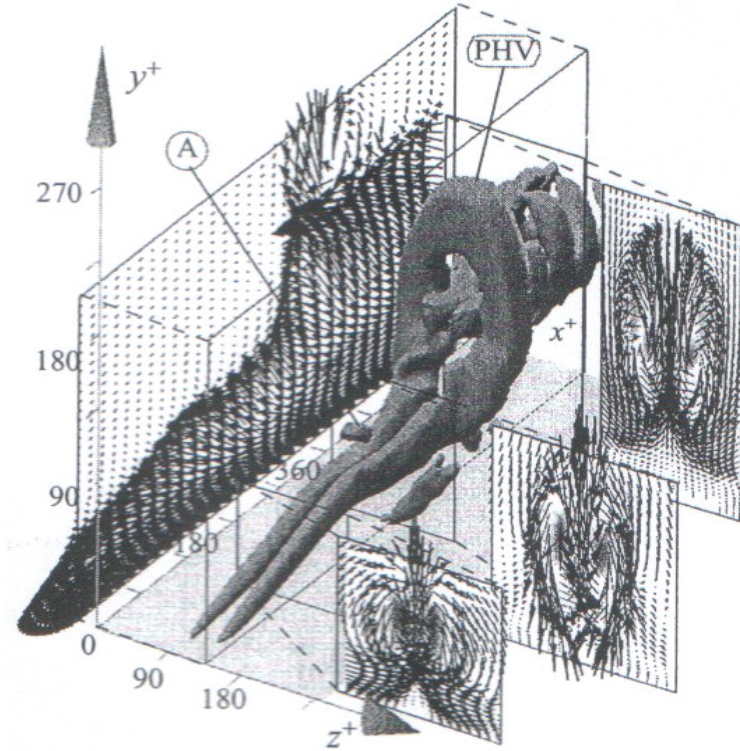
(b)

Figure 2.4.2. Redistribution of streamwise velocity U by streamwise vortices.

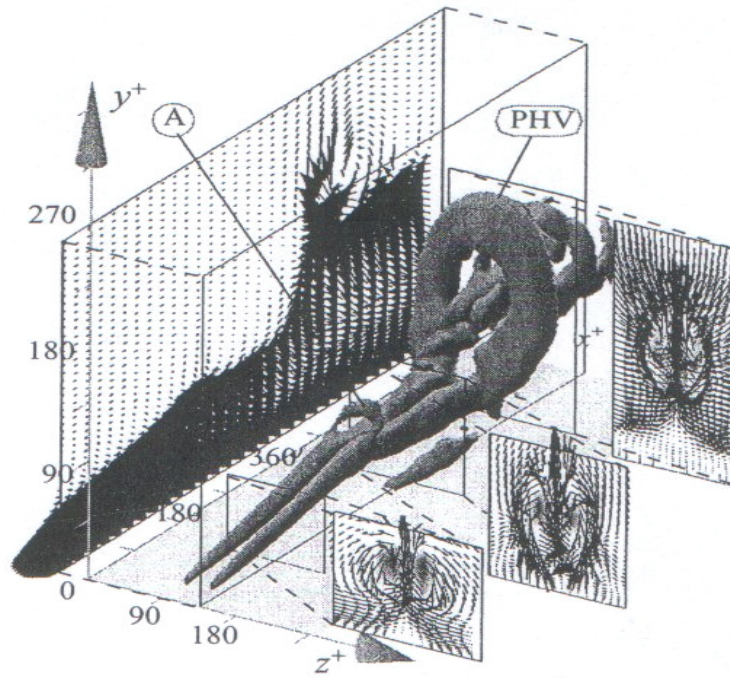
Contours of $U(y, z)$ at 0.2 intervals from -1 at $y = -1$ to 1 at $y = 1$. Negative contours dashed, zero contour dotted. From Waleffe and Kim (1997).



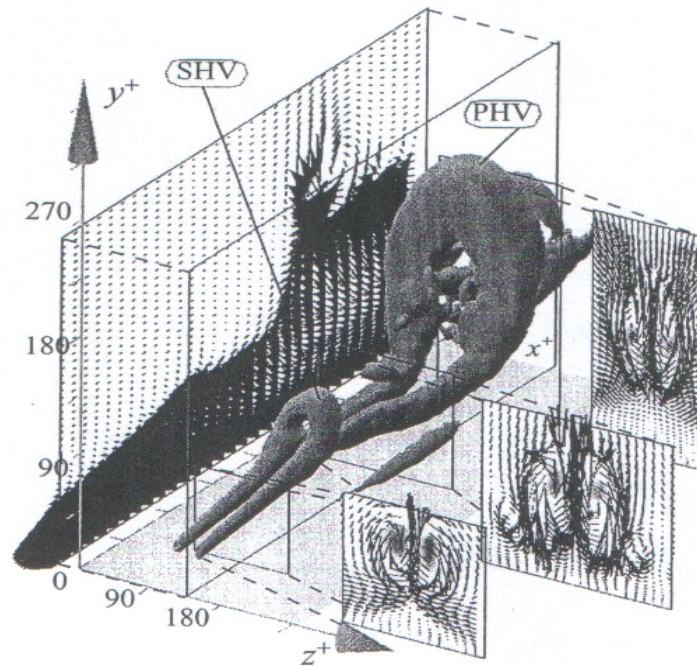
(a)



(b)

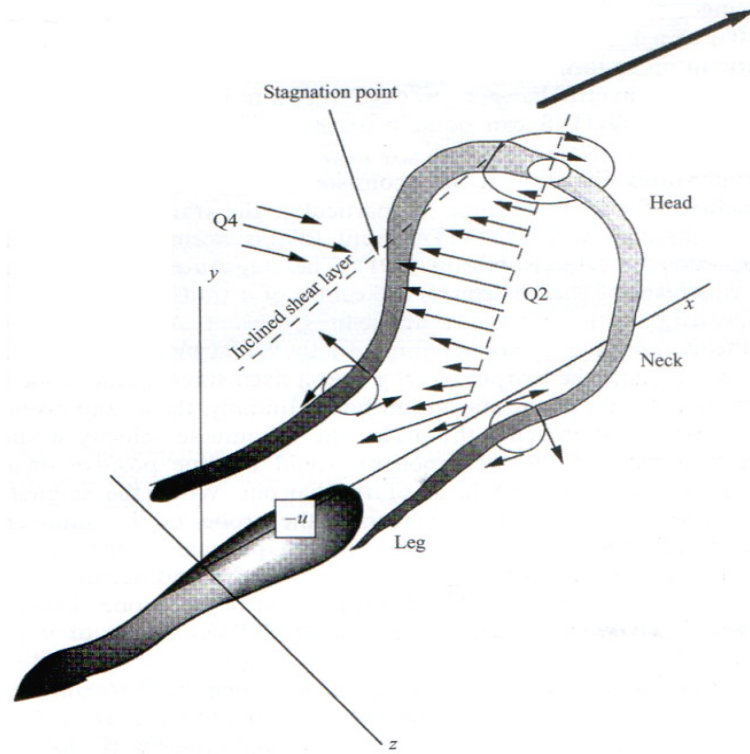


(c)

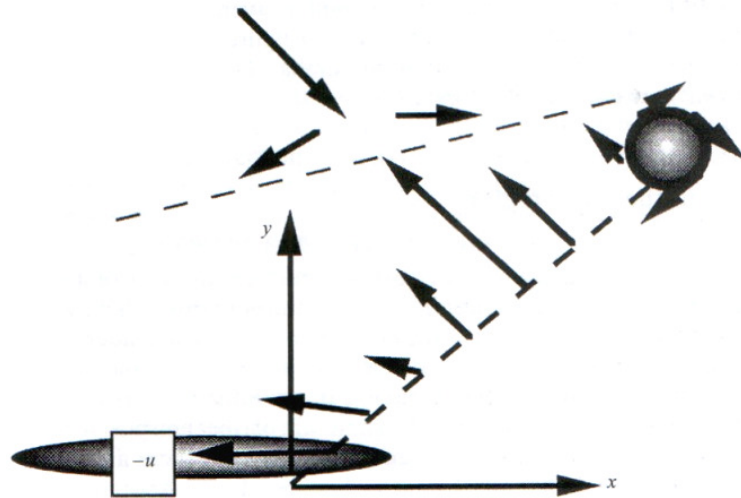


(d)

Figure 2.4.3. The generation of a secondary hairpin vortex, SHV, upstream of the Ω -shaped head of the primary hairpin vortex, PHV. Secondary vortex initiates from location marked A in b) and c). Also note formation of a downstream hairpin vortex, starting from streamwise vortices ahead of the head of the PHV. a) $t^+ = 63$, b) $t^+ = 72$, c) $t^+ = 81$, d) $t^+ = 117$. From Zhou *et al.* (1999).



(a)



(b)

Figure 2.4.4. (a) Schematic of a single hairpin vortex linked with an ejection event and the formation of a low-speed streak; (b) Signature of a hairpin in the x - y plane. From Adrian *et al.* (2000).

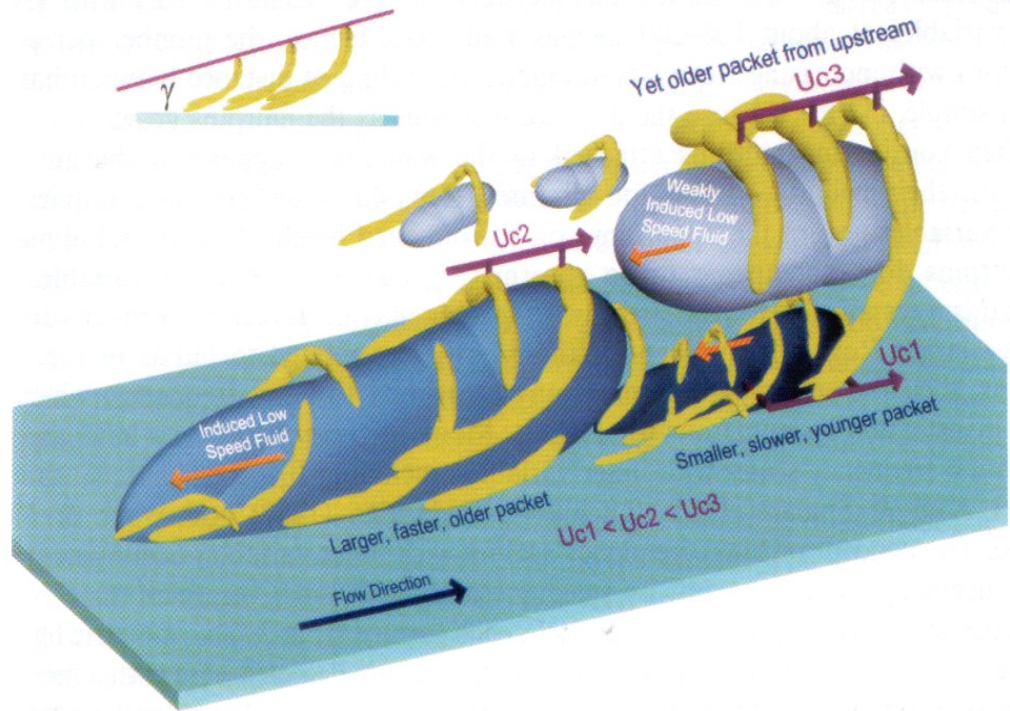
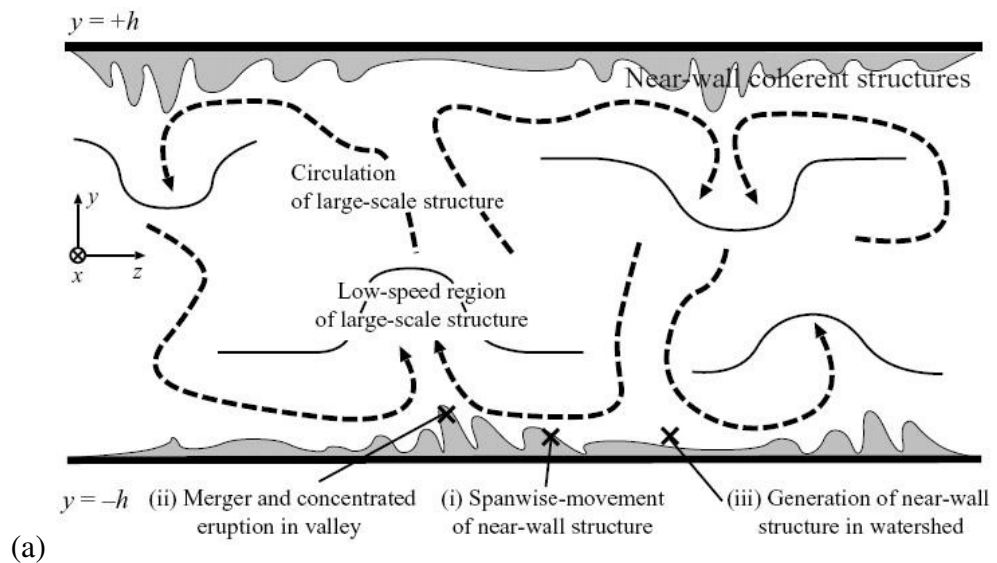


Figure 2.4.5. Conceptual scenario of nested packets of hairpins or cane-type vortices growing up from the wall. These packets align in the streamwise direction and coherently add together to create large zones of nearly uniform streamwise momentum. Large-scale motions in the wake region ultimately limit their growth. Smaller packets move more slowly because they induce faster upstream propagation. From Adrian *et al.* (2000).



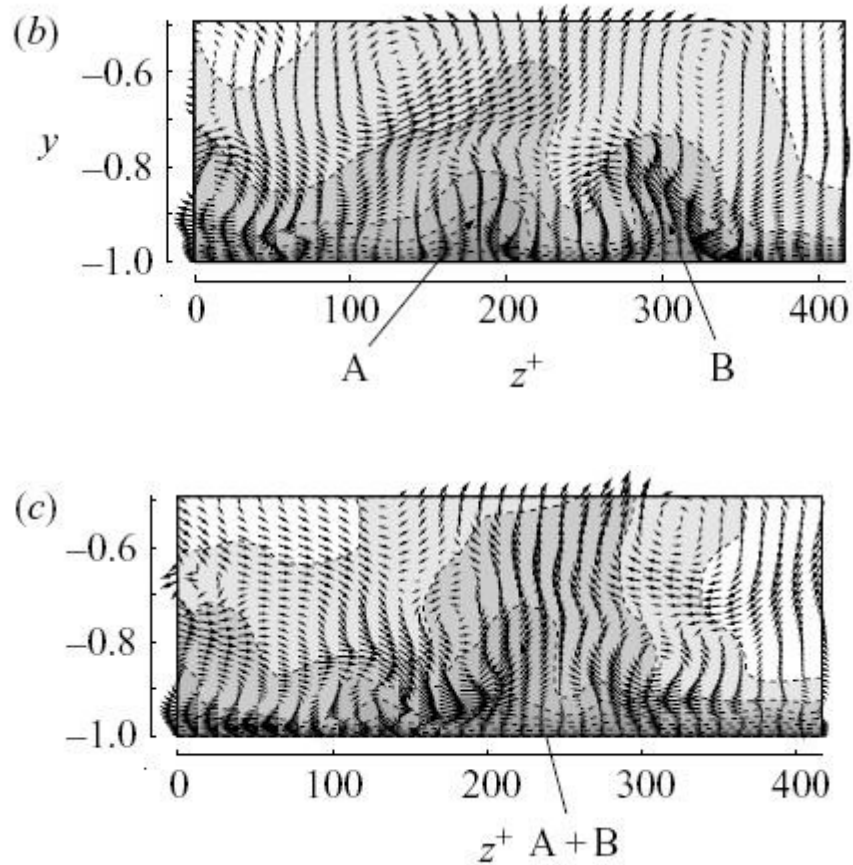


Figure 2.4.6. (a) Schematic view of a snapshot in our channel in a y - z cross-section, where three elementary processes of the co-supporting cycle are described. Thin solid curves indicate contours of u in the outer region, each bulge of which corresponds to the low-speed region of a large-scale structure.

The circulation of a large-scale structure is represented by a thick dashed curve. Shaded regions near the walls denote wall streaks. (b), (c) Snapshots of flow in the $Re = 9000$ ($Re_\tau = 349$) case in a z - y cross-section at $t = 120$ and 140, respectively (t is the computational time and its units are not specified in the paper). The vector field indicates (w, v) . The shaded region indicates $u < 0.7U_\infty$ and contour levels are $0.6U_\infty, 0.5U_\infty, \dots, 0.1U_\infty$. A concentrated eruption follows a merging event of near-wall structures as denoted by A and

B in (b). From Toh, and Itano (2005)

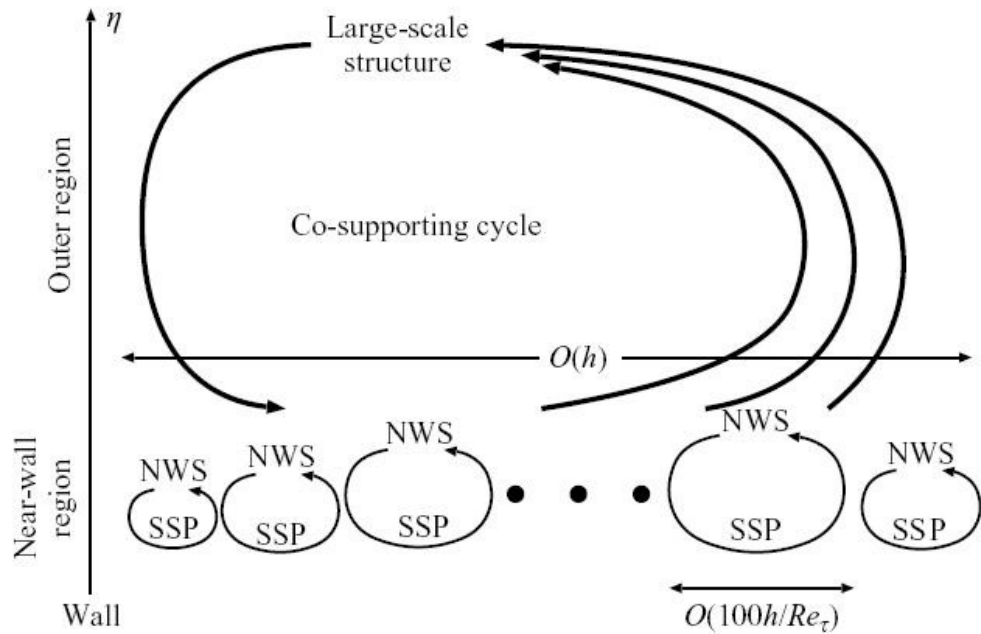


Figure 2.4.7. Co-supporting cycle of a large-scale structure and near-wall structures. SSP denotes self-sustaining process; NWS denotes near-wall structure. From Toh, and Itano (2005)

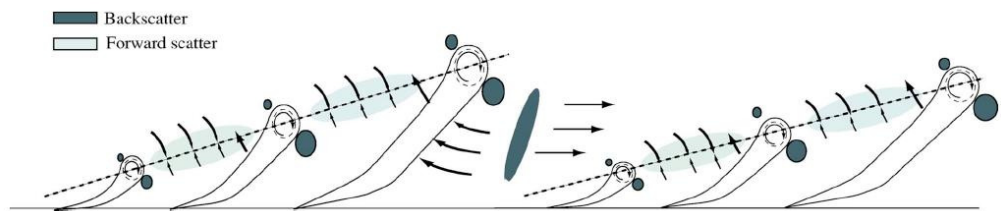


Fig 2.4.8. Conceptual model illustrating the role of hairpin vortices and their organisation into larger-scale packs in the transfer of energy within the log layer of wall turbulence. From Natrajan and Christensena (2006).

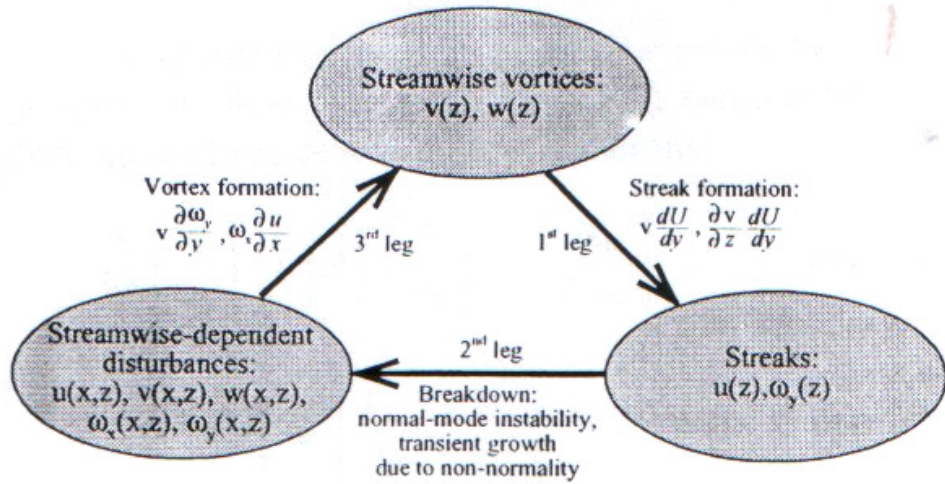


Figure 2.4.9. Schematic illustration of a self-sustaining process of near-wall turbulence. From Kim (2005).

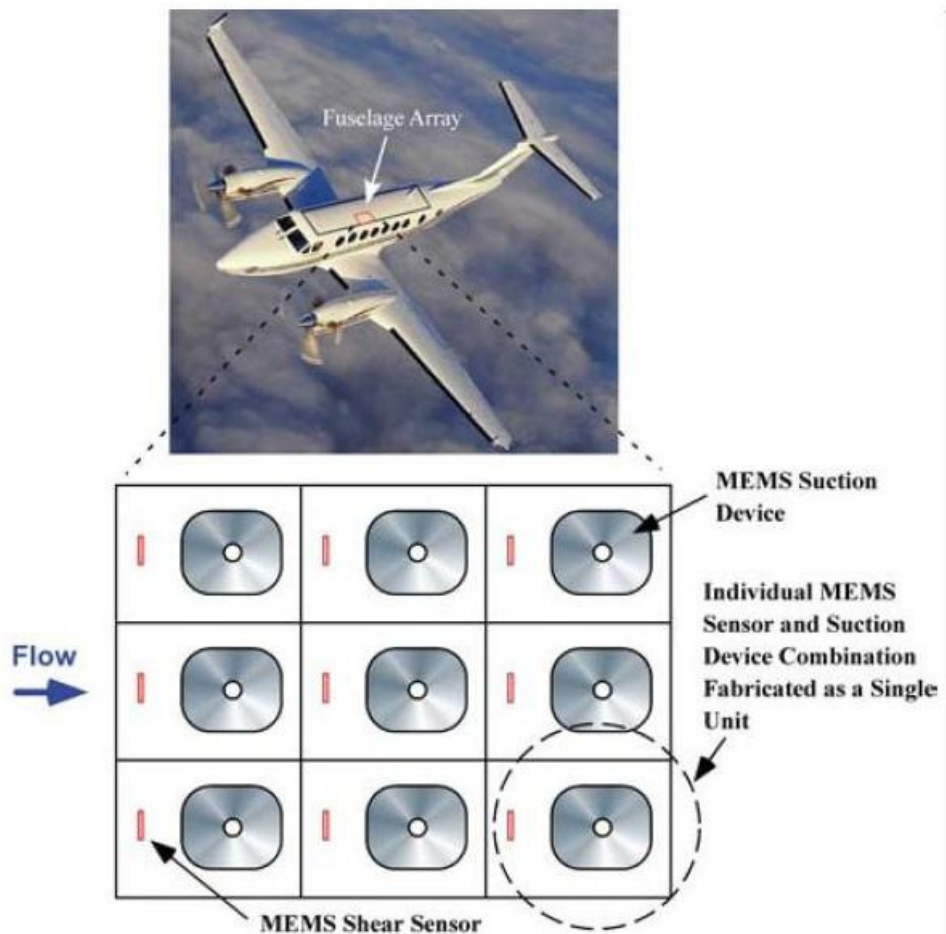


Figure 2.5.1. Schematic showing individual MEMS sensor and suction device combinations in a grid layout. From Kerho (2002)

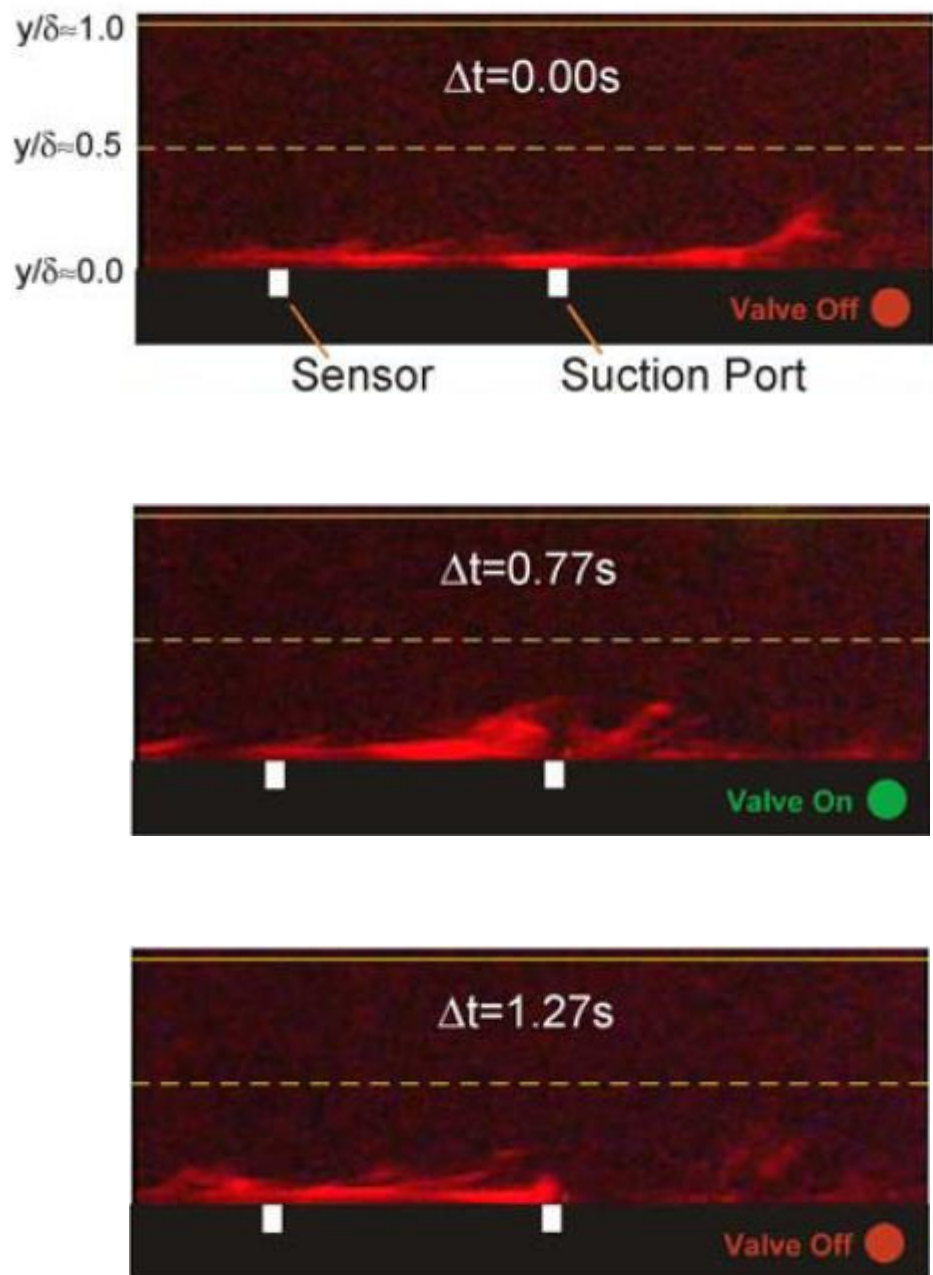


Figure 2.5.2 Flow visualisation in the boundary layer controlled by selective suction. The collective smoke is the low-speed streak. From Kerho (2002)

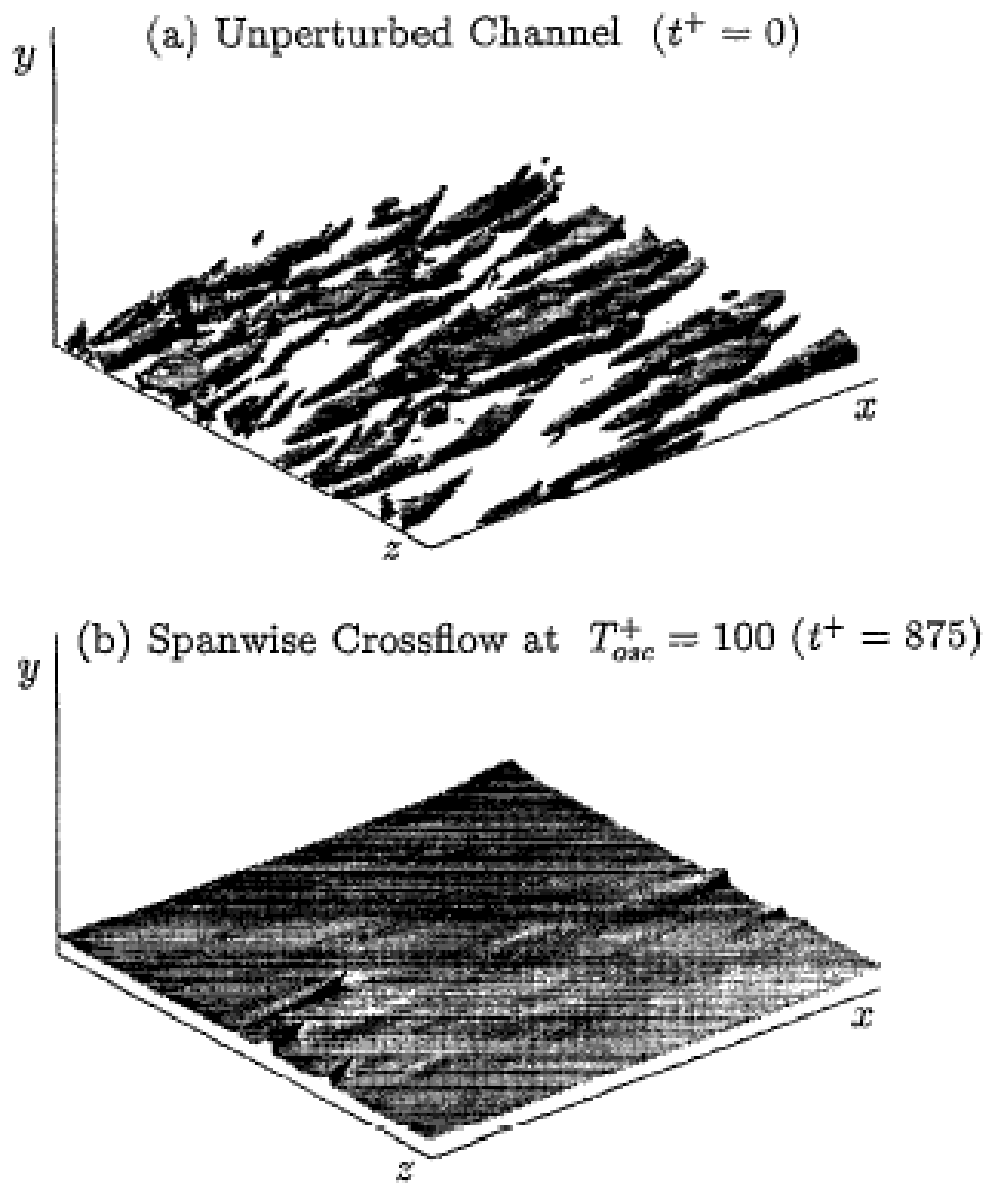
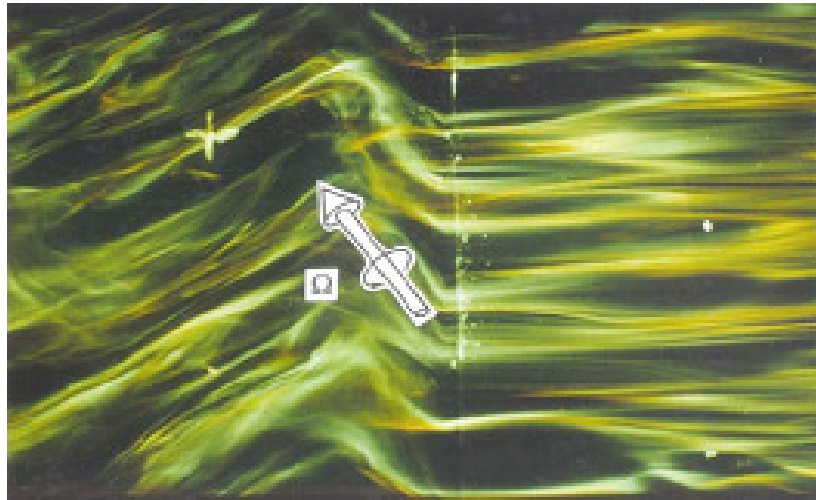
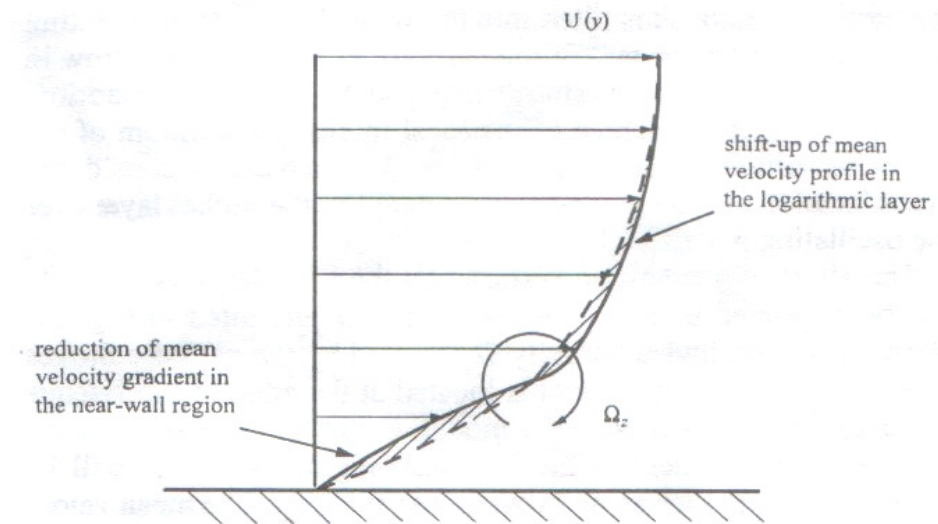


Figure 2.5.3. (a) Turbulence structures in the unperturbed channel compared to (b) a channel with cross-flow oscillations at $T^+ = 100$. The turbulent structures are represented by contour surfaces of constant vorticity magnitude; $|\omega| = 1.1u_\tau^2/\nu$. From Jung et al. (1992).



(a)



(b)

Figure 2.5.4. (a) Visualisation of the near-wall streaky structures with spanwise wall oscillating actuation. A negative spanwise vorticity created in the near-wall region of the boundary layer over the oscillating wall as shown in the picture. Flow direction is from the right to the left. (b) Conceptual model for a turbulent boundary layer over an oscillating wall showing a net spanwise vorticity, Ω_z , created by a periodic Stokes layer. From Choi et al. (1998).

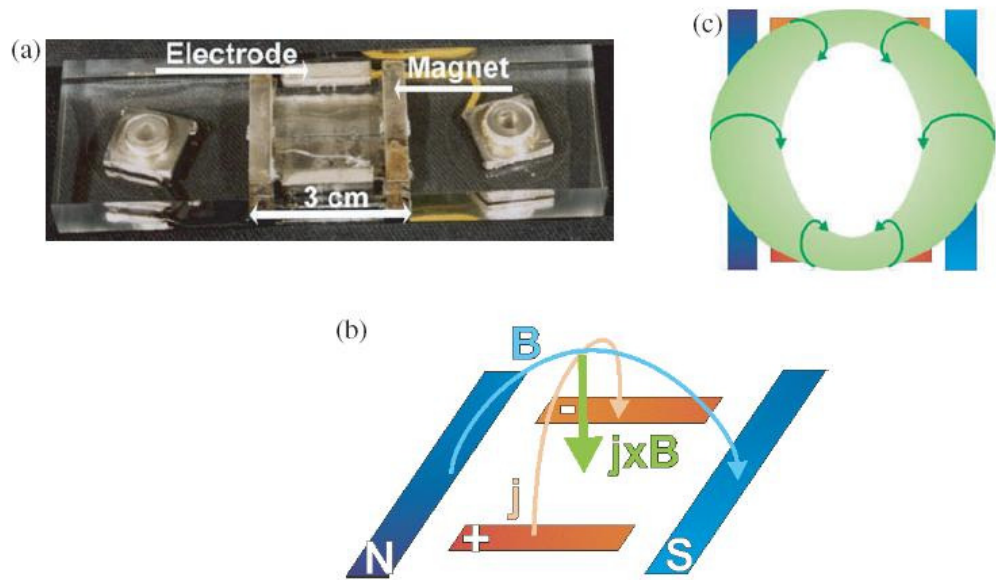


Figure 2.6.1. Wall-normal actuator: (a) photograph of the the EM actuator, (b) schematic of the magnet and electrode arrangement and associated EM forces, (c) sources of EM vorticity in the boundary layer due to Lorentz forces. From Thibault and Rossi (2003).

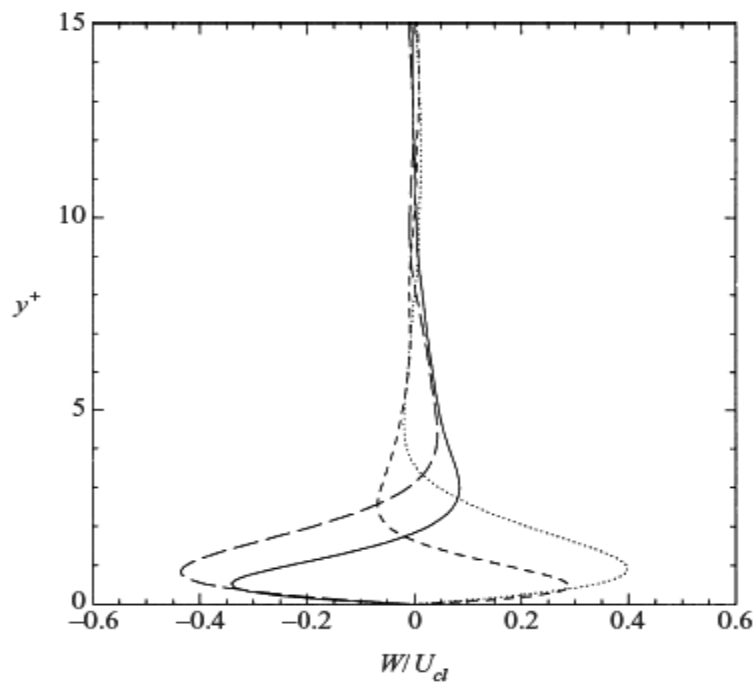


Figure 2.6.2. Spanwise velocity profiles (W) due to oscillatory Lorentz forcing normalised by the centre line streamwise velocity. From Du et al. (2002).

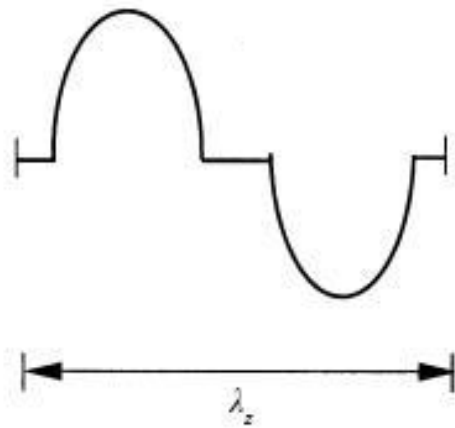


Figure 2.6.3. Two pump Lorentz force function, λ_z is the forcing wavelength.

From Du et al. (2002).

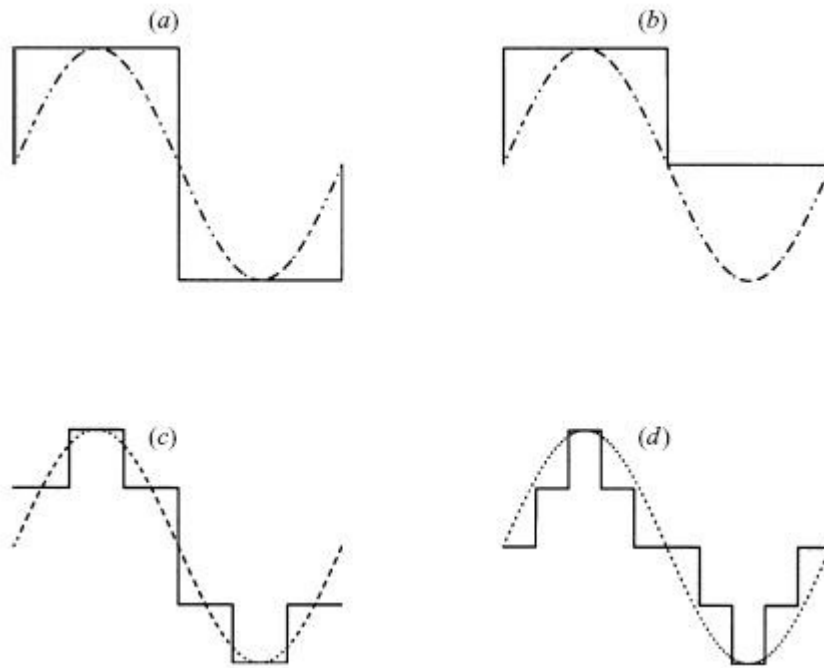


Figure 2.6.4. Generic non-ideal travelling waveforms. From Du et al. (2002).

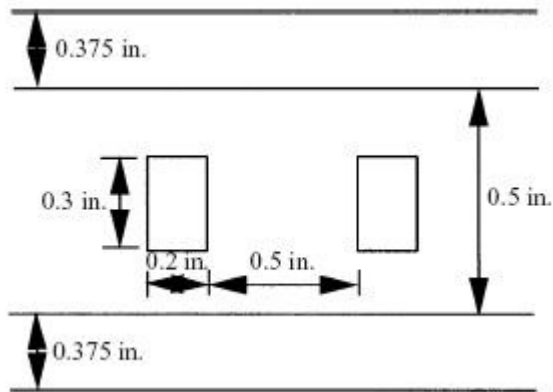


Figure 2.6.5. Plan view and dimensions of a single electro-magnetic tile used in the Princeton experiment. From Du et al. (2002).

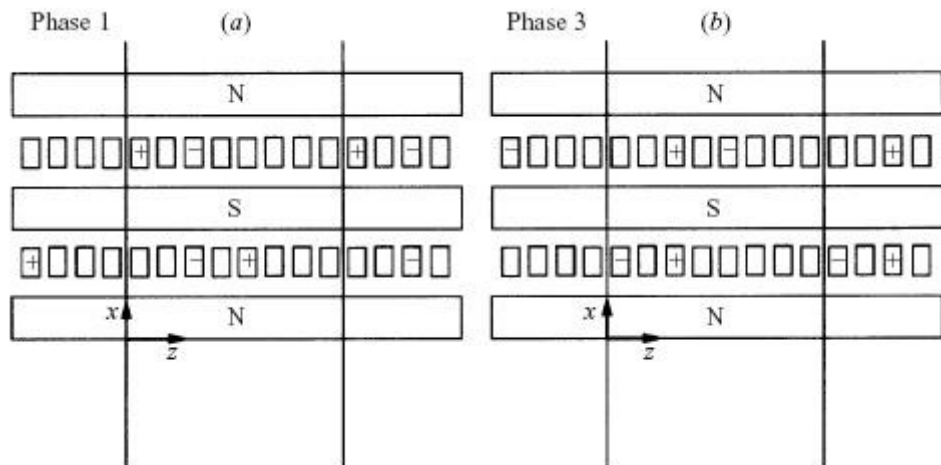


Figure 2.6.6. (a) Pattern of the first phase in Class 1; (b) Pattern of the first phase in Class 2. N and S refer to a magnet with North and South polarity respectively. '+' denotes positively activated electrodes and '-' denotes negatively activated electrodes. Phase 1 and Phase 3 on the plot refer to the global phase number in 1 to 16. The flow is perpendicular to the magnets.

From Du et al. (2002).

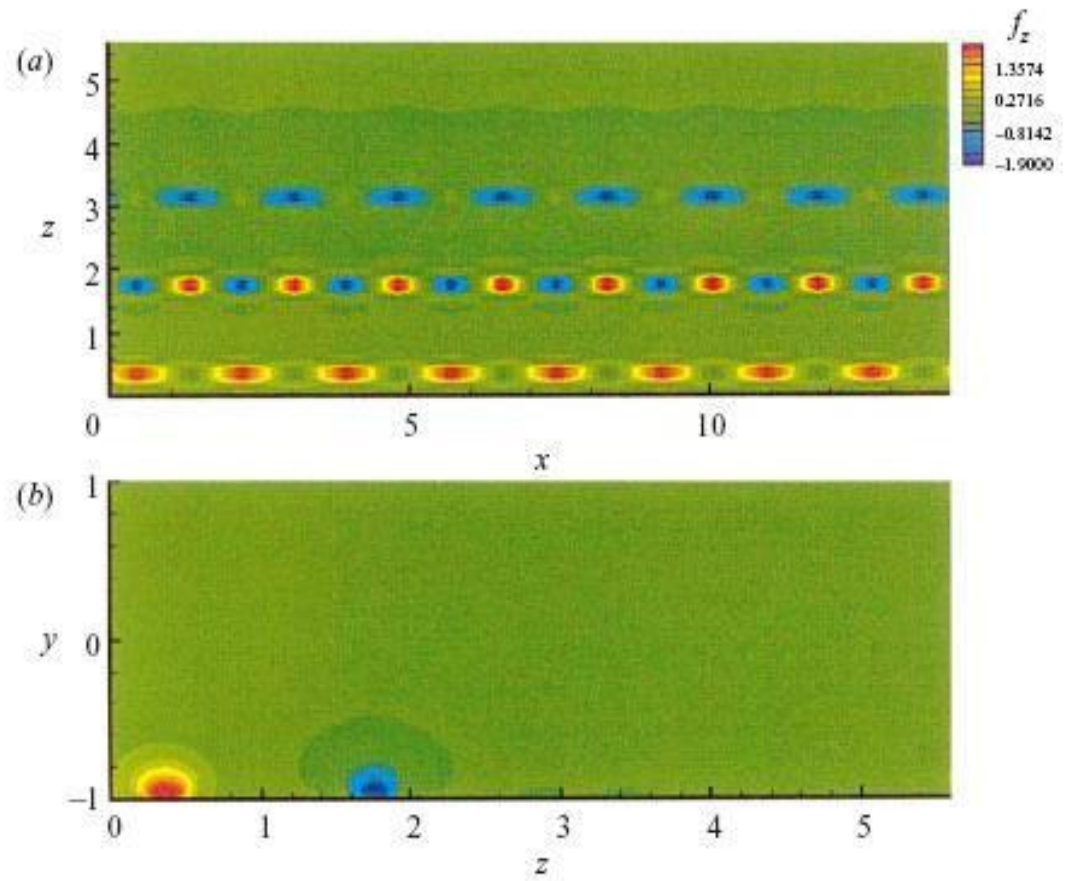


Figure 2.6.7. Contours of instantaneous spanwise Lorentz force generated during one phase in the 16-phase Princeton multi-tile configuration. (a) Plan view; (b) cross-flow view. From Du et al. (2002).

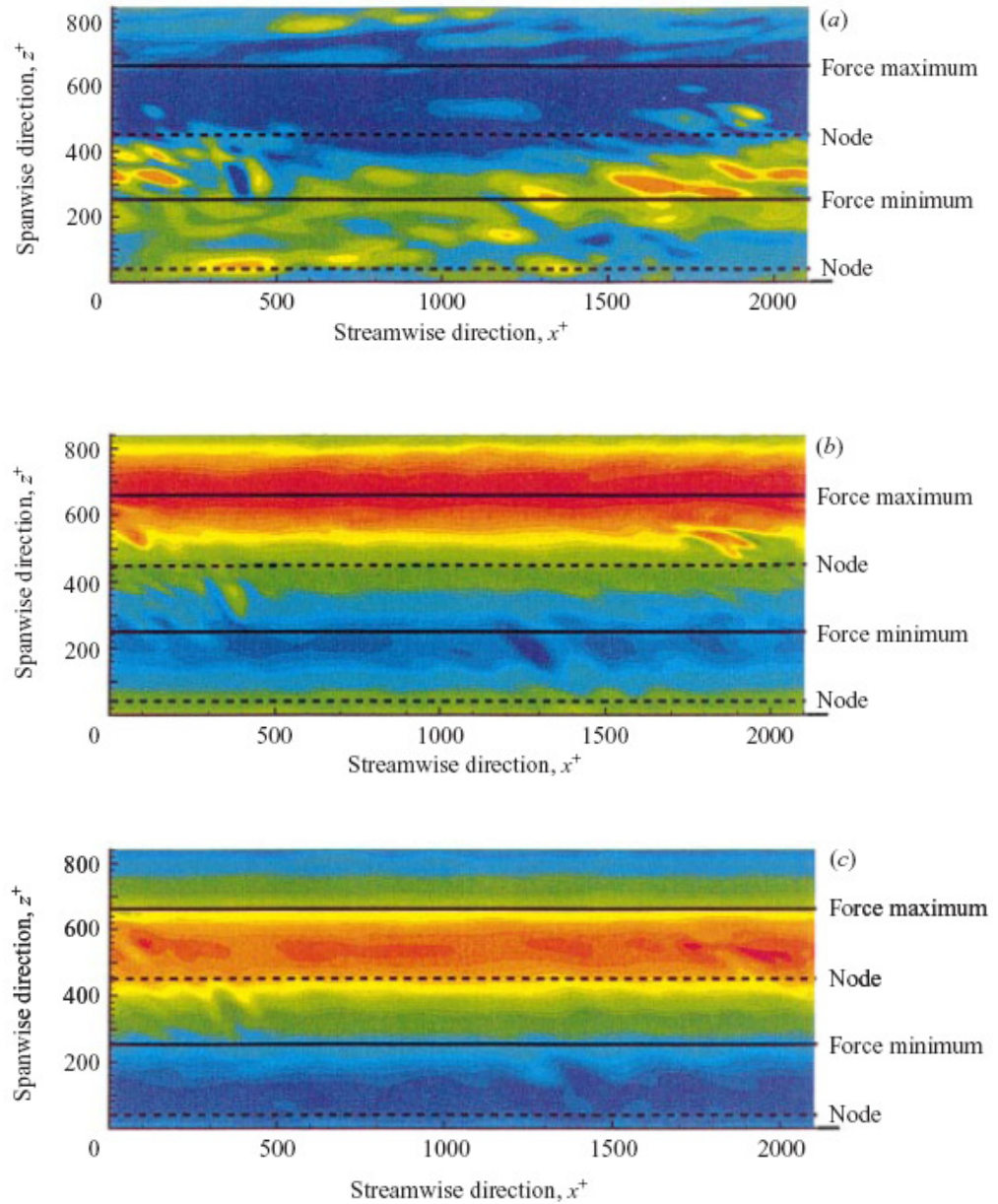


Figure 2.6.8. Visualisation of (a) instantaneous streamwise velocity, (b) streamwise vorticity, and (c) spanwise velocity at a distance $y^+ = 4$ from the wall controlled by a spanwise travelling wave. Red denotes high values and blue denotes low (or negative) values. All data correspond to time point B in figure 2.6. From Du et al. (2002).

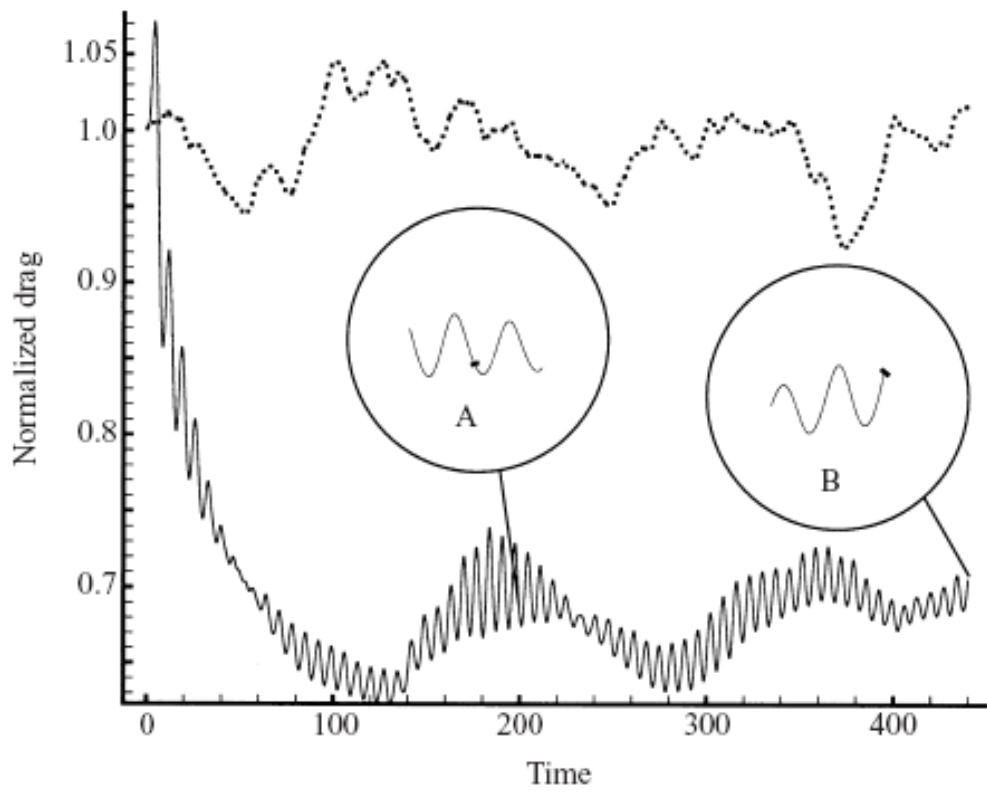


Figure 2.6.9. Time history for the normalised drag force for $\lambda_z = 5.6$, $T^+ = 50$. Time in global units. The no-control case is denoted by the dotted line. From

Du et al. (2002).

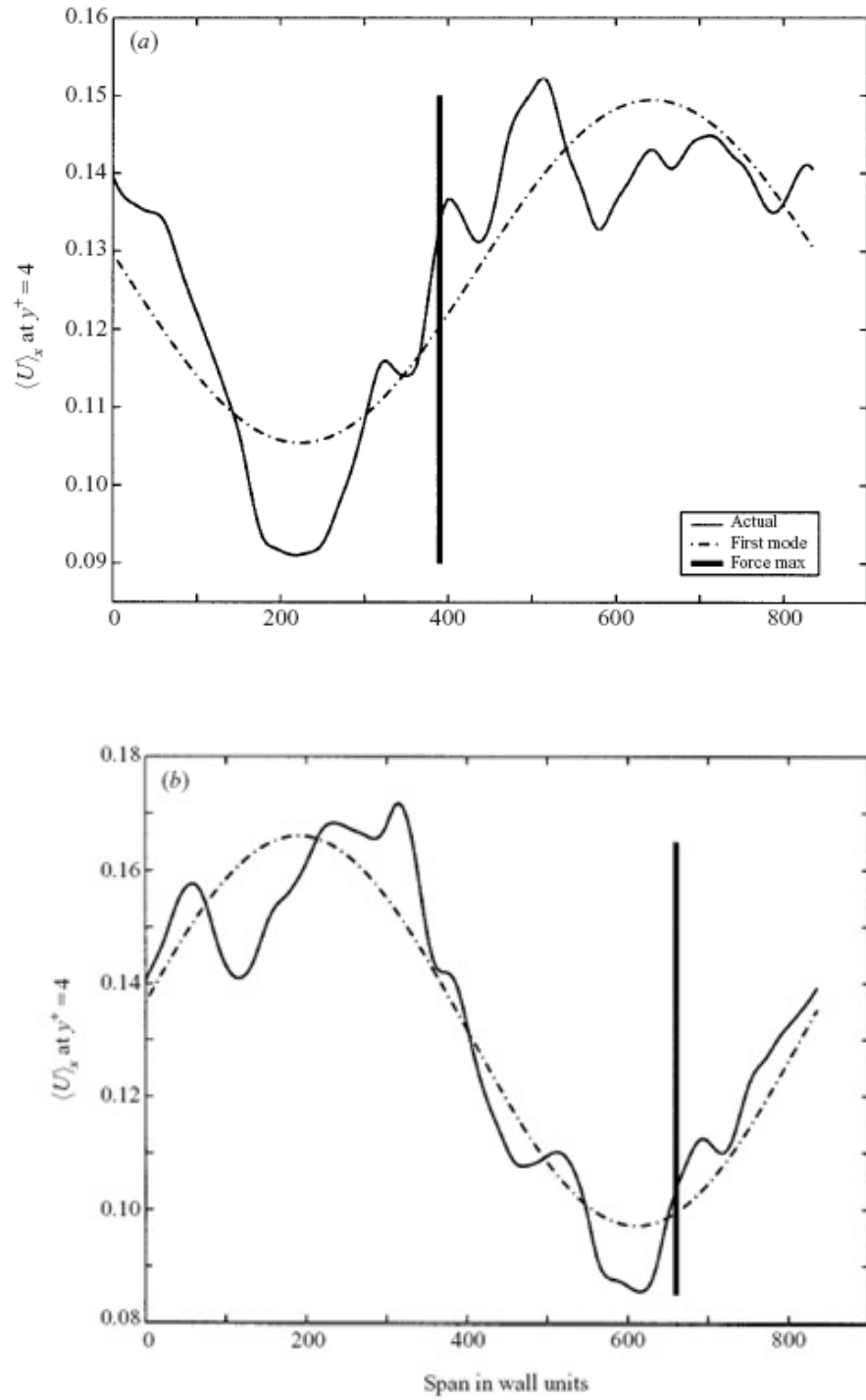


Figure 2.6.10. Instantaneous flow velocity averaged along the streamwise direction ($y^+ = 4$); (a) time = 200 (point A) and (b) time = 440 (point B) in figure 2.6.9. Time in global units. From Du et al. (2002).

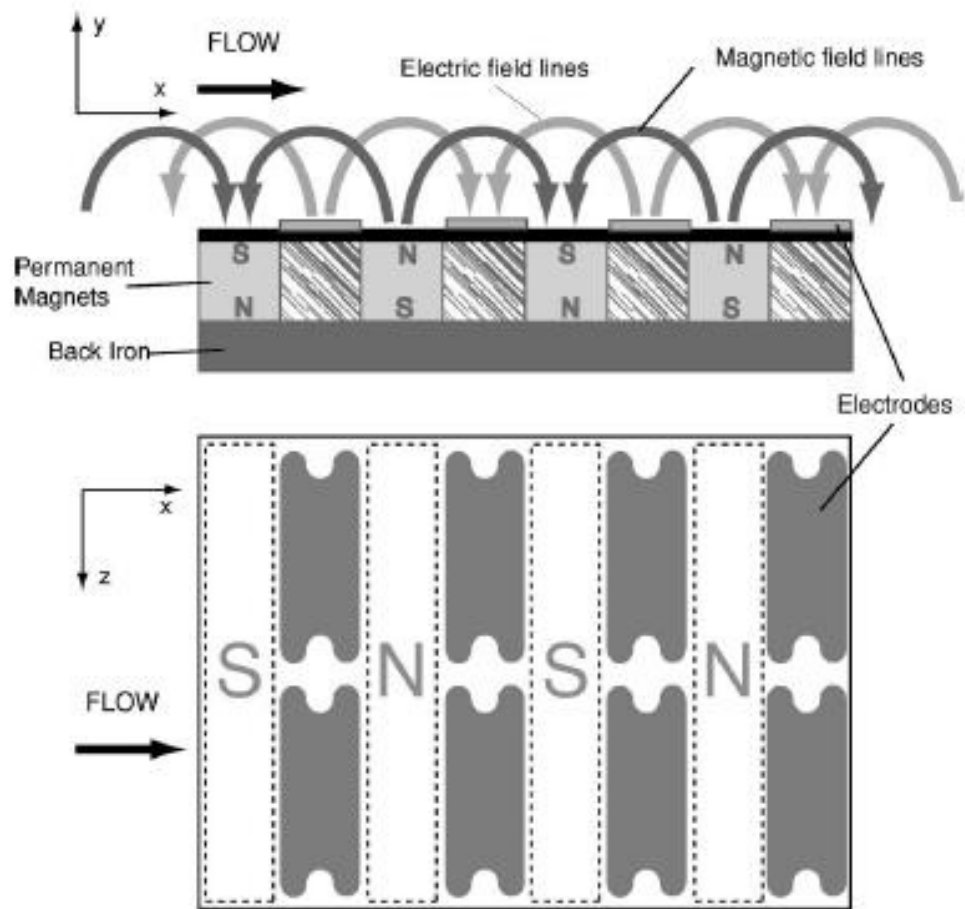


Figure 2.6.11. Schematic of the Lorentz force actuator showing side and top views, respectively. The Lorentz force acts in the spanwise direction, out of the page on the side view and from top to bottom on the top view. The contours of the electrodes are designed to reduce spanwise fringing fields which generate parasitic components of the Lorentz force. From Breuer et al (2004)

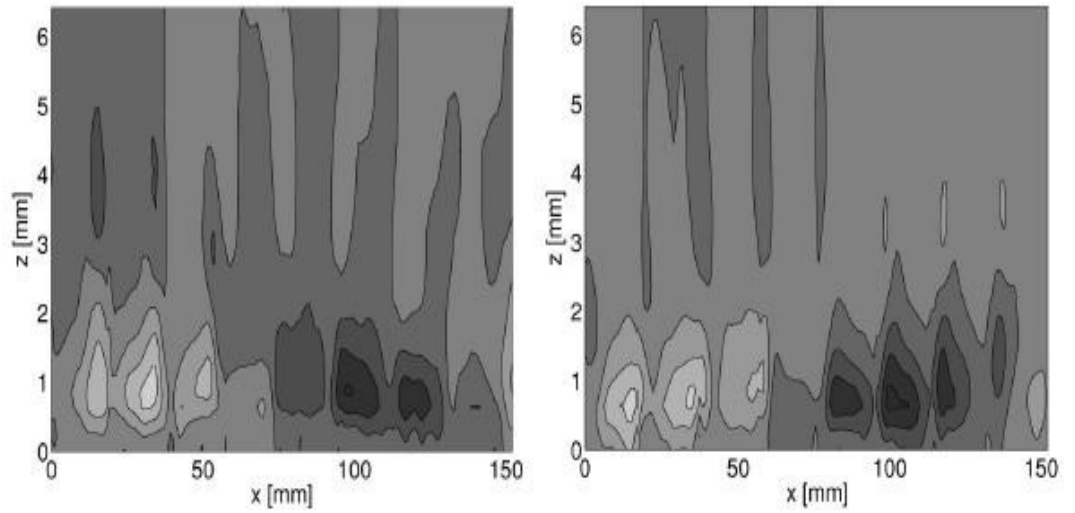


Figure 2.6.12. Shaded contours of spanwise velocity induced by a travelling wave moving to the right (left frame) and to the left (right frame). The picture is a composite image, formed from eight snapshots taken at equally spaced intervals during the cycle. Contour lines are equally spaced at intervals of 0.01 m/s. White indicates maximum positive velocity of 0.05 m/s and black indicates maximum negative velocity of 0.05 m/s. From Breuer et al (2004).

Chapter 3

Experimental Setup

3.1 Introduction

The experimental facilities and equipment used in this study are explained in this chapter. An open water channel is used to carry out all the experiments. Although this channel had been used by our research group for several years before this project started, the whole experimental facility has been improved for this project except for the original flume itself. The details are explained in section 3.3. A hot-film anemometer is used as the basic data collecting device. An electro-magnetic actuation system is also designed to control the turbulent flow in this study.

3.2 Open Water Channel and Test Section

The experiments have been carried out in a 7.3 meter long open water channel with a working section of 600 mm by 300 mm (Fig 3.2.1). The flow rate is controlled by the pump, the openings of the main valve and the bypass valve. A 4 meter long, 600 mm wide and 20 mm thick test plate with a 20:1 elliptic leading edge is placed in the channel, which is made of Perspex with an insert to mount EMTC actuators and an injection slot. To ensure a fully developed turbulent boundary layer over the working area of the test plate, two rows of 3mm diameter by 10 mm high rubber rods are placed 150mm downstream of the leading edge as a trip device (Pang and Choi, 2004).

3.3 Improvement of the Water Channel for Flow Quality

An over-flow hole is used to control and monitor the water level in this study instead of opening a gate. This can ensure a consistence of the water depth during the experiments. The hole is located on a side-wall of the down-stream section of the tank.

3.3.1 Free Surface Effects and Flap Setting

The test plate is carefully placed in the water channel parallel to the water surface, so that the pressure gradient within the working section can be kept to nearly zero. The static pressure distribution along a flat plate is mainly determined by the water surface head of the open water channel (Dake, 1972). The Froude (Fr) number is calculated and investigated because it directly relates to the speed of a surface disturbance (Henderson, 1966) and its effect can be viewed as a perturbation applied to a canonical boundary layer (Balachandar et al., 2001). In this study the Fr number is 0.0886 with 0.1 m/s of mean flow and a 130 mm of water depth; the turbulent boundary layer thickness is 89 mm at the velocity measurement point. Balachandar's water channel is only 50 mm deep and the maximum velocity is set at 0.78 m/s (2001), giving a much greater Fr number ($0.25 < Fr < 1.1$). In their study, Balachandar et al., (2001) confirmed the skin friction factor is not dependent on the Froude number and the Log-law is valid. There is no apparent Froude number effect on the skewness or kurtosis distributions, either. Although the turbulent intensity peak increases with the Fr number increasing in their study, the peak value is not affected by the free surface effect in this experiment.

A flap is set at the trailing edge, with an adjusted angle to avoid flow separation on the upper surface of the leading edge. The flow visualisation technique is used here to investigate the correct angle. A Pitot tube is used as the dye (food colouring) injector. The released dye is contained in the wake of the tube to prevent the wake of the dye ejector from becoming unstable or turbulent. The tube outer diameter is 2 mm which makes the Reynolds number less than 200 (Merzkirch, 1987). Figure 3.3.1 shows the experimental setup. Some results are shown in figure 3.3.2. When the trailing flap angle α is too small, the upper pressure P_1 is less than the bottom one P_2 and the stagnation point moves away from the centre line of the leading edge, as shown in figure 3.3.2a, where all the food colouring mixtures move along the upper surface of the leading edge. When the trailing angle is increased, less fluid moves along the upper surface and the stagnation point moves closer to the central leading edge (see figure 3.3.2b). When all the dye moves along the bottom surface with an increasing flap angle, a separation on the upper surface occurs (figure 3.3.2c). The situation becomes worse when the trailing angle is increased further as shown in figure 3.3.2d. The separation on the upper surface is avoided by adjusting the trailing flap angle to around 21° .

Stainless steel pins are used at the connection of the two plates and special treatment is applied to ensure a smooth surface with no gap in between.

3.3.2 Screens and Diffuser

The flow quality in this open channel was improved by placing screens, honeycombs and a diffuser in the upstream of the water tank in front of the test plate as shown in figure 3.2.1.

The application of the screens across the channel is one of the most effective methods to reduce the free-stream turbulence (Dryden, H. L. and Schubauer, G.B. 1947). The screens used for this purpose are of fine mesh and are placed upstream of the working section. The physical explanation (Dryden, H. L. and Schubauer, G.B. 1947) of the action of such a screen is that the large-scale eddies are removed at the expense of the introduction of a large number of eddies with much smaller scales which are found to decay rapidly. The screens thus decrease the turbulence at a sufficient distance downstream although it may considerably increase the turbulence at small distances. The scale of eddies brought about by a screen depends on the Reynolds number and is controlled by the diameter of the wire from which the screen is made. In this study, one of the wire diameters of the screens is 0.73 mm, the width is 7.3 mm and the porosity density is 0.8; the other is 0.1 mm of diameter and 1 mm wide. The Reynolds numbers of the screens are much less than 40. Therefore, no eddies are shed (Dryden, H. L. and Schubauer, G.B. 1947) and the screen creates no turbulence of its own.

It is generally assumed that the turbulence downstream of the screen is isotropic. Some experiments such as MacPhail (1940) have confirmed this. In total 4 screens are used in the current experiment due to the fact that it is better to use a number of successive screens rather than a single one (Dryden, H. L. and Schubauer, G.B. 1947). To ensure the distance between the screens and the working section, two screens are placed in the upstream tank. The sufficient distance between the screens and the working section allows the eddies to have more time to decay (Dryden, H. L. and Schubauer, G.B. 1947).

All the screens are bolted to the channel to ensure their consistent positions during the years of the study.

A diffuser shown in figure 3.2.1 is used in the upstream tank to improve the flow quality. The details are shown in figure 3.3.3.

The turbulence intensity of the main flow is reduced from 6% to 0.5% after the flow improvement work is done. The diffuser especially reduces the turbulent intensity by half.

3.3.3 Supporting Frame for the Hot-film Anemometry

A series of frequencies were found relating to the previous hot-film probe supporting frame. For example, the noises from 15.14 Hz to 16.6 Hz come from the vibration of the frame structure and the noise around 35 Hz is identified from the horizontal plate of the previous supporting frame.

An aluminium frame was designed to solve the vibration problem and is shown in figure 3.3.4. A 1200mm long by 300 mm wide by 10 mm thick stainless steel plate is selected as the top cross-member supporting base, whose maximum deflection is less than 0.3 mm; a stainless steel square section is used to further strengthen it.

Figure 3.3.5 shows the energy spectra of the velocity fluctuations before and after the application of the new supporting frame. Please note all the data are measured in the free-stream region. It shows that the energy of the frequencies around 15 Hz to 45 Hz are restrained.

Vibration damping tapes are also used between the different sections of the water flume.

3.3.4 Temperature Controlling and Monitoring

A 1 meter long and 10 mm diameter copper pipe was designed as a heat-exchanger to feed the conductive solution through the injection slot in the current study to avoid the temperature differences between the ambient and the injected flows. It is crucial for the measurement to be taken by the hot-film sensor. Figure 3.3.6 shows this heat exchanger.

The temperature is measured using an omega OL-703-PP stainless-steel linear thermistor probe with a custom made electronic circuit that allows the temperature signals to be recorded by a computer via an Iotech ADC 488/8SA eight channel 16-bit analogue-to-digital converter. Another thermistor probe is used to observe directly the water temperature changing to regulate the flow rate of the heat exchanger in the upstream tank.

Compared with the hot-wire probe, the hot-film sensor is more sensitive to temperature changes of the ambient fluid because of the lower over-heat-ratio. For example, 3°C of temperature change in water can give a 100% error in the velocity reading (Pang, 2006). In the current experiment, a heat exchanger is placed in the upstream tank to maintain the water temperature, with a tolerance of $\pm 0.1^\circ\text{C}$ which gives the velocity reading error within 4% (Bruun, 1996).

3. 4 Flow Visualisation Experimental Setup

Many experimentalists investigate and visualise the flow phenomena in water channels (see, e.g., Werlé ,1973, 1979, 1982; Erickson, 1979). If one could instantaneously release the dye along a line perpendicular to the mean flow

direction, it would be possible to visualise the local velocity profile by means of recording the distortion of this dye line in the flow (Merzkirch, 1987).

Food colouring is used in this experiment for the flow visualisation of the turbulent flow without control, because it can be diluted with the water from the operating channel to minimise density gradients and the filaments of the different colours can be generated for promoting the identification of the spatial flow structures (Han and Patel, 1979; Maxworthy 1972; Pullin and Perry, 1980; Merzkirch, 1987). The Copper Sulphate solution is injected when the velocity measurement is needed, while the Potassium Permanganate solution is employed for the flow visualisation with Lorentz forcing control, because of its good visual impact as well as its conductivity (Kotas, 1977).

The solution is injected tangentially by gravity-fed into the flow through a slot 0.5 mm wide and 250 mm long. A Cannon XM2 digital video camcorder is used to capture the pictures.

As mentioned above, tap water is made conductive by introducing the electrolyte solution with a conductivity of 1.0S/m through a wall slot 24 mm upstream of the electromagnetic (EM) actuators. The conductive solution has not been used to fill the full water channel because of the cost of the chemical as well as the potential corrosion problem of the test rig.

3.4.1 New Design of the Injection Slot

To improve the uniformity injection flow along the slot, the injection slot was improved and its details are shown in figure 3.4.1. There is a large chamber located just beneath the injection slot, which acts as a reservoir for the injected solution. There are 4 supply inlets at the bottom of the chamber. The distance between the supply pipe inlets and the slot outlet is as long as possible, which

is limited by the height from the test plate to the channel bottom. Before the injected fluid reaches the slot there is a screen along the slot width to reduce the fluctuations and to improve the uniformity of the injection. The injection rate is set to be about 0.0018m/s by the control of the valves and the free surface height of the feed tank. With the new design, the flow variation along the slot is less than 3%.

To maintain a constant injection speed, the height of the solution in the storage tank is kept at a constant level within 2 mm of variance. It is shown in figure 3.4.2. The injection effect is examined by comparing the turbulence statistics of the boundary layer with and without injection. Figure 3.4.3 shows the mean velocity and the turbulent intensity profiles with and without injection, where the velocity is measured 20 mm downstream of the slot. The negligible differences in the profiles suggest that the added momentum through the injection slot does not affect the boundary layer measurements.

3.4.2 Water Treatment

When the Copper Sulphate solution is injected into the channel filled with tap water, the precipitation of the Copper Carbonate and Copper Hydroxide occur. Figure 3.4.4a shows the contaminated water which occurs only after about 40 minutes after the injection of the Copper Sulphate solution during the experiment. If the water is allowed to stand for a while, the precipitate (the blue/green floc-like particles or powder) can be seen on the electrode sheet and the test plate surface, as shown in figure 3.4.4.b and c. A water treatment has to be taken to avoid this since they can deposit in the entire water channel and on the surface of the hot-film sensor which may change its characteristics. Sulfuric Acid is carefully selected (without inducing new chemical ions) to

keep the ambient water environment slightly acidic (pH < 6.2 in our experiments), which is monitored by the Jenway 350 pH meter. The conductivity is measured by the Hanna 9635 Conductivity/TDS Meter with the temperature compensation whose accuracy is about 0.03 S/m.

3. 5 New Designs of Electro-Magnetic Actuators

3.5.1 Introduction

As discussed in Chapter 2, the spanwise Lorentz force seems to be the most effective one among the three directional forces (Lim et al. 1998). The electro-magnetic actuator is designed so that only the spanwise force is generated. Figure 3.5.1 shows the configuration of the EM actuators for the spanwise oscillation and travelling wave excitations. A copper laminate is photo-etched and the electrode is 0.017 mm thick.

The electrodes are activated alternatively so that the spanwise force can be generated as shown in figure 3.5.1a. The permanent magnets (1.2T) are placed on either side of the electrodes so that the spanwise force can be created. The EM actuator covers a streamwise distance of 300 mm ($x^+=1580$) and a spanwise distance of 230 mm ($z^+=1214$). Because of the non-uniformity of the concentration distribution along the streamwise direction, the total current intensity to the entire actuator surface is used to demonstrate the strength of the Lorentz force and calculate the Stuart number (equation 3.5.1).

$$St = J_0 B_0 \delta / (\rho u_\tau^2) \quad (3.5.1)$$

Where, J_0 is the current density, B_0 is the magnetic flux density, δ is the boundary layer thickness, ρ is the fluid density and u_τ is the frictional velocity.

The penetration depth Δ^+ (Berger et al 2000 and Du et al 2000) given by:

$$\Delta^+ = a^+ / \pi \quad (3.5.2)$$

is about 7 in the experiment. Here, $a^+ = a \cdot u_\tau / \nu$ is the non-dimensional width of the electrode a (the same as the magnets and is 5 mm in this study). The same width of the electrode and the magnet ensures that equation (3.5.2) is valid.

3.5.2 The Geometry of the Electrode Sheets

The whole electrode sheets for the spanwise oscillation and the travelling wave are shown in figure 3.5.2. The dimensions are selected so that it can control around 10 low-speed streaks whose maximum length is around 1000 wall units and spanwise spacing is about 100 wall units. The spanwise gap between the electrodes shown in figure 3.5.2b is for the wiring that goes on the surface by taking advantage of the photo-etching. This avoids complex wiring, drilling and damage to the Mylar sheet. The copper stripes acting as connection wires are insulated and 1 mm wide, which ensures no thermal heat effects due to the low electrical resistance and has no major impact on the Lorentz forcing effects. The distance between the 1mm wide copper stripes is 1 mm as well to avoid the possibilities of short circuits. As explained in the following phasing strategy, the Lorentz forces are generated in every two alternate rows of electrodes in the spanwise direction. The spanwise gap can be classified as a non-active area. Although the smaller the gap the easier the low speed streaks are skewed to the next electrodes, it doesn't affect the Lorentz forcing effects in this study. There are also gaps between different units in the streamwise direction, which are mainly due to the structure requirement of the magnet holder as shown in figure 3.5.3, whose external effects increase the streamwise Lorentz forcing effect region. Because the low-speed streaks are 400~1000 wall units long in the streamwise direction,

each unit of around 220 wall units in the streamwise direction is reasonable to disturb and control the streaky structures. The gap between the units in the streamwise direction doesn't have noticeable effects on the performance. The new design obviously works and achieves the control effects as discussed in the following chapters.

3.5.3 The Phasing Strategy for Spanwise Travelling Wave

For the travelling wave actuator, the electrode pattern is important. To simulate the two-pump force, a pseudo-square wave force is introduced in this project as shown in figure 3.5.4a. The wavelength corresponds to around 500 wall units. This is adequate because the travelling wave needs to sweep faster along the spanwise direction due to the gap between the positive and the negative action regions of the Lorentz forces if the wavelength is bigger (Du and Karniadaks, 2002). Therefore, more power input is required. If the wavelength is smaller it cannot promise to capture enough low-speed streaks (whose average spacing is around 100 wall units).

The output signals should meet with the waveform shown in figure 3.5.4b. The electrodes are activated following a pre-set phase change via a custom-made controller. For example, the red colour indicates positively activated electrode and the black one negatively activated electrode. The phase changing strategy is shown in figure 3.5.5.

3.5.4 Mylar Sheet Surface Measurement

Due to the flexibility of the copper laminate, the surface roughness might induce a problem. To investigate it, I measured the surface waviness and roughness of the polyester plate.

Here, the Laser Gauge is applied to measure the surface profiles. The principle is shown in figure 3.5.6 and the specifications are shown in Table 3.5.1.

Table 3.5.1. Laser Gauge Specifications of Talysurf CLI 1000

Working distance	30mm
Vertical resolution	1 μ m
Accuracy*	The accuracy is equal to the resolution on diffusing surfaces with homogeneous optical properties
Maximum slope	Slopes of up to 40° can be measured in any direction (up to 90° depending on their direction)

* The accuracy is the smallest repeatable size, whereas the vertical resolution corresponds to one digit of the AD electronic converter (the signal is digitized over 16 bits, with the noise of the complete electronic string effecting only the last two bits).

The results are shown in figure 3.5.7. The maximum roughness is around $k = 0.21\text{mm}$, which equals to $k^+ \approx 1$. The surface roughness has no effect and the wall is hydraulically smooth if all the protuberances are contained within the viscous sublayer. For the flat plate at zero incidence, the condition for a hydraulically smooth wall is given by Schlichting (1951)

$$k^+ = \frac{u_* k}{\nu} \leq 5 \quad (3.5.3)$$

When the 0.017 mm thick copper electrodes are added, the maximum roughness is $k^+ \approx 1.1 < 5$. Therefore, the surface is treated as hydraulically smooth.

3.6 Velocity Measurement System

The freestream velocity of the present experiments is set around 0.1 m/s. The velocity measurements are taken 3.26 m downstream of the leading edge, where the boundary layer thickness δ is approximately 89 mm. Figure 3.6.1 shows the view from the top of the test plate with the spanwise Lorentz-forcing travelling wave actuators. The corresponding Reynolds number is about 388, based on the frictional velocity and the boundary layer thickness ($Re_\tau = u_\tau \cdot \delta / \nu$).

During the flow measurements the freestream speed U_∞ and the free-flow velocity are simultaneously recorded so that the hot-film data can be corrected. The freestream flow velocity is measured using the Nixon 403 Streamflo Velocity Meter, a vane-type anemometer, whose measuring range is from 2.5 to 150 cm/s with an accuracy of $\pm 3\%$ for velocities below 15 cm/s. Both of these signals are recorded by a computer via the Iotech ADC 488/8SA eight-channel 16-bit A/D converter. Quick Basic program is used to write the commands. All the programs used in this study are compiled by the author.

3.6.1 Hot-film Anemometry

The velocity signals are measured by a Dantec CTA 56C series quartz-coated hot-film anemometry system with a single component boundary-type sensor (Dantec 55R15). These probes are designed for applications in boundary layers. The shape of the prongs allows measurements close to a solid wall without disturbances from the probe body. The mounts of the probe axis are parallel to the direction of the flow.

The fibre-film (hot-film) probes with cylindrical thin film sensors are considerably more rugged than the wire probes and are less sensitive to contamination. The hot-film sensor is made of 70 μm diameter quartz fibres, 3 mm long, and covered by a nickel thin film approx. 0.1 μm in thickness. A 2 μm quartz coating on the hot-film sensor is used, to a large extent, to solve the electrolysis problem (Bruun, 1995). The probe body is a 1.9 mm diameter ceramic tube, equipped with gold-plated connector pins that are connected to the probe supported by means of plug-and-socket arrangements. The figure 3.6.3 shows the dimensions of the single-sensor hot-film probe.

The constant temperature mode is selected in this study, which means the hot-film is maintained at a constant operational temperature and hence at a constant resistance. There are major advantages of the constant temperature operation because the thermal inertia of the sensor element is automatically adjusted when the flow conditions vary (Bruun, 1995). The principle of a constant temperature circuit is shown in figure 3.6.4. The hot-film probe is placed in a Wheatstone bridge. As the flow conditions vary the error voltage $e_2 - e_1$ is a measurement of the corresponding changes in the film resistance. These two voltages form the input to the operational amplifier, G. The selected amplifier has an output current, i , which is inversely proportional to the resistance range of the hot-film sensor. The balance of the hot-film CTA Bridge is achieved by adjusting the resistance of one arm of the bridge via switching on the CTA Bridge.

Prior to the data acquisition, the hot-film voltage signal is fed through the 56N20 signal conditioner unit for a low-pass filter at 100Hz to decrease the electronic noise (Helmut Eckelmann 1974). For all the measurements, the

temperature difference between the water and the hot-film sensor is approximately 20 deg C, corresponding to an overheat ratio of 1.05. This temperature difference is chosen in order to ensure that the convection produced by the hot film itself remains as small as possible, and so that the frequency response of the hot film is still sufficiently high. This temperature difference also promises to eliminate the bubble formation problem by allowing the water to stand before use (Bruun 1996).

Figure 3.6.5 shows a typical Dantec CTA system. The voltage signals from the Wheatstone bridge are sampled by an A/D converter and become digital signals. Through linearization (also called calibration), the velocity signals are obtained and processed for the specific purpose.

3.6.2 Velocity Calibration

The calibration of the hot-film probes is performed in the freestream region of the water channel along with the Nixon 403 Streamflo Velocity Meter. Care has been taken to ensure that the water tunnel flow is steady prior to the data acquisition.

A 4th order polynomial curve fit is applied to the calibration data points in the form:

$$U = AE^4 + BE^3 + CE^2 + DE + F \quad (3.6.1)$$

Where A, B, C, D and F are calibration constants to be determined during the calibration.

The open-water channel cannot maintain a stable flow velocity below 0.05m/s in this investigation. However, the condition of the velocity being between 0 and 0.05 m/s is important for the study of the near-wall behaviour of turbulent boundary layer. Therefore, the velocities higher than 0.05m/s are calibrated by

moving a hot-film sensor in the still water using a stepper motor controlled by a traversing system. This approach has been used by many researchers (Aydin and Leutheusser 1980; Tsanis 1987).

A command is sent by the computer program via the controller to control the rotating speed of the stepping motor, then the probe moves at a known velocity. Figure 3.6.6 shows the output voltage from the sensor when the hot-film sensor moves at a speed of 0.03m/s. It is noticed that about 2 seconds after the sampling starts, the motor is triggered, and the sampling continues for another 2 seconds after the movement stops. Accelerations and decelerations are observed. Only periods at stable velocities are applied to the calibration. The mean values are calculated for this calibration by repeating the process. A 'Zero-velocity' is also used. It is important to note that there is a buoyant effect, driven by the heated film. Hence, this 'zero-velocity' is interpreted as 'no external flow'. Figure 3.6.7 shows one of the calibration curves of a hot film sensor with a relative polynomial fit in one experiment of this study where there is an overlap region and they agree with each other well.

3.6.3 Lorentz Forcing Effects On The Hot-film Sensors

In this study, no electromagnetic wave is generated. An electromagnetic wave only exists when the changing magnetic field causes a changing electric field, which then causes another changing magnetic field, and so on forever. Unlike a STATIC field, a wave cannot exist without moving. Once created, an electromagnetic wave will continue forever unless it is absorbed by matter. Therefore, electrolysis is the main effect that the electromagnetic actuator possibly puts on the hot-film sensor. Although the hot-film sensor is protected by a thin quartz coating, Pang (2005) reported an accident where the hot-film

sensor was damaged when it was too close to the electrodes. In this experiment, the hot-film sensor is 5 mm away from the electrode and no damage is caused due to the EM unit.

3.7 Error Analysis of Velocity Measurement

Consider a time-history record $u(t)$ which consists of a mean, U , and a fluctuating component $u'(t)$, related by

$$u(t) = U + u'(t) \quad (3.7.1)$$

For an infinitely long time-history record, the mean value, U , is simply the average of all values, which can be expressed as

$$U = \lim_{T \rightarrow \infty} \frac{1}{T} \int_0^T u(t) dt \quad (3.7.2)$$

When using digital data analysis, the continuous signal $u(t)$, $0 \leq t \leq T$ is replaced by a corresponding digital sample record $u(n)$, $n = 1, 2, \dots, N$. The total sample time is T and N is the corresponding number of samples. N and T are related by the sampling rate, SR (s^{-1}), by equation; that is

$$N = SR * T \quad (3.7.3)$$

And the time interval between samples, Δt , is given by

$$\Delta t = 1/SR = T/N \quad (3.7.4)$$

In digital form, the estimate (or measured value) of the mean value of a finite sample record, $u(n)$, $n = 1, 2, \dots, N$, can be expressed as

$$\hat{U} = \frac{1}{N} \sum_{n=1}^N u(n) \quad (3.7.5)$$

\hat{U} therefore is an unbiased estimate of the true mean value, U . The uncertainty for \hat{U} can be estimated by evaluating the variance of \hat{U} . The following time-series evaluation of the $\text{var}[\hat{U}]$ is based on the deviations given by Bendat and

Piersol (1971, 1986). The accuracy of a parameter estimate based on the measured values can be described by its mean square error. Since \hat{U} is an unbiased estimate, the mean square error will be equal to the variance of \hat{U} , which is defined as

$$\text{Var}[\hat{U}] = \sigma^2 [\hat{U}] = E[(\hat{U} - U)^2] \quad (3.7.6)$$

The uncertainty in the measured mean value, \hat{U} , can be specified as

$$U - z_{\alpha/2}\sigma[\hat{U}] < \hat{U} < U + z_{\alpha/2}\sigma[\hat{U}] \quad (3.7.7)$$

Denoting the true mean value by U, the variance of U_n can be expressed as

$$\text{Var}[U_n] = E[(U_n - U)^2] \quad (3.7.8)$$

If the samples are evenly distributed and statistically independent then it can be shown that

$$\text{Var}[U_n] = (1/N) \text{var}[U] \quad (3.7.9)$$

Where $\text{var}[U]$ is the mean-square value about the mean and it is given by

$$\text{Var}[U] = \sigma_u^2 \quad (3.7.10)$$

Consequently

$$\text{Var}[U_n] = \sigma_u^2/N \quad (3.7.11)$$

For an ergodic process, a statistic figure can be evaluated by either ensemble or time-mean averaging. Therefore, $\text{var}[U_n] = \text{var}[\hat{U}]$, and

$$\text{Var}[\hat{U}] = \sigma^2 [\hat{U}] = \sigma_u^2/N \quad (3.7.12)$$

For a given number of samples, N, sampling slowly will extend the measuring time without any significant increase in accuracy, and a faster sampling rate will increase the uncertainty because the samples will no longer be statistically independent (Bruun, 1995).

Finally, the normalised rms error

$$\varepsilon[\hat{U}] = \frac{\sigma[\hat{U}]}{U} = \frac{1}{\sqrt{N}} \frac{\sigma_u}{U} \quad (3.7.13)$$

The uncertainty in the measured mean value U , can be expressed in terms of $\varepsilon[\hat{U}]$ as

$$1 - z_{\alpha/2} \varepsilon[\hat{U}] < \frac{\hat{U}}{U} < 1 + z_{\alpha/2} \varepsilon[\hat{U}] \quad (3.7.14)$$

with a probability of $(1 - \alpha)\%$

The solution from the Table 3.7.1 follows that a 99% confidence level corresponds to $z_{\alpha/2} = 2.57$. The required accuracy given as a percentage from equation (3.7.14) is

$$\frac{\hat{U}}{U} < 1 \pm z_{\alpha/2} \varepsilon[\hat{U}] = 1 \pm 2.57 \varepsilon[\hat{U}] = 1 \pm 0.005$$

From which it follows, using equation (3.7.13), that

$$\varepsilon[\hat{U}] = \frac{\sigma[\hat{U}]}{U} = \frac{1}{\sqrt{N}} \frac{\sigma_u}{U} = \frac{0.005}{2.57} = 0.00195$$

Since the maximum turbulence intensity is 14%, the number of independent samples required is

$$N = \frac{1}{0.00195^2} \left(\frac{\sigma_u}{U}\right)^2 \approx 5155$$

Table 3.7.1 A Gaussian probability density distribution (Bruun, 1995)

$z_{\alpha/2}$	$(1-\alpha)\%$
1.65	90
1.96	95
2.33	98
2.57	99

In this study, the sample number for a given position is 12000 ~ 18000 in the boundary layer profile measurements at a sampling rate of 100 Hz, depending on the statistic objectives. To obtain a good VITA profile, more than 120000 samples are collected to give at least 40 ‘sweep’ events. Please see Chapter 1 and 5 for the details about the VITA technique.

Swaminathan et al. (1986b) also predicted the error of $\overline{(u')^2}$ increases as the turbulent intensity increases. The error reaches around 3.5% for turbulent intensity $\overline{(u')^2} \approx 15\%$ and 10% for turbulent intensity $\approx 40\%$. In general, the relative error of $\overline{(u')^2}$ due to the series expansion truncation is similar to the corresponding error of U. The errors of the values of U and $\overline{(u')^2}$ measured with a single probe are relatively small, provided that turbulent intensity is less than 30 ~ 40%. However, in the time-series analysis on a finite record, the corresponding error of U is much smaller than the error of $\overline{(u')^2}$ and the related normalised rms error (Brunn, 1995)

$$\varepsilon[\overline{(u')^2}] = \frac{\sigma[\overline{(u')^2}]}{\sigma_{u'}^2} \approx \frac{1}{\sqrt{N}} \quad (3.7.15)$$

Castro (1989) has discussed the standard deviations of the higher-order moments, and has given the standard deviations of the skewness and the kurtosis.

An account of the major factors which influence the reliability of the measurements of hot-film anemometry is given by Lekakisy (1996). The factors considered are: probe calibration, nonlinearity of the sensor-response equation, temperature effects, temporal and spatial resolution and probe design.

For a single-film probe positioned parallel to the wall and normal to the flow, Bakewell (1966) has made a fourth order estimate of the combined error in measuring the u component due to the additional sensitivity of the hot-film to the other component v normal to the film and to the nonlinearised signal. For larger y^+ values, the error becomes significantly smaller. An estimate of the error in the u component measurements with a single-film probe positioned normal to the wall and a flow due to w fluctuations, which are also normal to the probe, can be made from the work of Klatt (1973). Using a third-order approximation, a maximum error of 5% at $y^+ = 1$ is demonstrated. This decreases to about 2.5 % at $y^+ = 3$, agreeing fairly well with Bakewell's (1966) estimate.

3.8 Traverse System, Data Acquisition and Travelling

Wave Power Unit

A Star traverse gear with a stepper motor is used to position the probe. The coordinate system is defined as X for the streamwise direction, Y for the wall-normal direction, and Z for the transverse direction. The y-axis traverse positioning is achieved via a PC and Digiplan CD25 stepper motor controller. The stepper motors and controllers give positioning resolution of 6.25 μm in the y direction.

The analogue signals within $\pm 5\text{V}$ from the hot-film anemometers are converted to binary format by an Iotech ADC 488/8SA eight channel 16-bit analogue-to-digital converter. The sampling frequency is set at 100 Hz, giving an inner-scaled, temporal resolution of $\Delta t^+ \approx 0.2$. This frequency is sufficient

to capture all the turbulent activities whose maximum frequency is below 50 Hz in the experiments.

A 30 Volt DC power supply is used as the main power supply to the electromagnetic actuators. Figure 3.8.1 shows the voltage output and the control signal routines. The voltage output from the main power supply becomes oscillating as shown in figure 3.8.2a via the oscillator unit.

A relay switch then regulates the supply of the square-wave from the voltage to the electrodes by being switched on and off as shown in figure 3.8.2b. When the switch is on, the voltage is supplied to the electrode during $t = 0 \sim 0.25T$ as shown in figure 3.8.c. During $t = 0.25T$ to $0.5T$ (figure 3.8.2b), the switch is off and no voltage is supplied to the electrode sheet. Between $t = 0.5T$ and $0.75T$, the switch is on again and the electrode is activated. The only difference from the last 'on' stage is that at this time the supply voltage is negative as the polarity is changed. At the final phase, the relay switch is off to stop the supply to the actuator, which gives a required voltage sequence as shown in figure 3.8.2 (c). Because the timing is controlled precisely by the controller and has a very good repeatability, it is used in this study as a standard signal to phase averaging the velocities and synchronising the flow visualisation and the velocity distribution.

The input excitation voltage signal is important because it is used to ensemble average the streamwise velocity. Figure 3.8.2a illustrates one section of the continuously sampled excitation voltage signals. The voltage signals are divided into individual periods and each period starts from the excitation voltage of nearly zero volts to the maximum positive one. It shows that the timing is consistent therefore it can be used to get the phase averaged velocity.

Figure 3.8.3 shows a part of the streamwise velocity signals with the simultaneously sampled excitation voltage.

The experimental velocity data were compared with the DNS results (Moser et al. 1999) at a similar Re number. Figure 3.8.4, figure 3.8.5 and figure 3.8.6 show the mean streamwise velocity profile, the skewness profile and the kurtosis profile, respectively. The results show the data agree well with the DNS data.

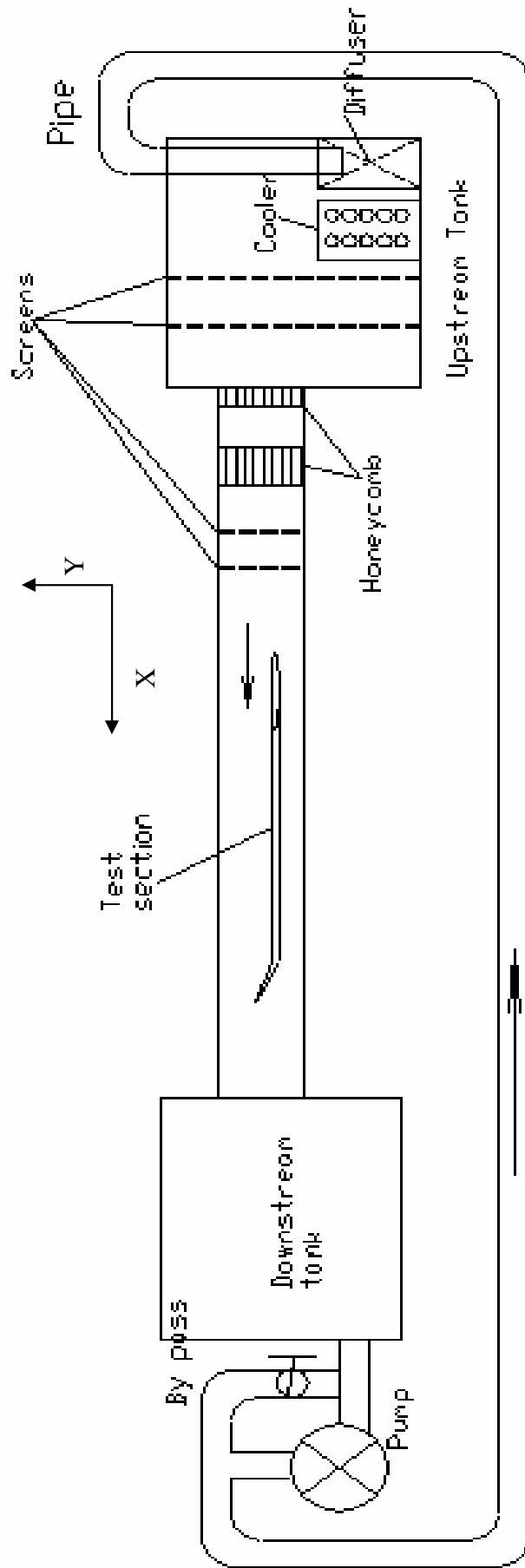


Figure 3.2.1. Water channel set up. X means streamwise

direction: Y means the wall-normal direction.

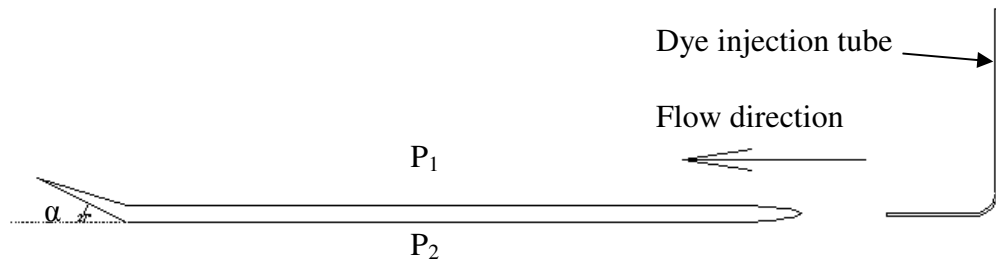
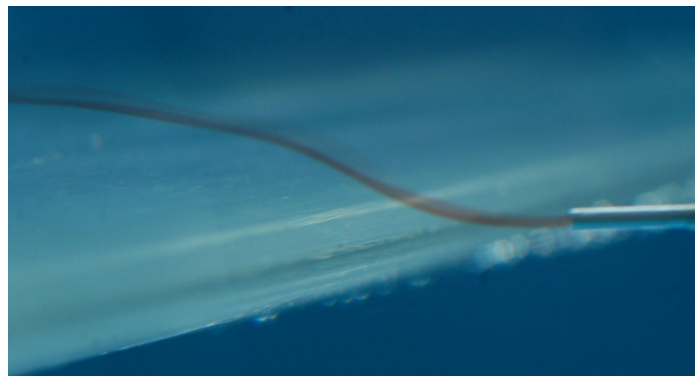
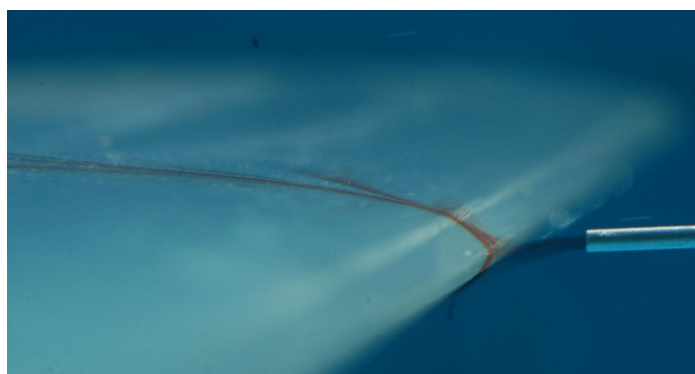


Figure 3.3.1 Experimental setup for the flow visualisation to decide the trailing edge angle.



(a)



(b)

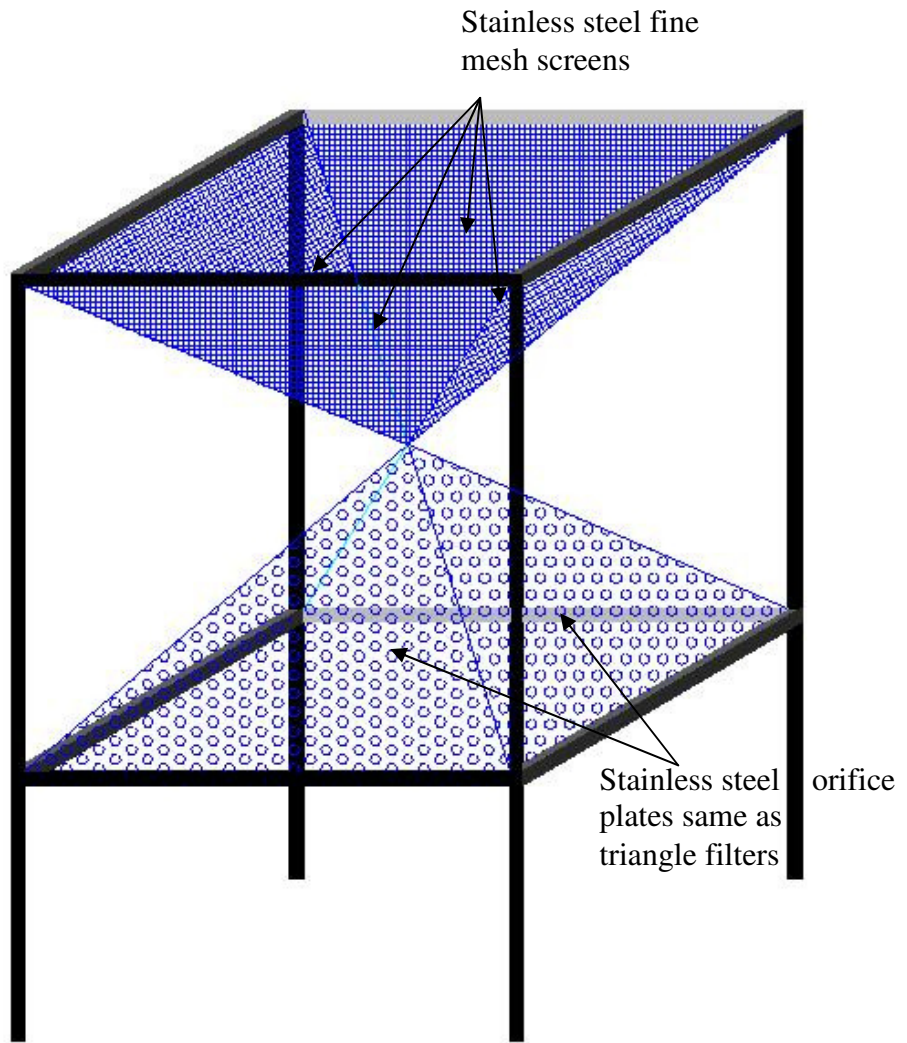


(c)

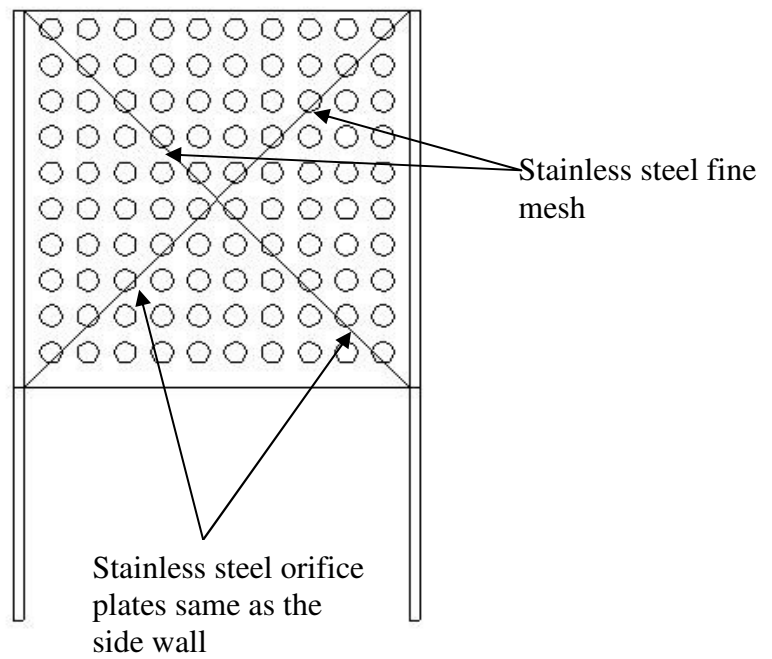


(d)

Figure 3.3.2 Flow visualisation for the trailing edge angle adjustment. (a) $\alpha = 12^\circ$; (b) $\alpha = 17^\circ$; (c) $\alpha = 20^\circ$; (d) $\alpha = 24^\circ$.



(a)

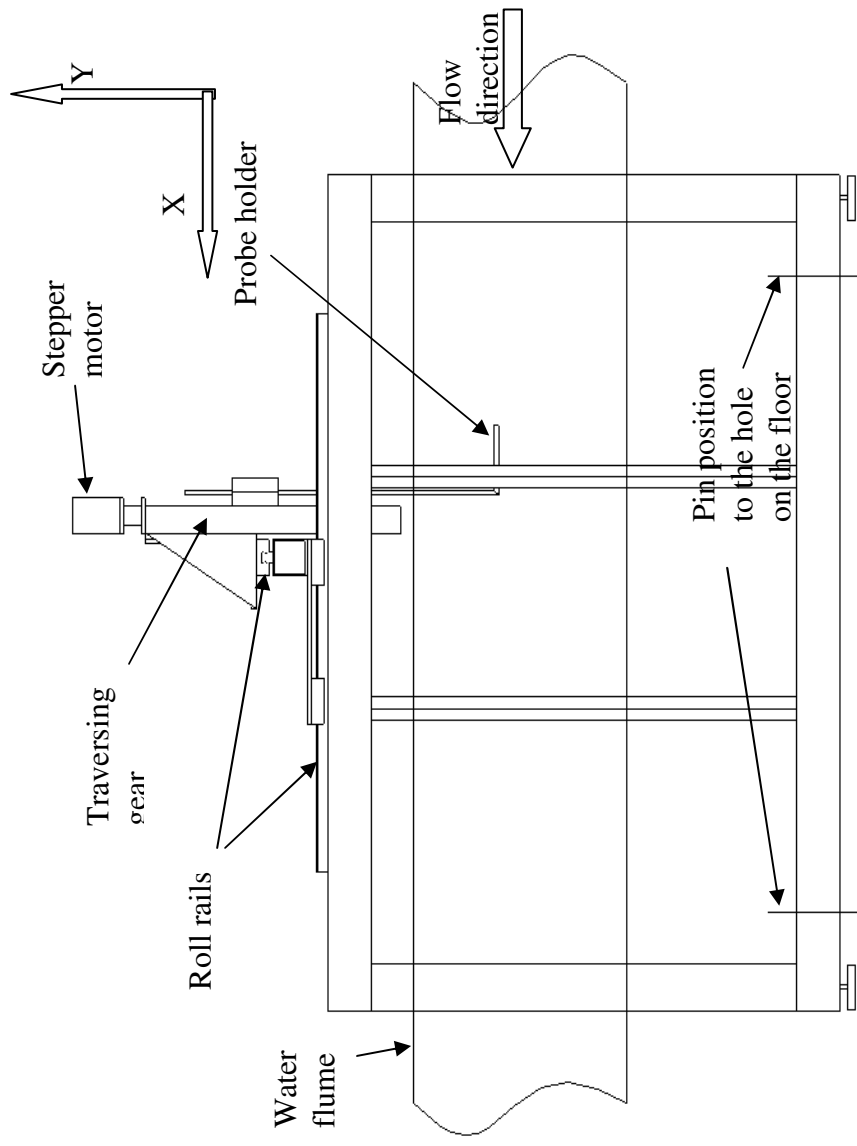


(b)

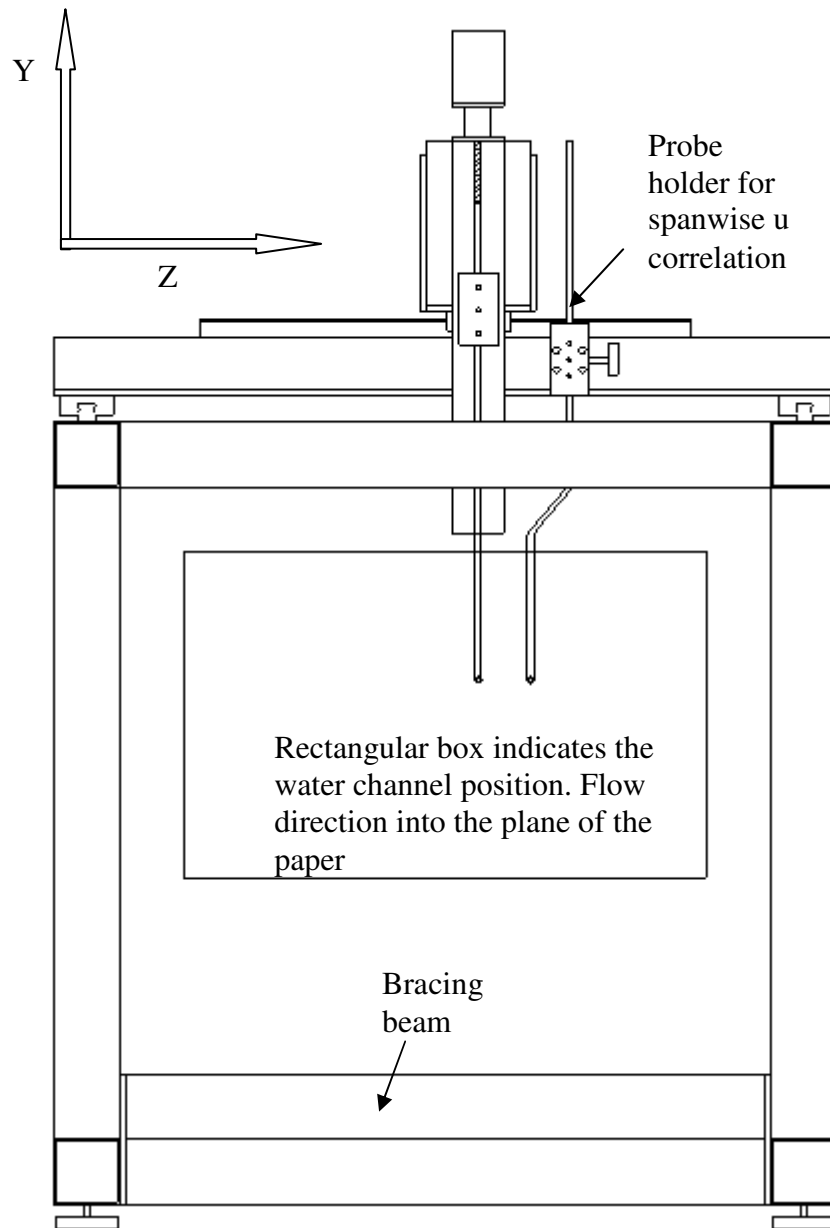


(c)

Figure 3.3.3. (a) The drawing of the internal structure of the diffuser (side walls and bottom are removed); (b) The side view with external side wall and the crossed lines indicate the internal structure shown in (a); (c) The setup of the diffuser in the tank.



(a)



(b)

Figure 3.3.4. The drawing of the new supporting frame. (a) side view; (b) front view.

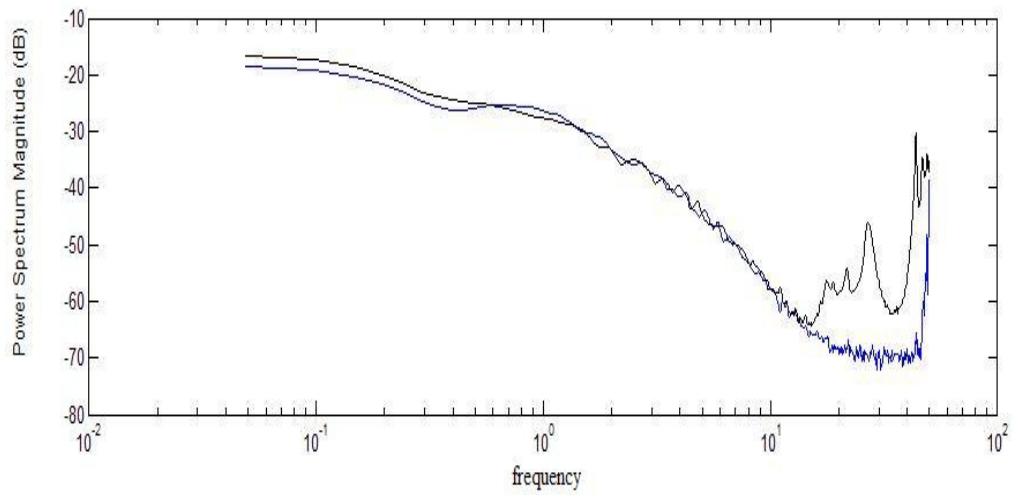
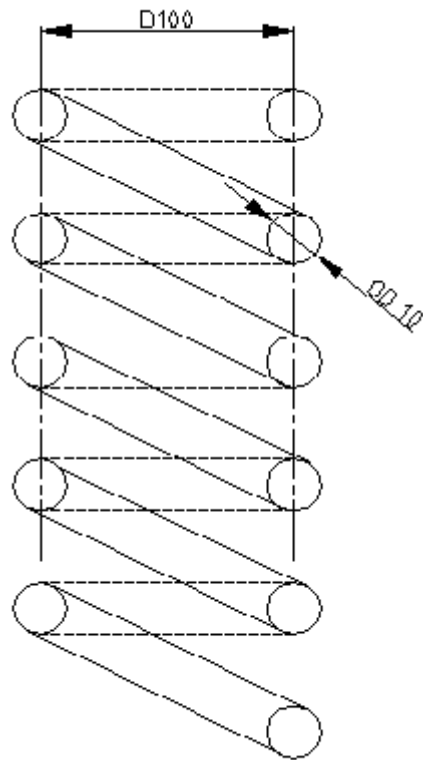
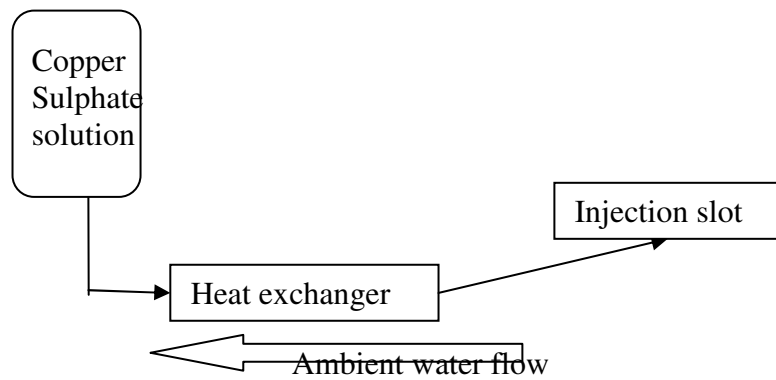


Figure 3.3.5 Results show the power spectrum of velocity fluctuations before and after the application of the new supporting frame. Blue line is the data sampled with the application of the supporting frame; black line is the one without the frame.

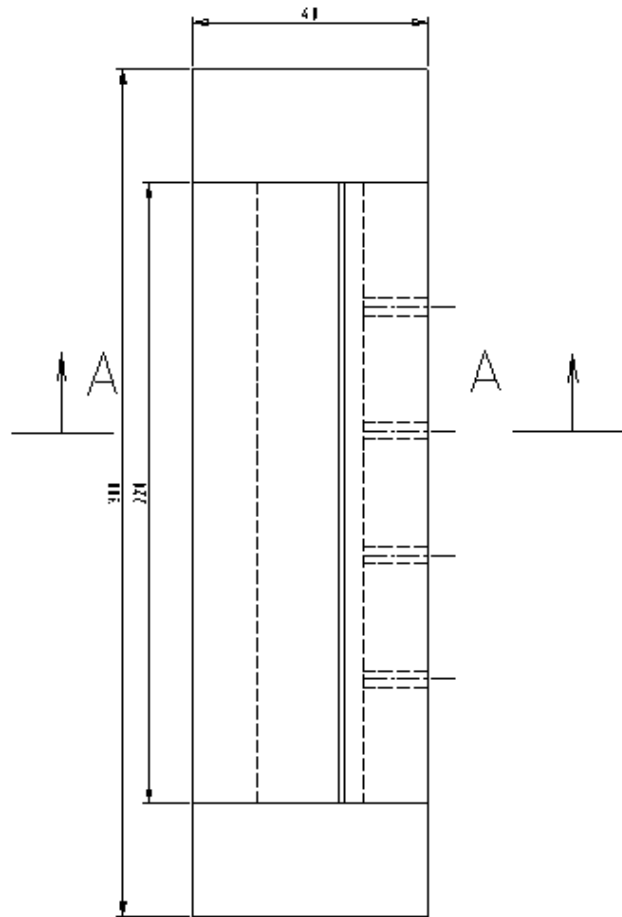


(a)

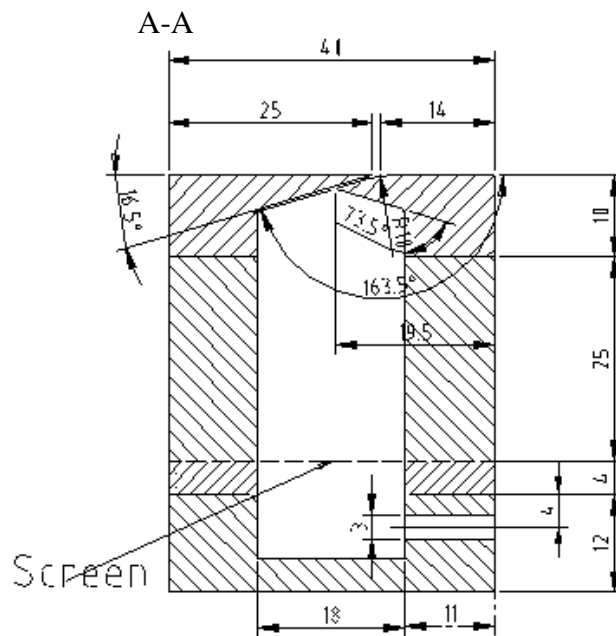


(b)

Figure 3.3.6. (a) The drawing of the small heat transfer unit; (b) The arrangement of the heat exchanger and the ambient water flow used to keep the Copper Sulphate solution the same temperature as the surrounding water.



(a)



(b)

Figure 3.4.1 (a) Top view of injection slot. (b) A-A cross section

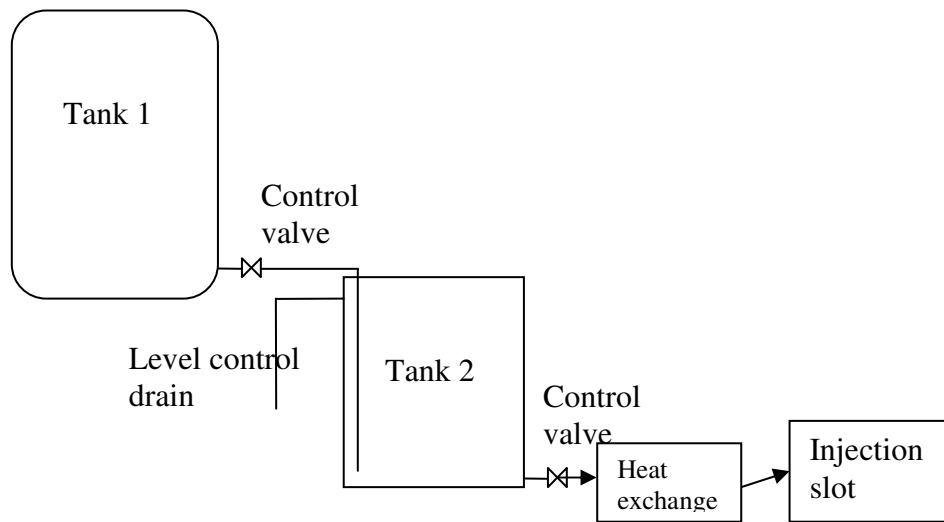
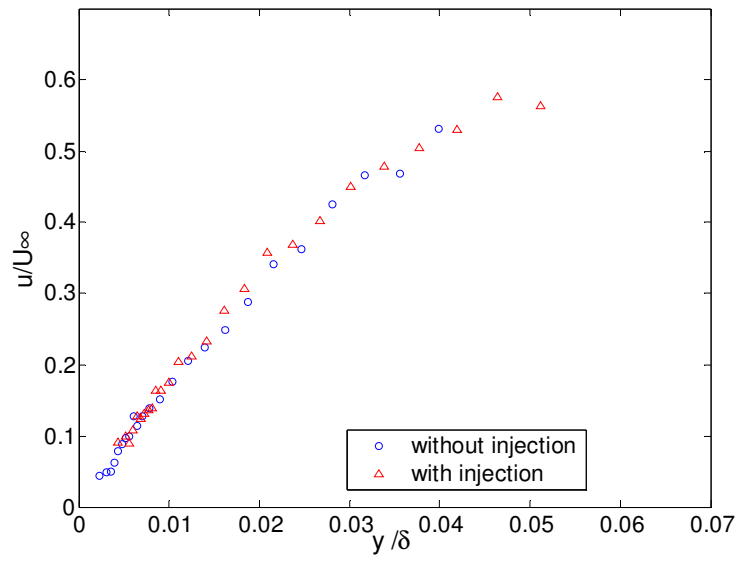
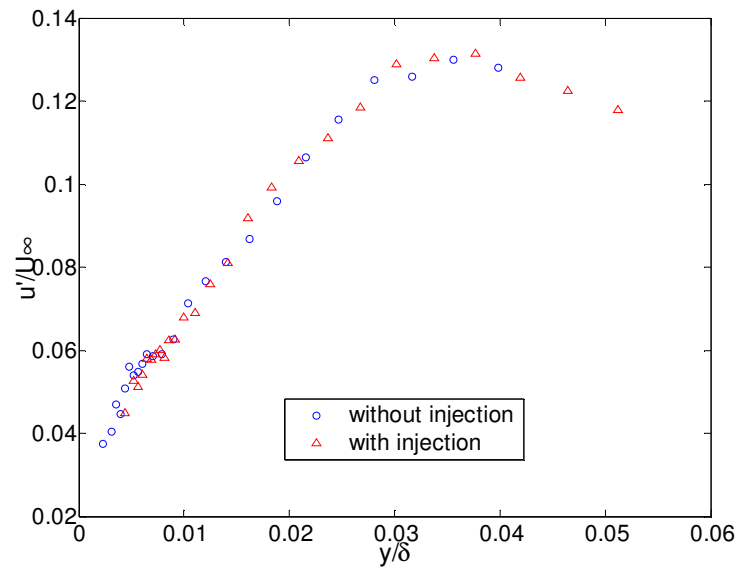


Figure 3.4.2. The arrangement of the injection tanks.



(a)



(b)

Figure 3.4.3. (a) Mean velocity profiles with and without injection; (b) turbulent intensity profiles with and without injection.

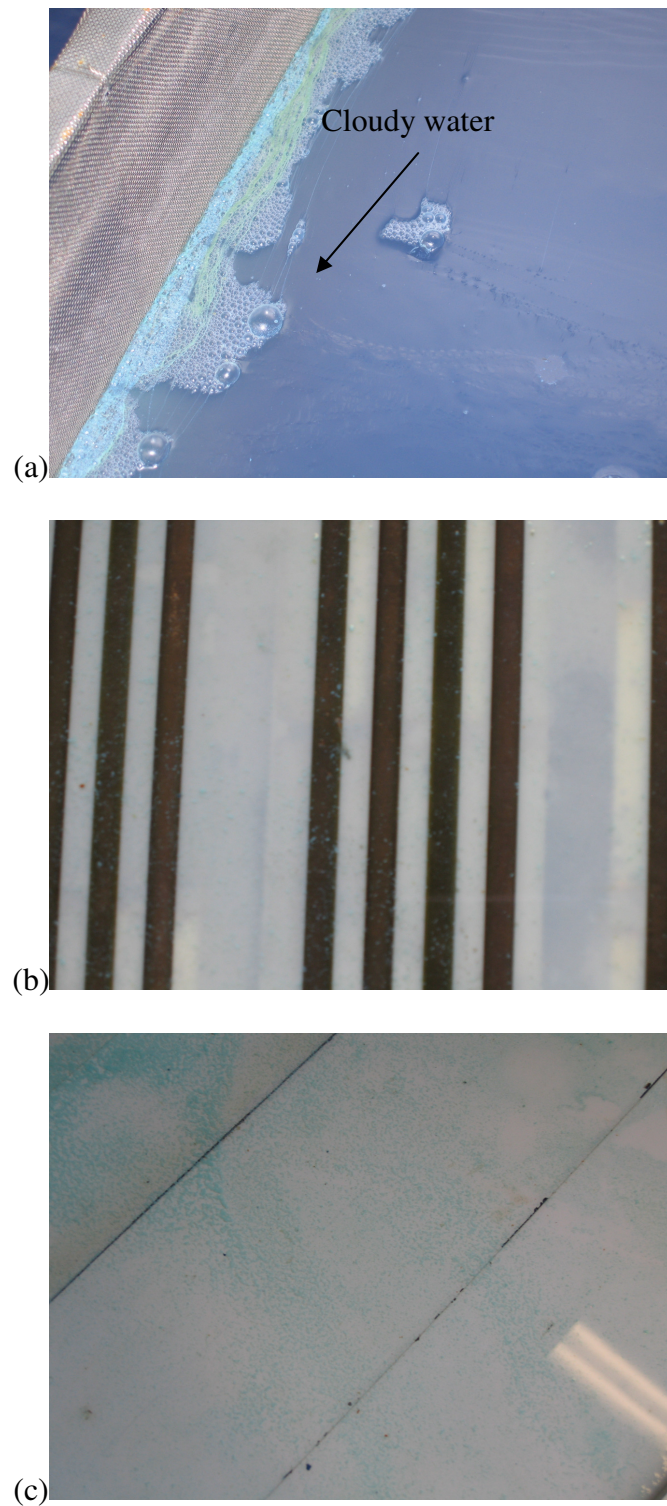


Figure 3.4.4. The contaminated water.(a) Water becomes cloudy just after 40 minutes of running since the injection of Copper Sulphate solution; (b) Precipitates (in green) accumulate on the EM unit surface; (c) Precipitates on the plate surface.

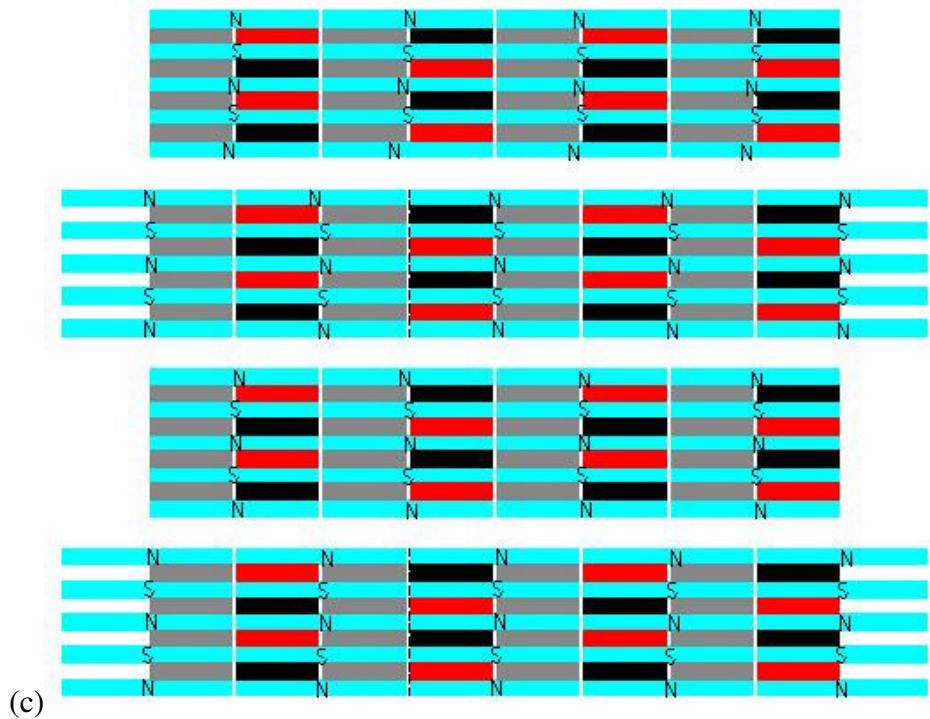
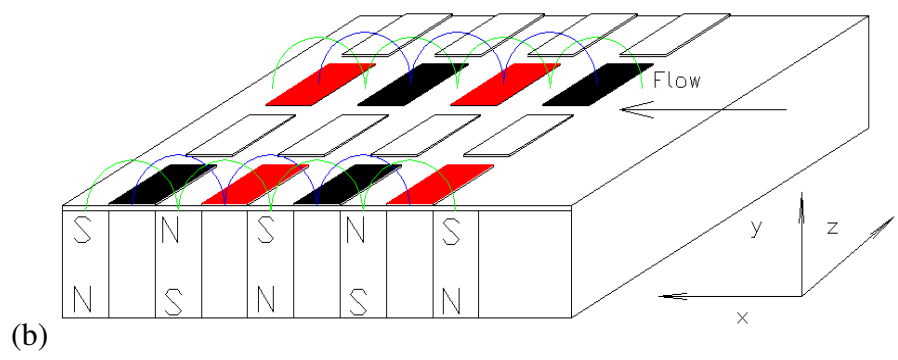
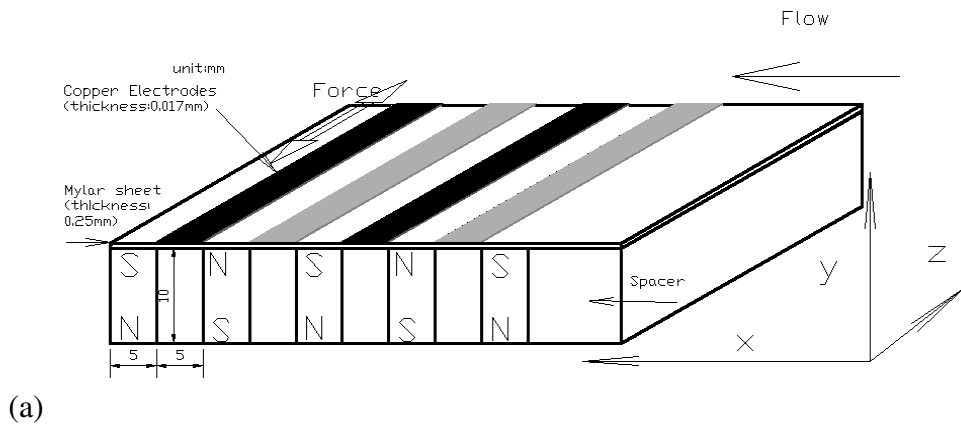


Figure 3.5.1 Configuration of electrodes and magnets for the spanwise oscillation (a) and spanwise travelling wave actuation (b). (c) The illustration of the travelling wave phasing. The flow direction is from top to bottom. N denotes the north pole of the magnets and S denotes the south pole. X denotes streamwise direction; Z denotes the spanwise direction; Y denotes the wall-normal direction.

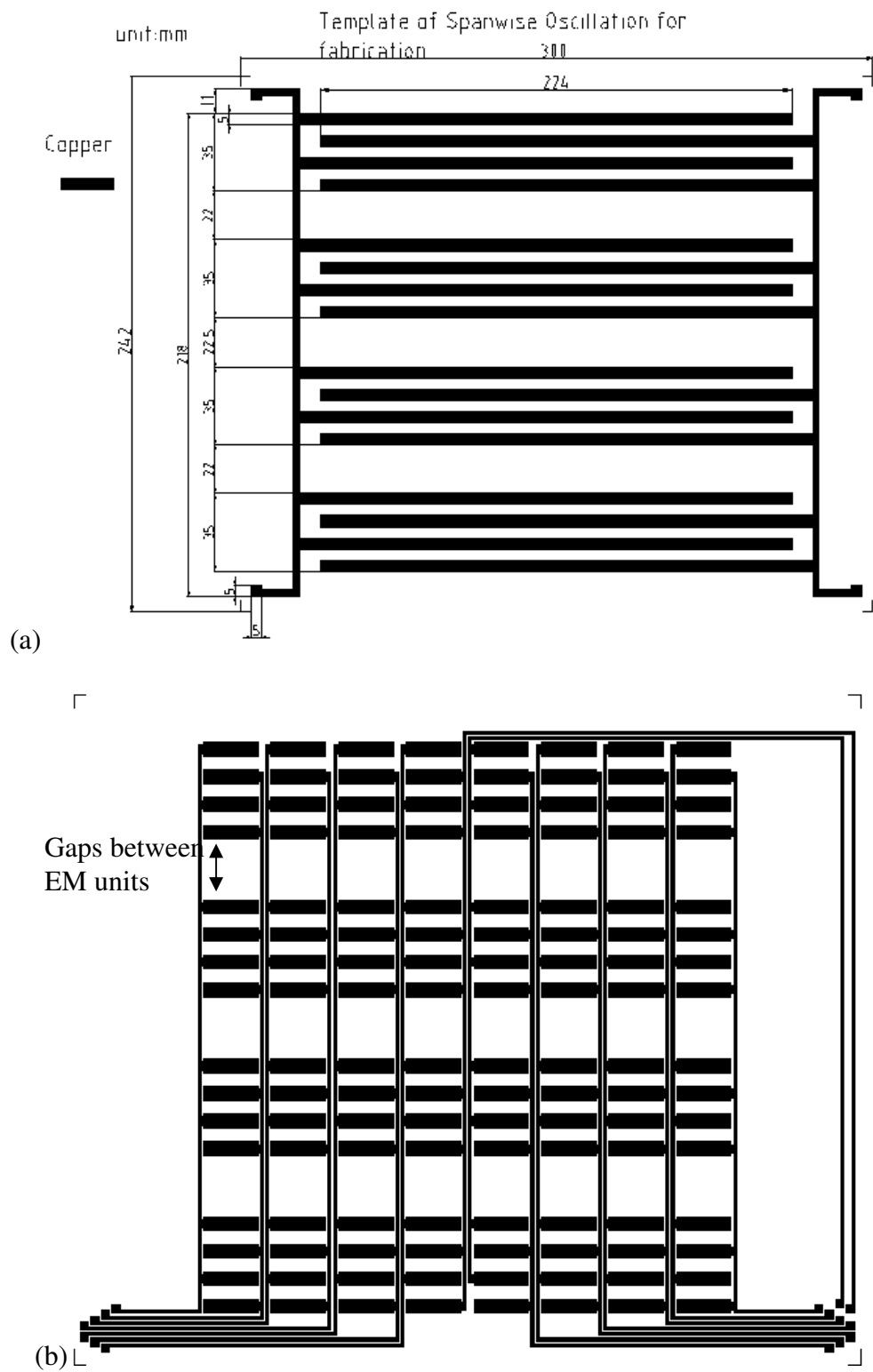


Figure 3.5.2 The photo-chemically-etched electrode pattern. (a) the electrode sheet for spanwise oscillation; (b) the electrode sheet for spanwise travelling wave. Flow direction is from top to bottom.

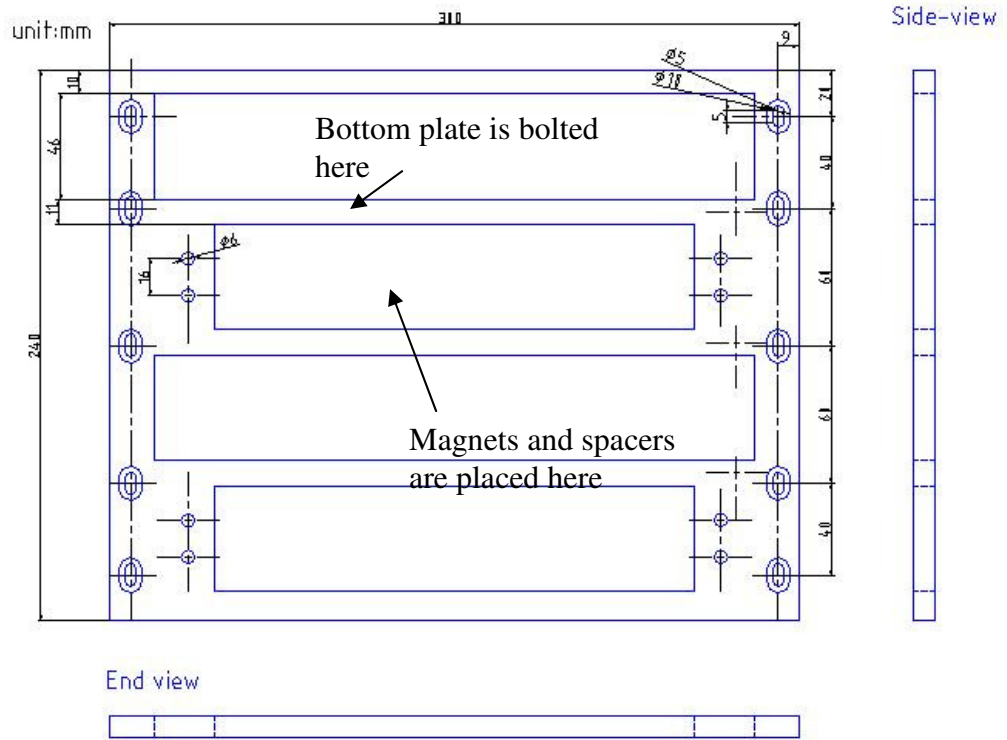
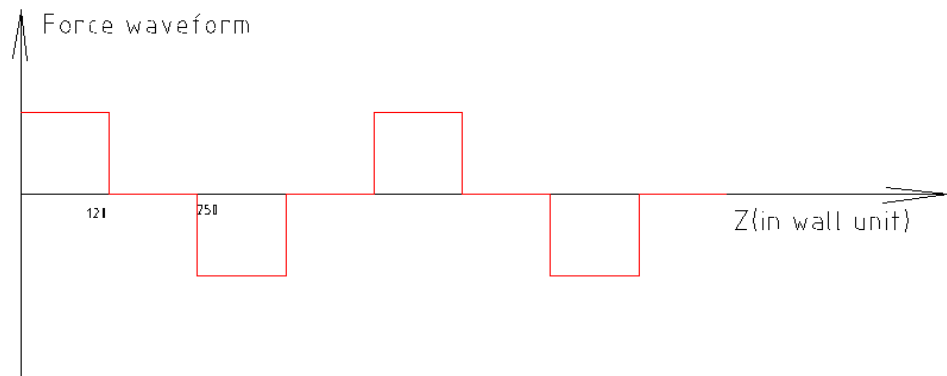
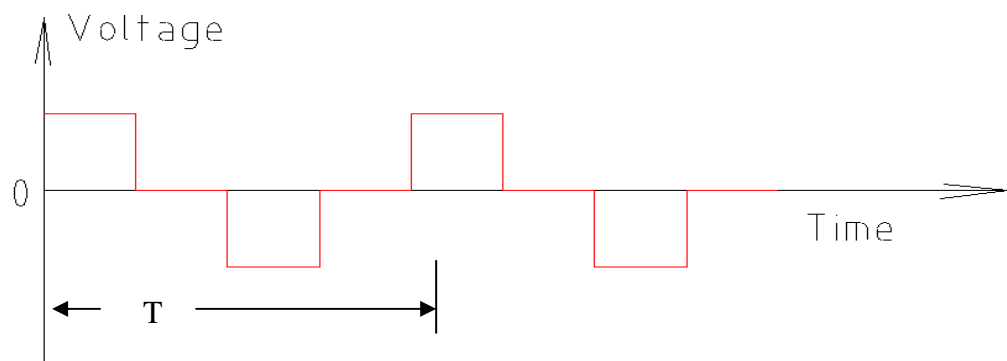


Figure 3.5.3. The base structure where the magnets and spacers are located.



(a)



(b)

Figure 3.5.4. (a) Force waveform corresponds to the wavelength of 500 wall units. (b) Output signal for a single tile. T denotes the time period.

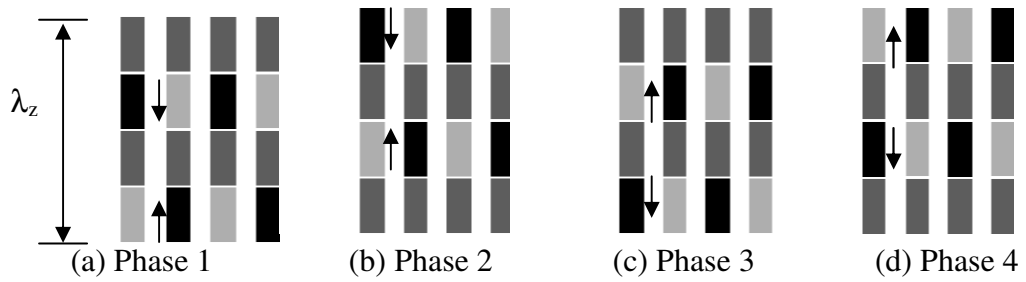


Figure.3.5.5. (a)-(d) 4 phases of the travelling wave actuation. Black colour denotes positively activated electrodes; light grey denotes negatively activated and dark grey not-activated. Arrows denote the forcing direction. Travelling wave direction is from the bottom to the top. Flow is from right to left.

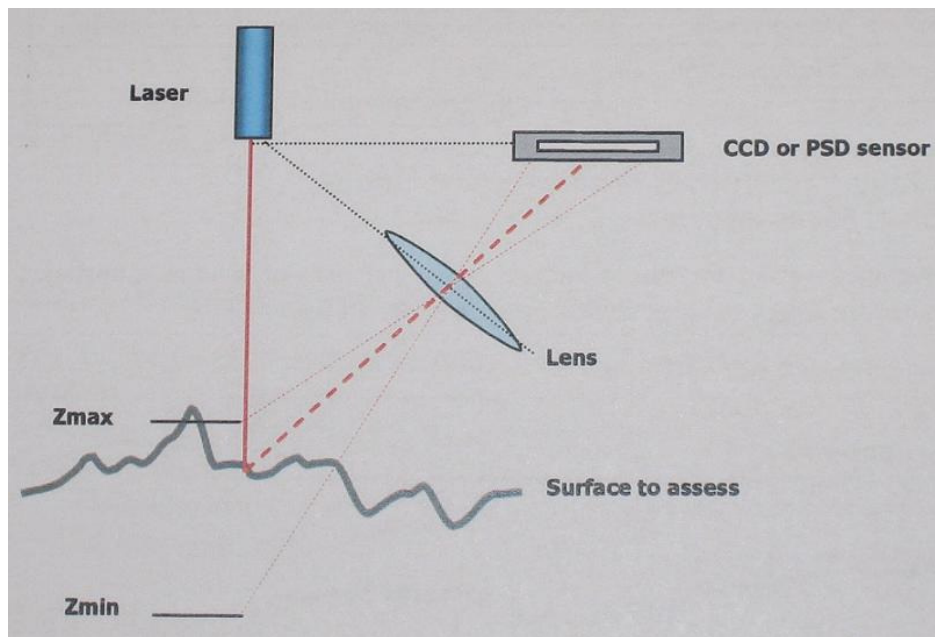


Figure 3.5.6. Working principle of the laser gauge (Non-Contact Large Range Measurement).

The technique used for the laser triangulation gauge deduces the height of a surface point by sensing the position of a laser spot on the surface using a detector placed at a certain angle away from the incoming laser beam (typically 45 degrees in the case of the gauges used on the Talysurf CLI system)

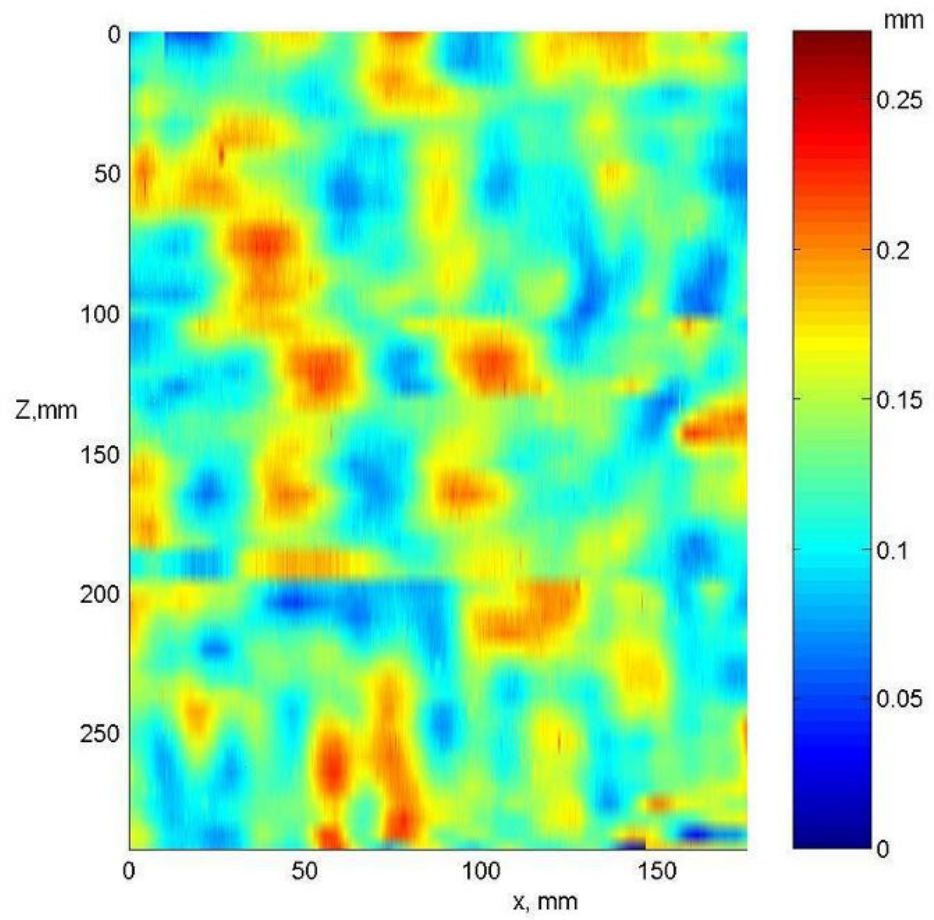


Figure 3.5.7. Surface profile of the mylar sheet sitting on the magnet holding base.

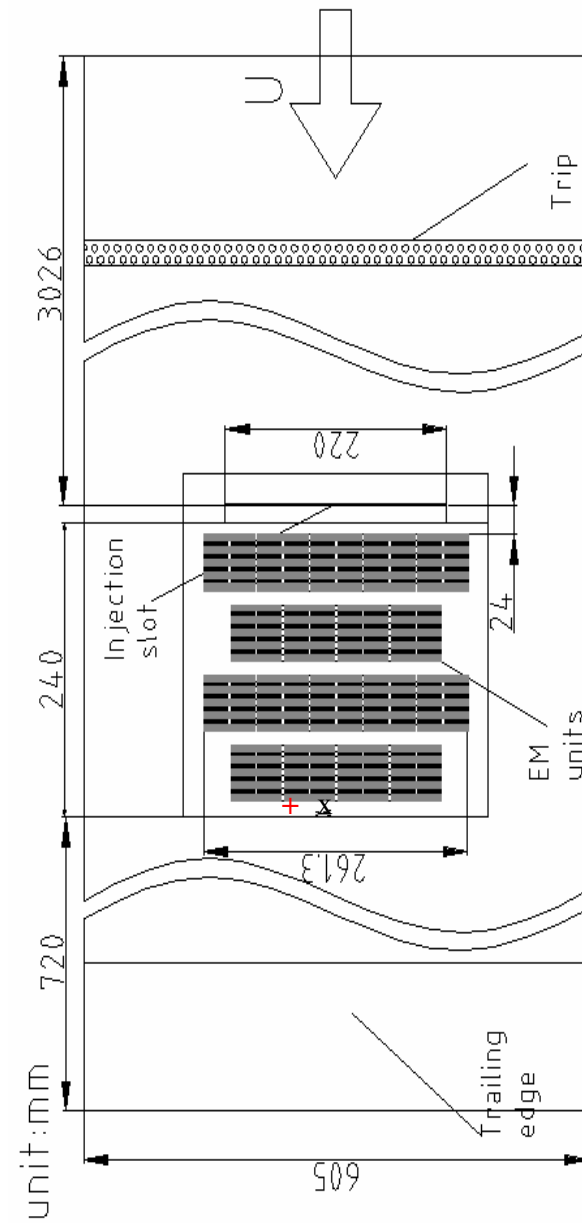


Figure 3.6.1. Top view of the test plate. 'X' is the measurement point of the boundary velocity profile and the moving position in the spanwise two-point correlation. '+' is the position of the fixed point in the spanwise two-point correlation measurement.

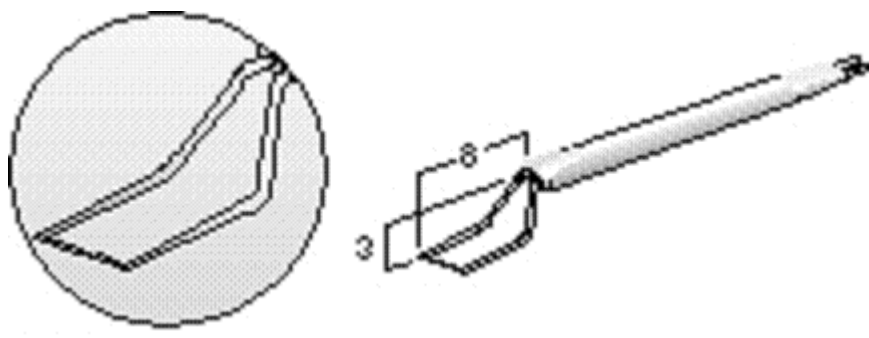


Figure 3.6.2. Dantec boundary-type hot-film probe. Model: 55R15 ($2\mu\text{m}$ thickness quartz coating). Units are in mm. From Dantec Dynamics.

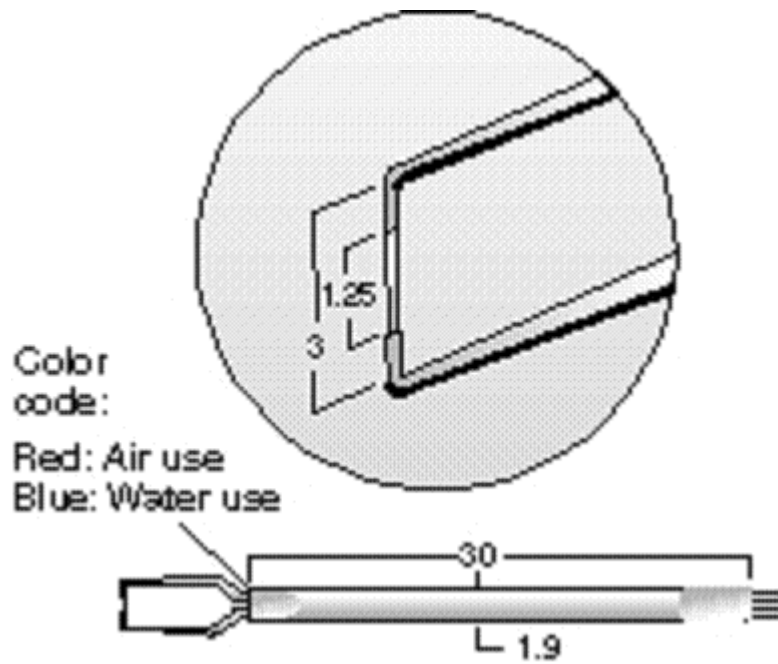


Figure 3.6.3 dimensions for the hot-film sensor. Units are in mm. From Dantec

Dynamics.

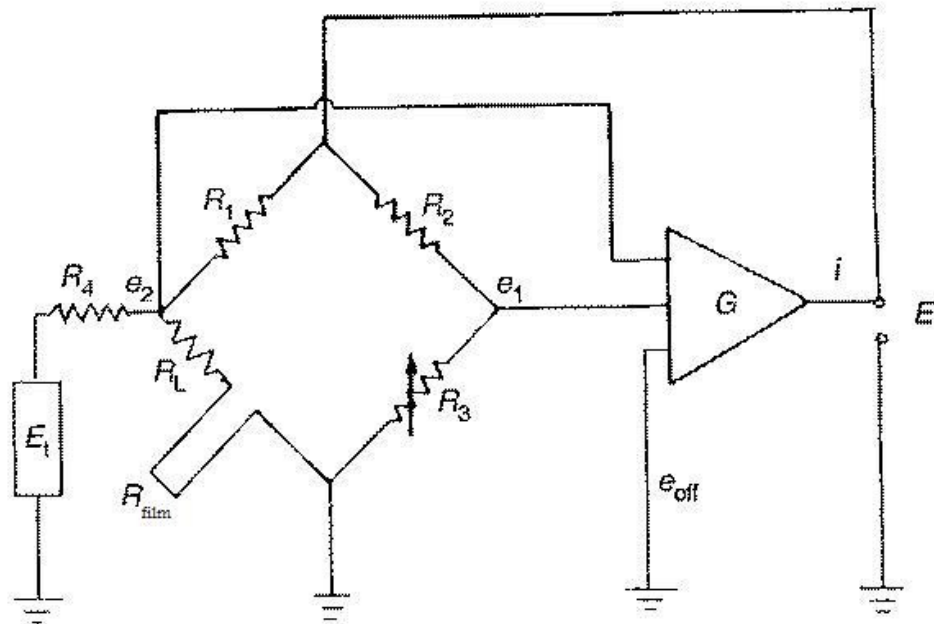


Figure 3.6.4 A constant temperature anemometer sketch containing a Wheatstone bridge, a feedback amplifier, and an electric-testing subcircuit.

From Bruun (1995).

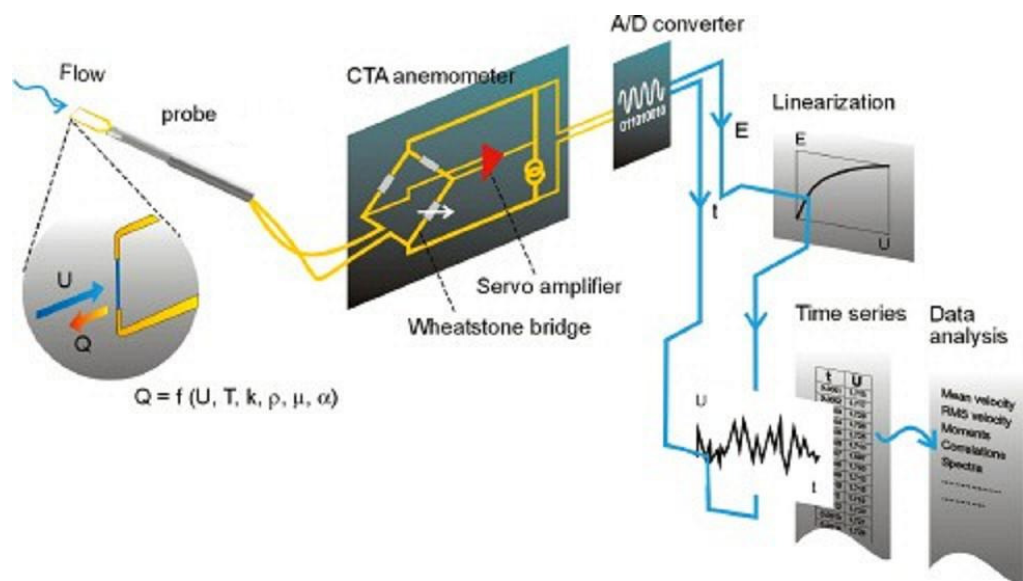


Figure 3.6.5. A typical CTA(constant temperature anemometer) system. From Dantec Dynamics.

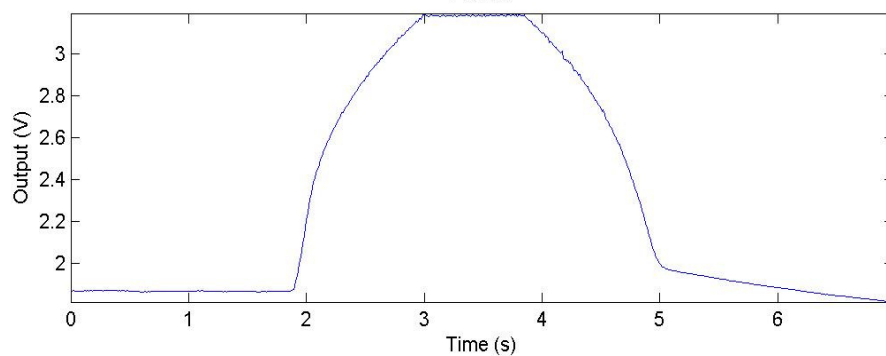


Figure 3.6.6. A voltage output signal from hot-film anemometry at a velocity of 0.03m/s.

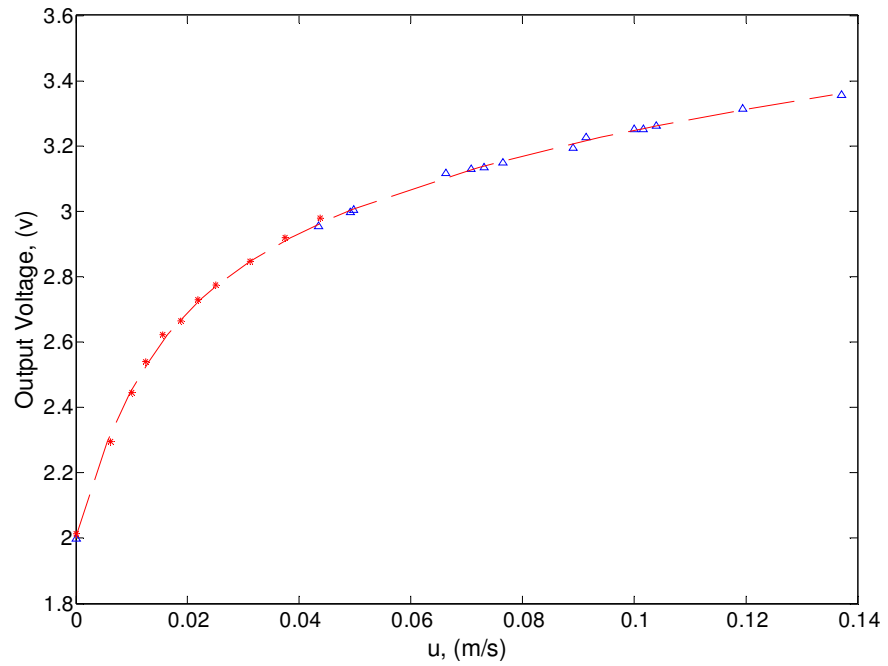


Figure 3.6.7. A calibration profile used in the present study. Red stars mean the calibration data from the low-speed calibration method introduced in this appendix; blue triangles denote the data from the normal calibration; and the dashed line is the polynomial profile.

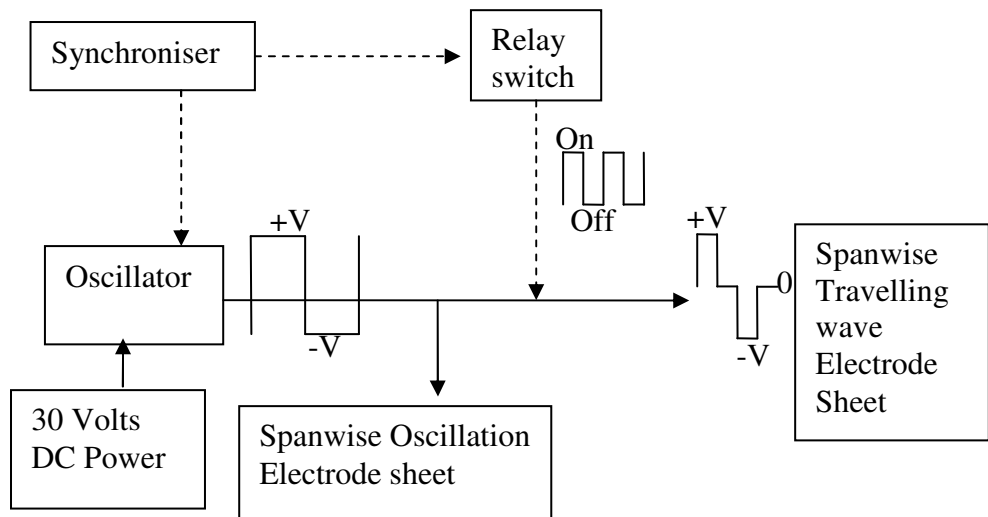
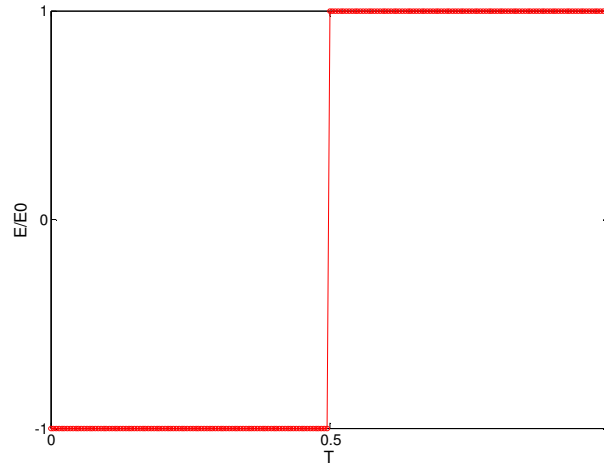
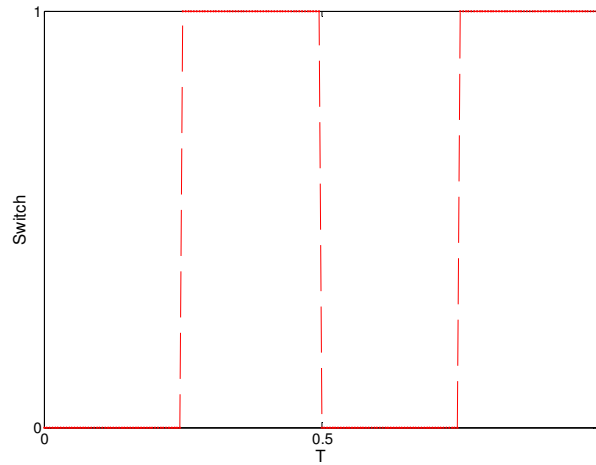


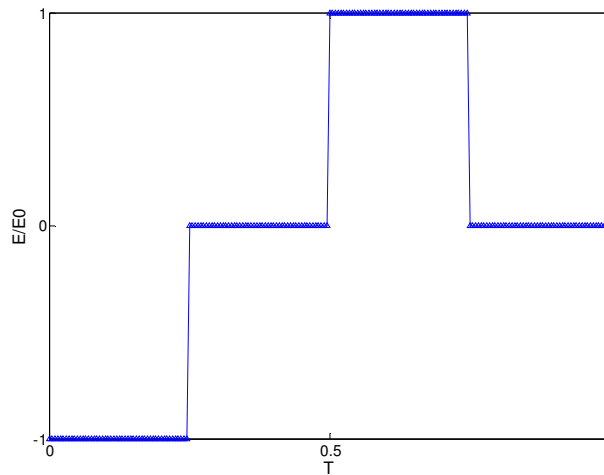
Figure 3.8.1. The control unit for the spanwise oscillation and spanwise travelling wave. Dashed lines are the control signals; solid lines denote the electrical output.



(a)

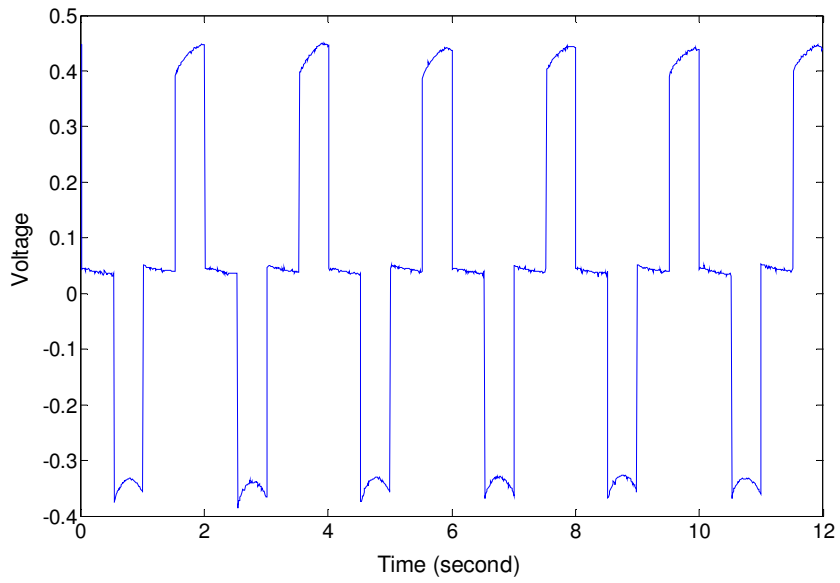


(b)

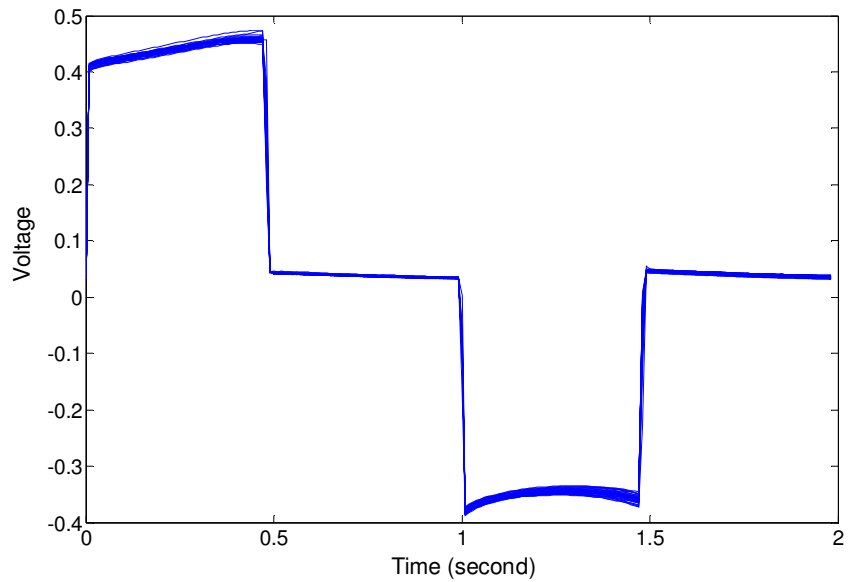


(c)

Figure 3.8.2. Demonstration of the generation of the required travelling wave forces. (a) Non-dimensional voltage output from the oscillator; (b) Controlling signals from a relay switch. '1' means switch and '0' means switch off then no voltage given to the electrodes. (c) Output voltage for travelling wave resulting from the combination effects of (a) and (b)



(a)



(b)

Figure 3.8.3 Lorentz forcing excitation voltage signals. (a) one section of continuous sampled voltage signal; (b) 60 one-period excitation voltage signals are plotted together.

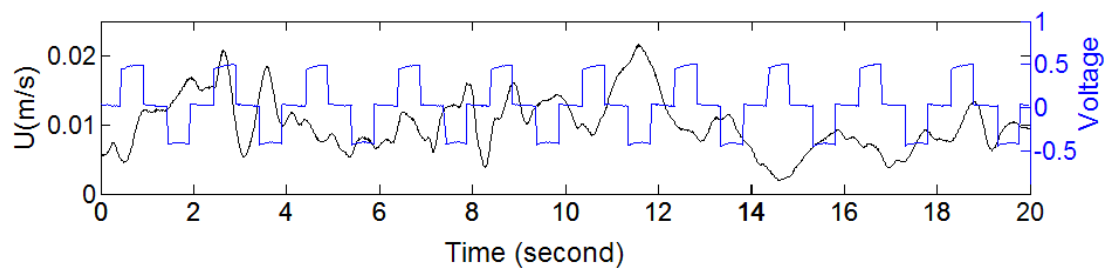


Figure 3.8.4. The excitation voltage and the streamwise velocity are sampled simultaneously.

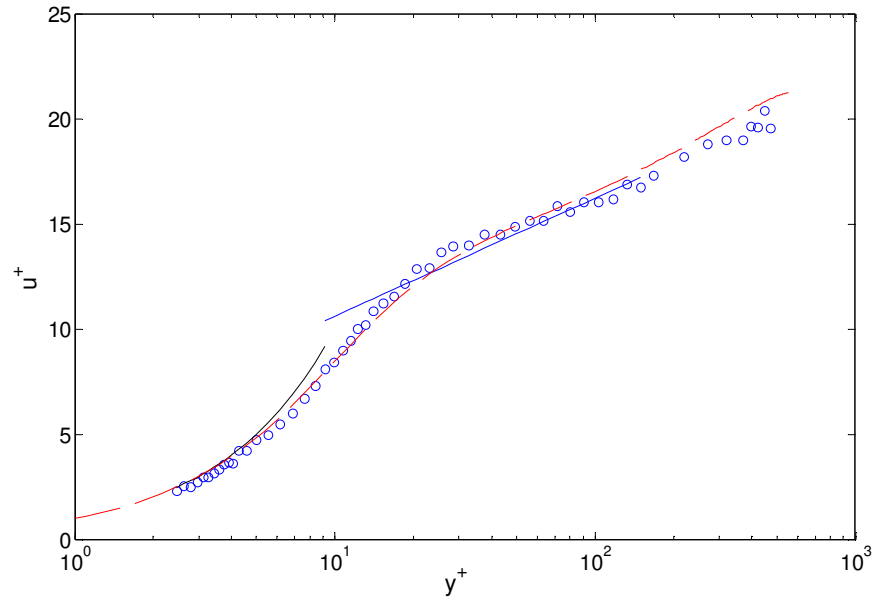


Figure 3.8.5 Mean streamwise velocity profiles in the turbulent boundary layer. The black line (-) denotes $u^+ = y^+$; the blue line (-) denotes $u^+ = (1/0.41) \cdot \ln(y^+) + 5$; the blue circles (\circ) are experimental data; the red dash line (--) is Moser's DNS data at similar Re number (Moser et al 1999).

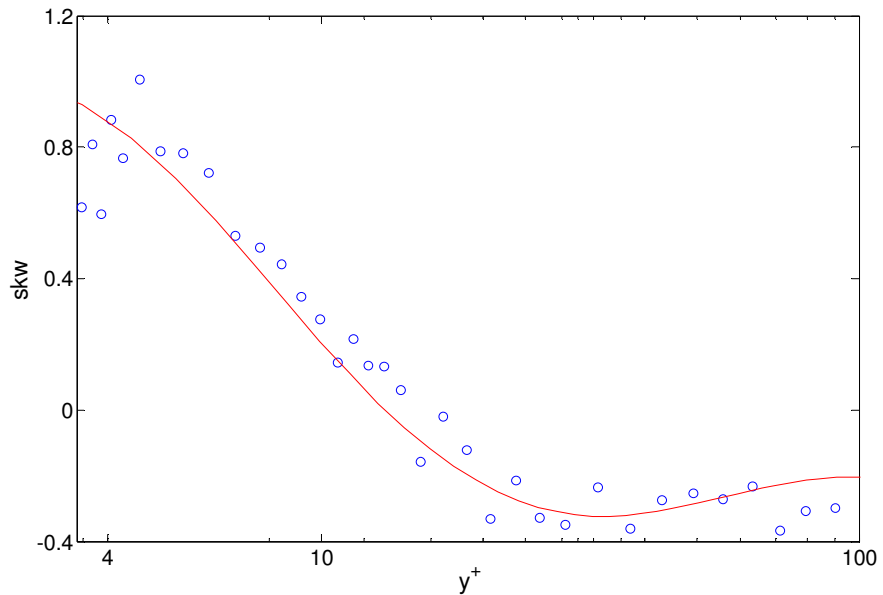


Figure 3.8.6. The skewness profile of the turbulent boundary layer. The blue circles (\circ) are experimental data; the red line (-) is Moser's DNS data at similar Re number (Moser et al., 1999).

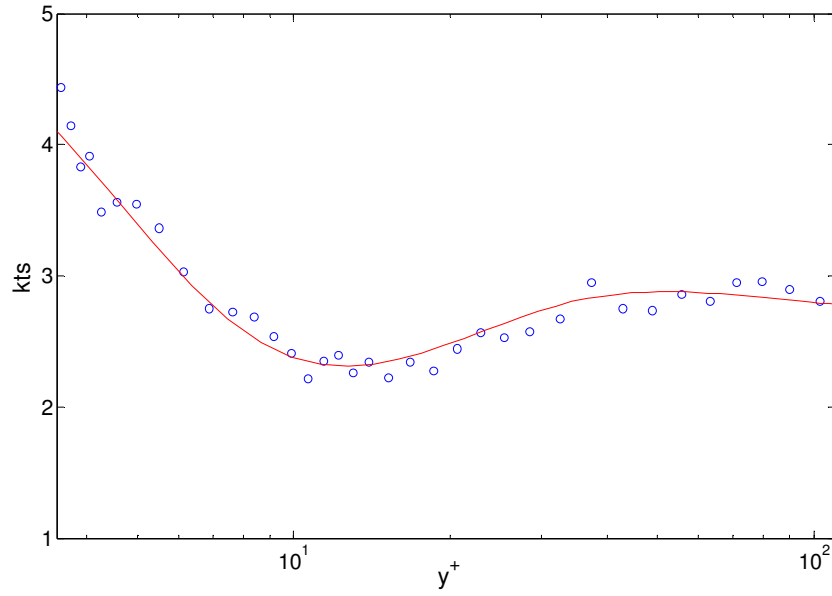


Figure 3.8.7 the kurtosis profile of the turbulent boundary layer. The blue circles (\circ) are experimental data; the red line (-) is Moser's DNS data at similar Re number (Moser et al., 1999).

Chapter 4

Effects of Lorentz-forcing Spanwise Travelling Wave Excitation On Near-wall Turbulent Structures

4.1. Introduction

Flow visualisation is one of the experimental methods developed to study the flow nature qualitatively. As a qualitative research method, flow visualisation techniques allow us to capture some significant and crucial 3-D structures by unlimited selections of light sources. This benefit is of great importance. For example, the low-speed streaks might move out of the thin 2-D laser sheet easily and the recording equipment relying on the 2-D light sheet will lose some vital information.

In this experiment, flow visualisations in the water channel are carried out in order to obtain a better understanding of the effects of Lorentz-forcing. Flow visualisations without control are also performed in order to offer a baseline for the control case. It is found that the travelling wave excitation greatly alters the near-wall structures of the turbulent boundary layer. The near-wall streaky structures are twisted into the spanwise direction and accumulated to form a wide low-speed ‘ribbon’ in the drag reducing cases. Similar observations are also made by Du et al. (2002), who proposed the appearance of the wide ‘low-speed ribbon’ is responsible for the drag reduction. In this study, the alternative high and low-speed regions are also found in the drag-increasing cases, suggesting that the low-speed ‘ribbon’ might not be the sole reason for

the drag reduction. To better understand the spanwise travelling wave motion via Lorentz forcing, flow visualisation in still water is performed.

Although the low-speed streaky structures are observed as bubbles, dye or smoke stripes in the flow visualisation experiments (please refer to the section 2.3.1), a correlation measurement is carried out in the flow when the travelling wave is applied. Figure 4.1.1a shows the arrangement. A video camera records the visual information. A LED is used to illustrate the sampling status of the hot-film anemometry. A command is sent to the ADC from the program written by the author, which triggers the hot-film sampling progress and switches on the LED. Therefore, the pictures are synchronised with the velocity measurement. When the green stripe pointed by the arrow in figure 4.1.1a passes the hot-film sensor, the time is boxed in figure 4.1.1b. Total sampling time is 1200 seconds for one correlation calculation and only a part is shown in figure 4.1.1b. A factor L_{ij} is defined so that

$$\begin{aligned} L_{ij} &= 1 && \text{if the data are judged as low-speed streaks (boxed)} \\ &= 0 && \text{if the time when no green stripe passes the sensor} \end{aligned}$$

The velocity fluctuation, u' , is calculated by instantaneous velocity – the mean velocity. Then a correlation can be obtained by

$$C_{Lv} = \frac{\sum L_{ij} \times u'}{\sum \sqrt{(L_{ij} \times u')^2}} \quad (4.1.1)$$

where C_{Lv} is the coefficient factor.

The hot-film sensor is placed at $y^+ \approx 5$ because it has a fairly high chance that the dye (Copper Sulphate) stripe passes by. For the cases of $T^+ = 42$ and 82 , the correlation factors are 0.76 and 0.79 , respectively. It shows that there is a high possibility that the observed dye stripes are the low-speed streaks.

4.2 Turbulent Boundary Layer Without Control

Fig 4.2.1 shows a sequence of pictures of the streaky structures in the turbulent boundary layer without control using the dye injection technique. In the pictures, the flow direction is from the top to the bottom, giving a view of x^+ (streamwise) ≈ 520 and z^+ (spanwise) ≈ 425 . The visible rectangular blocks in the background are the electrodes of $x^+ \approx 22$.

The streaks are universal and are always observed in near-wall turbulent flows (Smith & Metzler 1983), which become visible in the form of dye stripes when the food colouring is put into the flow. The streaks are the results of the slow fluid wall-normal motions induced by streamwise vortices or hairpin vortices, etc. (Kline et al. 1967; Kim et al. 1971; Choi 1996; Offen and Kline 1974; Smith & Metzler 1983; Robinson 1991; Chernyshenko & Baig, 2005).

The collection of the dye into the long streaks exhibits large variations in the spanwise velocities. The streaks move downstream and waver within the near-wall region like 'flags' such as the streak indicated by 'SA' in figure 4.2.1a. The streak 'SA' wavers in the following pictures. The characteristics of the streaks are naturally determined by both of the wall-normal motion and the pattern-forming properties of the combined action of lift-up, shear and diffusion (Chernyshenko & Baig, 2005).

Approximately 4 streaks are observed in each photograph. Hence, the mean value of the streak spacing is approximated to be $z^+ \approx 425/4 \approx 100$, confirming the observations from other studies (Smith & Metzler 1983; Blackwelder, 1997).

Some local oscillations and breakdowns (identified as X in the picture) of the wall-layer streaks can also be observed as shown in figure 4.2.1g. It seems that

the instabilities originate from the strong local shear stress. As discussed in Chapter 2, the streak velocity profiles have inflection points and are less stable than the mean velocity profile that is convex. It means that the perturbations of velocity profiles with inflection points grow much faster. The low-speed streaks are always accompanied with the high-shear regions. Some researchers suggest that this inflectional velocity profile is the main cause of the breakdown of near-wall structures (Asai et al. 2002). It is also suggested that the transient growth of perturbations of the streaky flow may be even more important in the turbulence regeneration cycle (Schoppa & Hussain 2002).

While the streaks are easily observed in the experiments or in the direct numerical simulations, observing the corresponding pattern of wall-normal motions away from the wall is not so easy. It may explain why there is no general agreement on which pattern of the wall-normal motions is responsible for the streaks even after several decades of researches (Chernyshenko & Baig, 2005).

A typical sweep is indicated by the arrow in figure 4.2.1.j to 4.2.1.m, which shows its beginning and growth. The high momentum fluid has emanated from the outer region and advanced towards the wall, hence displaced the dye in the wall region on impact, agreeing perfectly with Corino's observation (Corino and Brodkey 1969). In figure 4.2.1.k, the sweep is marked with an arrow. The sweep is at the early stage of its development and the dye movement has not shown a clear sign. The effect of the sweep has begun to show as the dye is being removed in figure 4.2.1.l; the sweep's further development can be seen from the following figures. Because of the flow continuity, we often expect a simultaneous ejection of the retarded wall region fluid outwards (Corino an

Brodkey 1969). However, these pictures only show the near-wall structures and do not capture the ejections.

Sometimes, the sweeps occur in groups as shown in figure 4.2.2. The sweep 'A' appears in figure 4.2.2a and develops in figure 4.2.2b. A weaker sweep 'B' just emerge itself on the top of sweep 'A' in the following figure 4.2.2c and figure 4.2.2d. In figure 4.2.2e and figure 4.2.2f, the sweep 'C' comes forth just next to the previous 2. The observations of the sweeps' locations in this study prove that sweeps occur randomly in space and time, which confirms Corino's remarks (Corino and Brodkey 1969). It also shows that the oscillations of the streaks, especially the local oscillations, are associated with the sweep events at the most of time.

4.3 Turbulent Boundary Layer With Lorentz-Forcing

Spanwise Oscillation Control

The Lorentz-forcing spanwise oscillation has been carried out in this study as well to verify the new electro-magnetic units. Pang (2005) designed the electro-magnetic unit with both of the copper block electrodes and the magnets exposed to the water directly. This could cause some problems such as the rough surface and the possible water penetrating through the gaps among the electrodes, magnets and the frame. The new electro-magnetic units are of the photo-etched electrode sheets, which can ensure the distances between the electrodes and the magnets are the same and have no gaps for the water on the surface to flow through the electro-magnetic units. Furthermore, the new electrode sheet offers a better background for the flow visualisation.

A maximum of 47% of drag reduction is achieved in this experiment of the spanwise oscillation, which agrees well with the results of Berger (2000) and

Pang & Choi (2004). As shown in Figure 4.3.1, the logarithmic velocity profiles are shifted upward, indicating that the viscous sublayer is thickened by the spanwise oscillating Lorentz force; similar to Pang & Choi (2004). This is also similar to the results of the spanwise wall oscillation (Choi 2002). The turbulent intensity profiles show a significant reduction as well, not only in the near-wall region but also in the logarithmic region of the boundary layer as shown in figure 4.3.2. Meanwhile, both skewness and kurtosis of the streamwise velocity fluctuations are increased in the viscous sublayer and the buffer layer as shown in figure 4.3.3 and figure 4.3.4. These increases in higher moments are the consequence of a reduction of the turbulence activities, consistent with the experiments carried out by Pang & Choi (2004) and others on the spanwise wall oscillation (Choi 2001; Baron & Quadrio 1996 and Quadrio & Sibilla 2000).

Figure 4.3.5(a) shows the visualisation pictures of the near-wall streaky structures with the Lorentz-force oscillation. The low-speed streaks are twisted into the spanwise direction due to the spanwise flow oscillation. These are very similar to those observed in the spanwise wall oscillation (figure 4.3.5(b)). Choi et al. (1998) proposed that a negative spanwise vorticity is created in the turbulent boundary layer due to the spanwise wall oscillation, which seems to apply to the Lorentz-force flow oscillation equally. This study has achieved a drag reduction up to 47% with a maximum spanwise velocity, w^+ , up to 12.2.

Through the study of the Lorentz forcing spanwise oscillation, my electromagnetic unit proves to work and is ready to move to the spanwise travelling wave actuations.

4.4 Turbulent Boundary Layer With Spanwise Lorentz-Forcing Travelling Wave

4.4.1 Flow Visualisation Without Flow

The flow-field set-up for flow visualisation in still water is shown in figure 4.4.1. The solution of Potassium Permanganate (KMnO_4) is carefully introduced through the tubes so that it does not affect or impact the induced thin-layer of the same solution on the wall. Note that there are some skewed trace lines due to the previous ambient flow motions when the water is settling down. But no obvious water movement is observed for more than 5 minutes when this frame of the video was taken. When the Lorentz forces are applied, the induced movement is very distinct.

Figure 4.4.2 shows the flow motion induced by the Lorentz forces and the blue and red arrows below the yellow line indicate the forces' directions. The travelling wave moves to the left. The flow patterns indicate that the effects remained the Lorentz forces in the previous phase. A sketch is shown in the top of the picture in figure 4.4.2a. It helps to understand the motions indicated by the lines. The dashed lines in the diagram indicate the motions maintained by inertia that is a property of an object to remain at a constant velocity unless it is acted upon by an external force. Generally speaking, the skewed line shows the spanwise velocity values.

As shown in figure 4.4.2a, the boxes I and II show the fluid is accumulated by the previous forces. At this phase, the induced leftward (blue) force and the rightward (red) force start to take effect. The fluid in box I starts to move to the left as illustrated in figure 4.4.2b and clusters at point D as shown in figure 4.4.2c. The rightward force also pushes the solution to migrate to point C and

forms a small region as shown in figure 4.4.2b and 4.4.2c. In the drag reducing cases, the fluid can move to the top or at least to part of the region of the adjacent electrode as shown in figure 4.4.2c. It is important for the travelling wave to continue.

As show in figure 4.4.2a, the motion in region BC is towards the right owing to the induced Lorentz force and the one in region AB is maintained to the left due to the inertia effects. Therefore a downwash movement is expected in the region near point A because of continuity. It is indicated by the downward arrow near point B.

At the next phase as indicated in figure 4.4.2d, regions AB and CD are activated. The fluid in point A advances to the left and mixes with the fluid left by the previous rightward force. The line pointed to by the green arrow in figure 4.4.2d shows the combined effects of the inertia and the induced motion of the Lorentz force. At first, the inertia keeps the fluid moving to the right, whereas, the leftward force tries to move the fluid to the left. The strongest force is located on the wall; therefore the fluid near the wall starts to respond to the force in the first instance. With time going on, more and more fluid moves away from the wall, changing directions as shown in figure 4.4.2e and figure 4.4.2f.

In figure 4.4.2f, an arrow points to the wandering trace-line near the left edge of the electrode that keeps its shape and does not change its direction even when this phase is close to finish. The behaviour might be due to the low-speed protuberance shown by the hexagon. Because the experiment is undertaken in still water, the flow might push the trace-line away from the wall and moves out of the forcing-effective region.

In the next phase, the fluid at point C advances further to the left. Then the fluid in box I in figure 4.4.2a is transported from region DE to the right and spreads out in its path.

Similar experiments are also carried out in the drag-increasing case of $T^+ = 17$ and $St = 232$. However, the amplitude in the z-direction is too small to notice in these pictures. Therefore, only one picture is shown in figure 4.4.3 to demonstrate the flow visualisation in still water with maximum amplitude. Figure 4.4.3a does show similar spanwise velocity gradient as the one in the drag-reducing case, but with much smaller amplitude value. No obvious low-speed regions are observed here. No fluid is transported along the travelling wave moving direction. In other words, only pseudo-local-oscillation occurred in the drag-increasing case.

4.4.2 Flow Visualisation With Flow

The flow field for flow visualisation is show in figure 4.4.4, which also indicates the velocity measurement positions. Note that the velocity profile can be extended to the whole wavelength although only one-fourth (about one electrode width) is measured here. This is due to the repeated cycles in time and space. The sequence of the pictures of the travelling-wave motion and the associated near-wall streaky structures are shown in figure 4.4.5 (a) for a drag-reducing case. The distribution of the phase-averaged u velocity is shown in figure 4.4.5(b) at the corresponding position and timing. The flow condition is $T^+ = 42$, $St = 232$ and $DR = 28.9\%$.

Figure 4.4.5.1a shows that the low-speed streaks are twisted to the right as indicated by a green octagon by the previous forces. The velocity distribution in figure 4.4.5.1b confirms that there is a low-speed region. The high-

momentum fluid is induced due to mass continuity, which is indicated by an oval and can be found through figures 4.4.5.1 to figures 4.4.5.6. The more important motions are the twisted low-speed streaks, which can be observed directly from the pictures. Hence, special attention should be paid to the low-speed streaky structures. The arrow in Figure 4.4.5.2a clearly indicates that the low-speed streaks are starting to twist to the left by the Lorentz forcing. They are propelled along the spanwise direction and are able to travel out of the activated force region into the adjoining area as seen in the following sequence. Then they migrate and meet with the low-speed region left by the previous forces shown in figure 4.4.5.3a. The streaks are clustered together to form 'ribbons' until the following non-activated region become active. The low-speed 'ribbon' has also been presented by Du et al (2002). This process continues from figure 4.4.5.1 to figure 4.4.5.6. The velocity profiles shown in figure 4.4.5.1b to figure 4.4.5.6b also indicate this change, where the velocities around $z^+ = 350$ are becoming smaller and expand the previous low-speed region presented by the octagon. Meanwhile, another low-speed region, indicated by a hexagon in figure 4.4.5.5 and figure 4.4.5.6, is formed. This low-speed region becomes more noticeable in figure 4.4.5.7, shown in figure 4.4.5.7a, which is similar to the one shown in figure 4.4.5.1. This finding seems to suggest that the observation of phenomenon around one electrode during the timing sequence of a cycle can recover states happening in the spatially sequential electrodes.

The second phase starts from figure 4.4.5.7. The low-speed region indicated by an octagon formed in the first phase is propagated further to the left, following the travelling-wave moving direction. The sequence of the pictures from figure 4.4.5.7 to figure 4.4.5.12 show that this low speed region indicated

by the octagon migrates and mixes with the other low-speed region induced by the opposite forces indicated by the hexagon. This can also be observed from the velocity profiles. One interesting finding is that the low-speed region doesn't move as a whole. It can be seen from figure 4.4.5.7b to figure 4.4.5.12b, where the lowest-speed region (or the valley of the low-speed region) doesn't move or change its location. For example, the valley of the low-speed region is about $z^+ \approx 300$ in figure 4.4.5.7b and does not move to the left such as $z^+ \approx 280$ in the following sequence. The fact is that the low-speed region seems to act like a 'water balloon'. When the 'water balloon' (low-speed region) is full of 'water' (low-speed fluid), the volume reaches the maximum. With the 'water' (low-speed fluid) being pumped out, the volume of the 'water balloon' (low-speed region) is becoming smaller and smaller. The low-speed fluid migrates from a low-speed region, indicated by an octagon in figure 4.4.5.7, to another low-speed region, indicated by a hexagon, through along a forcing-activated area (between $z^+ \approx 300$ and $z^+ \approx 200$). It can be seen that these two regions' valley values are changing to the opposite. At the end of this phase, a new low-speed region is formed in $z^+ \approx 200$ shown in figure 4.4.5.12b. The low-speed region (indicated by a hexagon) formed due to the previous right-ward force doesn't change its location which always hangs around $z^+ \approx 200$ during this phase. Phase 1 of the process shown in figure 4.4.5.1 to figure 4.4.5.6 will be repeated in the following electrode area along the travelling wave moving direction. The low-speed regions seem to act as a 'storage' that supplies low-speed fluids to the nearby forcing areas. With the help of the low-speed 'storage' and the Lorentz forcing, low-speed fluid spreads along the spanwise direction, which can be seen from the flow visualisation in still water.

During phase 3, a high-speed region is introduced as shown in figure 4.4.5.13, indicated by a green oval. This is shaped earlier and can be observed in figure 4.4.5.12 and figure 4.4.5.11 at the same position. This might be due to the movement of the low-speed fluid. As we can see from figure 4.4.5.12a, the low-speed streaks are twisted to the left near the left of the oval, but the leftward movement of the low-speed streaks in the right of the oval is getting weaker and weaker due to the effects of the inertia and the fluid viscosity. This phenomenon can also be observed and investigated from the earlier figures such as figure 4.4.5.10a and figure 4.4.5.11a. It is not surprising that the high-speed fluid moves in due to mass continuity if there is not enough low-speed fluid coming to refill it. When the right-ward force (positive force along positive z direction, opposite to the direction of travelling wave movement) is imposed, this becomes more significant as shown in figure 4.4.5.13 to figure 4.4.5.18. The velocity profiles confirm this. However, it is observed that the velocities near $z^+ \approx 350$ are reduced as shown from figure 4.4.5.13b to figure 4.4.5.15b, because the low-speed streaks are twisted by the positive force to the right in this area. With time going along, the high-speed fluid in the region around $z^+ \approx 300$ are transported into the region of $z^+ \approx 350$. This is reflected in the velocity profiles from figure 4.4.5.16b to figure 4.4.5.18b where the speed of the region $z^+ \approx 350$ isn't reduced further.

At the final phase, the new low-speed region will be formed and then a cycle is completed.

Figure 4.4.6 summarises the spanwise motions induced by the travelling wave. The low speed streak 1 is twisted to the left by the Lorentz forcing and mixes with streak 3. During the process, streak 2 is also brought in. Therefore, the three low-speed streaks mingle together. In the following phase the assembly

of streaks 1, 2 and 3 are going to meet streak 4 and form a new low-speed area. This study shows that at least two low-speed streaks get involved and blend jointly during one phase of the drag-reducing cases. The development of the fundamental sinusoidal mode of the streak instability is very sensitive to the streak spacing and is completely suppressed when the streak spacing is smaller than a critical value - about 2.5 times the streak width for the low-speed streaks examined (Konishi and Asai 2004). If the streaks are somehow suppressed, the turbulence intensity is reduced significantly (Schoppa & Hussain 2002). Therefore the action of eliminating or modifying the low-speed streaks disturbs the turbulence regeneration cycle. The rightward force that twists streak 4 has an opposite sign against the leftward one that drives the travelling wave ahead. This force is also important in order to achieve drag reduction. It acts to ensure that the streamwise vorticity induced by the force of the travelling wave direction is just effective enough to disturb the turbulent activities and reduce the skin friction drag. This is consistent with the observations of Du et al.(2002) that only one direction of Lorentz forcing travelling wave increases the drag instead of reducing it.

As we discussed above, most of the low-speed streaks are twisted and move to the left from one low-speed region ('storage') to another, although small part of the low-speed streaks migrate to the right and form an assistant 'storage'. This spanwise motion of the travelling streaky structures repeats across the entire section and the spanwise displacement of the low-speed 'ribbons' can happen covering up to the total width of the test sheet ($z^+ = 1214$ wall units). To achieve the drag reductions, it is found that the spanwise displacement of the low-speed 'ribbons' must cover a width greater than 115 wall units (in z^+ ,

which is about one electrode width in this experiment). This is almost comparable to the spacing between the low-speed streaks ($z^+ \sim 100$).

Figure 4.4.7 shows the flow visualisation for the drag increasing case of $T^+ = 17$ and $St = 232$. The term ‘spanwise travelling wave excitation’ is still used here to describe the motion of the pseudo-local oscillation, not only to keep consistent but also because of the travelling-wave-like force form.

The spanwise travelling wave excitation seems to enhance the local flow oscillation. As seen in figure 4.4.7a, the dashed lines indicate the motions of the streaky structures’ pseudo-local oscillation. The nearby local-oscillations appear to form the converging and the diverging motions, which is captured by most of the pictures, especially for those where the twisted streaks are not in the same forcing area (within the same electrode area). Obviously, the pseudo-local spanwise oscillation is different from the Lorentz-forcing spanwise oscillation or the spanwise wall oscillation. Does this pseudo-local spanwise oscillation increase the instability of the low-speed streaks to increase the skin-friction, or induce or enhance the wall-normal or the spanwise vorticity?

Figure 4.4.8 shows the streamwise velocity distribution along the spanwise direction. It is found that there are low-speed regions and high-speed regions appearing alternatively, although no low-speed fluid moves across the whole test section as observed in the drag-reducing case. This seems to suggest that the appearance of the low-speed ‘ribbons’ isn’t the sole reason for achieving drag reduction.

4.5 Conclusions

A visualisation study of the near-wall streaky structures has been undertaken both on a non-control condition and a controlled condition with a Lorentz-forcing spanwise travelling wave. The most distinguished near-wall structures and the low-speed streaks are observed, confirming the observation of Kline et al. (1967). The development of the sweeps is similar to that described in a previous study (Corino and Brodkey 1969).

The induced motion by the Lorentz-forcing spanwise travelling wave is described by both diagram and flow visualisation in still water. The motions maintained due to the inertia effects are also implied and the combined effects are presented particularly when new forces are applied.

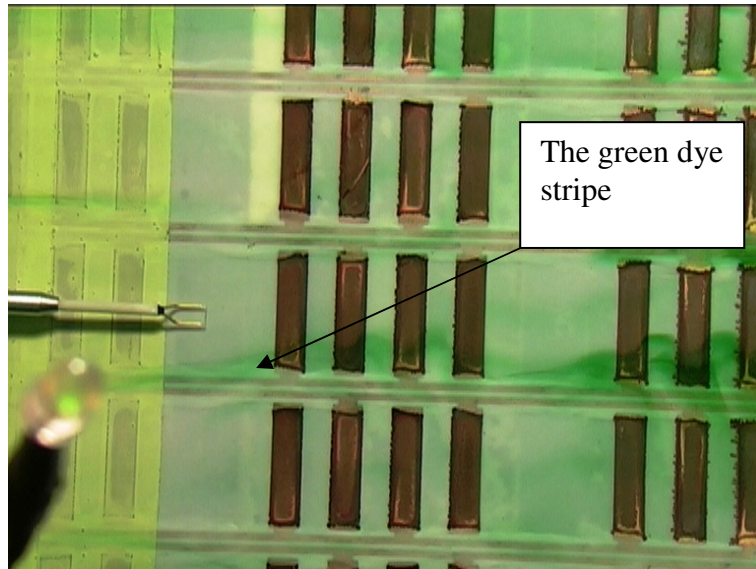
In both of the drag-reducing and drag-increasing cases, the low-speed streaks were twisted into the spanwise directions. In the drag-reducing case, the low-speed streaks were twisted and clustered together to form a low-speed region which seems to act as storage of low-speed fluid. This 'storage' supplied the low-speed streaks to the Lorentz forces and then the low-speed region spread out in the entire spanwise direction. Whereas, the low-speed streaks just oscillate locally in the drag-increasing case. The streaky structures' pseudo-local oscillation might form converging and diverging motions near the forcing-activation area, which is different from the pure spanwise oscillation by either the Lorentz forces or the mechanical wall. In the spanwise oscillation, the low-speed streaks are twisted to one direction in the whole modified area and no converging and diverging motions have been observed. In the pseudo-local oscillation, these converging and diverging might act to pump the low-speed fluid away from the wall and induce the high-speed fluid

towards the wall. Orlandi and Jimenez (1994) found that the transport of high-speed fluid towards the wall is more important than low-speed fluid away from it. In other words, the downwash of the high-speed fluid plays a more important role in the production of skin friction, so that the net effect is that the averaged wall stress is increased. This might explain the drag-increasing mechanism in this study.

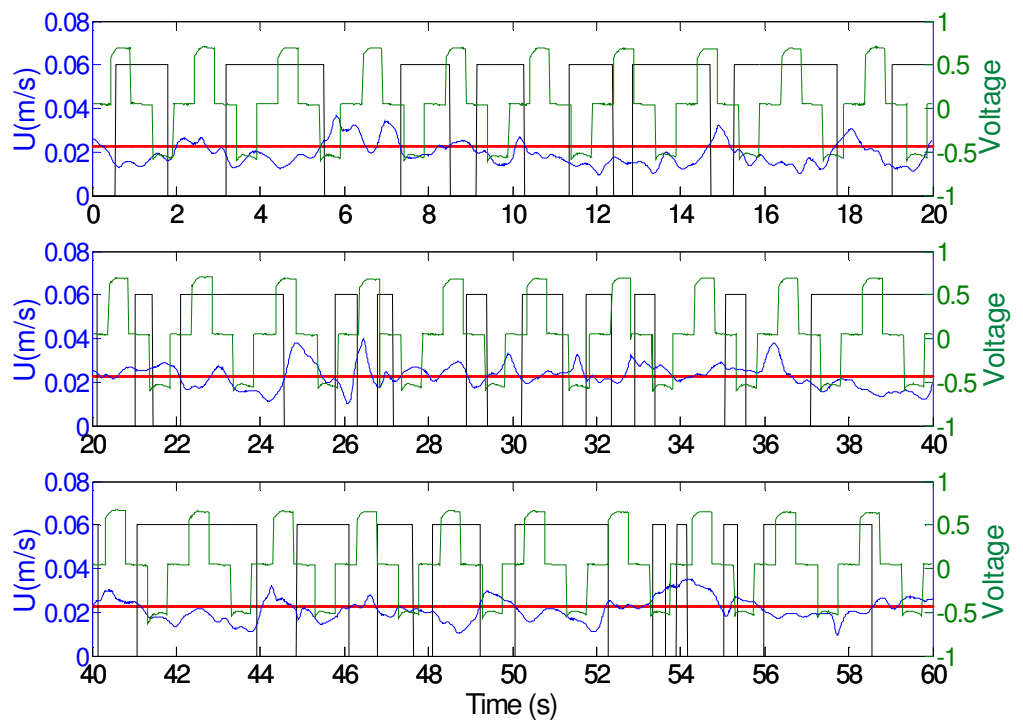
To gain drag reduction, it is found that the spanwise displacement of the low-speed 'ribbons' must be greater than 115 wall units (in z^+ , which is about one electrode width in this experiment). This is comparable to the spacing between the low-speed streaks ($z^+ \sim 100$). Otherwise, drag increase was observed.

From flow visualisation studies of with and without-flow, repeated action of the low-speed streaks around different electrodes are found, which indicates that the observation of the phenomenon around one electrode during timing sequence of a cycle can recover states happening in the spatially sequential electrodes. In other words, there is a correlation between time and space in the spanwise motion.

The velocity distribution for both of the drag-reducing and drag-increasing cases shows that there is an alternative appearance of low-speed and high-speed regions. This suggests that the appearance of the low-speed 'ribbons' isn't the sole reason for the drag reduction.



(a)

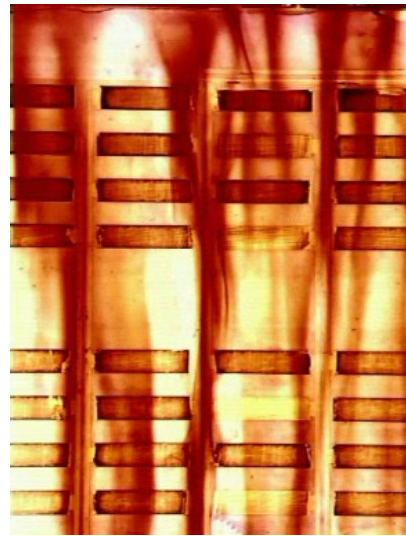


(b)

Figure 4.1.1 The correlation between the dye stripe and the velocity measurement. (a) The measurement arrangement. The LED is triggered by the ADC. When it is ‘ON’, it means the velocity sampling is in process. (b) One illustration of part of the signals. Blue lines denote u velocity; red lines denote the mean velocity; green lines denote the excitation voltage and black boxes denote the low-speed streaks observed in the video.



(a)



(d)



(b)



(e)



(c)



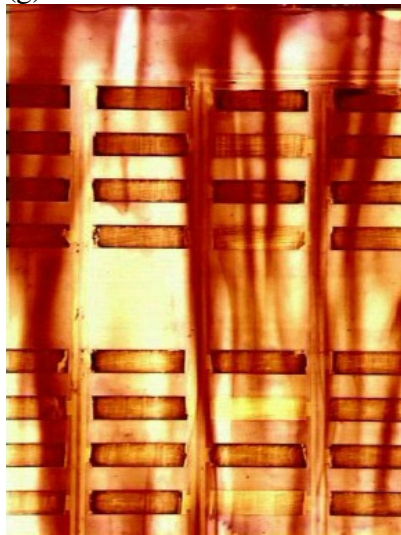
(f)



(g)



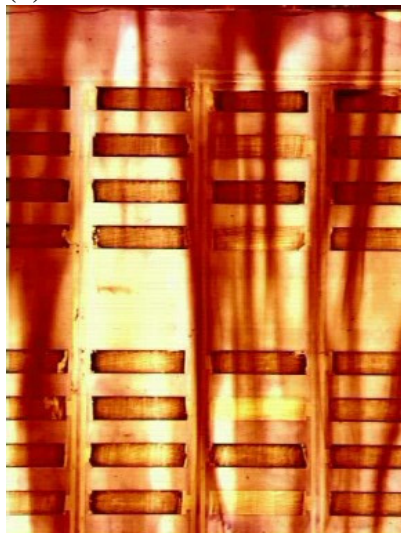
(j)



(h)



(k)



(i)



(l)

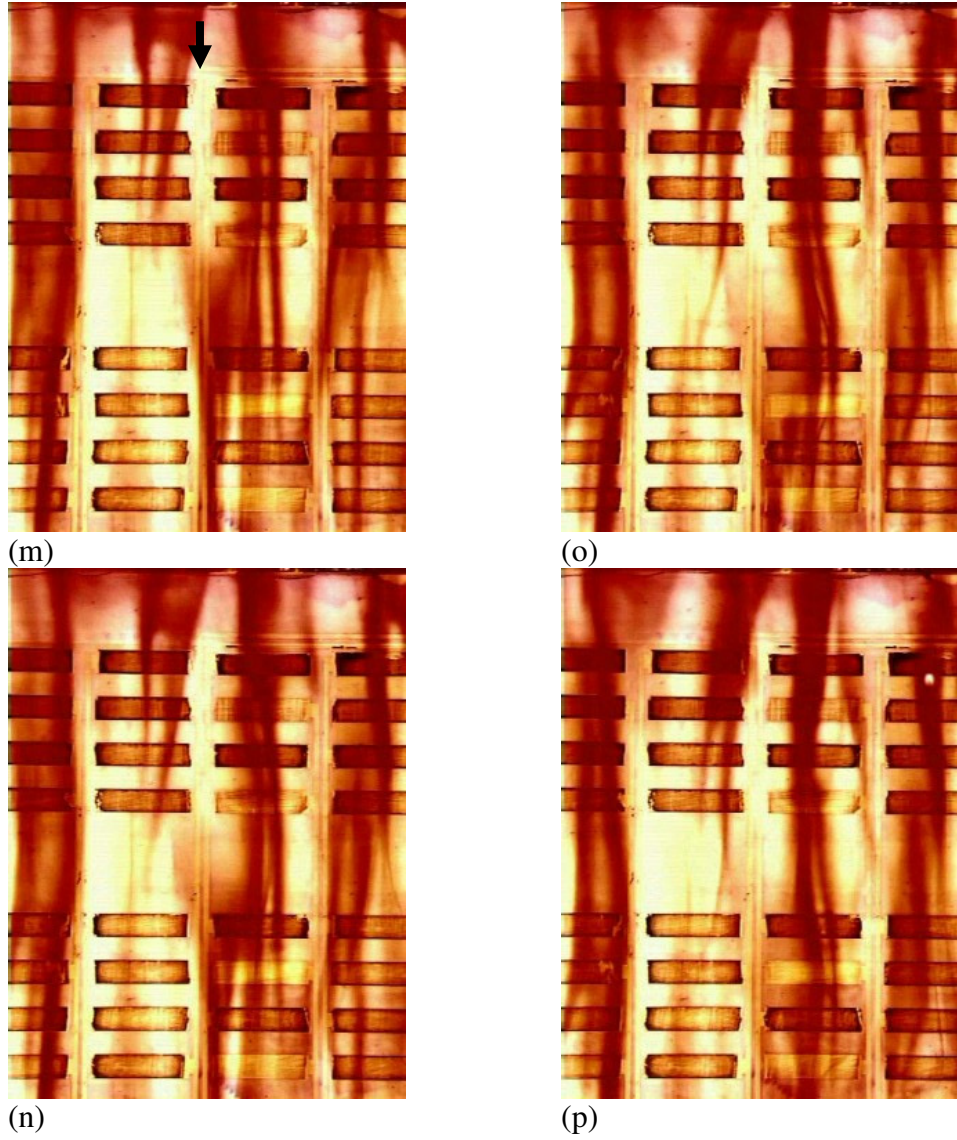
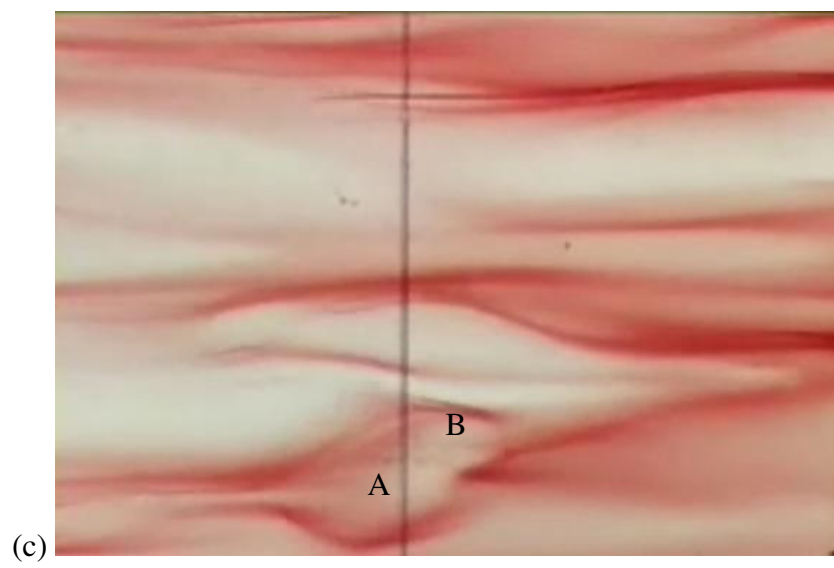
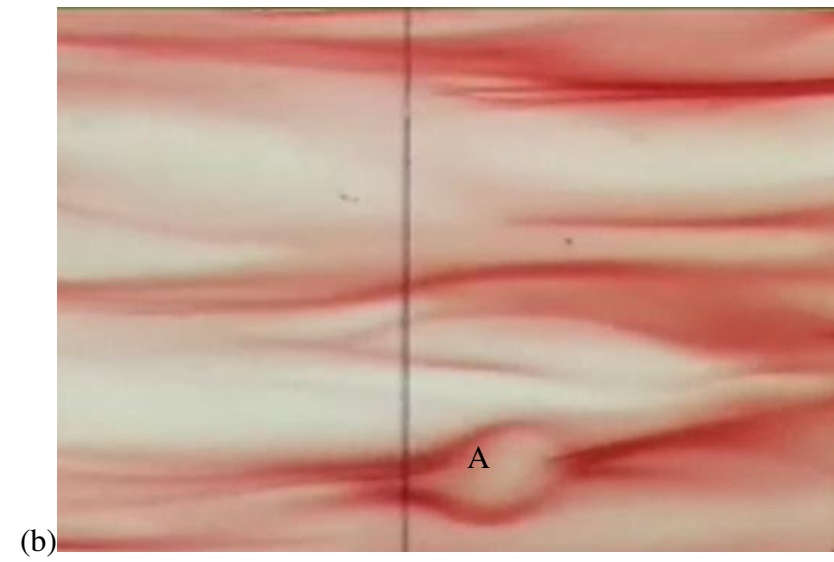
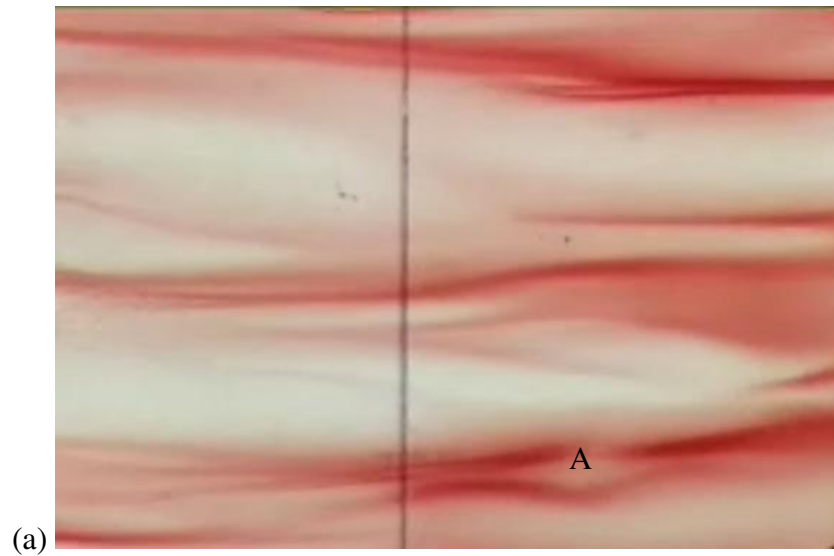


Figure 4.2.1. Flow visualisation of low-speed streaky structures of the turbulent boundary layer without control. Every time interval for the pictures is 0.16 seconds. Flow field size: $520 (x^+)$ by $425 (z^+)$. The video is shown in the attached CD.



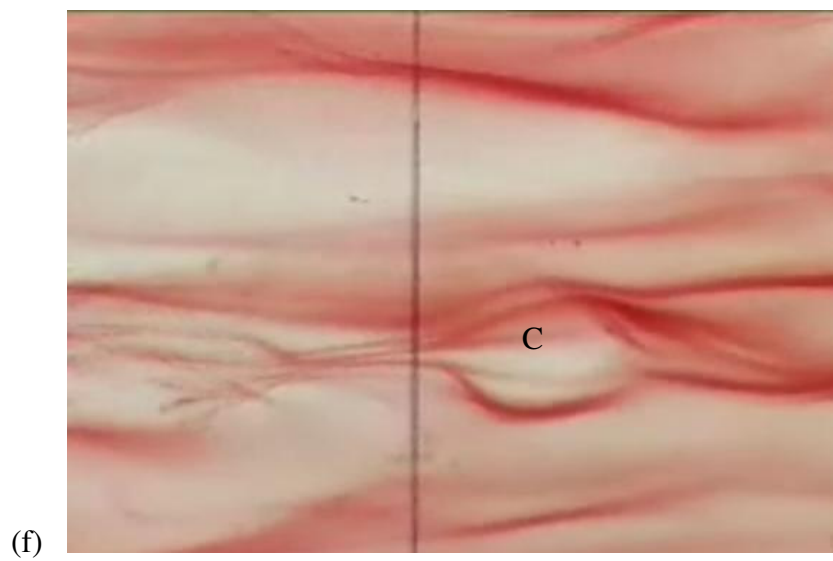
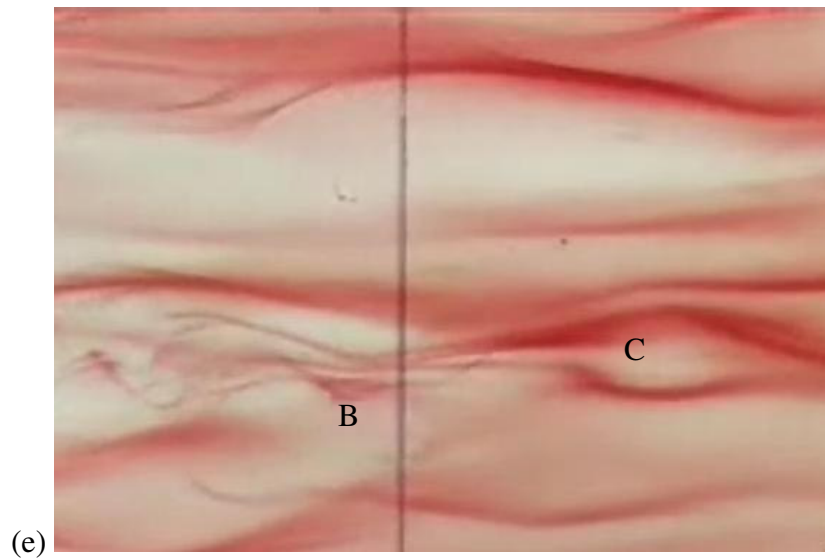
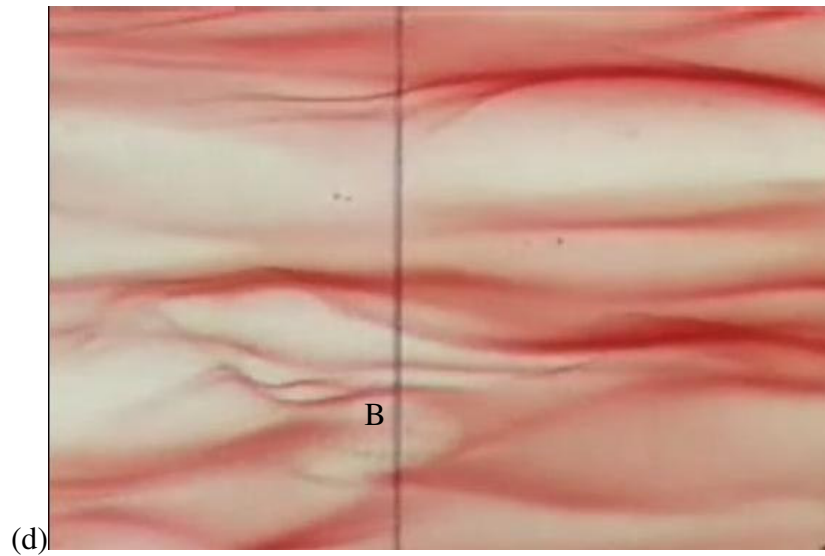


Figure 4.2.2 Sweeps appear in a sequent. Flow direction is from the right to the left.

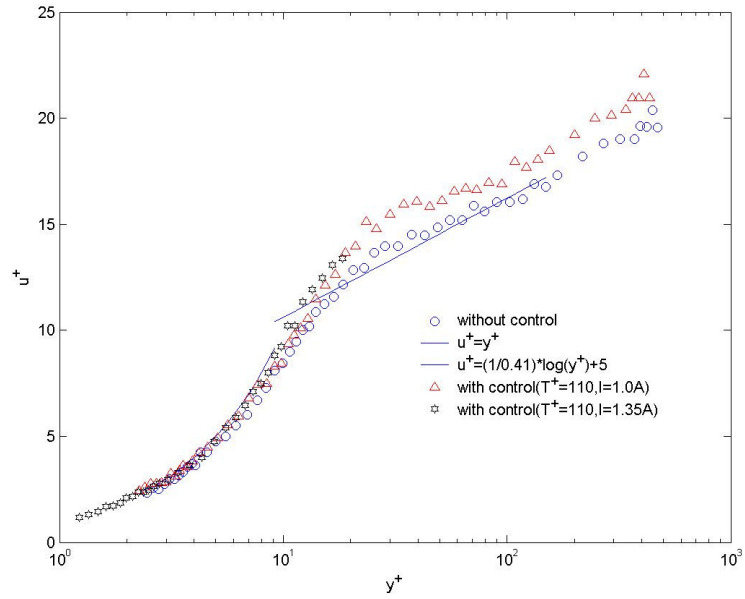


Figure 4.3.1. The logarithmic velocity profiles with and without Lorentz force spanwise oscillating actuation. Current strength, $I = 1.0\text{A}$ corresponds to $St = 232$, and $I = 1.35\text{A}$ corresponds to $St = 313$. Measurement point is 5 mm downstream of the Electromagnetic actuator. The drag reductions shown here are up to 47%

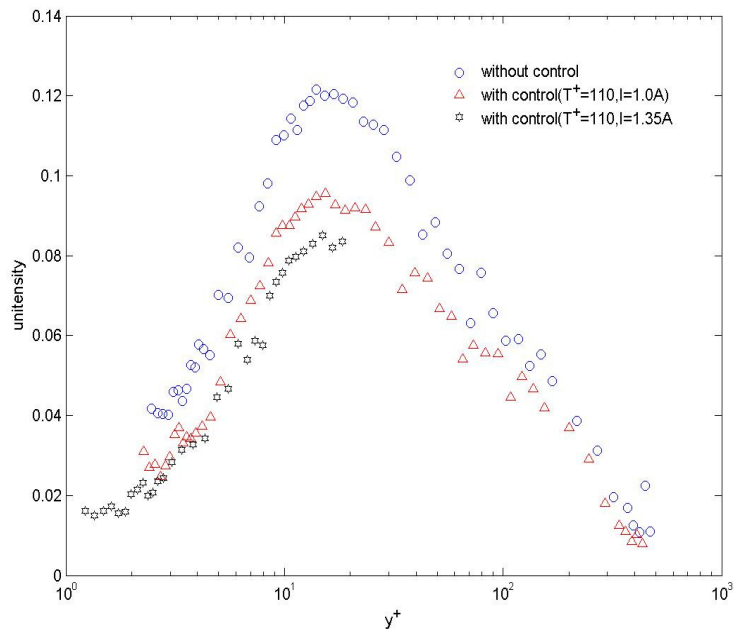


Figure 4.3.2. Turbulence intensity profiles with and without Lorentz force spanwise oscillating actuation. DR = 47%.

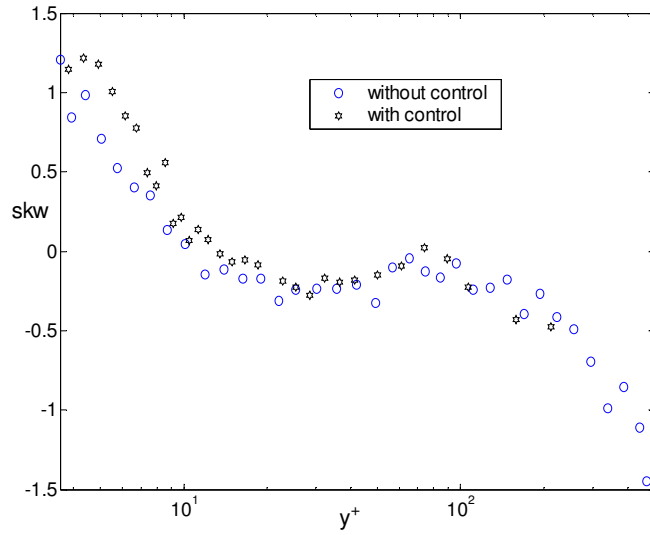


Figure 4.3.3. Skewness of the streamwise velocity fluctuations. The conditions for the control case are $T^+ = 110$, $St = 232$. $DR = 47\%$

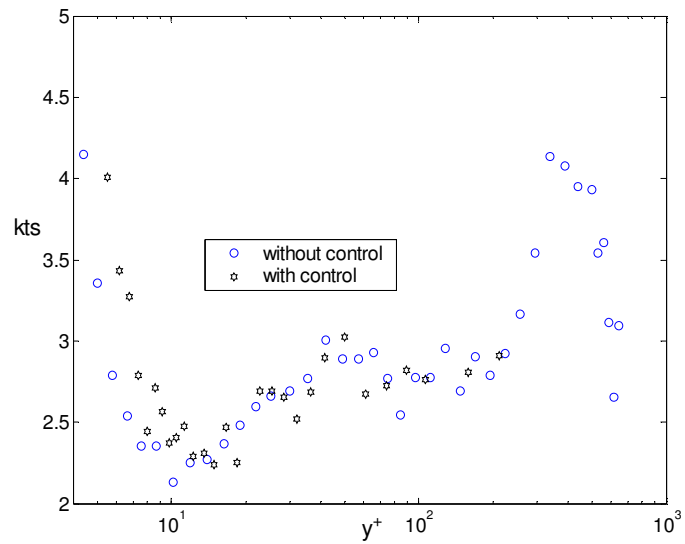
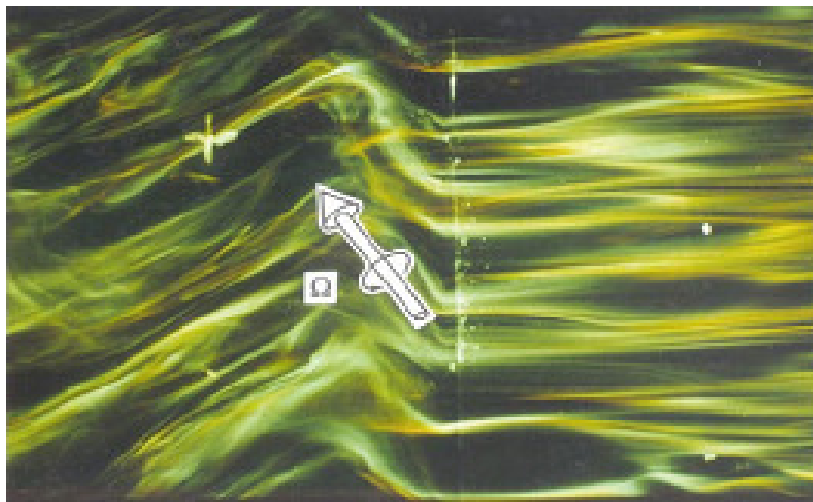


Figure 4.3.4. Kurtosis of the streamwise velocity fluctuations. The conditions for the control case are $T^+ = 110$, $St = 232$. $DR = 47\%$

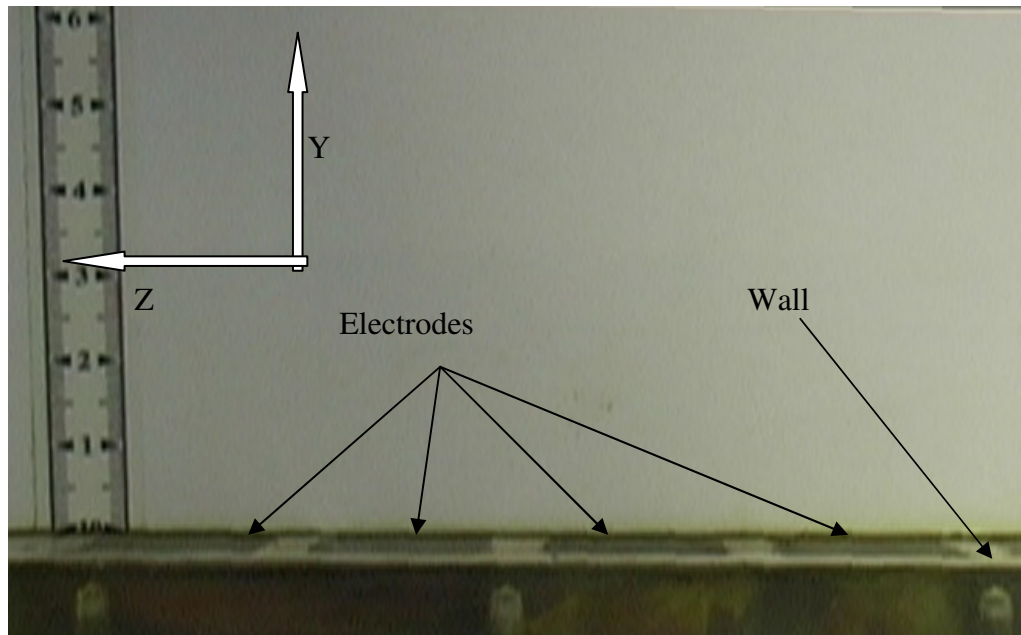


(a)

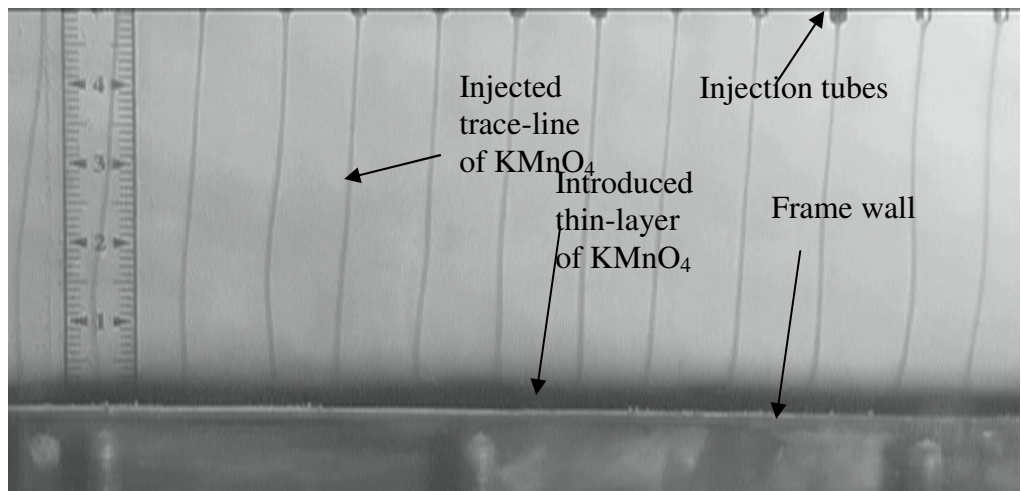


(b)

Figure 4.3.5. (a) Visualization of near-wall streaky structures with Lorentz force spanwise oscillating actuation. Window area is $475 (x^+)$ by $382 (z^+)$ wall units. The video is shown in the attached CD. (b) Visualization of near-wall streaky structures with spanwise wall oscillating actuation (Choi et al 1998). A negative spanwise vorticity created in the near-wall region of the boundary layer over the oscillating wall as shown in the pictures. Flow direction is from the right to the left.



(a)



(b)

Figure 4.4.1. (a) Electrode positioning and (b) Flow-field set-up for flow visualisation in still water. Units are in mm.

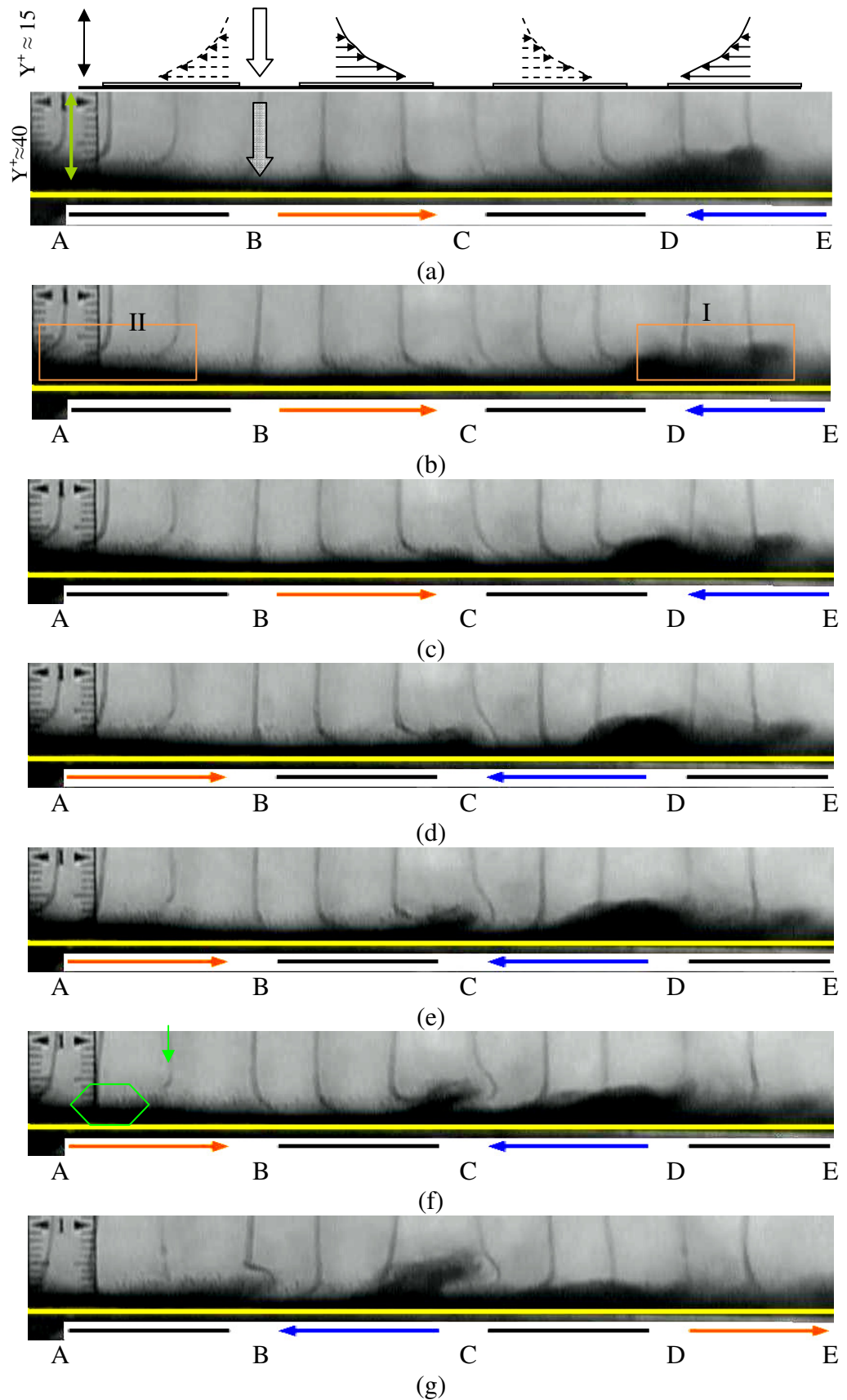


Figure 4.4.2. Flow visualisation without flow in the drag reducing case ($T^+ = 42$). The yellow line shows the wall. The lines and arrows below the yellow line show the electrode positions. Arrows mean the Lorentz forcing directions. The straight lines indicate the electrodes are in non-activated phases.

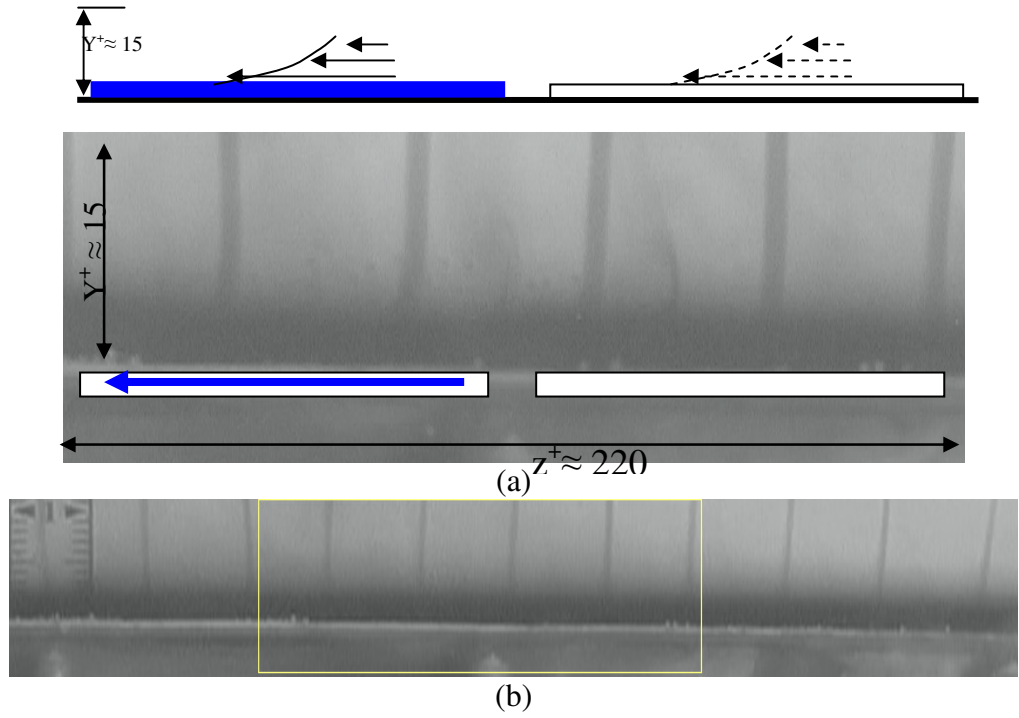


Figure. 4.4.3. Pictures of the flow visualisation in still water for the drag-increasing case. (a) Zoomed region of the yellow rectangle from (b).

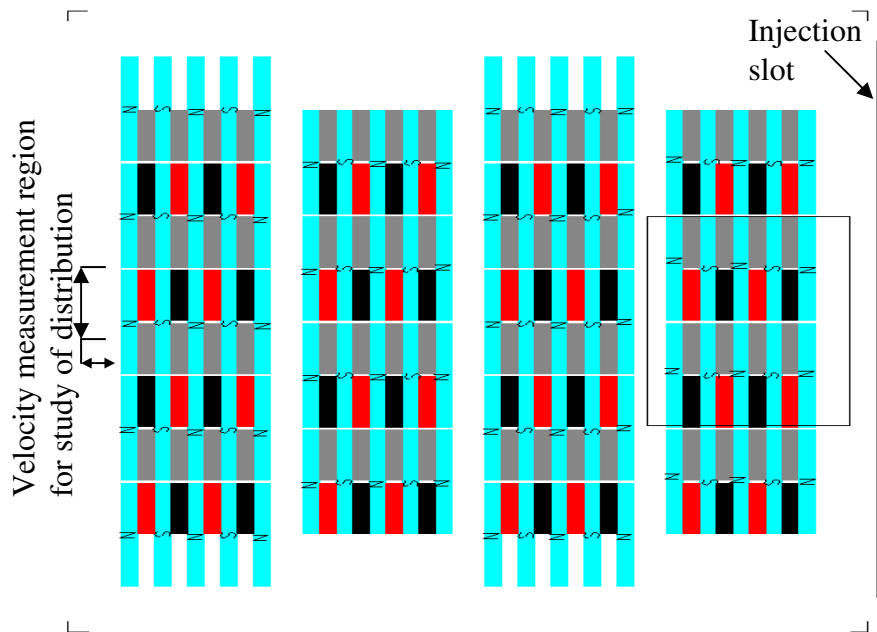
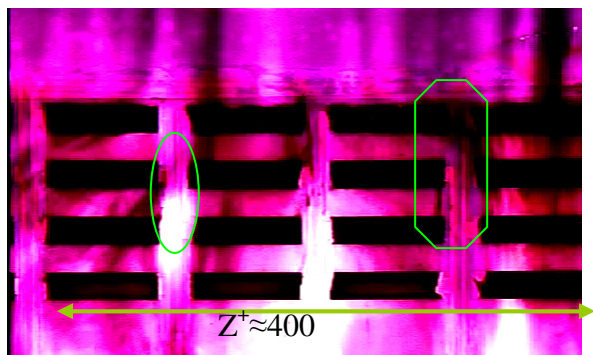
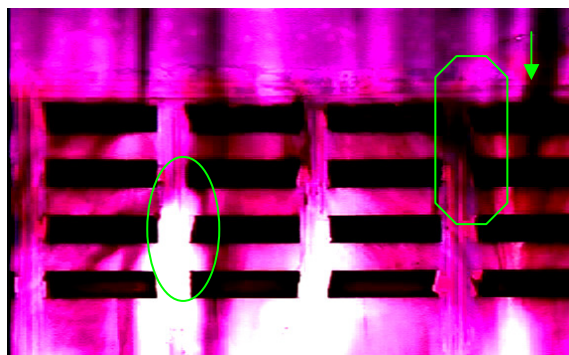


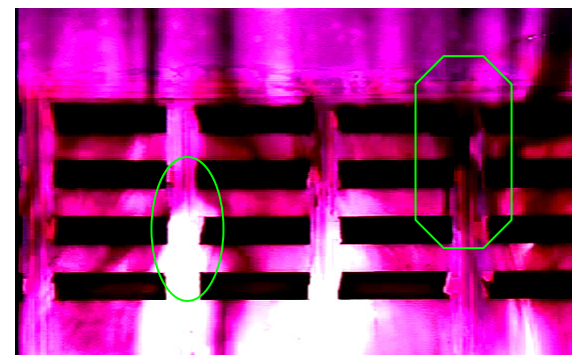
Figure 4.4.4. Flow field for flow visualisation with flow is indicated by the rectangle. Red, black and grey blocks indicate positions of electrodes; cyan indicates positions of the magnets although they are underneath the polyester sheet and cannot be seen.



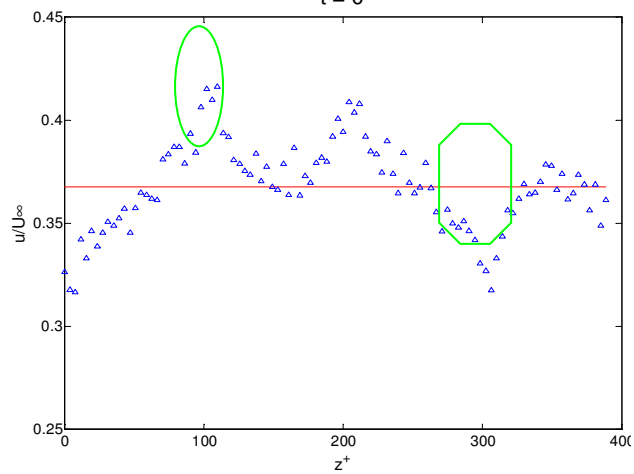
(1a)
t = 0



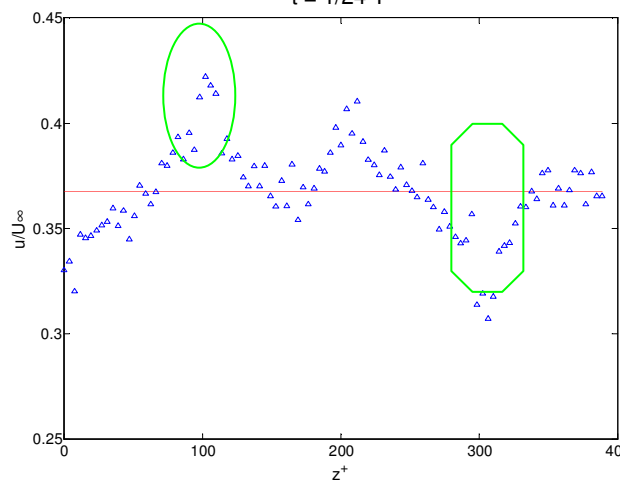
(2a)
t = 1/24 T



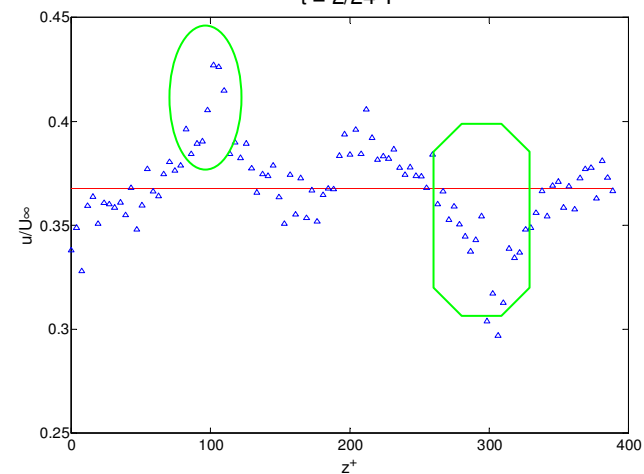
(3a)
t = 2/24 T



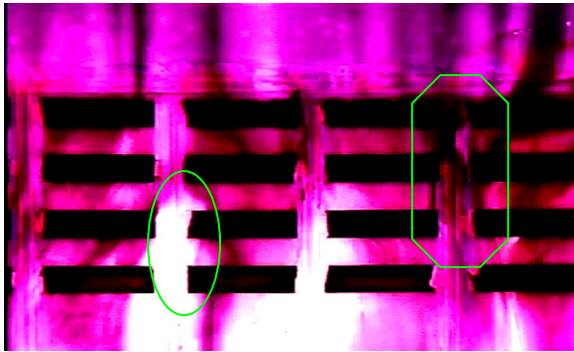
(1b)



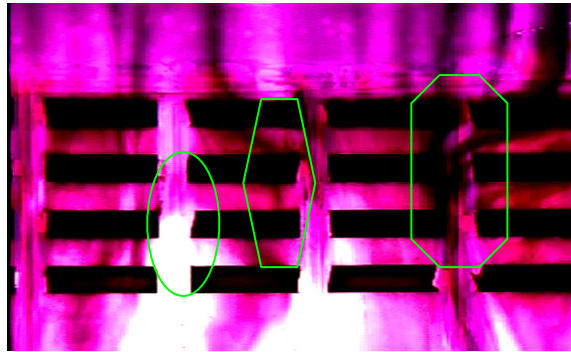
(2b)



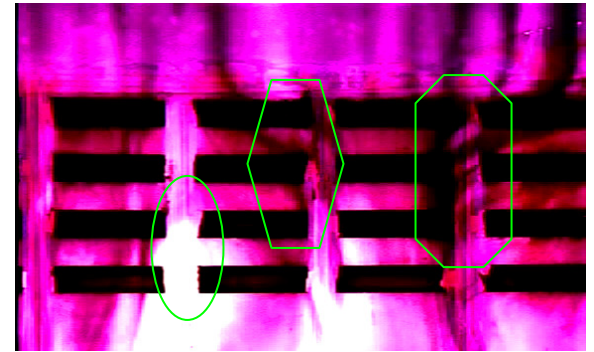
(3b)



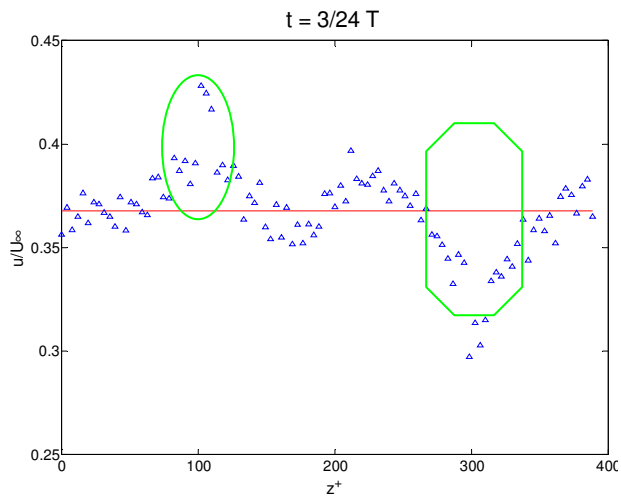
(4a)



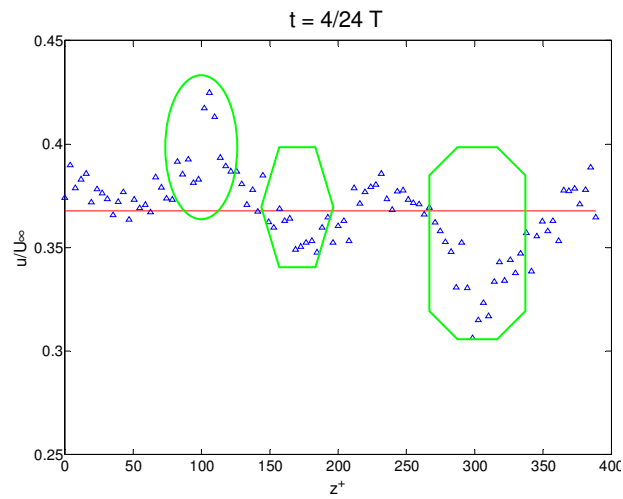
(5a)



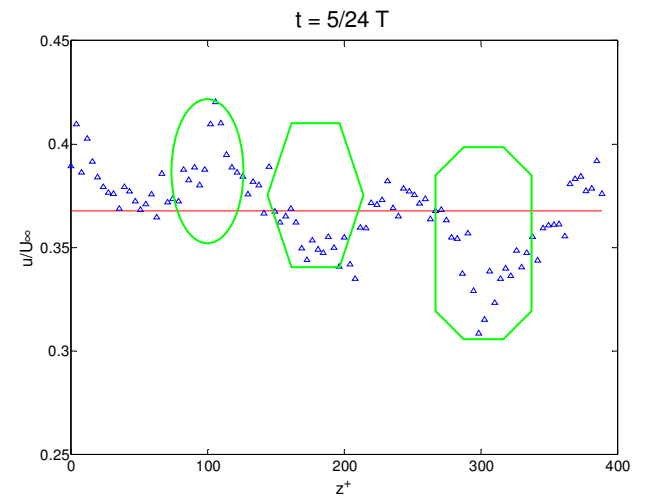
(6a)



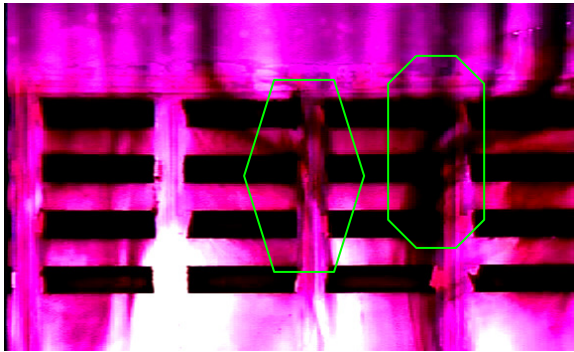
(4b)



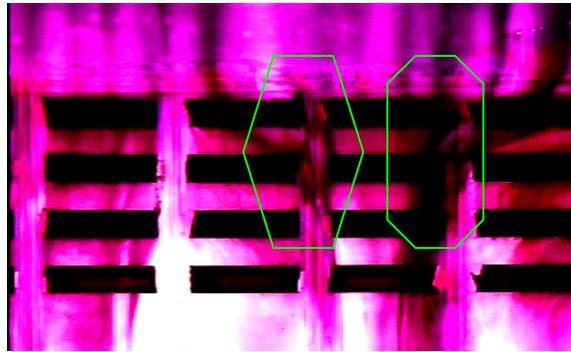
(5b)



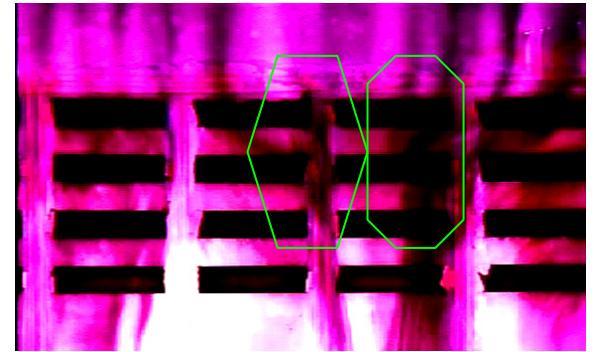
(6b)



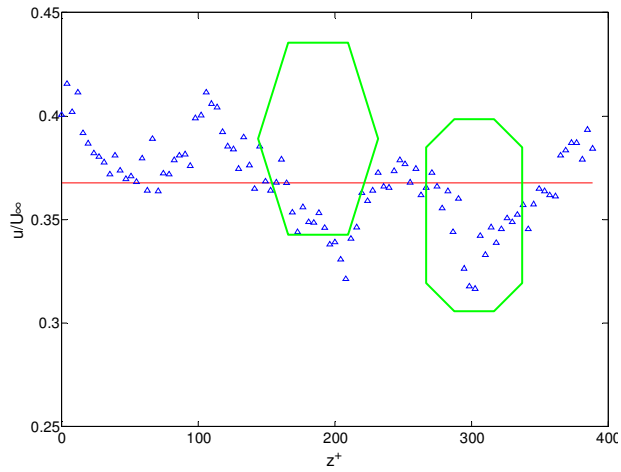
(7a)
 $t = 6/24 T$



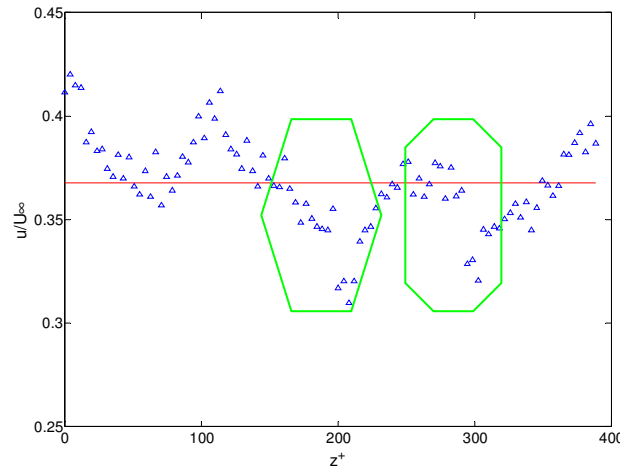
(8a)
 $t = 7/24 T$



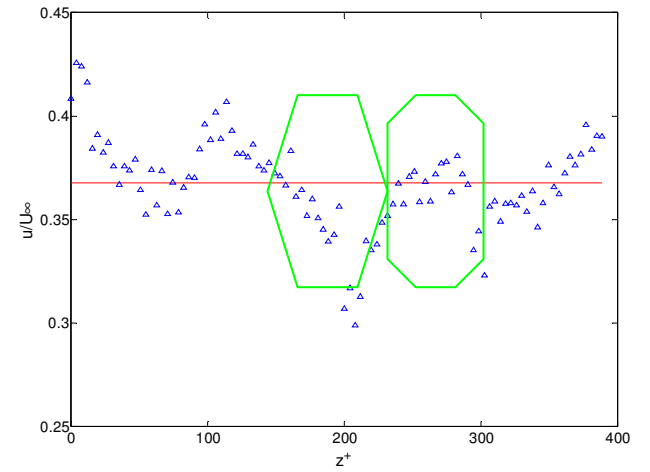
(9a)
 $t = 8/24 T$



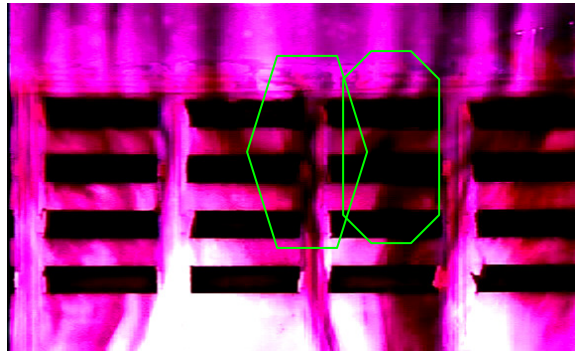
(7b)



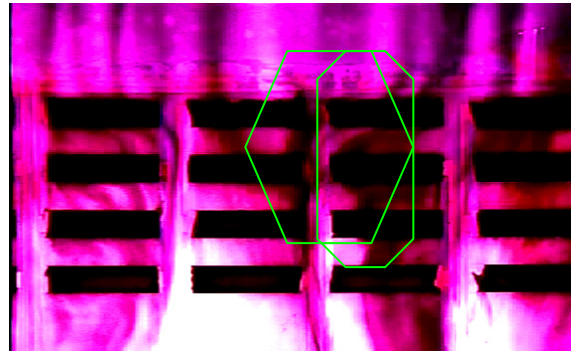
(8b)



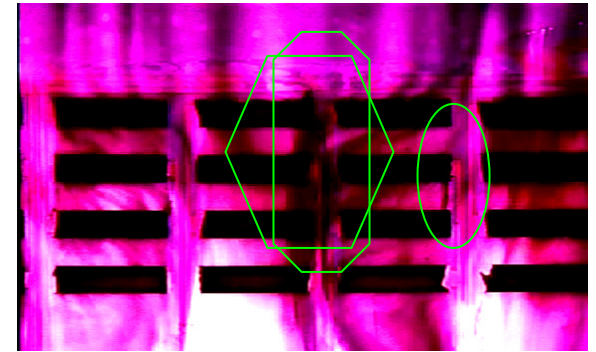
(9b)



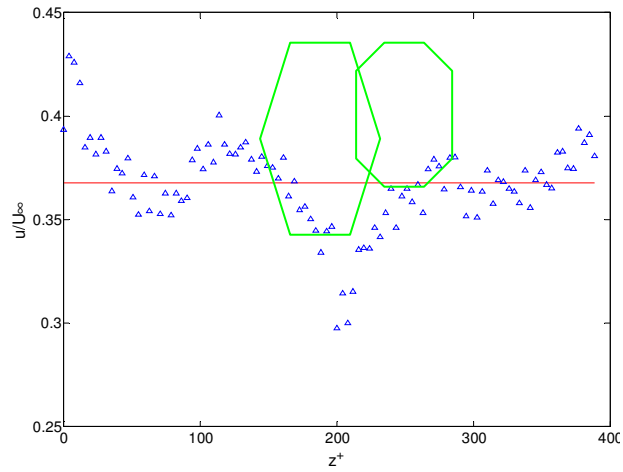
(10a)
 $t = 9/24 T$



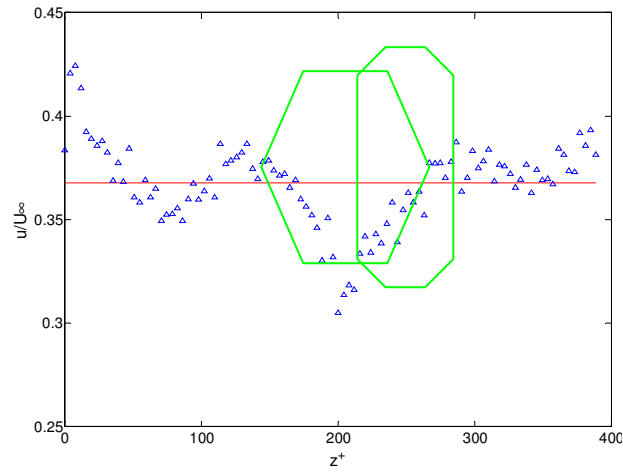
(11a)
 $t = 10/24 T$



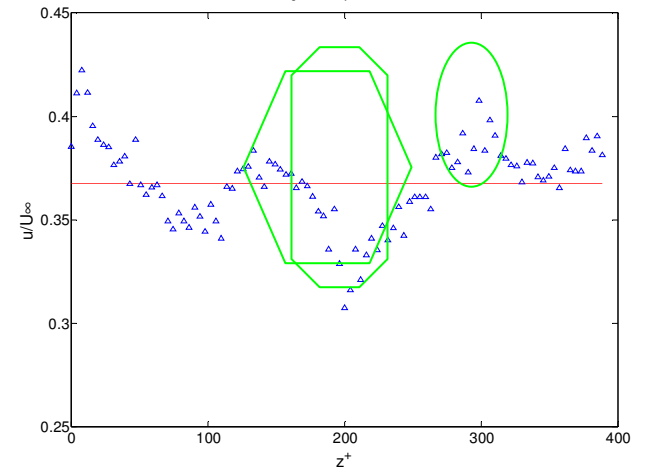
(12a)
 $t = 11/24 T$



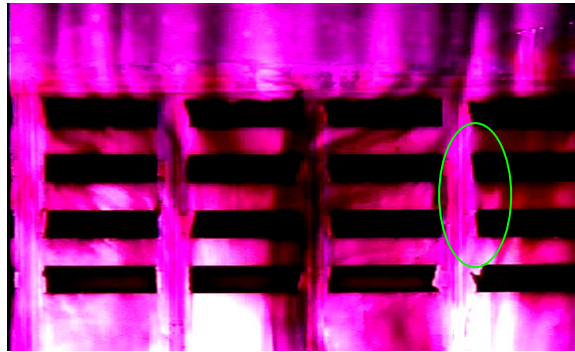
(10b)



(11b)



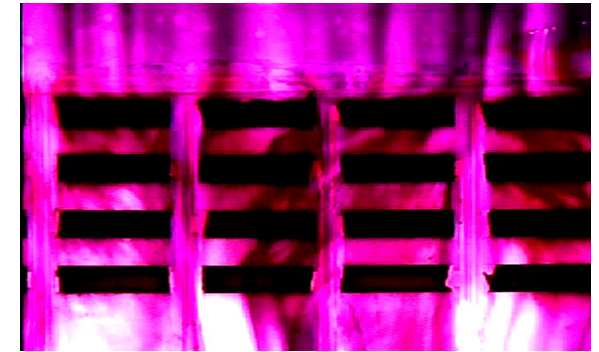
(12b)



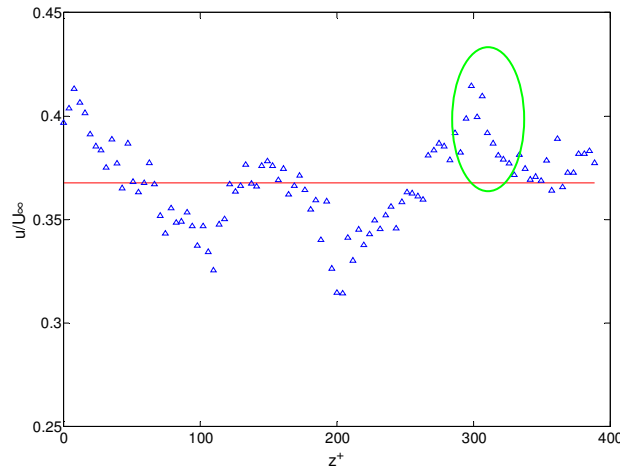
(13a)
 $t = 12/24 T$



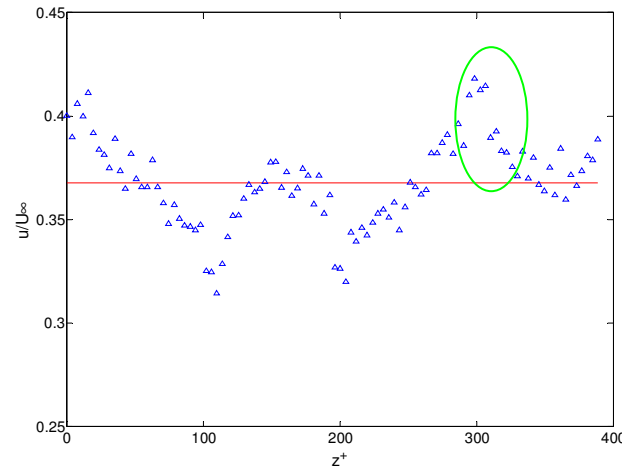
(14a)
 $t = 13/24 T$



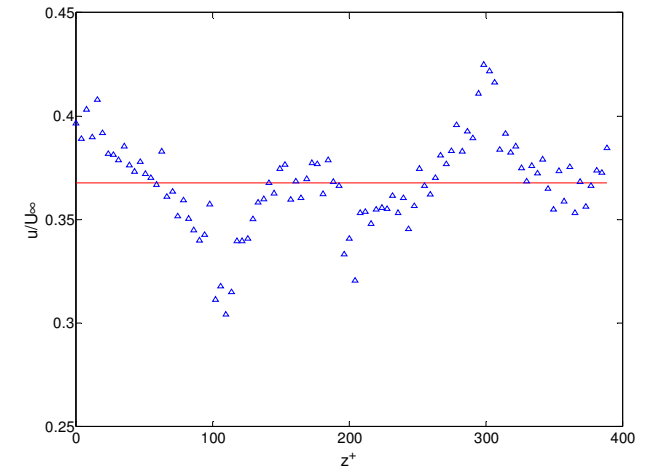
(15a)
 $t = 14/24 T$



(13b)



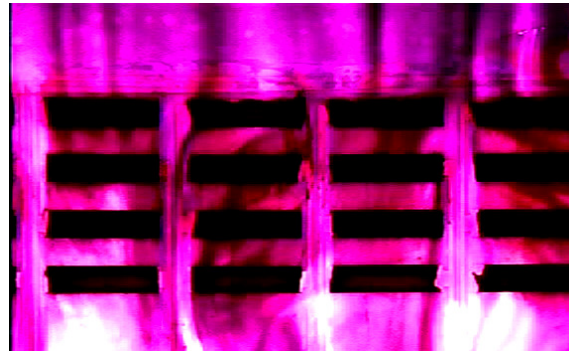
(14b)



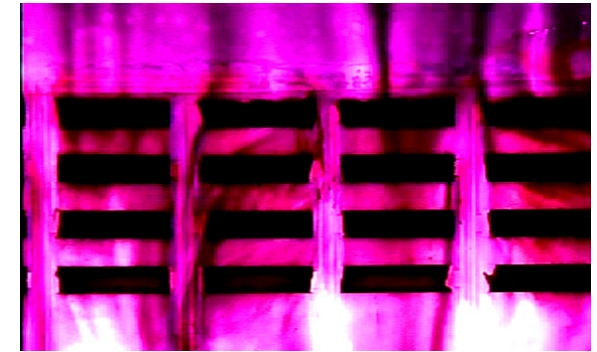
(15b)



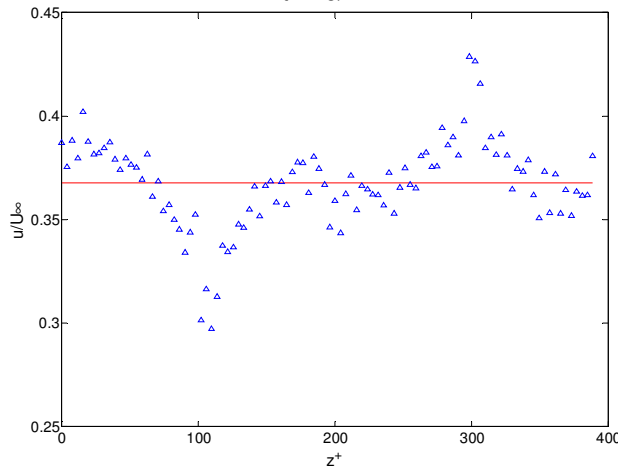
(16a)

 $t = 15/24 T$ 

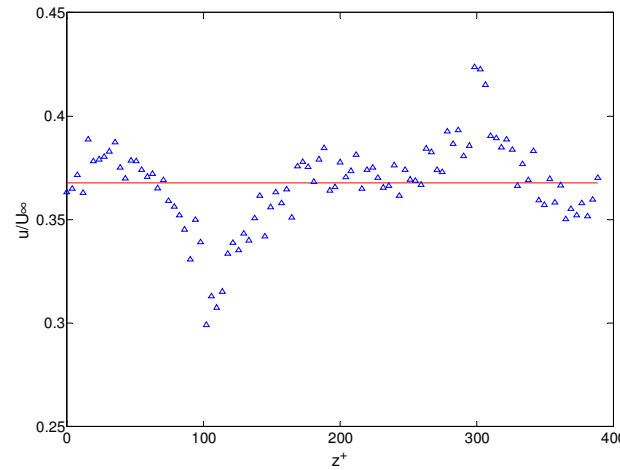
(17a)

 $t = 16/24 T$ 

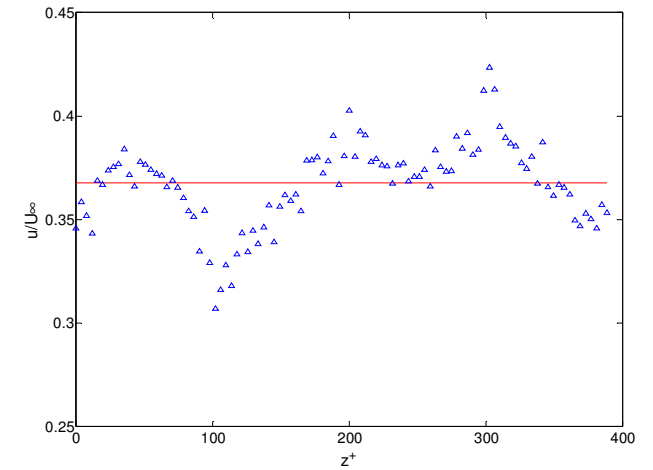
(18a)

 $t = 17/24 T$ 

(16b)



(17b)



(18b)

Figure 4.4.5 (a) Flow visualisation with flow (Top view). Flow direction from top to bottom; (b) Velocity (u component) distribution along z^+ . Velocity is measured at $y^+ \approx 7$. The figures and pictures are aligned in the spanwise direction (Z). $T^+ = 42$ and $St = 232$. The video is shown in the attached CD.

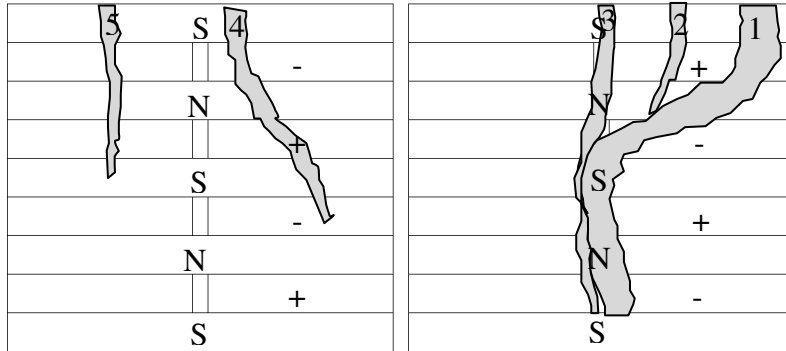
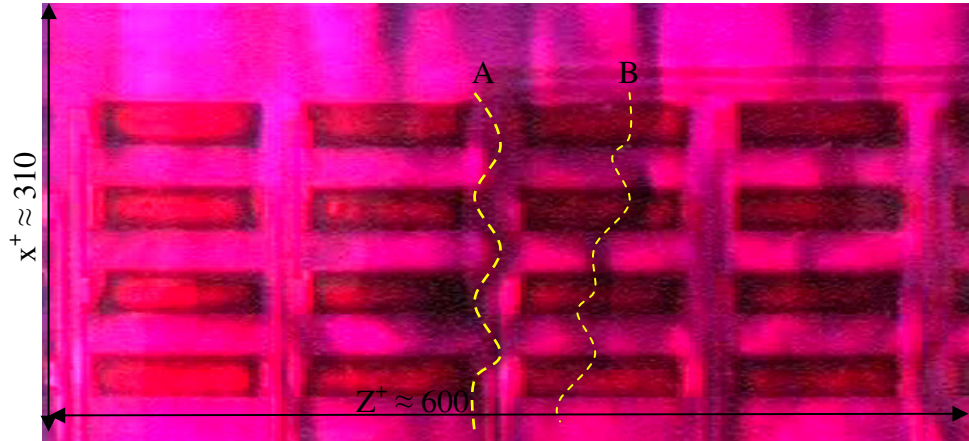
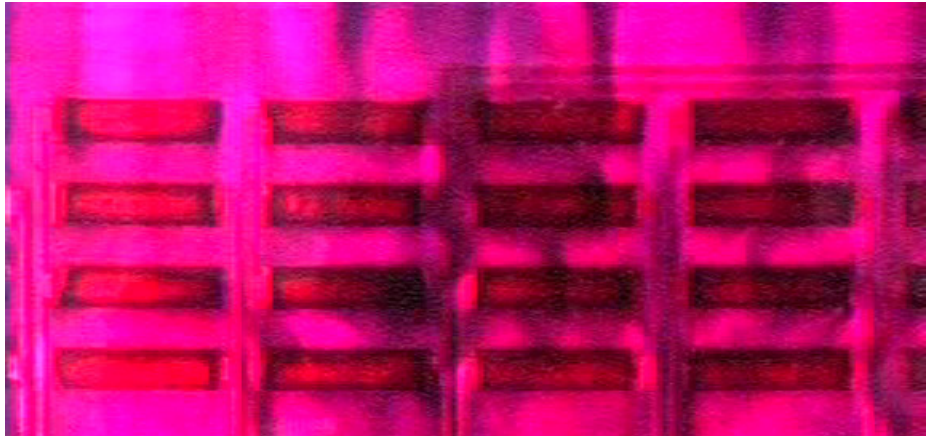


Figure 4.4.6. The spanwise travelling wave actuation in the drag reducing case.

‘N’ denotes the North magnetic pole and ‘S’ denotes the South pole; ‘+’ denotes the electrode positively activated and ‘-’ denotes the negatively activated electrode. Grey bands denote the low-speed streaks.



(a)



(b)

Figure 4.4.7 Flow visualisation of spanwise travelling wave excitation at condition of $T = 0.77s$, $T^+ = 17$ and $St = 232$. $DR = -22.8\%$. Flow direction is from the top to the bottom.

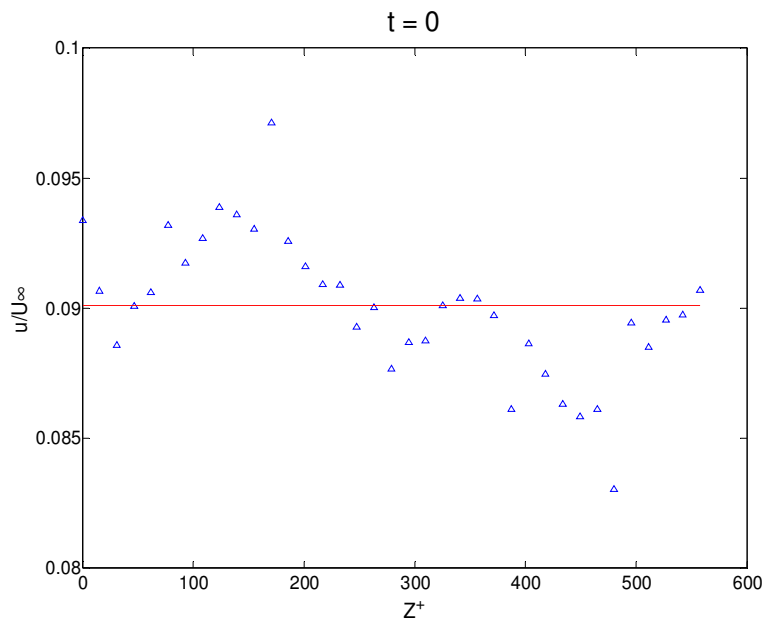


Figure 4.4.8. Velocity (u component) distributions along z^+ of spanwise travelling wave excitation in the drag reducing case of $T^+ = 17$ and $St = 232$.

$DR = -22.8\%$. Velocity is measured at $y^+ \approx 7$.

Chapter 5

Effects of Travelling Wave on the Turbulent Boundary Layer

5.1. Introduction

The turbulent boundary layer profiles have been studied at various experimental conditions with and without the travelling wave actuations. The travelling wave excitation parameters are set at the following conditions, which are the total currents applied to the actuators, $I = 0.6\text{A}$, 0.8A and 1.0A , corresponding to $St = 139.2$, 186 and 232 ; the timing periods, $T = 0.77\text{s}$, 1.99s and 4.02s , corresponding to the non-dimensional time, $T^+ = Tu^{*2}/\nu = 17$, 42 and 82 . Most of the measurements are taken 5 mm downstream of the Electric-Magnetic (EM) actuators as shown in figure 3.6.1

The free-stream velocity, U_∞ , is set at 0.10m/s and the water depth, from the test-plate surface to the water surface, is 130 mm , so that the flow is deep enough to contain the entire turbulent boundary layer thickness, and the turbulent intensity in the free-stream is about 0.5% . At the measurement position the boundary layer thickness, δ , is 89mm . The Reynolds number based on the boundary layer thickness and the friction velocity $Re_\tau = u_\tau\delta/\nu$ is 388 .

The results show that the spanwise travelling wave forcing can reduce or increase the skin-friction drag depending on the operating conditions which offers flexibility for flow control. The maximum of 30% drag reduction and 22.8% drag increase have been achieved.

5.2. Skin Friction Measurement and Wall Positioning

There are several techniques that can be used to measure the wall shear stress as seen in a review by Winter (1977). The near wall velocity gradient (Andreopoulos, 1984) is used to obtain the skin friction in the present experiment. This technique relies on the measurement of the velocities within the viscous sublayer ($y^+ < 5$), where the velocity distribution is linear ($u^+ = y^+$). By definition:

$$\tau_w = \mu \left. \frac{\partial U}{\partial y} \right|_0 \quad (5.2.1)$$

Thus, the wall shear stress τ_w can be determined from the near-wall velocity gradient. Although there is the wall effect on the hot-wire measurement in a wind tunnel (Bruun, 1995), there is no similar effects found in the present experiment in the open water channel. This might be due to the higher heat-conductivity of the water and the low over-heat ratio of the hot-film sensor (Pang and Choi 2004). Figure 5.2.1 illustrates the near wall velocity profile.

Hutchins and Choi (2002) developed a technique in wind tunnels to position the hot-wire probe more accurately via placing one prong of the hot-wire sensor against the wall. However in the water channel, it turns out that the linear velocity gradient near the wall can be achieved more easily due to the lack of ‘wall-effects’. The exact position of the sensor is decided by extending the velocity gradient in the viscous sublayer to the wall where the velocity is zero. The friction velocity u_τ and skin-friction coefficient c_f are then calculated from the velocity gradient within this region from the equations 5.2.2 and 5.2.3:

$$u_\tau = \sqrt{\frac{\tau_w}{\rho}} = \sqrt{v \frac{dU}{dy}} \quad (5.2.2)$$

$$c_f = \frac{\tau_w}{\frac{1}{2} \rho U_\infty^2} = 2 \left(\frac{u_\tau}{U_\infty} \right)^2 \quad (5.2.3)$$

The wall shear stress for the developed flow can also be determined by the Clauser-plot method (Clauser, 1954), which is based on the assumption of the existence of a universal logarithmic region in a constant pressure turbulent boundary layer flow. Here, the section of the velocity profile described by the Prandtl's law of the wall (the inner flow region) overlaps von Karman's velocity-defect law (the outer law, or core, or region). This overlap region can be represented in terms of the inner-scaled and outer-scaled variables. Respectively, by

$$U^+ = \frac{1}{k} \ln y^+ + A \quad (5.2.4)$$

and

$$\frac{U - U_0}{u_\tau} = -\frac{1}{k} \ln \eta + B \quad (5.2.5)$$

$$\eta = y / \delta \quad (5.2.6)$$

where A and k are universal constants, and B is dependent on the large-scale flow geometry. Because equations 5.2.4 and 5.2.5 must be valid simultaneously in the outer layer (core region for pipe flow), we can get

$$\frac{U_0}{u_\tau} = -\frac{1}{k} \ln \text{Re}_\tau + A - B \quad (5.2.7)$$

Accordingly, the friction velocity can be obtained.

The friction velocity measured using the near-wall gradient technique is within 5% of the difference from the Clauser plot method (Jukes, 2007).

A reduction in the near-wall velocity gradient thus constitutes a reduction in the skin-friction drag. The amount of drag reduction is defined such that a positive quantity implies that the drag has been reduced:

$$D.R. = \frac{c_f - c_{f0}}{c_{f0}} . \quad (5.2.8)$$

The skin-friction drag reductions in percentage are shown in figure 5.2.2, against different $St = 139.2, 186, \text{ and } 232$. As this figure shows, the maximum drag reduction is 30%, which agrees well with Du et al. (2002), but up to 22.8% drag increase is also achieved at $T^+ = 17$ and $St = 232$. The drag increase was also observed in a large-scale control strategy (Schoppa and Hussain 1998) and the numerical simulations of the spanwise travelling wave (Du et al 2002). It also indicates that when the St number is fixed, the drag reduction ratio is increased with increased T^+ until T^+ reaches a critical value. After that the drag reduction seems to keep constant during this experimental study.

Meanwhile, in Fig 5.2.3 the skin-friction drag reduction verses T^+ is presented. It is clearly shown that for a fixed value of T^+ , the stronger the Lorentz force is (which means higher St number), the bigger effect the spanwise travelling wave puts on. However, this may result in either drag increase or reduction. There seems to be a critical St number, which is 232 in this study. When the force increases above this critical St number, dramatic drag reduction (or increase) is achieved.

5.3. Boundary Layer Velocity Profiles

Mean streamwise velocity profiles of the boundary layers for both drag reducing and increasing cases are shown in figure 5.3.1. It shows that the spanwise travelling wave forcing only affects the velocity profile within $y/\delta \leq 0.8$, which means the boundary layer thickness is not affected. Mean velocity profiles in the log law plot are also shown in figure 5.3.2, where both u^+ and y^+ are non-dimensionalised using friction velocity. For the drag reducing case where $T^+ = 82$ and $St = 186$, the logarithmic velocity profile is shifted upwards, suggesting that the viscous sublayer is thickened as a result of the skin-friction reduction. For the drag-increasing case, the logarithmic velocity profile is shifted downwards. Surprisingly, for both the drag-increasing and the drag-decreasing cases, the turbulence intensity profiles show significant reductions across the entire region of the turbulent boundary layer as shown in figure 5.3.3 in spite of the fact that Lorentz forces only act in the near-wall region. The similar trend is also found in the Lorentz-forcing spanwise oscillation in both DNS results of Berger et al (2000) and experimental results (Pang & Choi 2004; Xu & Choi 2008). Furthermore, the experimental results by Laadhari et al. (1994), Choi et al. (1998), and the numerical data by Jung et al. (1992) and Baron and Quadrio (1996) present similar behaviour showing the reductions in the turbulence intensities in all three components of the turbulent boundary layers with the spanwise-wall oscillation. This indicates that the spanwise travelling wave flow control has a global effect on the turbulent boundary layer although the force is only applied to the near-wall region.

Figure 5.3.4 and 5.3.5 show the inner-scaled mean velocity profiles and turbulent intensity profiles for different drag reducing cases in the near-wall region. It shows the largest streamwise velocity fluctuation amplitudes occur at $y^+ \approx 13$ in the no-control case, which is also observed by Bakewell (1966) and Kreplin (1973). The results suggest that the more skin-friction drag is reduced, the more the logarithmic velocity region is shifted up and the more turbulent intensity is reduced.

Figure 5.3.6 shows the skewness of the velocity fluctuations for the drag-reducing and canonical cases. The data in the canonical case are positively skewed for $y^+ < 13$ which is consistent with the previous zero-pressure gradient boundary layer studies (Ueda and Hinze, 1975; Simpson et al. 1981). For the drag-reducing condition ($T^+ = 42$ and $St = 232$), the skewness is increased in the near-wall region especially when $y^+ < 14$. It means the positive values of u' occur more frequently in this region (Simpson et al. 1981). This is consistent with other drag-reducing experiments (Pang & Choi 2004; Choi, et al. 1998; Baron & Quadrio 1996; and Quadrio & Sibilla 2000). The skewness value becomes zero in the drag-reducing case around $y^+ \approx 13$. It suggests there still are coherent structures in the drag-reducing flow, which is indicated by the change in sign of the skewness factor (Nagano and Tagawa, 1987). The probability density distribution is symmetric at this distance from the wall, but is not Gaussianly distributed. A Gaussian distribution has a flatness factor of 3 and is not skewed. At $y^+ \approx 13$, only the latter is fulfilled (Schraub and Kline 1965).

The kurtosis values of the drag-reducing case are increased as is shown in figure 5.3.7. The increased kurtosis means that the probability distribution of

the velocity fluctuations is much sharper in the drag-reducing case (Gad-el-Hak and Bandyopadhyay, 1994). The increasing skewness and kurtosis of velocity fluctuations suggest the turbulent activities have been modified by the spanwise travelling wave actuation. The similar results are observed in other drag-reducing experiments, for example, Lorentz-forcing spanwise oscillation (Pang and Choi 2004), and spanwise-wall oscillation (Choi, DeBisschop et al. 1998; Baron and Quadrio 1996; Quadrio and Sibilla 2000).

Figure 5.3.8 shows the inner-scaled mean velocity profiles for drag-increasing cases. It indicates that profiles shift down more with an increased drag ratio. As shown in figure 5.3.9, the turbulent intensity profiles for the drag-increasing cases are decreased for $y^+ > 6$, which indicates that the turbulent activities have been weakened even at the drag-increasing conditions. Similar results were found by Crawford and Karniadakis (1997), skin friction increases whereas the turbulence intensity is reduced.

Figure 5.3.10 shows the skewness profiles for the drag-increasing case ($T^+ = 17$ and $St = 232$). When $y^+ < 6$, the skewness is decreased; while for $y^+ > 6$, it is increased as the drag-reducing case. The reduced skewness is opposite to the increased ones observed in the drag-reducing case. There seems to be other structures or activities induced by the spanwise travelling wave. A similar trend is also found for the kurtosis shown in figure 5.3.11, where the kurtosis of the drag-increasing case hasn't been changed when $y^+ < 6$, but the value is increased at the region of $y^+ > 6$.

The results above show that the turbulent activities above $y^+ = 6$ have been weakened in the drag-increasing case. It is suggested that the drag increase is due to the effects of the spanwise travelling wave in the viscous sublayer.

5.4. Energy Spectra and Probability Density Function

The following section will focus on a better understanding of how the spanwise travelling wave alters the turbulence structures by analysing the data at key spatial positions in the boundary layer. Analyse has been undertaken at $y^+ = 5, 12, \text{ and } 20$. Both the probability density function (PDF) and the energy spectra with and without travelling wave for the drag-reducing and the drag-increasing cases will be presented at each location.

The goal of spectral estimation is to describe the distribution (over frequency) of the power contained in a signal, based on a finite set of data. The power spectrum of a stationary random process is mathematically related to the correlation sequence by the discrete-time Fourier transform. Welch's averaged and modified periodogram method is used to estimate the Power Spectral Density of the velocity fluctuation signals. The velocity fluctuation signal is divided into the overlapping sections, each of which is windowed by the Hanning window parameter, then zero-padded to a length of 1024. A data size of 120000 points at a sampling frequency of 100 Hz is long enough to avoid the leakage. Similar parameters are also used by Pang (2005) and Jukes (2007).

Figure 5.4.1 shows the energy spectra for the drag-reducing case ($T^+ = 42$ and $St = 232$). The spectra show that due to the spanwise travelling wave actuation, there is an energy transfer from the large-scale eddies to the small-scale eddies in the near-wall region. The spanwise travelling wave appears to break down the large-scale turbulence structures near the wall. The similar results are also observed by Pang (2005) and Jukes (2007).

The energy spectra for the drag-increasing case ($T^+ = 17$ and $St = 232$) are shown in figure 5.4.2. The energy in large-scale structures (low frequency) is slightly decreased at $y^+ = 5$. This is more obvious in the area further away from the wall, $y^+ = 12$ and 20 (figure 5.4.2b and c).

The probability density functions (PDF) of the u -component velocity fluctuations are shown in figure 5.4.3 and figure 5.4.4 for the drag-reducing and drag-increasing cases, where the fluctuations have been normalised by their own standard deviation. For the drag-reducing case, the PDF in the viscous sublayer (figure. 5.4.3a) shows a slightly positive skewing and narrowing, reflecting an increase in skewness and kurtosis. This behaviour has also been observed in the boundary layer with spanwise wall and flow oscillation (Choi 2001; Jukes 2007). The PDF at $y^+ = 20$ (figure 5.4.3c) has the most dramatic changes, suggesting that the velocity fluctuations have become more positive and spiky. This is also reflected in a large increase in the skewness and the kurtosis at this location.

Figure 5.4.4 shows PDFs in the drag-increasing case, which again indicates that the turbulent activities only in the area $y^+ > 6$ are weakened similar to the drag-reducing cases. The spanwise travelling wave seems to break down or weaken the large near-wall structures in both of the drag-increasing and the drag-reducing cases. It will be discussed later whether the travelling wave introduces different effects within the viscous sublayer, depending on the operating conditions of the spanwise travelling wave.

In this study, no spiky travelling wave frequency is observed from the power spectrum profiles, which is 1.3 Hz ($T^+ = 17$), 0.50 Hz ($T^+ = 42$) and 0.25 Hz ($T^+ = 82$). The reason could be that the energy contained by the modified

streamwise velocity is very small comparing with other turbulent activities and cannot emerge out.

5.5. Conditionally Sampled Signals – VITA Analysis

Blackwelder and Kaplan (1976) developed a conditional sampling technique of Variable Interval Time Averaging (VITA) to detect coherent turbulent structures in the near wall regions of turbulent boundary layers. A review of this and other conditional sampling techniques is given by Antonia (1981). The technique basically utilises a small temporal window of T_{win} to scan through the signal, and compares the variance of the signal within the window with the variance of the entire data. If this comparison ratio reaches a threshold value an event is detected, corresponding to a turbulent activity of rapidly changing quantity (e.g. velocity) such as sweeps or ejections passing by a sensor. For a velocity signal the local mean, $\hat{u}(t, T_{win})$, of the fluctuating velocity component, $u'(t)$, is defined in equation 5.5.1 (Bruun, 1995):

$$\hat{u}(t, T_{win}) = \frac{1}{T_{win}} \int_{t-1/2T_{win}}^{t+1/2T_{win}} u'(s) ds \quad (5.5.1)$$

where T_{win} is the window length. This is a moving average, where the local mean over a given window length is calculated for every temporal position in the velocity signal. The local variance, $var_t(t, T_{win})$ (VITA variance), is defined by:

$$var_t(t, T_{win}) = \hat{u}^2(t, T_{win}) - [\hat{u}(t, T_{win})]^2 \quad (5.5.2)$$

(i.e. the windowed variance of the signal with respect to the windowed mean).

The variance of the entire signal, $var(t)$, is defined as:

$$var(t) = \lim_{t \rightarrow \infty} \frac{1}{t} \int_0^t u^2(t) dt \quad (5.5.3)$$

The detection criterion is such that if the local variance, $\text{var}_t(t, T_{win})$, is greater than $k \cdot \text{var}(t)$, a VITA event is detected. Here, k is the coefficient and its value is equal to 1 in this study. The smaller the k value is, the more events the VITA detects. However, the above criteria will detect on both a rapid positive change of the velocity signal ($du/dt > 0$, i.e. a sweep event), and a rapid negative change ($du/dt < 0$, i.e. an ejection event). The detector function, $D(t)$, is thus defined as follows in this study:

$$\begin{aligned}
 D(t) &= 1 && \text{if } \text{var}_t(t, T_{win}) > k \cdot \text{var}(t) \text{ and } du/dt > 0 \text{ (sweeps)} \\
 &= -1 && \text{if } \text{var}_t(t, T_{win}) > k \cdot \text{var}(t) \text{ and } du/dt < 0 \text{ (ejections)} \\
 &= 0 && \text{otherwise.}
 \end{aligned} \tag{5.5.4}$$

An averaged VITA event can then be acquired by ensemble averaging all the events detected over a window of size T_{ens} ($T_{ens} > T_{win}$). In this study, the point of detection is defined as the maximum du/dt during each period for which $\text{var}_t(t, T_{win}) > k \cdot \text{var}(u)$. Further to this criterion, it is decided to ignore multiple detections that occur within the window, T_{ens} . This ensures that the ensemble averaged event will only contain contributions due to isolated VITA events. Here, the threshold burst detection is set to equal the entire variance of the velocity fluctuation ($k = 1.0$) averaging over the non-dimensional integral time of $T_{win}^+ = 10$ (based on canonical u_τ). The ensemble window of T_{ens}^+ is set to $= 90$ ($T_{ens}^+ = -30$ to 60). These parameters are selected so that the accuracy can be satisfied but no long computing time is required.

Figure 5.5.1 illustrates the VITA averaging program. The u -velocity fluctuation component at $y^+ = 12$ is shown on the top of the plot. The local variance is shown in figure 5.5.1(b), along with the threshold detection level

indicated by the green straight line. Figure 5.5.1(c) shows the detection function, $D(t)$, and the detection function after multiple events have been removed. The ensemble averaged VITA event corresponding to the entire signal is shown in figure 5.5.2.

In the near-wall region ($y^+ \leq 20$), the majority of the events are associated with positive du/dt (sweeps) as can be seen by the number of VITA events in figure 5.5.2. The negative du/dt events (ejections) frequently occur in groups such as hairpin packets as described by Adrian *et al.* (2000) as well. However, the sweep events are shown only in this study, because they are responsible for the majority of the skin-friction drag (Orlandi and Jimenez, 1994) and take place more frequently than the ejection events.

Fig 5.5.3 and figure 5.5.4 show the conditionally sampled signatures of the near-wall burst signals with and without Lorentz-forcing spanwise-travelling-wave excitation using the VITA technique (Blackwelder and Kaplan 1976; Antonia 1981) at $y^+=5$, $y^+=12$ and $y^+=20$ respectively.

Figure 5.5.3 shows the results for the drag-reducing case. The changes in the sweep signature are clear in the near-wall region of the boundary layer, especially $y^+=5$, where the burst duration has been reduced to about half of that without control. The intensity of the near-wall sweeps (peak to peak value of the fluctuations) are also reduced by 40% at $y^+ = 5$, suggesting that the Lorentz-forcing travelling wave is effective at diminishing the near-wall sweeps, and hence enabling drag reduction. At $y^+ = 12$ (Fig 5.5.3(b)), the effects of the travelling Lorentz forces on the sweeps are still strong, where the sweep duration is reduced by about 28% and the sweep intensity is reduced by 38%. At $y^+ = 20$, the effect of the Lorentz forcing to the sweeps is less, but we

can still see about 18% reduction in the duration and 30% reduction in the intensity. Similar observations were also found by Pang's study (Pang and Choi 2004) on the Lorentz-forcing spanwise oscillation and Choi et al. (Choi and Clayton 2001) in the spanwise-wall oscillation.

In the drag-increasing cases, it is observed (see Fig. 5.5.4) that the travelling wave causes a large reduction in sweep intensity in the buffer layer. For $y^+ = 12$ and 20, for example, the intensities of sweeps have been decreased by around 50%. However, within the viscous sublayer at $y^+ = 5$, the intensity of sweeps for the drag-increasing case is nearly the same as that for the no-control case and the duration of the sweep events is increased by about 23%, which is comparable with the 22.8% of drag increase. This is strong evidence to indicate that sweep events, especially in the viscous sublayer, are responsible for producing most of the skin-friction drag. The increased duration is also observed for $y^+ = 12$ in the drag-increasing case, but the duration seems to have no changes at $y^+ = 20$.

The induced spanwise motions caused by the spanwise travelling wave appear to cause premature sweep events in the drag-reducing case, as also observed for riblets by Choi (1989). In other words, the streamwise vorticity induced by spanwise travelling wave interrupts the turbulence regeneration cycle and hence affects the turbulent activities such as disrupting or cancelling the quasi-streamwise vortices responsible for the sweep motion of high-momentum fluids towards the wall. Furthermore, the behaviour of the induced streamwise vorticity decides the results of the skin-friction drag, which leads to either drag increase or drag decrease.

5.6. Spanwise Two-point Correlation of u Velocity

Spanwise two-point correlation of u-component velocity is presented as a function of Δz^+ in figure 5.6.1 for the drag-reducing case, which is measured at $y^+ = 9$. More precisely, it is the fluctuation velocity that is used to do the correlation calculation. The correlation for the canonical case (without control) shows a broad minimum at $\Delta z^+ \approx 50$, indicating a mean streak spacing of 100. The correlation coefficient is close to zero for $\Delta z^+ > 100$. This results agree well with other experiments and simulations at low Reynolds numbers, see Kline et al. (1967), Kreplin and Eckelmann (1979), Smith and Metzler (1983), Kim et al. (1987) and Moser et al. (1999). For the drag-reducing case, the minimum value is at $\Delta z^+ \approx 70$ (shown in figure 5.6.1.a) when a negative force is applied, reflecting the increased streak spacing. At phase 2 when no force is applied, the broad minimum of the correlation coefficient is reduced slightly, indicating less drag reduction. At phase 3 when the positive force is applied, the broad minimum occurs at $\Delta z^+ \approx 70$, showing the increased streak spacing and the flow achieving higher drag reduction again. The similar trend is found in other drag-reducing flows (such as Lee and Choi 2001; Iuso et al 2003 and Li et al. 2004). At phase 4, when the flow reaches the minimum drag reduction, the correlation coefficient shows the minimum value of $\Delta z^+ \approx 60$, very close to the canonical case.

Figure 5.6.2 shows the spanwise two-point correlation of u-component velocity for the drag-increasing case at $y^+ = 9$ as a function of Δz^+ . It shows the similar trend with that of the drag-reduction case, although the Δz^+ of broad minimum is less than the one of the drag-reducing case in each corresponding phase. It again suggests the travelling wave weakens or

modifies the near-wall turbulent activities in the buffer layer and above in both of the drag-reducing and drag-increasing cases.

5.7. Phase-Averaged Skin-friction Drag, Momentum and Correlations

To investigate the effects of Lorentz forces on the local skin-friction drag, changes in drag reduction at each phase of actuation are plotted in figure 5.7.2 and 5.7.3 for the drag-increasing and drag-reducing cases. The forcing profile with time is shown in figure 5.7.1. It shows that the drag becomes less when the negative force is applied for both of the drag-increasing and drag-reducing cases. It should be noted there is about $t = 0.1T$ of phase lag, since the velocity is measured 5 mm downstream of the actuators. This timing delay was estimated with a convection velocity of $13u_\tau \pm 2 u_\tau$. Rebbeck and Choi (2006) gave the convection velocity of about $14 u_\tau$ for $y^+ < 25$; Kreplin et al. (1979) found coherent structures convected at a velocity of $12.1u_\tau$; Johansson et al. (1986) obtained the convection velocity to be nearly constant ($\approx 13u_\tau$) up to $y^+ \approx 30$. With the VISA method and the observation of high variance detected at $y^+ = 15$ moved through the flow region, Johansson et al. (1991) found this convection velocity was $10.6u_\tau$ with a standard deviation of $\pm 1 u_\tau$.

The main differences between the drag-increasing case and the drag-reducing one are found during the phases without forcing. For the drag-increasing case (Figure 5.7.2), the drag changes with time are close to a sinusoidal profile. Basically, the skin-friction drag only experiences one drag-increasing peak and one drag-reducing one (please note it only means the weaker drag increase, not true drag reduction). It might result from the newly generated streamwise vorticity by the Lorentz-forcing in the drag-increasing cases as

shown in figure 5.7.4 where the dash and solid circles indicate the streamwise vorticity maintained by the inertial effects and the Lorentz forcing, respectively. The mechanism of the generation of streamwise vorticity by Lorentz forcing is discussed later in this section. At phase 1 (figure 5.7.4a), the high-speed fluid moves away from the detection point due to the introduced streamwise vorticity. And this moving-away action is going further in phase 2 (figure 5.7.4b) when the streamwise vorticity is maintained by the inertial effects. When coming into phase 3 (figure 5.7.4c), a new streamwise vorticity of the opposite direction is generated by the Lorentz forcing. High-speed fluid is approaching the detection point and the skin friction is increased. This increase finally reaches the maximum at the end of phase 4 (figure 5.7.4d).

For the drag-reducing case (Figure 5.7.3), there is a drag increase (less drag-reducing) occurring between $t = 0.3T$ and $t = 0.55T$, which corresponds to the period of $t = 0.25T$ to $t = 0.5T$ when no forcing is applied. It suggests that the effect by the previous Lorentz force is getting weaker during this no-forcing period. Please note that the increased drag here is still less than the mean-value of reduced drag. At the end of the positive forcing stage, the drags of both the drag-increasing and drag-decreasing cases are increased due to the strong downward motion of high momentum fluid.

For further investigation of the changes of skin-friction drag in different phases of forcing, a correlation between the drag and the momentum of fluid is calculated by function (5.7.1).

$$R_{MC_f} = \int_0^{T^+} \frac{M'(t^+) \bullet C_f'(t^+)}{\sqrt{(M'(t^+))^2} \sqrt{(C_f'(t^+))^2}} dt^+ \quad (5.7.1)$$

Here, R_{MCF} is the correlation coefficient; M' is the phase-averaged momentum fluctuation and C_f' is the phase-averaged skin-friction coefficient fluctuation.

The phase-averaged momentum is calculated by function (5.7.2);

$$M(t^+) = \int_{y_0^+}^{y^+} u^+(t^+) \times u^+(t^+) \times dy^+ \quad (5.7.2)$$

$$M'(t^+) = M(t^+) - \bar{M} \quad (5.7.3)$$

$$\bar{M} = \frac{\sum M(t^+)}{\sum t^+} \quad (5.7.4)$$

The correlation coefficient of R_{MCF} is plotted as a function of y^+ in figure 5.7.5 and figure 5.7.6 for the drag-increasing case and the drag-reducing one, respectively. For the drag-increasing case, figure 5.7.5 shows good correlation for all near-wall region apart from the region between $y^+ = 8$ and 10. The results seem to show that there is a ‘barrier’ within the region around $y^+ = 8$ and 10, which is comparable with the current Lorentz force effective region $\Delta^+ \approx 7$. The results corresponds well to the other turbulence statistics especially for the VITA results that show the intensities of the sweep events do not change at $y^+ = 5$ but are significantly reduced after $y^+ = 12$. For the drag-reducing case, it appears that the phase-averaged momentum and the skin-friction are correlated well in most of the near-wall region. The small deviation close to the wall might result from the phase differences between the skin friction drag and the streamwise velocity. It was also found by Du et al. (2002) that there is a phase difference between the external Lorentz force and the filtered streak curve, and a phase difference between the drag force and the excitation force as well especially.

For a better comparison, figure 5.7.7 and figure 5.7.8 are plotted to show the phase-averaged skin-friction factor, C_f .

Figure 5.7.9 shows the phase-averaged momentum profiles for the drag-reducing case where there are significant momentum changes during the cycle near the wall. In the region of $y^+ \leq 2.5$ the low momentum region spreads out in the whole period, resulting from the Lorentz forcing. The travelling wave broadens the low-speed streaks in the spanwise direction under drag-reducing conditions. The local low momentum appears during $t = 0.2T$ to $0.8T$ in the viscous sublayer below $y^+ = 6$, which agrees well with the low phase-averaged drag shown in figure 5.7.8. The low-momentum fluid seems to come from the transportation of low-speed streaks by the Lorentz forcing. For example at $y^+ = 3$ the momentum becomes locally less from $t = 0.1T$ to $t = 0.4T$, which appears to be the introduction of low-speed fluid from underneath and sides by the introduction of streamwise vorticity owing to the travelling wave. This result tallies with the observations from flow visualisations where the low-speed streaks are twisted and propelled from nearby regions into the detection point. Between $0.4T$ and $0.8T$, the momentum increases a little and then decreases, which is accordant with the drag history. The increase during this period is more significant around $y^+ = 5$ where the high momentum is brought downwash when t is between $0.45T$ and $0.55T$. It could be explained by the findings of the flow visualisation and the spanwise distribution of u velocities where there is high-speed fluid moving downward as a result of mass continuity. Figure 5.7.9 also shows that the momentum in the drag reducing case is lower than the no-control case in most of the region of $y^+ < 12$.

The phase-averaged momentum map for the drag-increasing case is shown in figure 5.7.10 where the momentum distribution appears more trenchant than the drag-reducing case and seems to be well regulated. It shows that the momentum is much higher within the region of $y^+ \leq 7$. The locally low momentum appears around $t/T = 0.6$, which agrees well with the position where locally low drag is found in the skin-friction history shown in figure 5.7.7. It could be argued that the Lorentz forcing induces streamwise vorticity layers and increases the duration of high-momentum downwash motions as to increase the skin-friction drag. This high-momentum downwash motion takes around $t^+ = 23$ from the VITA analysis when the motion is treated as a ‘sweep’ event. The Lorentz-forcing time for a cycle in the drag-increasing case is only $T^+ = 17$, similar to the sweep duration.

According to this study, the inertial effects might play an important role in introducing new streamwise vorticity. Through the combination of inertial effects and Lorentz forcing, a sequence of streamwise vortices are produced which can explain the reason of drag increases. Figure 5.7.11 illustrates the 2-D conceptual model of the induced motions by the Lorentz-forcing spanwise travelling excitation for the drag-increasing cases. It is arranged in a time sequence. In the drag-increasing condition when $T^+ = 17$, the spanwise displacement of the low-speed streak is very small and only local pseudo-spanwise oscillation is formed as is discussed above. When the Lorentz force is applied, the streamwise velocity and vorticity are introduced and the velocity profiles have been studied by different groups such as Berger et al. (2000). As shown in figure 5.7.11a, the clockwise vorticity (vorticity 1) is introduced when there is a leftward force. The assistance of the lift-up of the

low-speed streak moves the streamwise vorticity upward, and when no force is applied it is under the function of inertia effects. Vorticity 1 indicated by dash circle in figure 5.7.11(b) illustrates such vorticity generated by the previous leftward force and being sustained by the inertia effects. With time going on, the rightward force is introduced in phase 3. A new streamwise vorticity, vorticity 2, is created accordingly and the vorticity 1 moves up due to the lift-up movement of the low-speed streak. As seen in figure 5.7.11(c), vorticity 2 intensifies vorticity 1. When time moves to the next phase, vorticity 2 becomes maintained by the inertia effect the same as vorticity 1. When a new travelling wave actuation cycle starts, vorticity 3 is generated and their positions are shown in figure 5.7.11(e). As we can see from the process above, the new streamwise vorticity always tends to intensify the existing one. Therefore, a relatively stable streamwise vorticity layer is possibly formed by pseudo-local-oscillation in the viscous sublayer. By the analysis above, the importance of the non-forcing period is realised. The periods shown in figure 5.7.11(b) and 5.7.11(d) are of great influence because they allow the existing streamwise vorticity to stay longer so that the streamwise vorticity layer and the sequence can sustain. To demonstrate this, figure 5.7.12 is shown. In figure 5.7.12(a) the clockwise streamwise vorticity, vorticity 1, is generated by the leftward force. When entering the next phase, vorticity 1 is weakened by the newly introduced streamwise vorticity, vorticity 2, of opposite sign. Therefore, no streamwise vorticity can stay as long as the ones shown in figure 5.7.11. Actually, figure 5.7.12 shows the concept of the spanwise oscillation. It also confirms that the pseudo-local spanwise oscillation is different from the spanwise oscillation.

Figure 5.7.13 shows the produced streamwise vorticity sheets by the spanwise travelling wave under the drag-increasing conditions. It suggests that the new streamwise vorticity always intensifies the existing one, and therefore the streamwise vorticity layer is self-sustained. This might be the reason that the phase averaged momentum in the drag-increasing case is better regulated than the one in the drag-reducing case. The streamwise vorticity originated by spanwise travelling wave seems to extend the duration of the sweep events and Orlandi and Jimenez (1994) claimed that the sweep events are more important than ejection events in the production of skin-friction drag. It can be argued that the streamwise vorticity layer induced by the pseudo-spanwise oscillation is the reason for the drag increase. Wassen et al. also found that the strong secondary flow is the cause of drag increase in their riblet experiment (Wassen et al. 2008).

5.8. Summary

By utilising the Lorentz-forcing spanwise-travelling-wave actuators, a maximum viscous drag reduction of 30% is achieved in a turbulent boundary layer at the Reynolds number of $Re_\tau = 388$. A maximum drag increase of 22.8% is also obtained when the period of the travelling wave cycle is reduced to $T^+ = 17$.

The experimental results show that the turbulence intensities in both the drag-reducing case and the drag-increasing case are reduced in the whole boundary layer. The higher moments of turbulence statistics like skewness and kurtosis are increased near the wall when $T^+ = 42$, $St=232$ in the drag-reducing case. For the drag-increasing case, however, the skewness and the kurtosis decrease in $y^+ < 6$; while increase in $y^+ > 6$. The turbulent activities above $y^+ \approx 6$ have

been weakened as indicated by the reduction in the turbulent intensities, suggesting that the drag increase is due to the near-wall streamwise vorticity induced by the Lorentz forcing.

The energy spectra in the drag-reducing case ($T^+ = 42$ and $St = 232$) show that there is a transfer of energy from the large-scale eddies to the small-scale eddies in the near wall region ($y^+ \leq 20$). For the drag-increasing case ($T^+ = 17$ and $St = 232$), the energy in the large-scale structures (low frequency energy) is slightly decreased at $y^+ = 6$. Clearer reductions in turbulence energy are found further away from the wall, ($y^+ = 12$ and 20).

In the drag-reducing case ($T^+ = 42$ and $St = 232$), the PDF in the viscous sublayer shows a slightly positive skewing and narrowing ($y^+ = 6$), which also is observed in other drag reducing flows. The PDF at $y^+ = 20$ is more positively skewed and narrowing, suggesting that the velocity fluctuations have become more positive and more spiky. Similar effects are found in the drag-increasing case for $y^+ > 6$. Therefore the spanwise travelling wave appears to break down or weaken the large-scale structures in both cases.

VITA results show that both the intensity and the duration of sweep events decrease in the near wall region of the drag-reducing case. The maximum reduction happens at $y^+ = 5$ where the reductions are 50% of the duration and 40% of the intensity, respectively. Whereas, the intensity of the sweeps is nearly the same as that in the no-control case at $y^+ = 5$ in the drag-increasing cases. The significant increase in the sweep duration happens at $y^+ = 5$ and $y^+ = 12$, although it does not seem to change at $y^+ = 20$. It is speculated that the drag increase might be due to the increased duration of the sweep events.

The spanwise two-point correlations of u-component velocity are presented as a function of Δz^+ for both the drag-reducing case and the drag-increasing one, which is measured at $y^+ = 7$. The correlation for the canonical case shows a broad minimum at $\Delta z^+ \approx 50$, indicating a mean streak spacing of 100. For both drag-reducing and drag-increasing cases, Δz^+ of the broad minimum of the correlation coefficient is reduced when higher drag is achieved. The value increases when less drag is obtained.

It appears that the spanwise travelling wave has a global effect on the turbulent regeneration cycle in spite of its direct effects on the near-wall region. In both drag-reducing and drag-increasing cases, the turbulent activities have been weakened for $y^+ > 6$. By carefully examining the behaviours of both cases, a common feature is that the streaky structures were twisted, similar to that in the spanwise oscillation. A negative spanwise vorticity is proposed by Choi (2001) to explain the drag reduction with spanwise-wall oscillations. It is shown that this negative spanwise vorticity is created as the periodic Stokes layer is tilted in the spanwise direction. This spanwise vorticity acts to hamper the stretching of the quasi-streamwise vortices and reduce the streamwise velocity near the wall. This concept might be applied here to explain the reduced turbulent activities. However, close to the wall, the induced motion by Lorentz-forcing spanwise travelling wave excitation seems to play an important role. The discussion below will focus on this and a scenario is proposed and shown in figure 5.8.1 and 5.8.2 for the drag-reducing case and the drag-increasing one, respectively.

Here, the induced negative forcing phase is recognised as the first phase of the actuation as shown in figure 5.8.1b. Although only the flow motion within one

phase of the actuator is shown in this analysis, it can be extended to the whole cycle for the reason mentioned before.

At phase 1 (for region D-E in figure 5.8.1.b), the negative force starts moving the low-speed region formed by the previous forcing phase as seen in region D-E in figure 5.8.1.a. With time going on, this force is able to pump more low-speed fluid to position D and this low-speed fluid will meet another low-speed region shaped by the previous opposite force as shown in C-D of figure 5.8.1.c and figure 5.8.1.d. This process takes place from $t \approx 0.1T$ to $t \approx 0.35T$ when the drag is reducing. Then the region D-E becomes non-active as shown in figure 5.8.1.e when the second phase starts. The region D-E in figure 5.8.1.d and the region A-B in figure 5.8.1.a. have exactly the same force pattern and should have the same induced flow motions. Region D-E in figure 5.8.1.e and region A-B in figure 5.8.1.b are also similar. Therefore, the description of the second phase can start from A-B in figure 5.8.1.b. During phase 2, the spanwise migration of the low-speed fluid becomes weaker although it is still maintained due to the inertia effects. Accordingly, the drag reduction becomes less. Indeed, the drag is slight increased between $t \approx 0.35T$ and $t \approx 0.6T$ as shown in figure 5.7.8. At phase 3, a positive force is introduced as shown in region A-B in figure 5.8.1.e and region B-C in figure 5.8.1.b. The drag is reduced when this positive force transports the low-speed fluid to the right. With time progressing, there seems to be high-momentum fluid induced by the corporate action of region A-B and B-C in figure 5.8.1.c. Consequently, the impact of high-speed fluid towards the wall increases the skin friction drag. As shown in figure 5.7.8, the drag is similarly reduced and then increased during $t = 0.6T$ and $t = 0.85T$. At the final phase, the inertia effect keeps bringing high-

speed fluid to region C-D as shown in figure 5.8.1.b to figure 5.8.1.d, although this effect is slightly weak.

An alternative, simpler explanation can be given as following. Again starting with phase 1 as shown by D-E in figure 5.8.1.b, the negative force carries the low-speed fluid from the ‘storage’ formed in the previous phase. Later, the low-speed fluid reaches position D and clusters with other low-speed regions in figure 5.8.1.c and figure 5.8.1.d. In the drag-reduction case, the low-speed fluids can be forwarded to the neighbouring electrode area (C-D here), which seems to be the essential condition for achieving drag reduction. In the area around position D and even in some part of region C-D, a new low-speed region (‘ribbon’ or ‘storage’) is formed. Subsequently, this low-speed region acts as the ‘storage’ of low-speed fluid that will be transported further to the left. Here, the low-speed region formed by the positive force has to be mentioned, which is also an important part to achieve drag reduction. Apart from reducing the drag and helping to create the ‘storage’, another additional function of the motions seems to act as a ‘brake’ to stop the other force inducing a new structure and engendering a higher drag. One-direction-forcing travelling wave was studied by Du et al (2002) where only the positive forces were applied; they found a drag increase rather than a drag reduction.

The mechanism for the drag-increasing case is explained in figure 5.8.2, where the high-momentum wall-ward motion (‘sweep’ event) is maintained and extended by the Lorentz-forcing spanwise travelling wave. The following section demonstrates how the wall-ward motion is extended starting from region B-C of figure 5.8.2.b (Phase 3), where a wall-ward motion is introduced by the collective effects of nearby spanwise motions at position A.

This corresponds to $t \approx 0.65 T$ in figure 5.7.7 where the drag starts to increase. In the next phase, the inertia effects still work strongly to maintain the drag increase in area C-D in figure 5.8.2.b and 5.8.2.c. These two phases are shown during $t \approx 0.65T$ to $t \approx 1.15T$ (equivalent to $t \approx 0.15T$) in figure 5.7.7. In the following phases, the downward motion still seems to be maintained, although an ejection induced by the Lorentz forces might have prevented them. During this process, the drag is reduced at $t \approx 0.15T$ to $t \approx 0.65T$ as shown in figure 5.7.7. Before the flow in the downward motion diffuses, the next cycle starts and keeps moving the high-momentum fluid towards the wall. In other words, the drag increase is the net effect of the converging and diverging motions induced by the pseudo-local-oscillation. This net effect is explained by Orlandi and Jimenez (1994), who claimed that the sweep events are more important than the ejection events in the production of the skin-friction drag.

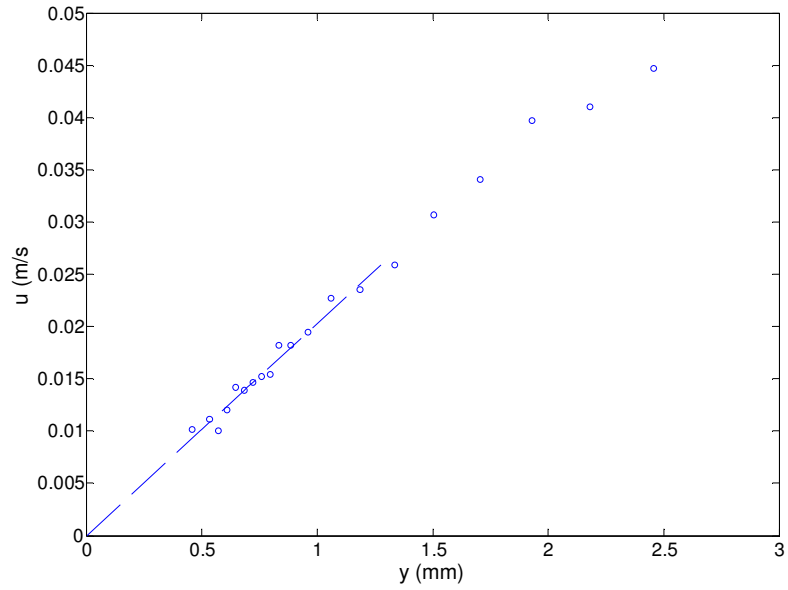


Figure 5.2.1. Near-wall velocity profile. Determination of the hot-film sensor position relative to the wall was achieved by interpolating the mean velocity gradient to wall from the region $y^+ < 5$. The friction velocity, u_τ , and skin-friction coefficient, c_f , were calculated from the slope in this region.

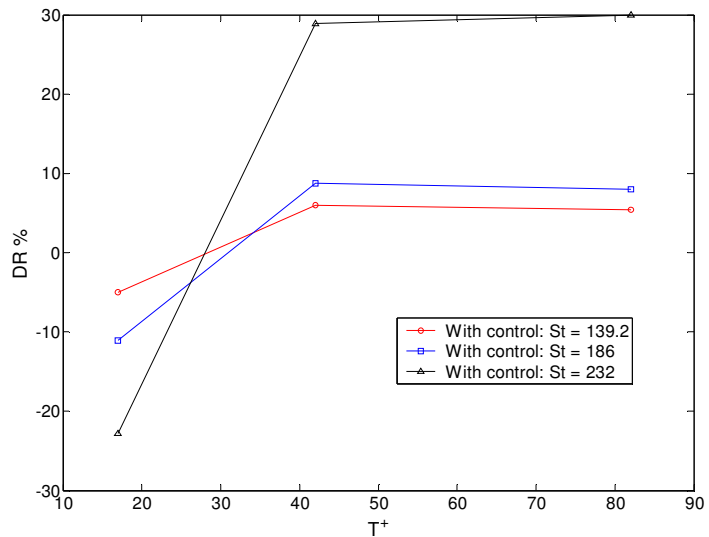


Figure 5.2.2. Skin-friction drag reductions at different T^+ .

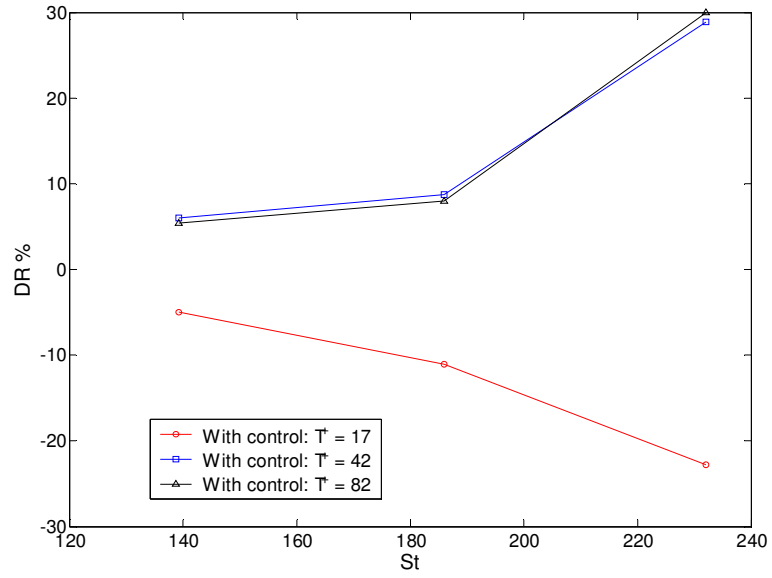


Figure 5.2.3. Skin-frictional drag reductions at different St .

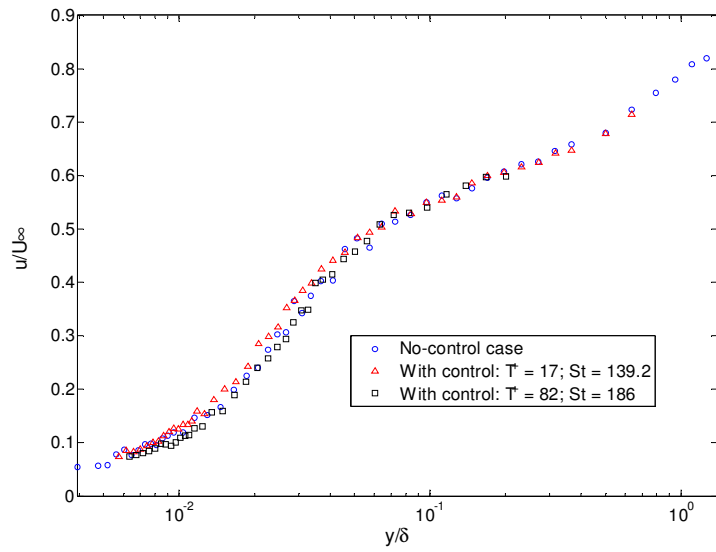


Figure 5.3.1. Mean streamwise velocity profiles for the cases without and with control.

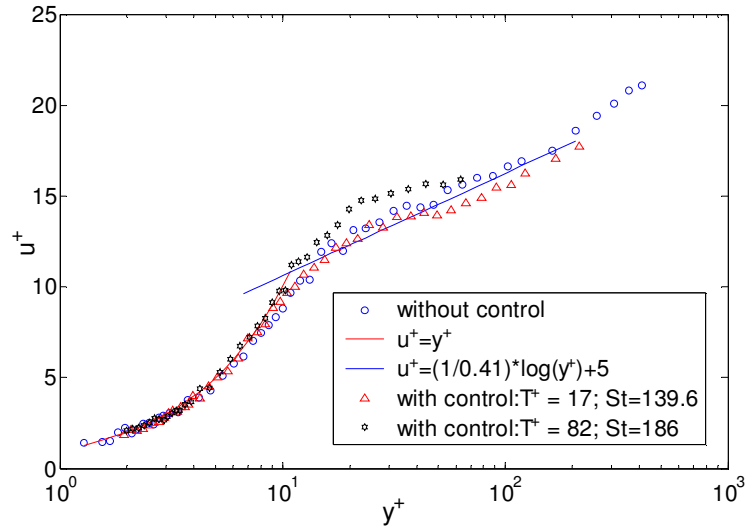


Figure 5.3.2. Inner-scaled mean velocity profiles for the cases without and with control

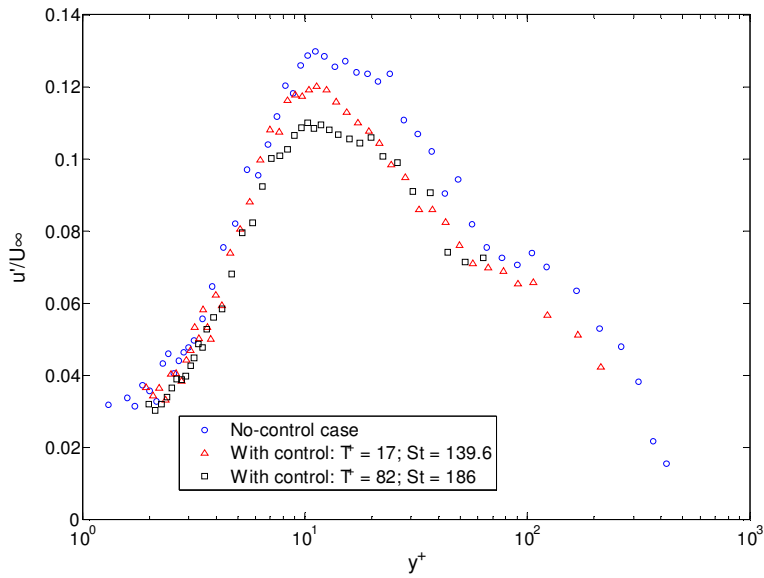


Figure 5.3.3. Inner-scaled turbulent intensity profiles for the cases without and with control.

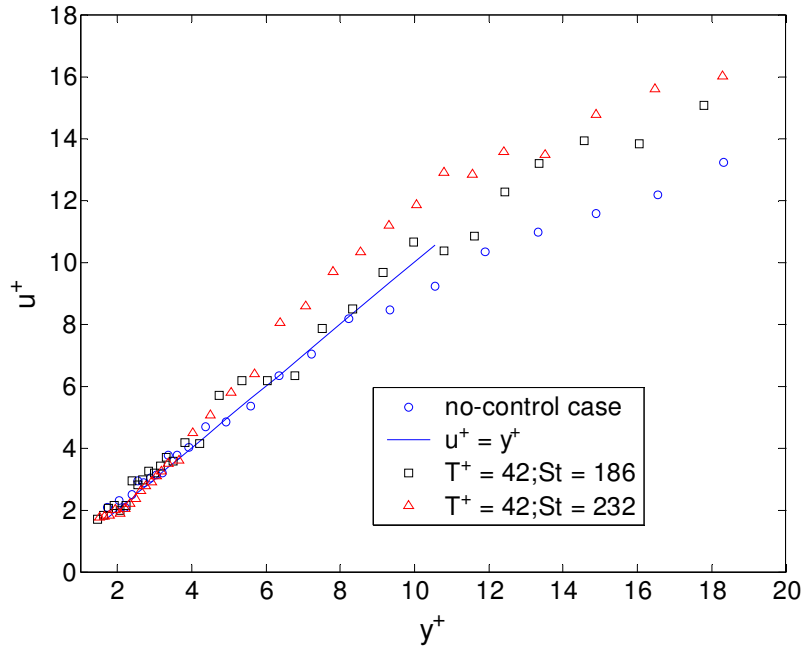


Figure 5.3.4. Inner-scaled mean velocity profiles for cases without and with control at $T^+ = 42$. Drag reducing cases.

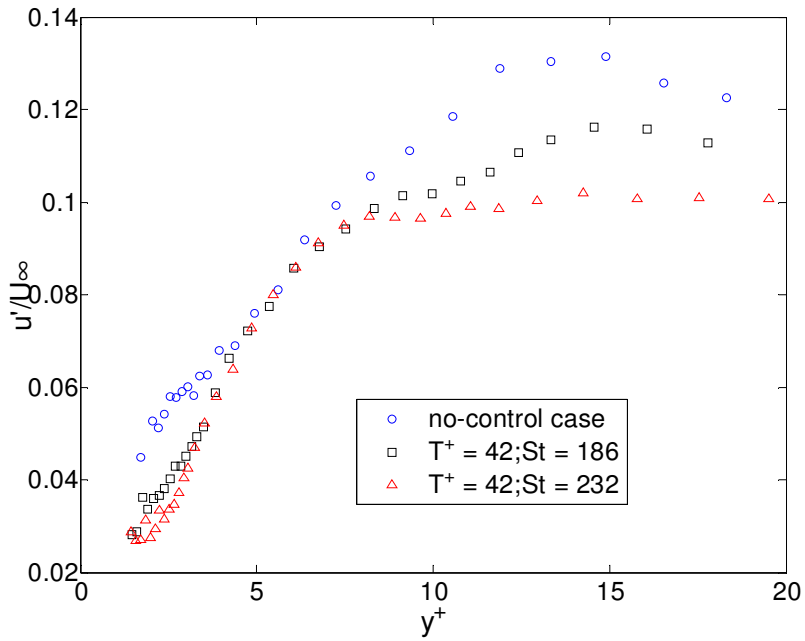


Figure 5.3.5. Inner-scaled turbulent intensity profiles for cases without and with control at $T^+ = 42$. Drag reducing cases.

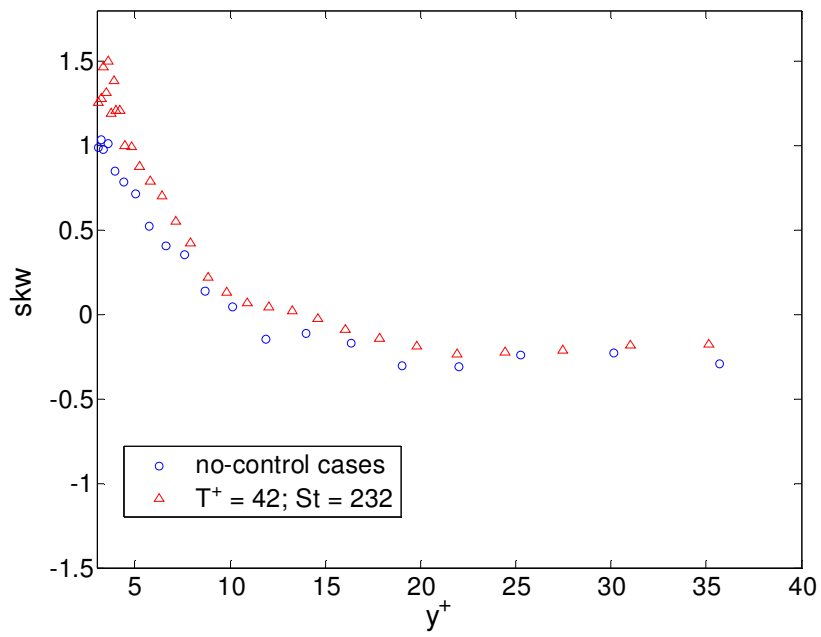


Figure 5.3.6. Skewness profiles for cases without and with control. Travelling wave condition: $T^+ = 42$; $St = 232$. DR = 28.9%

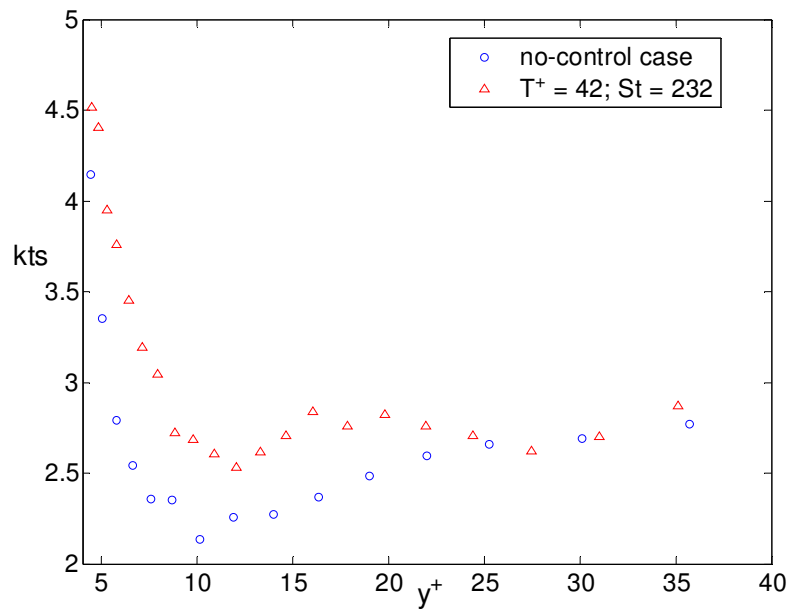


Figure 5.3.7. Kurtosis profiles for cases without and with control. Travelling wave condition: $T^+ = 42$; $St = 232$. DR = 28.9%

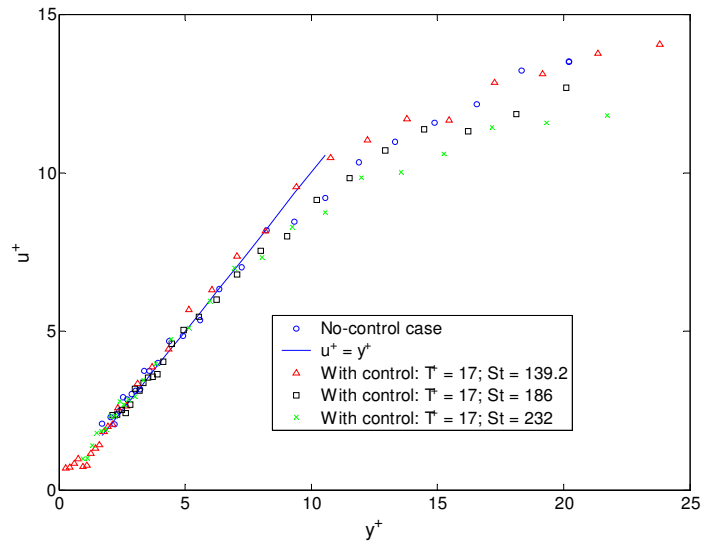


Figure 5.3.8. Inner-scaled mean velocity profiles for cases without and with control at $T^+ = 17$. Drag increasing cases.

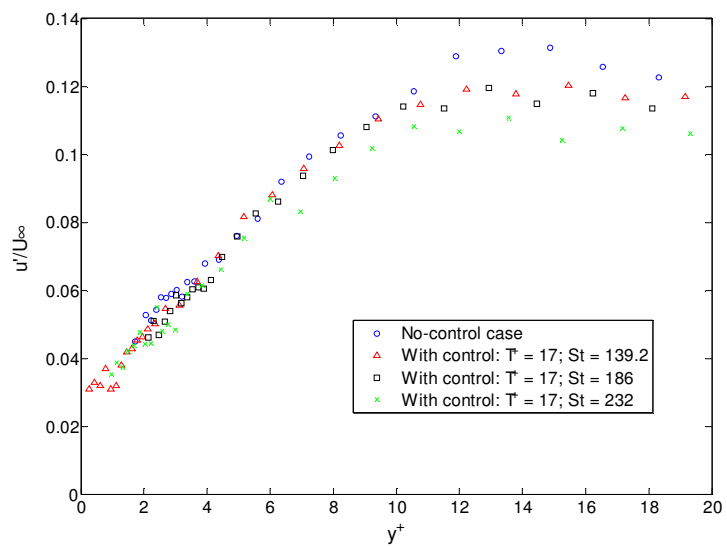


Figure 5.3.9. Inner-scaled turbulent intensity profiles for cases without and with control at $T^+ = 17$. Drag increasing cases.

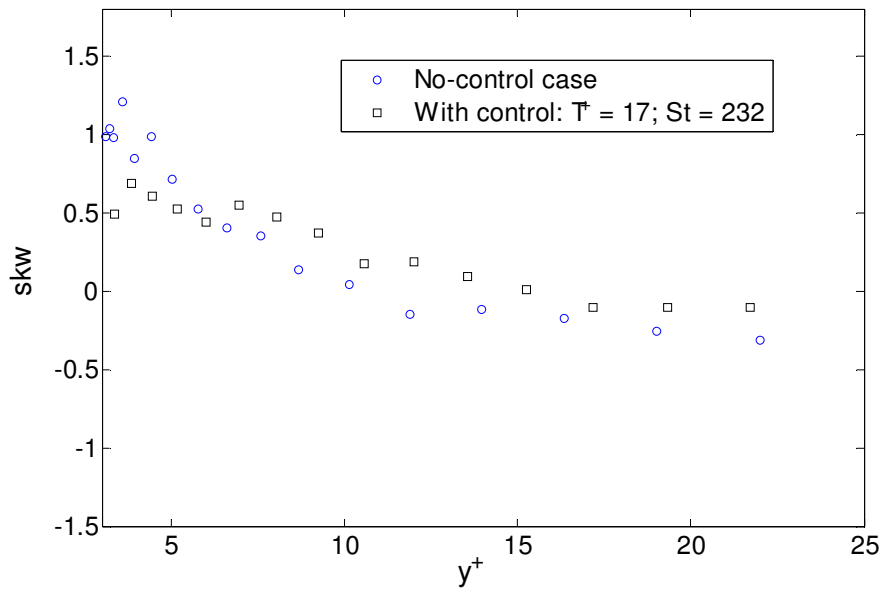


Figure 5.3.10. Skewness profiles without and with control. Travelling wave condition: $T^+ = 17; St = 232$. DR = -22.8%

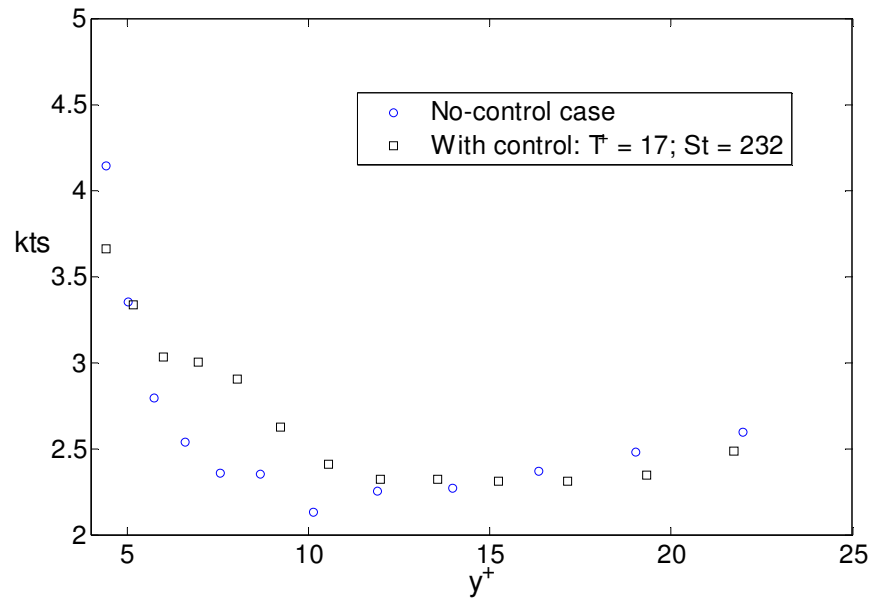
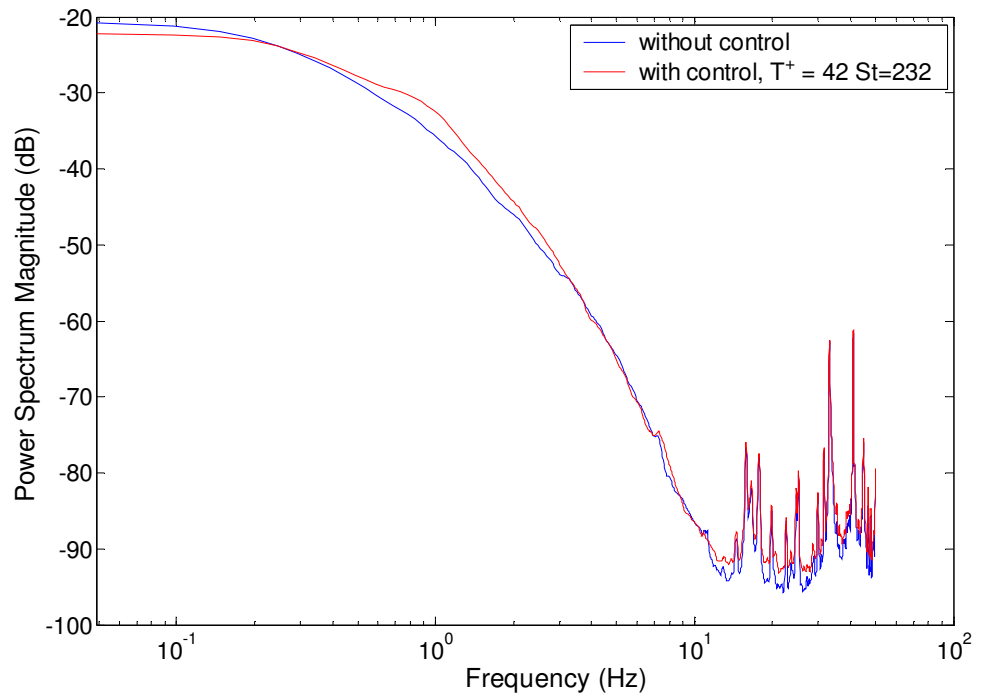
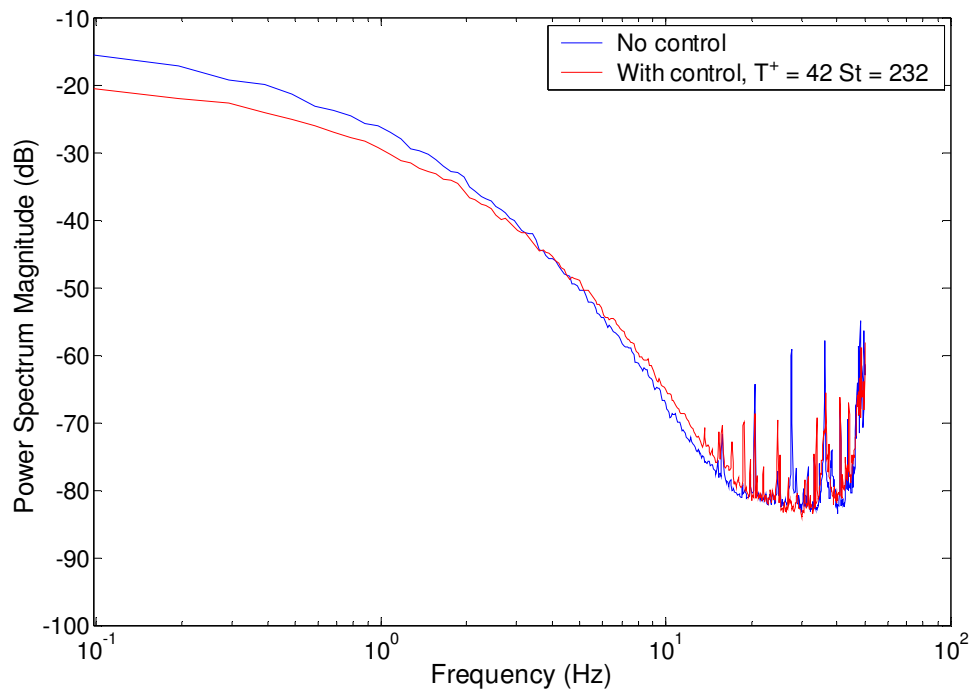


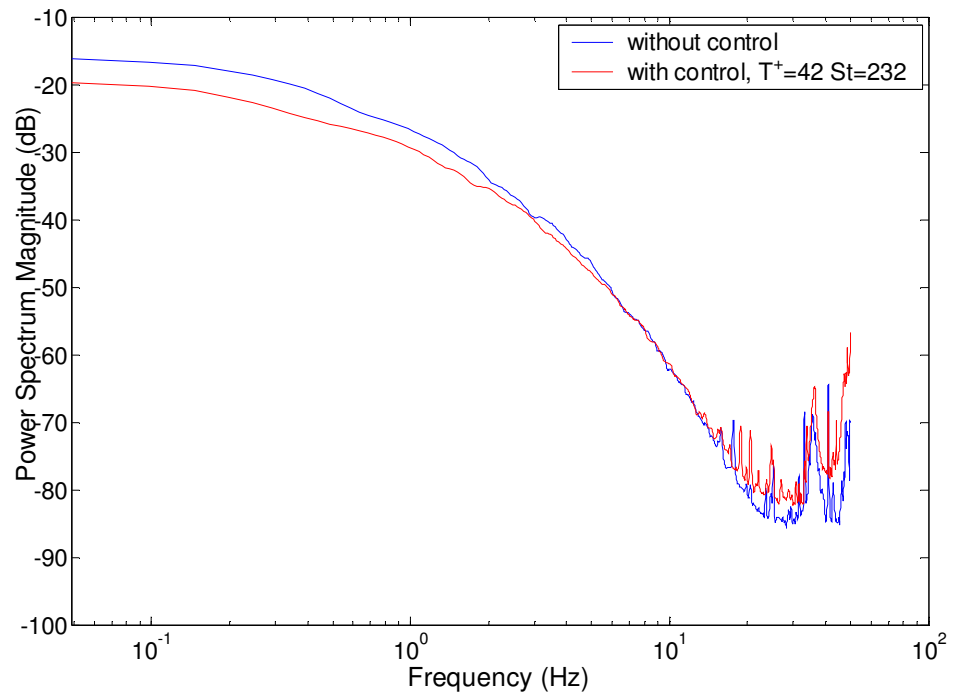
Figure 5.3.11. Kurtosis profiles without and with control. Travelling wave condition: $T^+ = 17; St = 232$. DR = -22.8%



(a) $y^+ \approx 5$

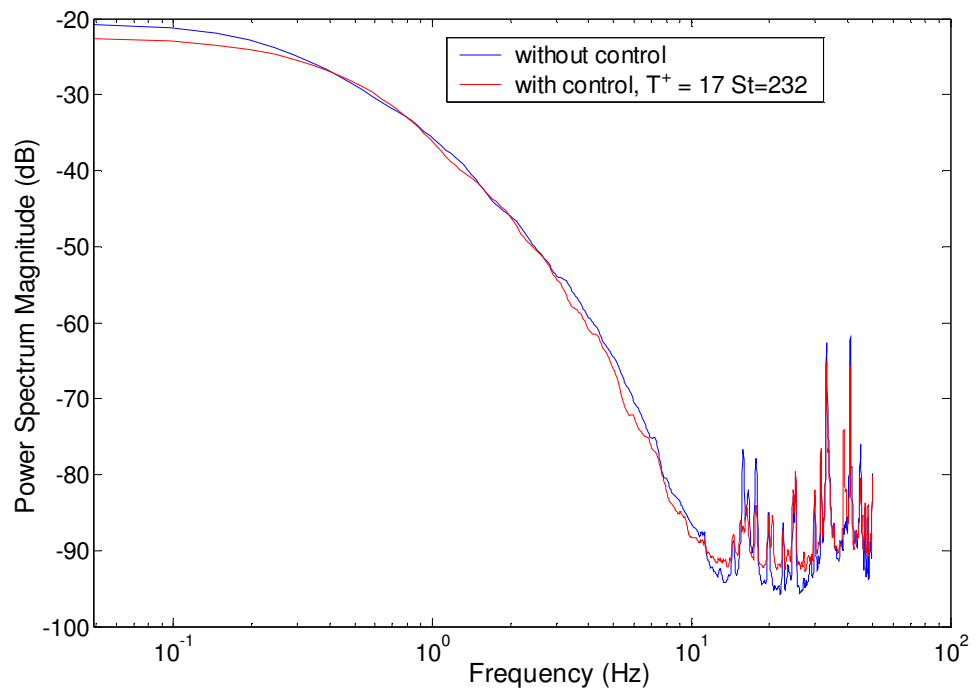


(b) $y^+ \approx 12$

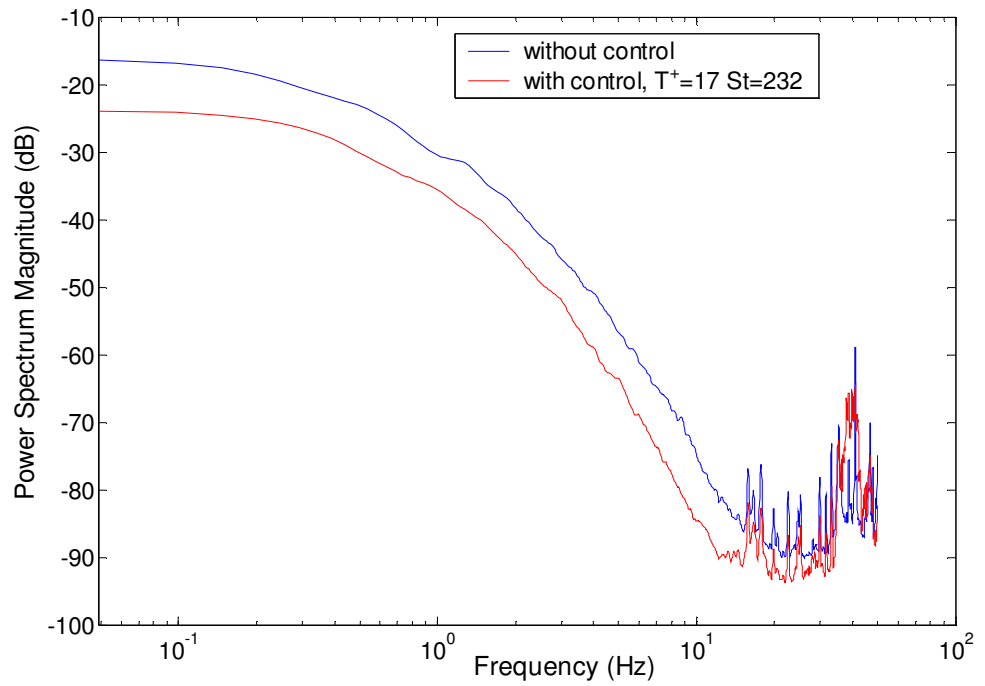


(c) $y^+ \approx 20$

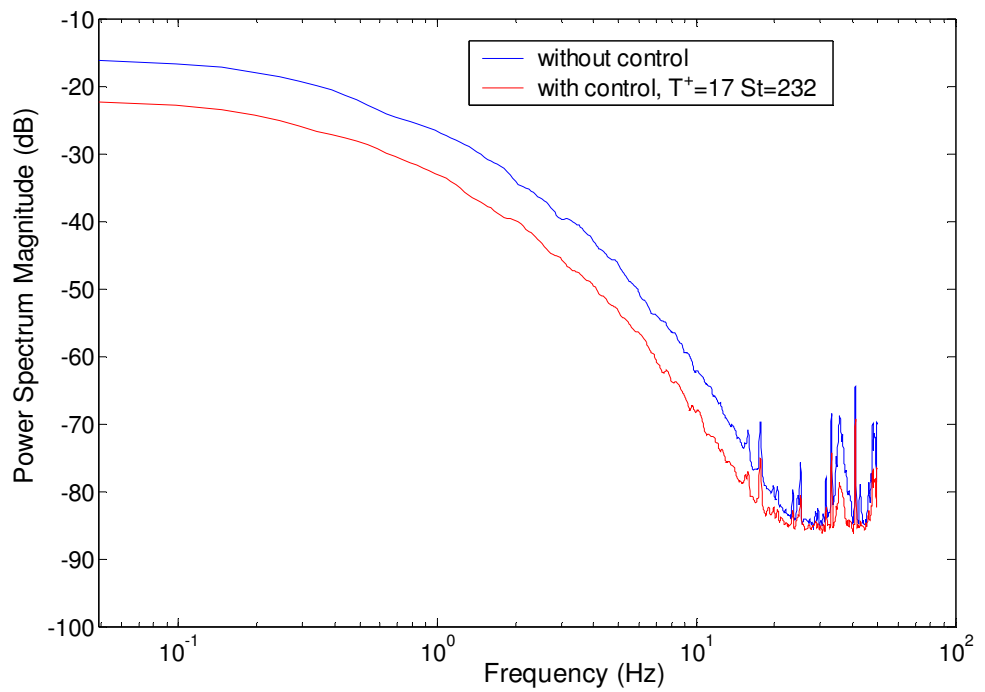
Figure 5.4.1. Energy spectra of u' without and with control in the turbulent boundary layer. Control condition: Lorentz forcing frequency $\approx 0.5\text{Hz}$; $T^+ = 42$; $St = 232$. DR = 28.9%



(a) $y^+ \approx 5$

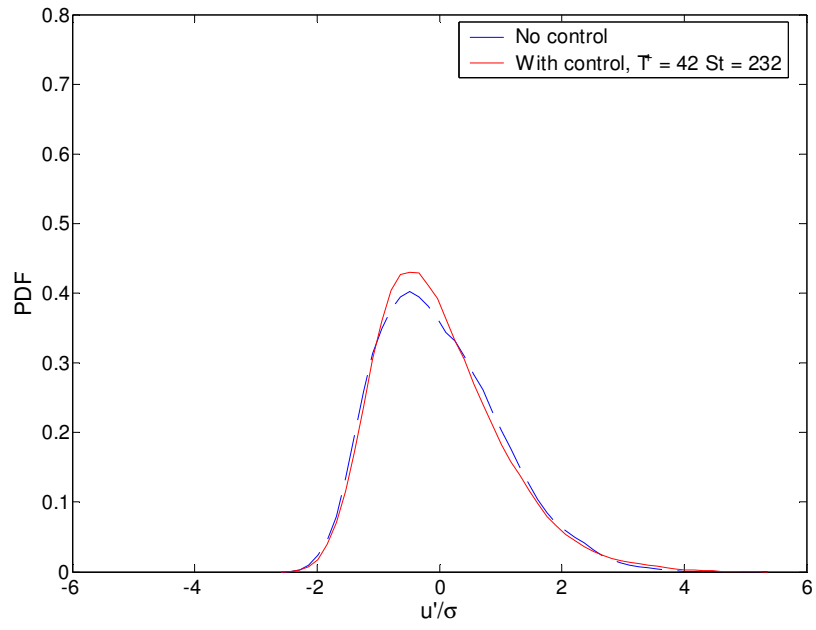


(b) $y^+ \approx 12$

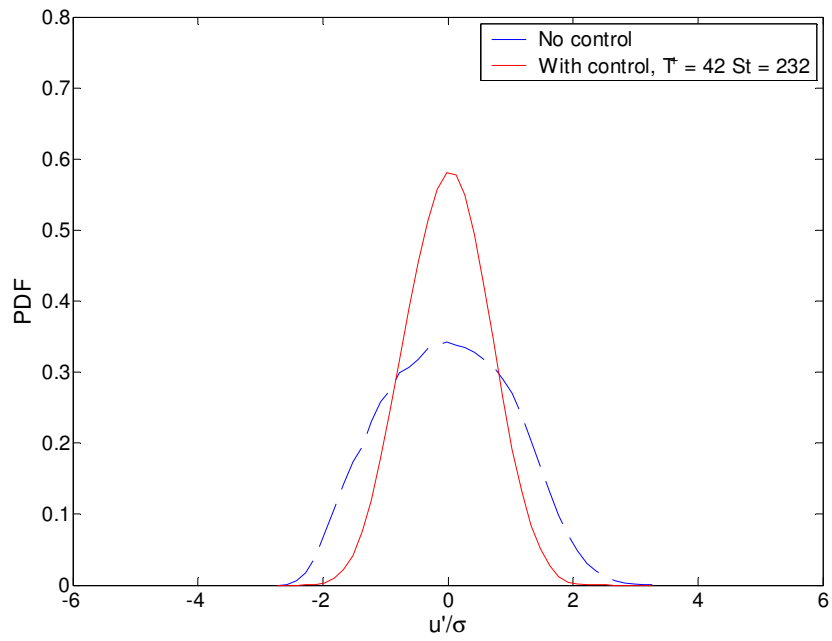


(c) $y^+ \approx 20$

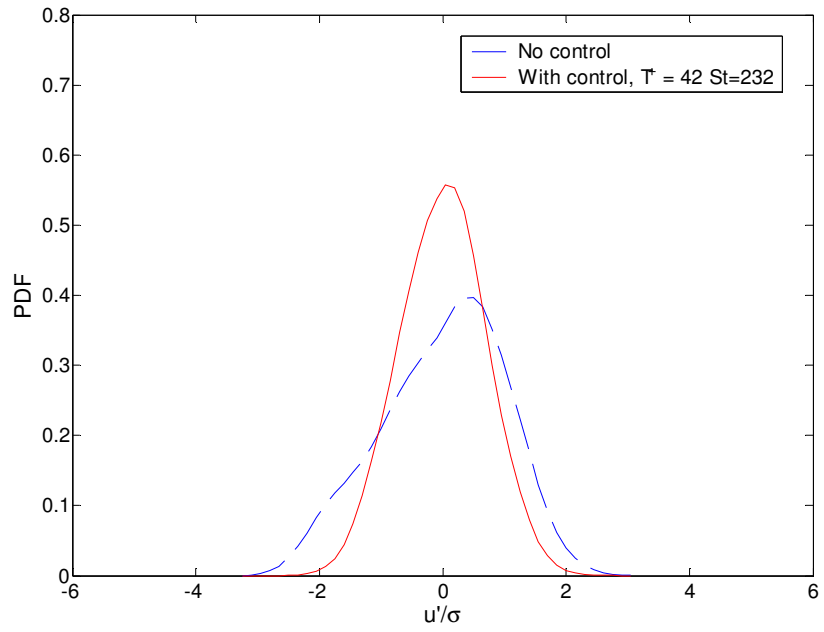
Figure 5.4.2. Energy spectra of u' without and with control in the turbulent boundary layer. Control condition: Lorentz forcing frequency $\approx 1.3\text{Hz}$; $T^+ = 17$; $St = 232$. $DR = -22.8\%$



(a) $y^+ \approx 5$

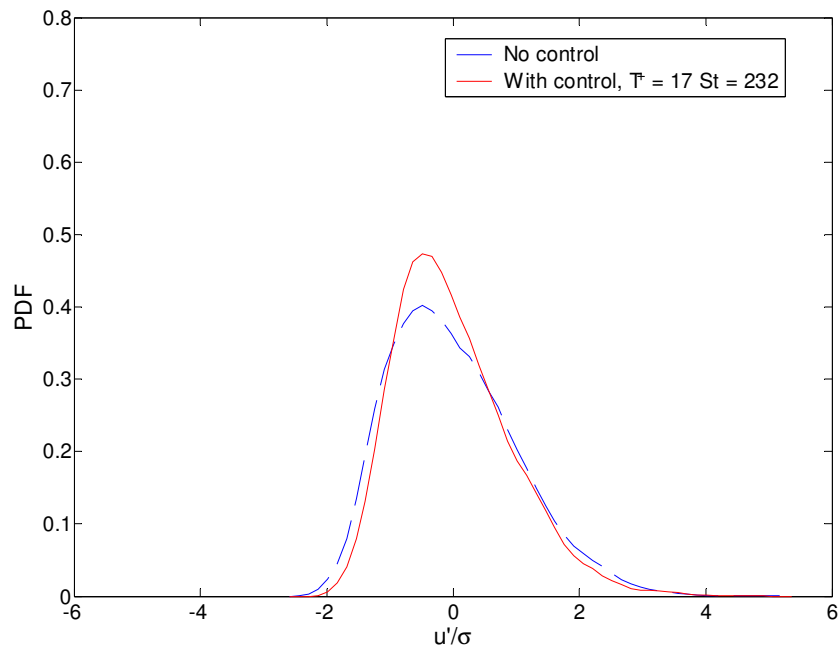


(b) $y^+ \approx 12$

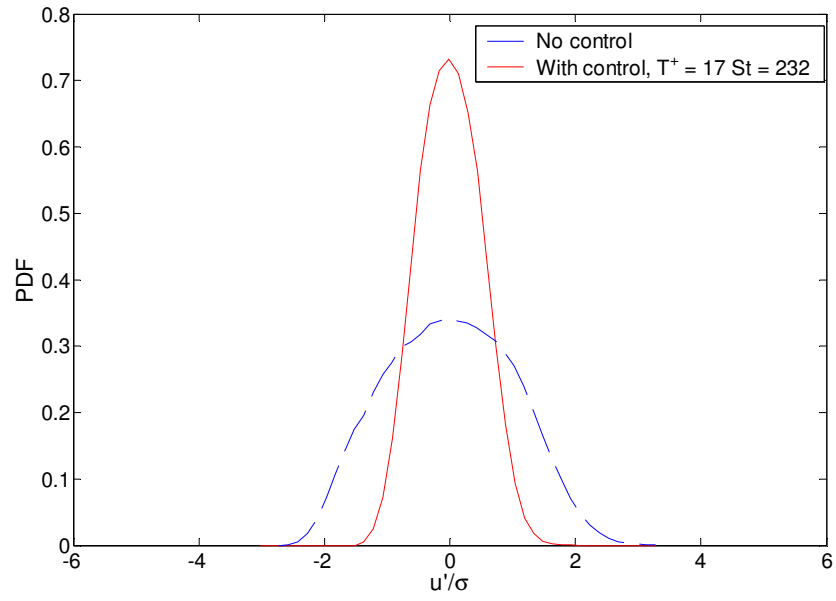


(c) $y^+ \approx 20$

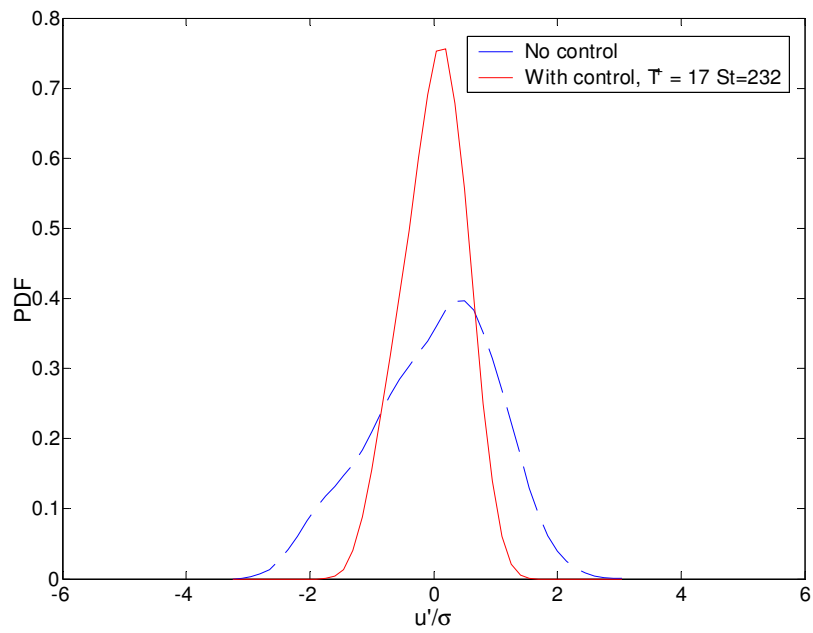
Figure 5.4.3. Probability Density Function of u' with and without control in the turbulent boundary layer. Control condition: $T^+ = 42$; $St = 232$. $DR = 28.9\%$.



(a) $y^+ \approx 5$



(b) $y^+ \approx 12$



(c) $y^+ \approx 20$

Figure 5.4.4. Probability Density Function of u' with and without control in the turbulent boundary layer. Control condition: $T^+ = 17$; $St = 232$. $DR = -22.8\%$.

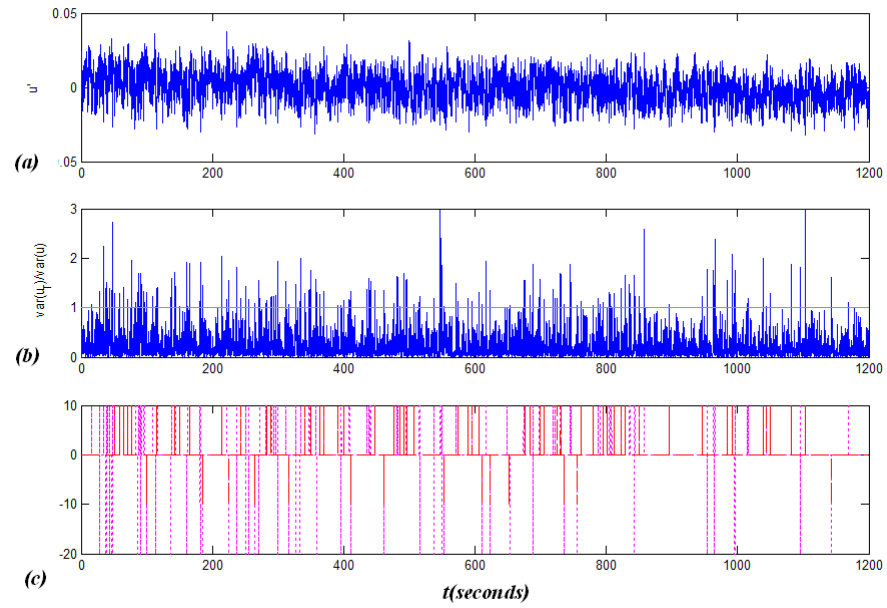


Figure 5.5.1. VITA detection scheme at $y^+ = 12$. a) velocity fluctuation, u' . b) ratio of local variance to mean variance and threshold detection level (-). c) detector function, $D(t)$, without discrimination against multiple events (--) and with discrimination (-).

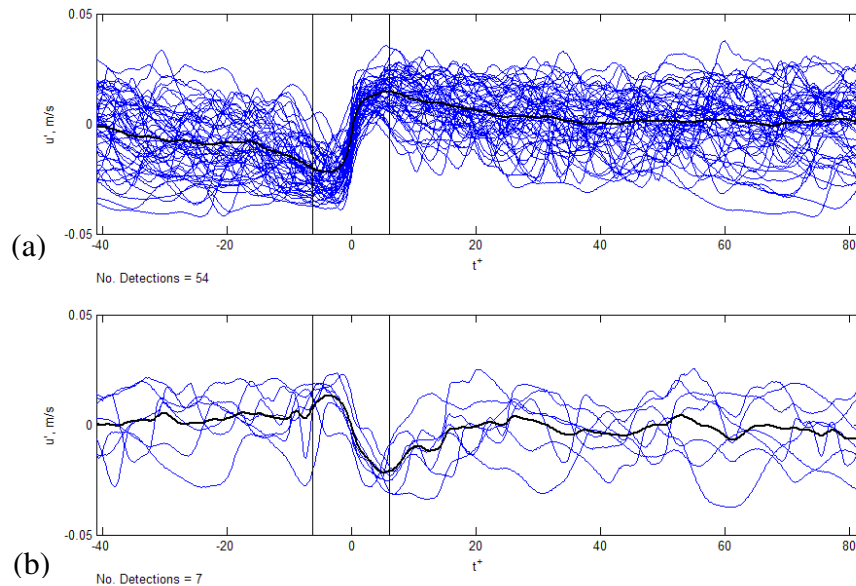
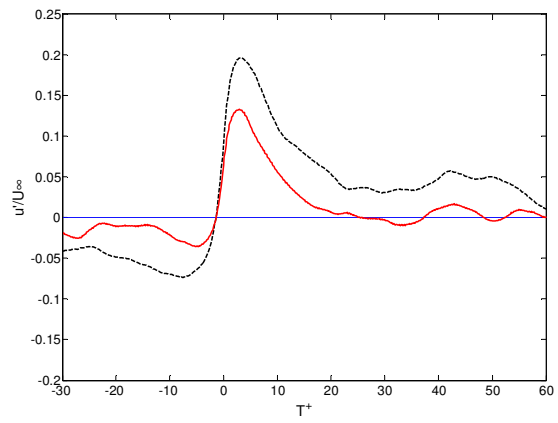
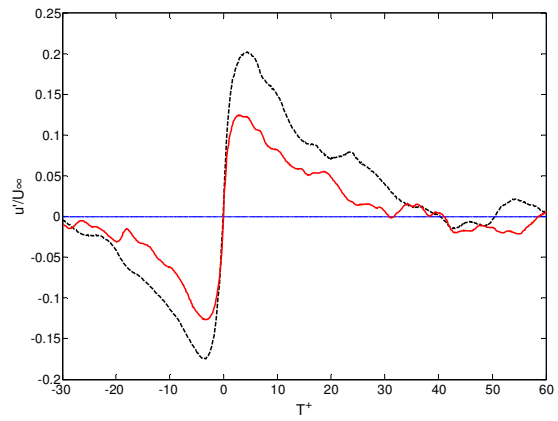


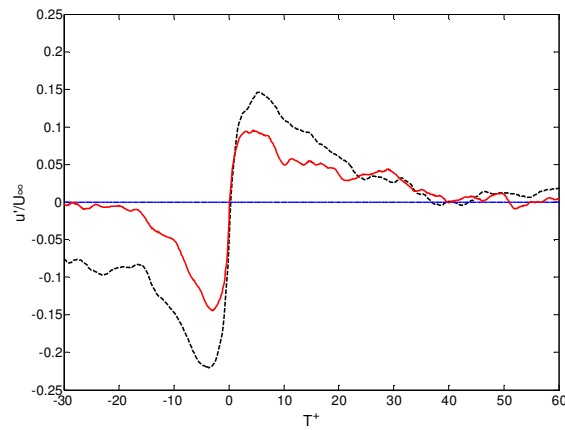
Figure 5.5.2. Ensemble averaging VITA events across the window T_{ens} , at $y^+ = 12$. a) $du/dt > 0$ events and b) $du/dt < 0$ events. Black lines indicate the window size, T_{win} .



(a) $y^+ \approx 5$

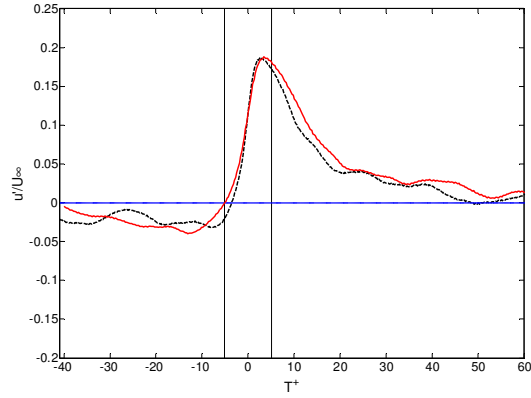


(b) $y^+ \approx 12$

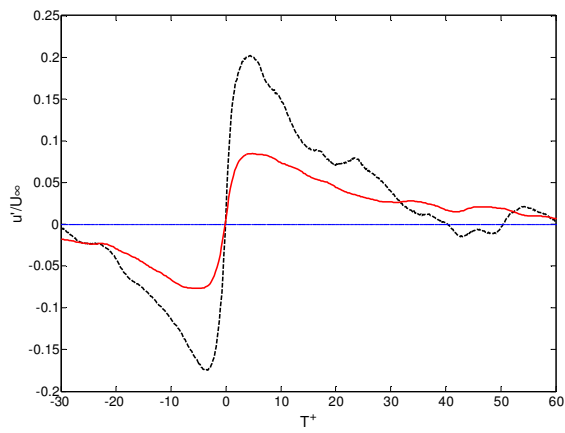


(c) $y^+ \approx 20$

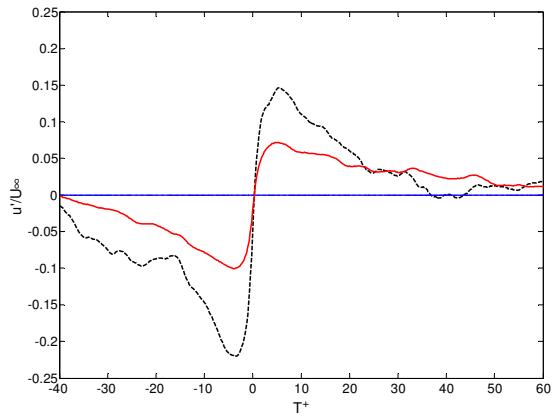
Figure 5.5.3. Ensemble averaged VITA events without (--) and with (-) control. Control condition: $T^+=42$; $St=232$. $DR=28.9\%$



(a) $y^+ \approx 6$

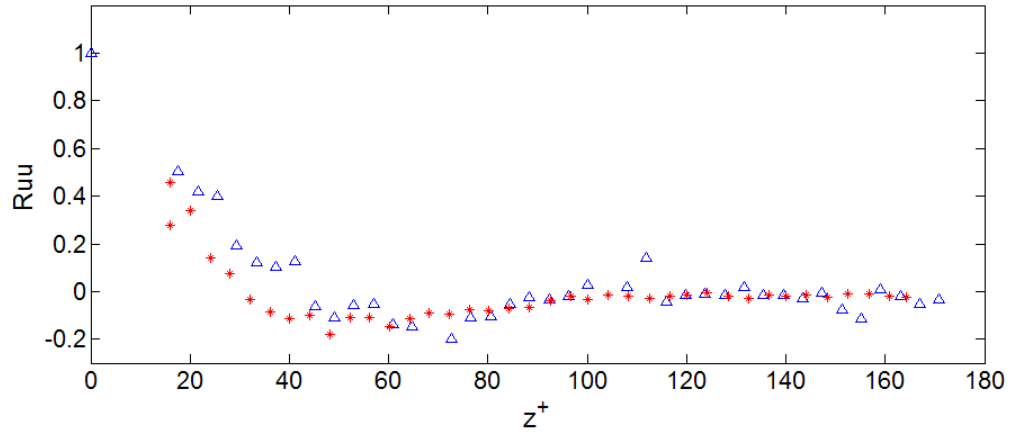


(b) $y^+ \approx 12$

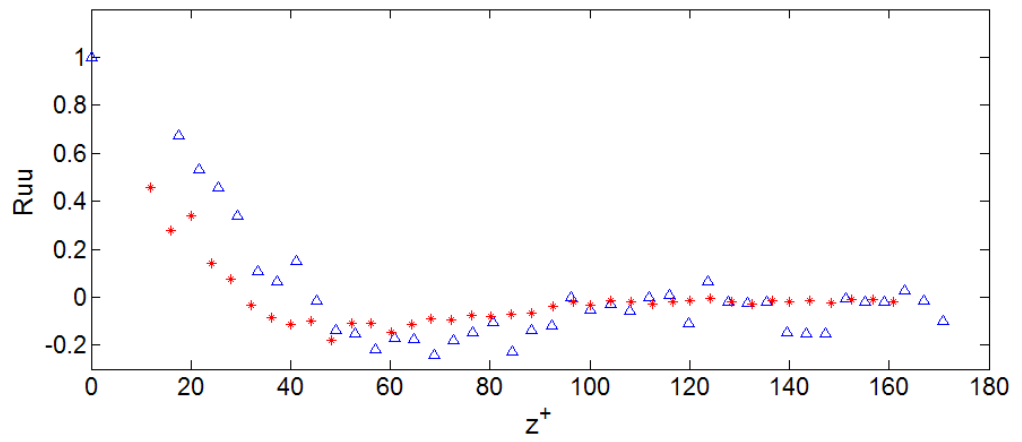


(c) $y^+ \approx 20$

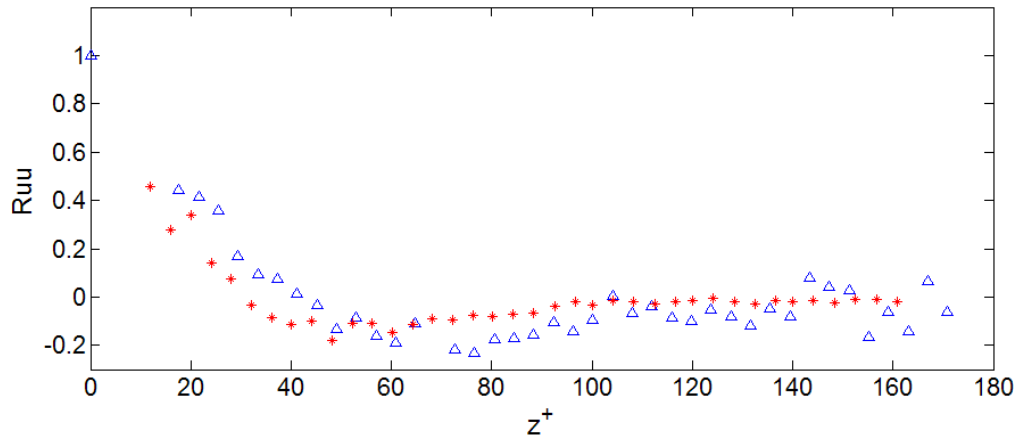
Figure 5.5.4. Ensemble averaged VITA events without (--) and with (-) control. Control condition: $T^+=17$; $St=232$. $DR= -22.8\%$



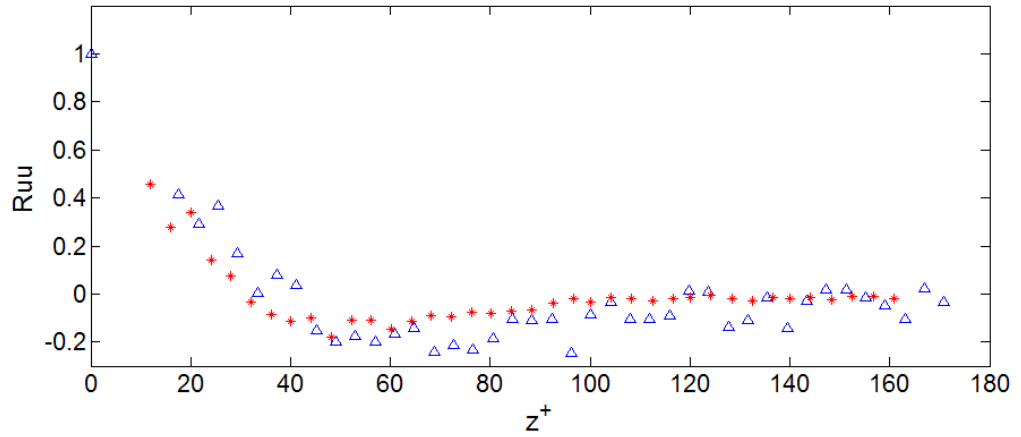
(a) Phase 1



(b) Phase 2

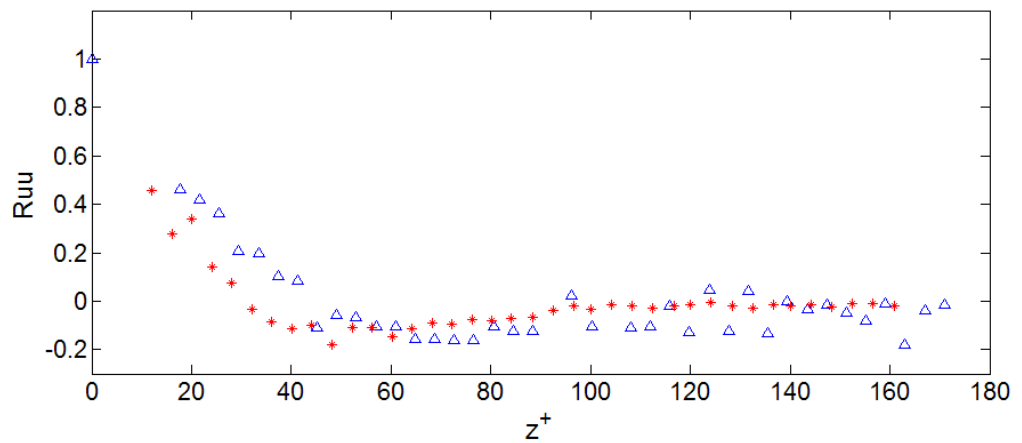


(c) Phase 3

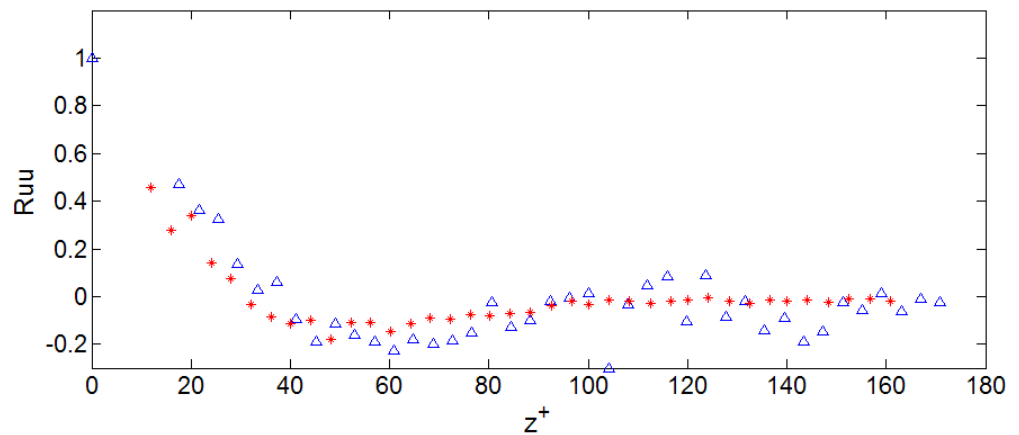


(d) Phase 4

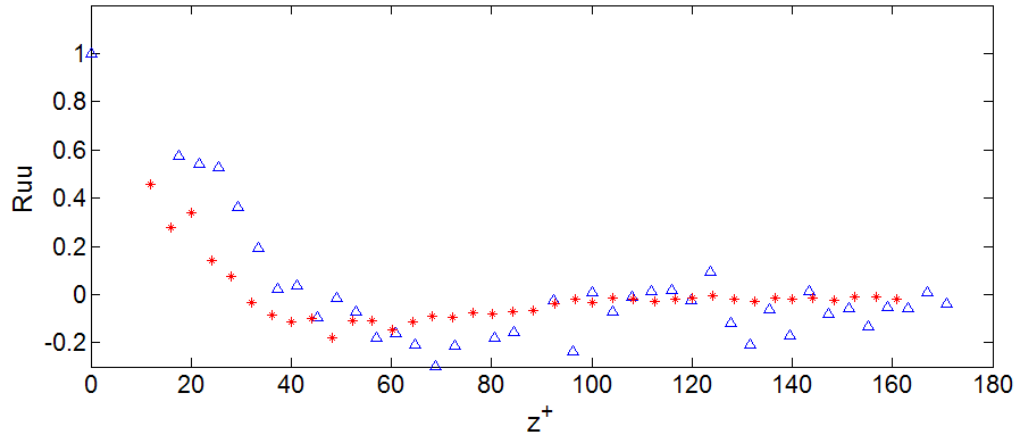
Figure 5.6.1. The spanwise correlation of the streamwise velocity. Red star (*) denotes no-control case; blue triangle (Δ) denotes the drag-reducing case ($T^+ = 42$, $St = 232$ and $DR = 28.9\%$). Note: $R_{uu} = 1$ is a theoretical value, meaning perfect correlations. The definition is show in equation (2.2.12). $R_{uu} = C_{ij}$.



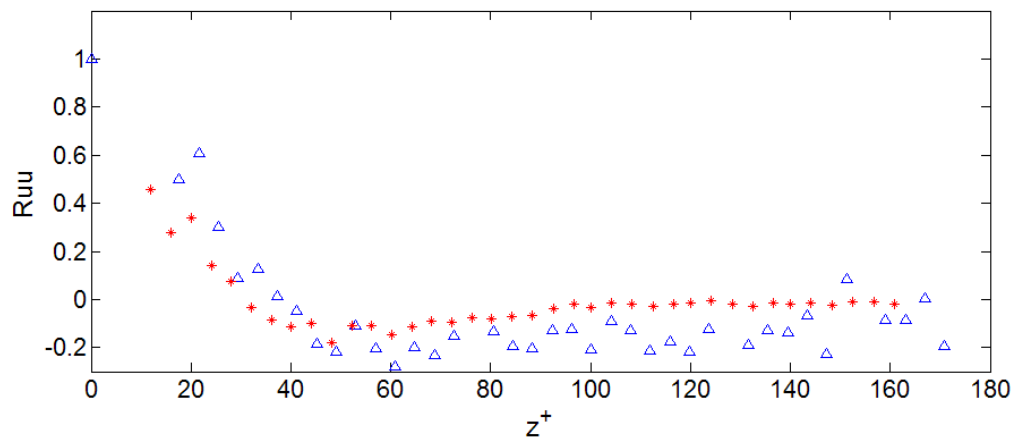
(a) Phase 1



(b) Phase 2



(c) Phase 3



(d) Phase 4

Figure 5.6.2. Transverse correlation of streamwise velocity. Red star (*) denotes no-control case; blue triangle (Δ) denotes the drag-increasing case ($T^+ = 17$, $St = 232$ and $DR = -22.8\%$). Note: $R_{uu} = 1$ is a theoretical value, meaning perfect correlations. The definition is show in equation (2.2.12). R_{uu}

$$= C_{ij}.$$

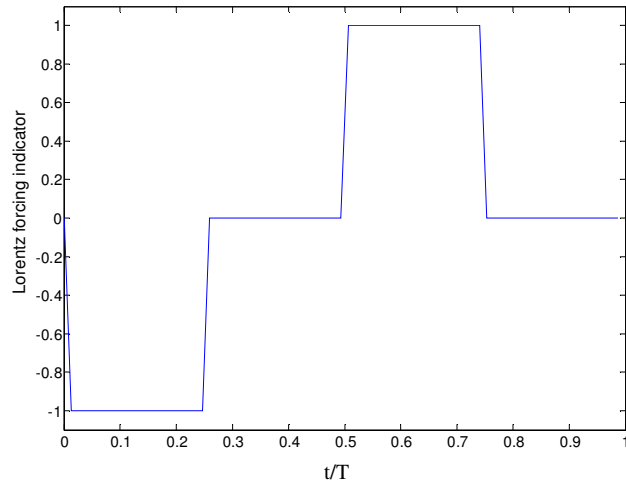


Figure 5.7.1. Lorentz forces with timing.

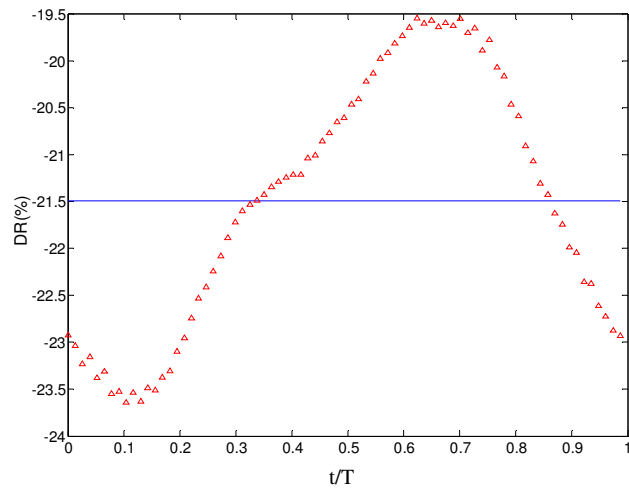


Figure 5.7.2. Drag reduction ratio for the control case at $T = 0.77$ s, $T^+ = 17$; $St = 232$.

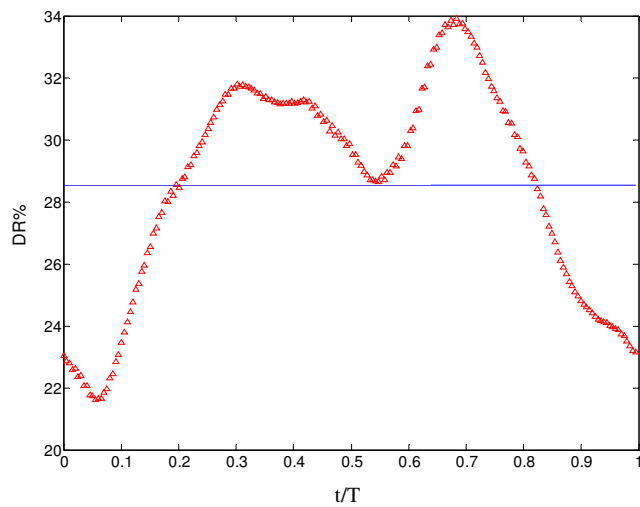


Figure 5.7.3. Drag reduction ratio for the control case at $T = 1.99$ s, $T^+ = 42$; $St = 232$.

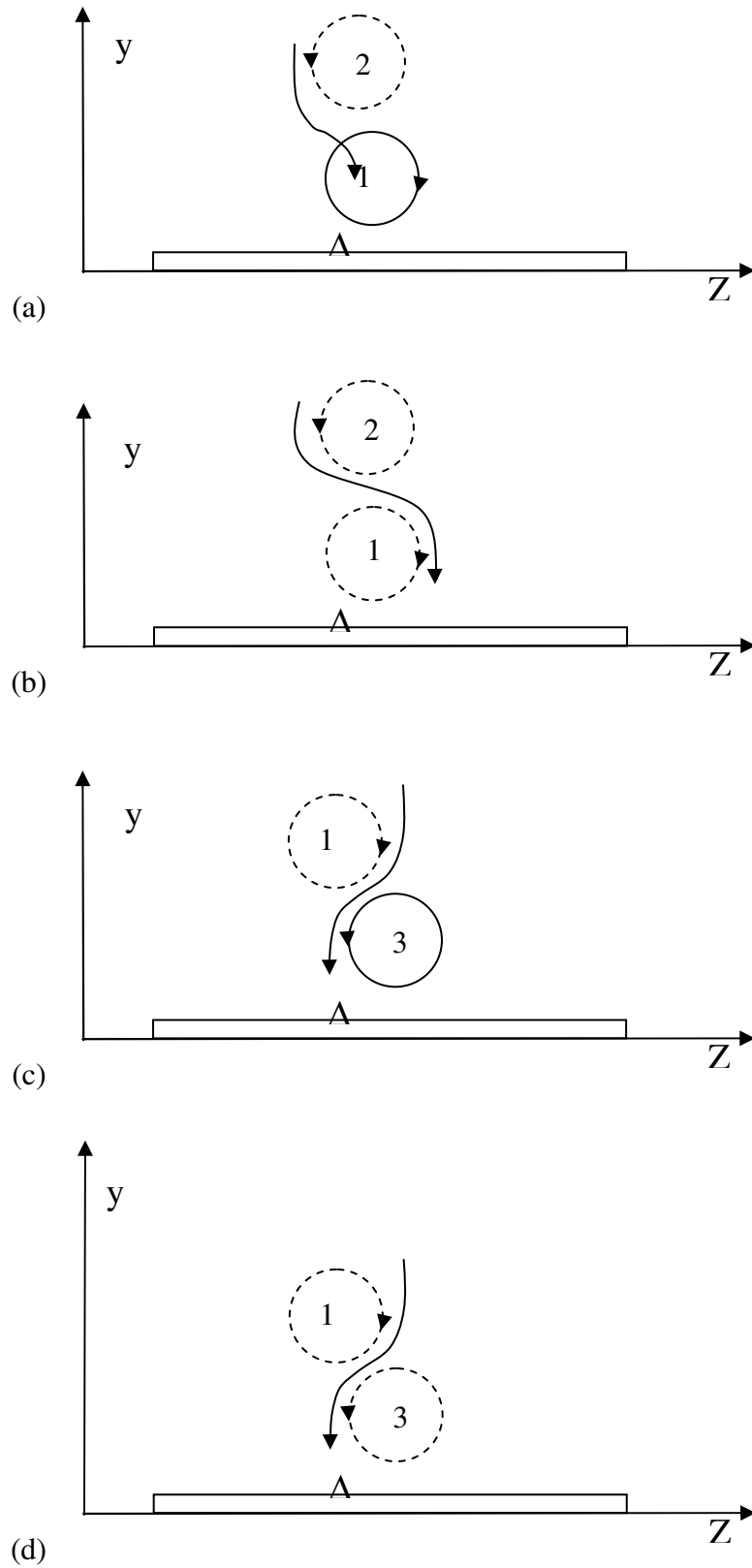


Figure 5.7.4. The mechanism of the change of the high-speed fluid moving path by the Lorentz forcing in drag-increasing case. Δ is the position of the hot-film sensor; Curved arrow denotes the high-speed fluid moving path.

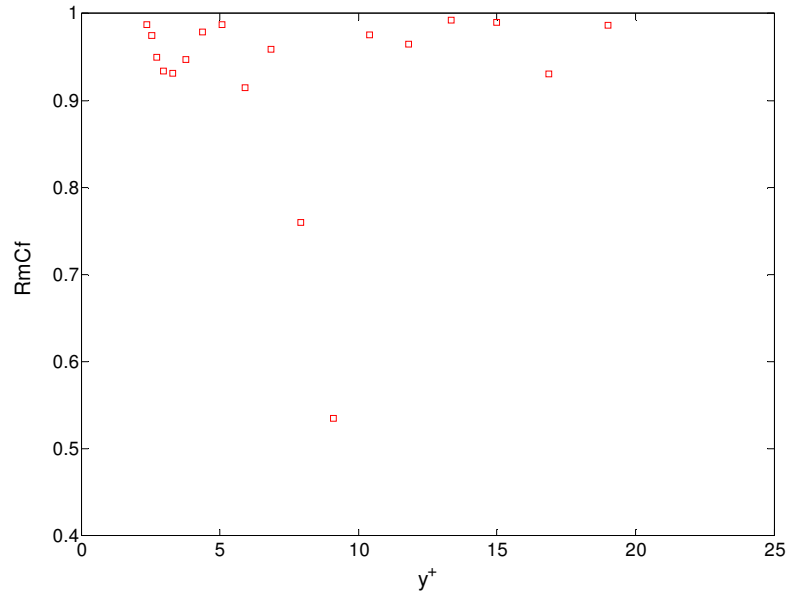


Figure 5.7.5. Correlation of the skin-friction coefficient C_f/C_0 and phase-averaged momentum for drag-increasing case. Travelling wave condition: $T^+ = 17$; $St = 232$. $DR = -22.8\%$

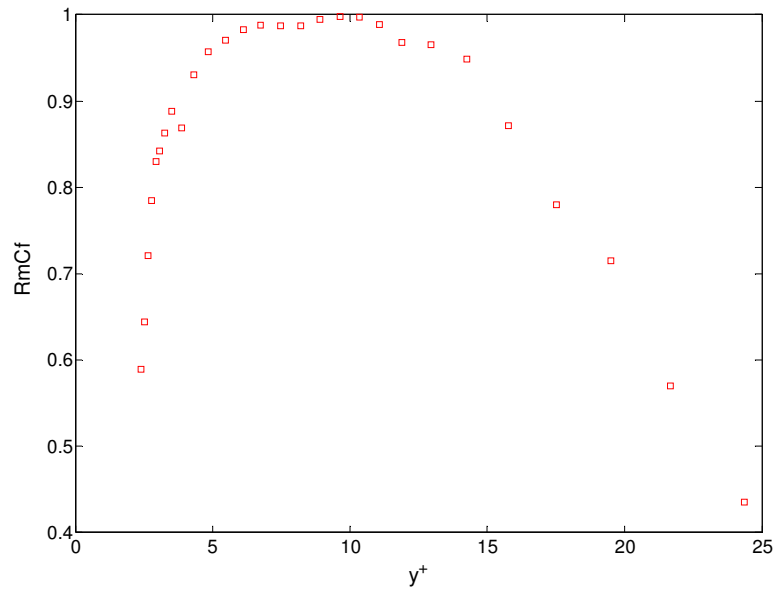


Figure 5.7.6. Correlation of the skin-friction coefficient C_f/C_0 and phase-averaged momentum for drag-reducing case. Travelling wave condition: $T^+ = 42$; $St = 232$. $DR = 28.9\%$

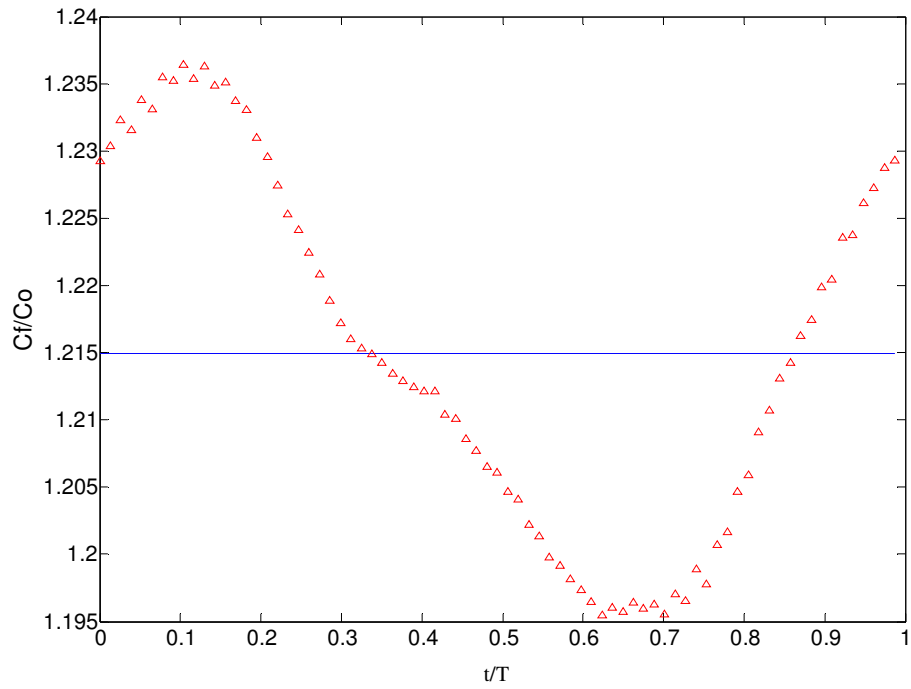


Figure 5.7.7. Phase-averaged drag history for $T = 0.77$ s, $T^+ = 17$; $St = 232$.

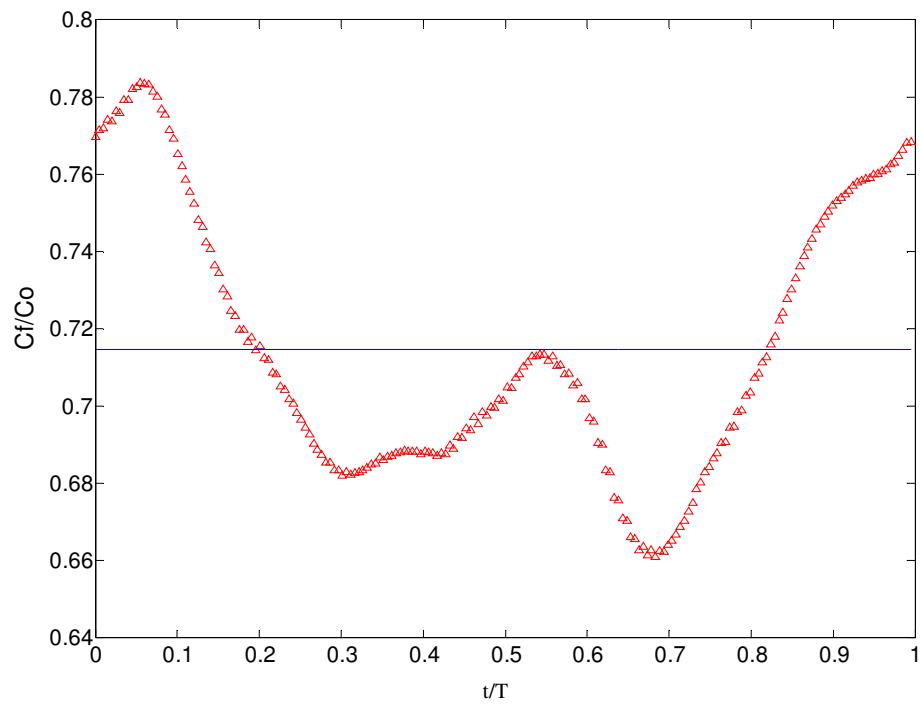


Figure 5.7.8. Phase-averaged drag history for $T = 1.99$ s, $T^+ = 42$; $St = 232$.

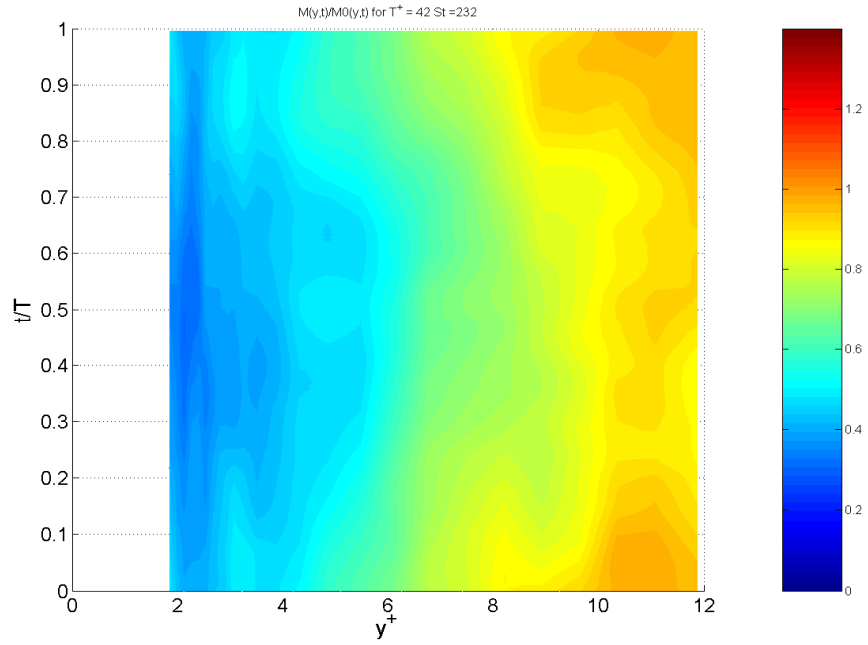


Figure 5.7.9. Phase-averaged momentum distribution of spanwise travelling wave actuation normalised by momentum of the no-control case for the drag-reducing condition: $T^+ = 42$ and $St = 232$; $DR = 28.9\%$.

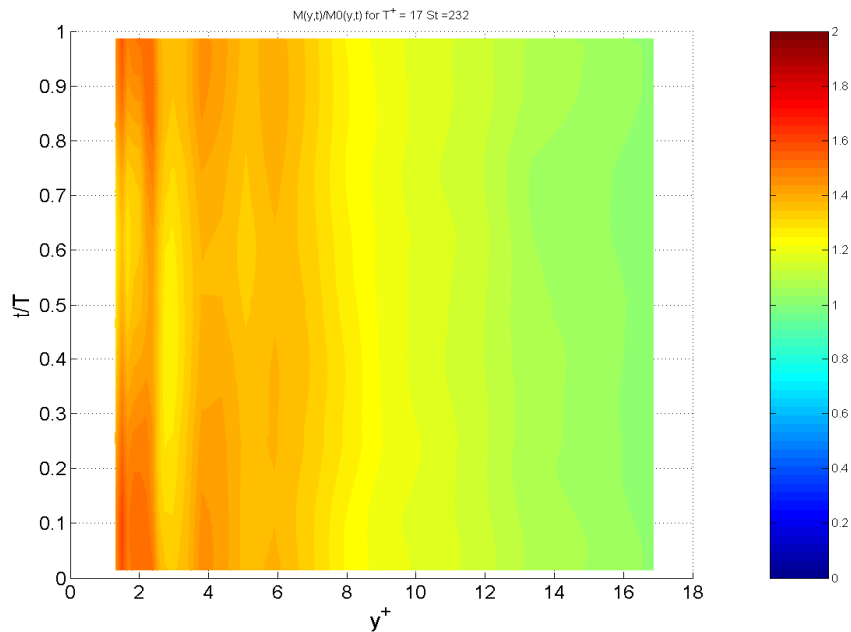
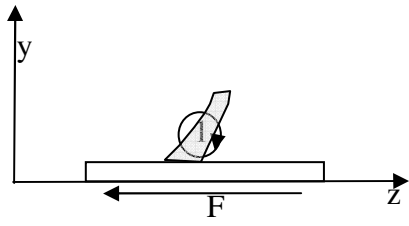
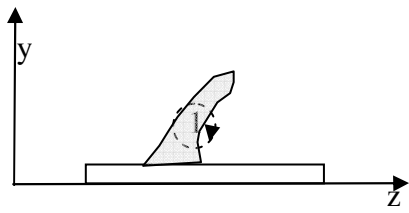


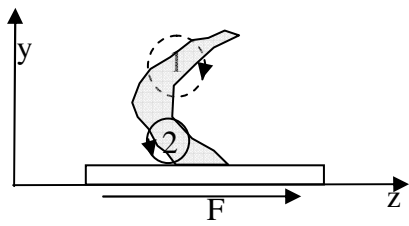
Figure 5.7.10. Phase-averaged momentum distribution of spanwise travelling wave actuation normalised by momentum of the no-control case for the drag-increasing condition: $T^+ = 17$ and $St = 232$; $DR = -22.8\%$.



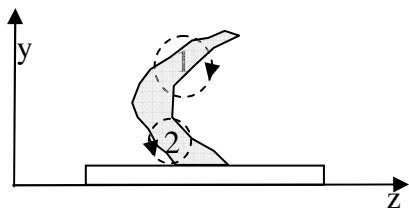
(a)



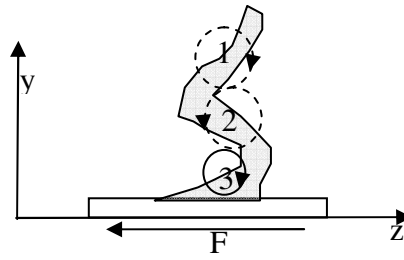
(b)



(c)



(d)



(e)

Figure 5.7.11. The mechanism of the introduction of streamwise vortices by Lorentz forcing under drag-increasing conditions. Grey band denotes the twisted low-speed streak; solid circles denote the streamwise vorticity being introduced by the Lorentz forcing and dashed circles denote the vorticity maintained by inertial effects; the block denotes the electrode and the arrow with F denotes the Lorentz force.

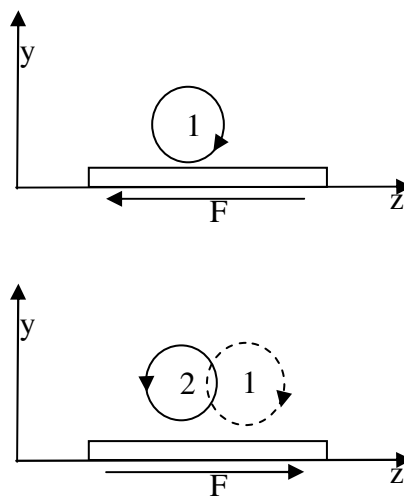


Figure 5.7.12. The mechanism of the introduction of streamwise vortices by Lorentz forcing for spanwise oscillation. Solid circles denote the streamwise vorticity being introduced by the Lorentz forcing and dashed circles denote the vorticity maintained by inertial effects; the block denotes the electrode and the arrow with F denotes the Lorentz force.

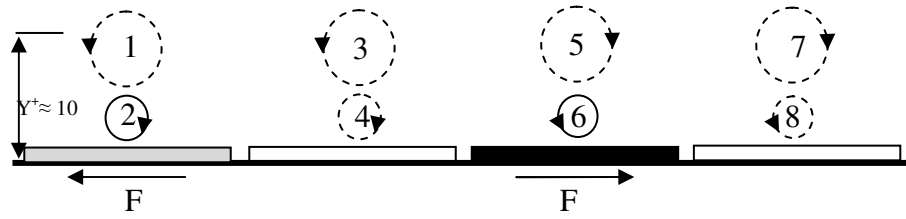
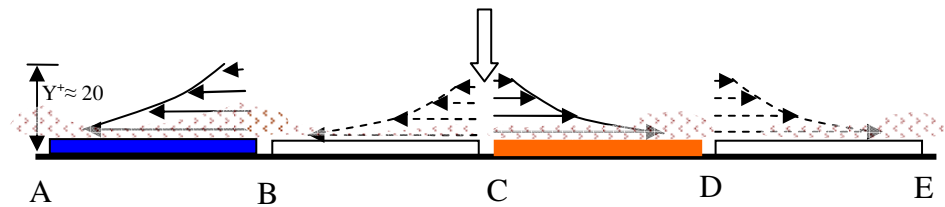
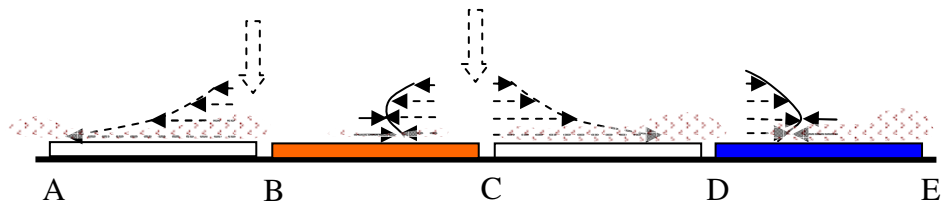


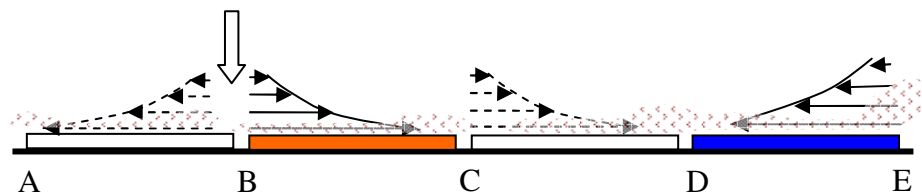
Figure 5.7.13. Generated streamwise vorticity by a travelling wave in the drag increasing conditions. Dash circles are indicated that the motions are maintained due to inertia effects and the solid circles are the secondary flow being generated by the Lorentz forcing.



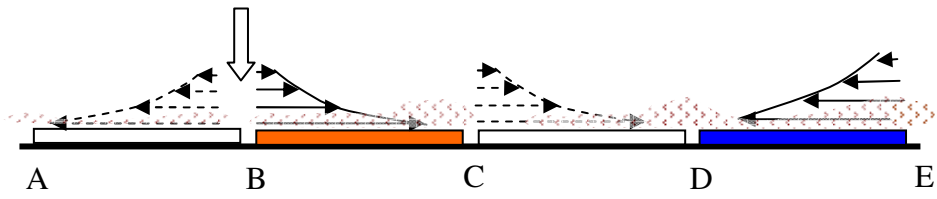
(a) End stage of the last phase



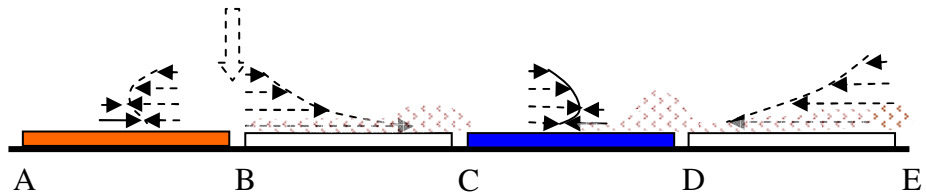
(b) Starting stage of the current phase



(c) Middle stage of the current phase

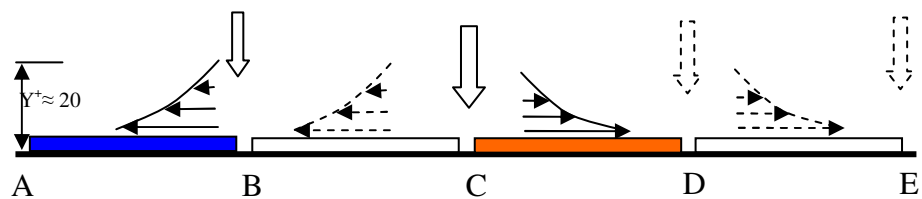


(d) End stage of the current phase

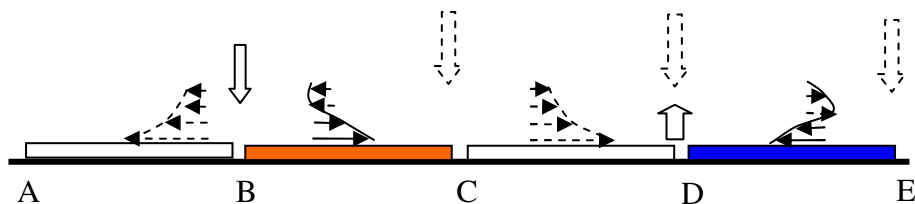


(e) Starting stage of the next phase

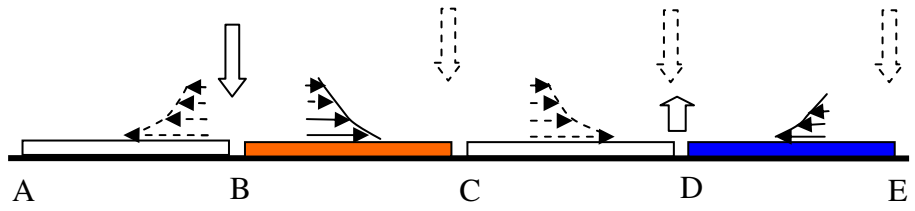
Figure 5.8.1. A 2-D conceptual model of the induced motions by the Lorentz-forcing spanwise travelling wave excitation for drag reduction. Solid arrows indicate motions induced by Lorentz forces; dashed ones indicate motions maintained by inertia effects; hatched regions indicate low-speed fluids. The blue block indicates a negative force (left-ward); the red block indicates positive force (right-ward). Travelling wave moving direction is from the right to the left (negative in z)



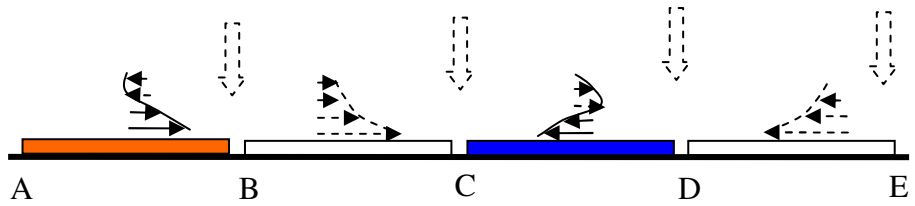
(a) End stage of the last phase



(b) Starting stage of the current phase



(c) Mature stage of the current phase



(d) Starting stage of the next phase

Figure 5.8.2. A 2-D conceptual model of the induced motions by the Lorentz-forcing spanwise travelling wave excitation for the drag-increasing case. Solid arrows indicate motions induced by Lorentz forces; dashed ones indicate motions maintained by inertia effects; the red block indicates a positive force (right-ward).

Chapter 6

Conclusions and Future Work

6.1. Conclusions

The new electro-magnetic actuator designed for this project has been proven to be as effective as that used by Du et al (2002) while needing fewer phase changes. The design allows using only 4 phases and whereas 16 phases were used in the study of Du et al. (2002). A maximum of 30% drag reduction is achieved by the Lorentz-forcing spanwise travelling wave at $T^+ = 82$, $St = 232$, as well as a maximum of 22.8% drag increase at $T^+ = 17$, $St = 232$. In the drag reducing cases, the drag reducing behaviours show similar results at $T^+ = 42$ and 82. Although the drag reduction ratios are similar to that observed by Du et al (2002), the drag increase doesn't occur in the maximum forcing values for the drag reducing cases ($T^+ = 42$ and 82). Du et al (2002) found that, the excitations with $I = 1$ and $I = 2$ lead to drag increase but $I = 0.5$ leads to drag decrease at a period of $T^+ = 100$ in their experiments, where I is the strength factor used in their simulation and has global units.

The turbulence intensities for both of the drag-reducing and the drag-increasing cases are reduced, which shows that the spanwise travelling wave weakens the turbulent activities in all cases. The higher moments of turbulence statistics, like skewness and kurtosis, are increased near the wall when $T^+ = 42$, $St=232$ (the drag-reducing case). For the drag-increasing case, the skewness and kurtosis are decreased at the region of $y^+ < 6$; while for $y^+ > 6$, they are increased similarly to the drag-reducing case, which suggests that the

drag increase is due to the near-wall modified activities within or close to the viscous sublayer by the Lorentz forcing.

This study also shows the Lorentz-forcing spanwise travelling wave twists the low-speed streaks and breaks down the large-scale coherent structures in the turbulent boundary layer for both the drag-increasing and the drag-reducing cases.

In the drag-reducing case, the low-speed streaks migrate and form the low-speed regions ('ribbons'), which acts as 'storage' of the low-speed fluid and supplies the low-speed fluid to the nearby forcing region in the same direction as the travelling wave movement. To achieve drag reduction, it is found that the spanwise displacement of low-speed 'ribbons' must be greater than 115 wall units (in z^+ , which is about one electrode width in this experiment). This compares to the spacing between the low-speed streaks ($z^+ \sim 100$).

In the drag-increasing case, pseudo-local spanwise oscillation is observed by the induction of the Lorentz-forcing spanwise travelling wave. The motions of the converging and diverging are found due to pseudo-local spanwise oscillation. It is argued that these motions cause similar motions to the 'sweep' and the 'ejection' events in the turbulent boundary layer. Sweep events are more important for the production of the skin friction as proposed by Orlandi and Jimenez (1994). The results also show that the duration of the sweep events are increased at region of $y^+ \leq 12$. Especially, at $y^+ = 5$, the intensity of sweeps isn't reduced but the duration is increased by 23% and is comparable with the drag increase ratio (22.8%). This suggests that the modified sweep events might be responsible for the drag increase. Furthermore, the

introduction of the external streamwise vorticity sheet is proposed as the main reason of the near-wall activity modification.

The main difference between the spanwise travelling wave excitation (especially for the drag-reducing cases) and the spanwise oscillatory excitation, as well as other drag reduction techniques such as riblets and polymers etc. (see Gad-el-Hak 2000), is in the modification of the near-wall streaks. Most of the low-speed streaks are tempered and the ‘low-speed ribbons’ are shown as the results of the modifications. But not all the streaks are eliminated in this study; otherwise turbulence could not be sustained (Jimenez & Pinelli 1999). Moreover, the spanwise velocity has a travelling wave form similar to the excitation of Lorentz forces, which re-regularises the existing streamwise vorticity. The Lorentz forcing spanwise travelling wave actuation is different from most of the other wall-streak control methods either, where only individual streaks are controlled (Du et al., 2002).

A lower-amplitude spanwise standing wave type of excitation used by Schoppa & Hussain (1998) has the same strategy of aiming at stabilising the near-wall streaks, despite that their standing wave is applied throughout the flow domain. Indeed, the spanwise travelling wave seems to act similarly with the spanwise oscillation in the suppression of turbulent production, which causes the net spanwise vorticity to be enhanced resulting in the weakening of the streamwise vortices (for example, see Nosenchuck & Brown, 1993 and Choi, 2002). However, it is the introduction of the external streamwise vorticity by the spanwise travelling wave in the viscous sublayer that contributes the leading role to the flow control effects. The introduced streamwise vorticity is the main reason for the suppression of the near-wall

streaks in the drag-reducing cases and the enhancement of the sweep events leading to the opposite effects of drag increases. Dhanak & Si (1999) and Du et al. (2002) also suggest this regularisation of streamwise vorticity as the mechanism for the drag reduction in the spanwise motion control methods.

6.2. Future Work

Single-component hot-film anemometry and flow visualisation techniques are used in this study for the spanwise travelling wave with fixed wavelength and penetration depth of Lorentz-forcing. It is recommended that various wavelengths should be studied to investigate the effects of spanwise displacement of the low-speed streaks.

In the current study, the experiments are carried out at one Reynolds number only. The spanwise travelling seems insensitive to the free-stream velocity (Reynolds number), which gives hope that it can be used in higher Reynolds numbers. Iwamoto et al. (2005) suggest that the large drag reduction can be attained even at high Reynolds numbers if the turbulence fluctuations adjacent to the wall are damped. Therefore, studies at various Reynolds numbers are essential to conclude this argument that the spanwise travelling wave actuation will be promising in high Reynolds number flows of real applications.

A maximum of 1 A total current has been used in this study. The saved energy at the case of 30% drag reduction is increased by 275%, but the consumed electricity energy is only increased by 56%, comparing with the energy saving and consumed electricity at the case of 7% drag reduction, respectively. This finding suggests that the energy efficiency is increased with a higher drag reducing ratio.

For further applications, the materials of the electrodes need to be investigated. In this experiment, a very thin layer of copper ($17\mu\text{m}$) is used, which runs out very quickly when using high currents. This is because the copper electrode is getting involved in the generation of Lorentz forces and the balance between gaining and losing of the copper ions sometimes isn't achieved. Copper electrodes are good in the application of the lab study together with the conductive solution of Copper ions because it eliminates the production of bubbles and helps to create a clean surrounding for the velocity measurement using the hot-film anemometry. However, in the real world, there are not enough copper ions in the ambient environment for the copper electrodes to make up the loss. An inactive electrode should be used with bubbles generated accordingly. The investigation of the bubbles and the spanwise travelling wave might be interesting because it seems to combine micro-bubble and spanwise travelling wave flow control methods. PIV is an appropriate technique to perform the measurements in this situation.

Meanwhile, the relatively small penetration depth, Δ , of the excitation force into the fluid suggests several surface-based techniques could be cost-effective actuation candidates (Du et al. 2002).

Last but not least, a further study of the spanwise travelling wave has been carried out in our research group at the University of Nottingham. Plasma is used to generate the spanwise travelling wave pattern in air, which shows a promising application for the future.

References

Adrian, R. J., 2007, "Hairpin Vortex Organization in Wall Turbulence", *Physics of Fluids*, **19**, pp. 1-16.

Adrian, R. J., Meinhart, C. D. and Tomkins, C. D., 2000, "Vortex Organization in the Outer Region of the Turbulent Boundary Layer", *J. Fluid Mech.*, **422**, pp. 1-54.

Akhavan, R., W. J. Jung, et al. (1993). "Turbulence Control In Wall-bounded Flows by Spanwise Oscillations." *Appl. Sci. Res.*, **51**, pp. 299-303.

Almquist, P. and Legath, E., 1965, "The Hot-Wire Anemometer at Low Velocities", *DISA Info.*, No. 2, pp. 3-4.

Anders, J. B., 1989. "Outer-layer manipulators for turbulent drag reduction. Viscous Drag Reduction in Boundary Layers," *Progress in Astronautics and Aeronautics*. eds. D. M. Bushnell and J. N. Hefner, AIAA. **123**. pp.263-284.

Andreopoulos, J., Durst, F., Zanic, Z., and Jovanovic, J., 1984, "Influence of Reynolds Number on Characteristics of Turbulent Wall Boundary Layers", *Exp. in Fluids*, **2**, pp. 7-16.

Antonia, R. A., 1981, "Conditional Sampling in Turbulence Measurement", *Ann. Rev. Fluid Mech.*, **13**, pp. 131-156.

Asai, M., Minagawa, M., and Nishioka, M., 2002, “The instability and breakdown of a near-wall low-speed streak” *J. Fluid Mech.*, vol. 455, pp. 289-314.

Aydin, M. and Leutheusser, H. J., 1980, “Very Low velocity Calibration and Application of Hot-Wire Probes”, *DISA Info.*, No. 25, pp. 17-18.

Babiano, A. and Dubos, T., 2005, “On The Contribution of Coherent Vortices to The Two-dimensional Inverse Energy Cascade”, *J. Fluid Mech.* **529**, pp. 97–116.

Balachandar, R., and Ramachandran, S., 1999, “ Turbulent Boundary Layers in Low Reynolds Number Shallow Open Channel Flows”, *ASME J. Fluids Eng.*, **121**, pp. 684-689

Balachandar, R., et al., 2001, “A Study on Turbulent Boundary Layers on a Smooth Flat Plate in an Open Channel”, *ASME Fluids Engineering*, **123.**, pp394-400

Bandyopadhyay, P. R., 1986, “Mean Flow in Turbulent Boundary Layers Disturbed to Alter Skin Friction”, *J. Fluids Eng. Trans. ASME*, **108**, No. 2, pp. 127-140.

Bandyopadhyay, P. R. and J. M. Castano (1996). “Micro-tiles for Electromagnetic Turbulence Control in Saltwater-preliminary Investigations.” *Proceedings of the Forum on control of transitional and turbulent flows, Fluids Engineering Division Conference, ASME.*

Bandyopadhyay, P. R. Henoch, C. et al., 2005, “Experiments on the effects of aging on compliant coating drag reduction”, *Physics of Fluids*, **17**

Baron, A., and Quadrio, M., 1996, “Turbulent Drag Reduction by Spanwise Wall Oscillations”, *App. Sci. Res.*, **55**, pp. 311-326.

Batchelor, G.K. 1945, “On the Concept and Properties of the Idealized Hydrodynamic Resistance,” *A.C.A.* 13

Bechert, D. W., 1997. “Biological Surfaces and their Technological Application-laboratory and Flight experiments on Drag Reduction and Separation Control.” *AIAA paper 97-1960.*

Benzi, R, et al., 2006, “Maximum drag reduction asymptotes and the cross-over to the Newtonian plug” *J. Fluid Mech.* **551**, pp. 185–195.

Berger, T. W., Kim, J., Lee, C., Lim., J., 2000, “Turbulent Boundary Layer Control Utilizing the Lorentz Force”, *Phys. Fluids*, **12**, No. 3, pp. 631-649.

Berman, N. S., 1978, "Drag Reduction by Polymers", *Ann. Rev. Fluid Mech.*, **10**, pp. 47-64.

Blackwelder, R. F., and Kaplan, R. E., 1976, "On the Wall Structure of the Turbulent Boundary Layer", *J. Fluid Mech.*, **76**, pp. 89-112.

Blackwelder, R. F., 1997, "An Experimental Model for Near-Wall Structure," in *Self-sustaining Mechanisms of Wall Turbulence*, Ed. Panton, R. L., Computational Mechanics Publications, Boston, pp. 49-64

Blennerhassett, P. J. and Basson, A. P., 2006, "The Linear Stability of High-frequency Oscillatory Flow In A Channel", *J. Fluid Mech.* **556**, pp. 1–25

Branover, H., Eidelman, A. and Golbraikha, E. et al., 2004, "On the universality of large-scale turbulence", *Physics of Fluids*, **16**, 2004 pp845-847

Breuer, K. S., Park, J., and Henoch, C., 2004, "Actuation and Control of a Turbulent Channel Flow Using Lorentz Forces", *Phys. Fluids*, **16**, No. 4, pp. 897-907.

Brooke, J. W. & Hanratty, T. J. 1993, "Origin of turbulence producing eddies in a channel flow." *Phys. Fluids A* **5**, pp. 1011–1021.

Brown, G. L. & Thomas, A. S. W. 1977, "Large Structure In A Turbulent Boundary Layer." *Phys. Fluids*, **20**, pp. 243.

Bruun, H. H., 1995, *Hot-wire Anemometry: Principles and Signal Analysis*, Oxford University Press, New York, ISBN 0198563426.

Bruun, H. H., 1996, “Hot-film Anemometry In Liquid Flows”, *Meas. Sci. Technol.* **7**, pp. 1301 – 1312.

Bushnell, D. M. and J. N. Hefner, 1977. “Effect of Compliant Wall Motion on Turbulent Boundary Layers.” *Phys. Fluids* **20**(10, Pt II), pp. S31-S48.

Bushnell, D. M., 2003, “Aircraft Drag Reduction Review”, *J. Aerospace Eng.*, **217**, pp.1-18

Cantwell, B. J. 1981 “Organized Motion In Turbulent Flow.” *Annu. Rev. Fluid Mech.* **13**, pp. 457–515.

Carrier, J. and Stanislas, M., 2005, “Experimental study of eddy structures in a turbulent boundary layer using particle image velocimetry”, *J. Fluid Mech.*, **535**, pp. 143–188.

Casciola, C. M. and Angelis, E. DE, 2007, “Energy transfer in turbulent polymer solutions”, *J. Fluid Mech.*, **581**, pp. 419–436.

Chernyshenko, S.I. and Baig, M.F., 2005, “The Mechanism of Streak Formation in Near-wall Turbulence”, *J. Fluid Mech.* **544**, pp. 99–131.

Choi, H., P. Moin, et al., 1993. "Direct Simulation of Turbulence Flow over Riblets." *J. Fluid Mech.* **255**, pp. 503-539.

Choi, H., P. Moin, et al., 1994. "Active Turbulence Control For Drag Reduction in Wall Bounded Flows." *J. Fluid Mech.* **262**, pp. 75-110.

Choi, J, Jeon, W.-P. and Choi, H., 2006, "Mechanism of Drag Reduction By Dimples On A Sphere", *Physics of Fluids*, **18**

Choi, K.-S., 1987, "On Physical Mechanisms of Turbulent Drag Reduction using Riblets", In Hirata, M., and Kasagi, N., eds., *Transport Phenomena in Turbulent Flows*. New York: Hemisphere, pp. 185-198.

Choi, K.-S., 1989, "Near-wall Structure of Turbulent Boundary Layer with Riblets", *J. Fluid Mech.*, **208**, pp. 417-458.

Choi, K.-S., 1996. *Turbulent drag reduction strategies. Emerging Techniques in Drag Reduction*. eds. K.-S. Choi, K. K. Prasad and T. V. Truong. London, MEP, pp. 77-98.

Choi, K.-S., 2001, "Turbulent Drag-Reduction Mechanisms: Strategies for Turbulence Management", In *Turbulence Structure and Modulation*, CISM Courses and Lectures No. 415, eds. Soldati, A., and Monti, R., Springer-Verlag.

Choi, K.-S., 2002, "Near-wall Structure of Turbulent Boundary Layer with Spanwise-Wall Oscillation," *Phys. Fluids*, **14**, No. 7, pp. 2530-2542.

Choi, K.-S., and Clayton, B. R., 2001, "The Mechanism of Turbulent Drag Reduction with Wall Oscillation", *Int. J. Heat and Fluid Flow*, **22**, pp. 1-9.

Choi, K.-S., and Graham, M., 1998, "Drag Reduction of Turbulent Pipe Flow by Circular-Wall Oscillation", *Phys. Fluids*, **10**. No. 1, pp. 7-9.

Choi, K.-S., Yang, X., Clayton, B. R., Glover, E. J., Atlar, M., Semenov, B. N., and Kulik, V. M., 1997, "Turbulent Drag Reduction using Compliant Surfaces", *Proc. Royal Society. A453*, pp. 2229-2240.

Choi, K.-S., DeBisschop, J.-R., and Clayton, B. R., 1998, "Turbulent Boundary-Layer Control by Means of Spanwise-Wall Oscillation", *AIAA J.*, **36**, No. 7, pp. 1157-1163.

Chow, V.T., 1988, *Open Channel Hydraulics*, McGraw-Hill, New York

Clark, J. A. and E. Markland, 1971. "Flow Visualization in Turbulent Boundary Layers." *J. Hydr. Div ASCE* 97.

Clauser, F., 1954, "Turbulent Boundary Layers in Adverse Pressure Gradients", *J. Aero. Sci.*, **21**, 91-108.

Corino, E. R. and Brodkey, R. S., 1969, "A Visual Investigation of the Wall Region in a Turbulent Flow", *J. Fluid Mech.*, **37**, 1, pp. 1-30.

Coustols, E. 1996, "Control of Turbulent Flows For Skin Friction Drag Reduction," *Control of Flow Instabilities and Unsteady Flows*, ed. G.E.A. Meier and G.H. Schneer, Springer-Verlag, New York, pp. 155-202

Crawford, C. H., and Karniadakis, G. E., 1997, "Reynolds Stress Analysis of EMHD-controlled Wall Turbulence. Part I. Streamwise Forcing", *Phys. Fluids*, **9**, No. 3, pp. 788-806.

Dhanak, M. R., and Si, C., 1999, "On Reduction of Turbulent Wall Skin Friction through Spanwise Wall Oscillations", *J. Fluid Mech.*, **383**, pp. 175-195.

Diorio, J., Kelley, D. H., and Wallace J. M., 2007, "The Spatial Relationships Between Dissipation And Production Rates And Vortical Structures In Turbulent Boundary And Mixing Layers", *Physics of Fluids*, **19**

Dryden, H. L. and Schubauer, G.B. 1947, "the Use of Damping Screens for the Reduction of Wind Tunnel Turbulence", *J. Ae. S.*, **14**, pp. 221

Dring, R. P. and Gebhart, B., 1969, "Hot-Wire Anemometer Calibration for Measurements at Very Low Velocity", *ASME J. Heat Transfer*, **91**, pp. 241-244.

Du, Y. and G. E. Karniadakis, 2000. "Suppressing wall turbulence by means of transverse traveling wave." *Science* **288**, pp. 1230.

Du, Y. and G. E. Karniadakis, 2002. "Drag reduction in wall-bounded turbulence via a transverse travelling wave." *J. Fluid Mech.* **457**, pp.1-34.

Falco, R. E., 1977, "Coherent Motions in the Outer Region of Turbulent Boundary Layers", *Phys. Fluids*, **20**, pp. S124-S132.

Falco, R. E., 1991. "A Coherent Structure Model of The Turbulent Boundary Layer and Its Ability to Predict Reynolds Number Dependence." *Phil. Trans. R. Soc. Lond.* **336**, pp. 103-129.

Flores, O. and Jiménez, J. 2006, "Effect of wall-boundary disturbances on turbulent channel flows", *J. Fluid Mech.*, **566**, pp. 357–376.

Frohanpfel, B., Jovanovic, J. and Delgado, A., 2007, "Experimental Investigations of Turbulent Drag Reduction by Surface-embedded Grooves", *J. Fluid Mech.*, **590**, pp. 107–116.

Gad-el-Hak, M., and Bandyopadhyay, P.R.,1994, " Reynolds Number Effects in Wall-bounded Turbulent Flows," *Appl. Mech. Rev.*, **47**, pp 307-365

Gad-el-Hak, 2000, *Flow Control: Passive, Active and Reactive Flow*, Cambridge University Press.

Gailitis, A.K. and Lielausis, O.A., 1961. "On the Possibility of Drag Reduction of A Flat Plate in An Electrolyte." *Applied Magnetohydrodynamics*, Trudy Inst. Fiziky A N Latvia SSR, **12**, pp. 143-146

Ganapathisubramani, B., Hutchins, N et al., 2005 "Investigation of Large-scale Coherence in A Turbulent Boundary Layer Using Two-point Correlations", *J. Fluid Mech.* , **524**, pp. 57-80

Gao, P and Lu X.-Y., 2006, "Effects of wall suction/injection on the linear stability of flat Stokes layers", *J. Fluid Mech.*, **551**, pp. 303-308

Gavarini, M. I., Bottaro, A. and Nieuwstadt, F. T. M., 2005, "Optimal and robust control of streaks in pipe flow", *J. Fluid Mech.* **537**, pp. 187-219.

George, W., and Castillo, L., 1997, " Zero-pressure-gradient Turbulent Boundary Layer," *Appl. Mech.Rev.*, **50**, pp 689-729

Grass, A. J., 1971. "Structural Features of Turbulent flow over Smooth and Rough Boundaries." *J. Fluid Mech.* **50**.

Green, M. A., Rowley, C. W. and Haller, G., 2007, "Detection of Lagrangian coherent structures in three-dimensional turbulence", *J. Fluid Mech.* **572**, pp. 111-120.

Guala, M. Hommema, S.E. and Adrian, R.J., 2006, "Large-scale And Very-large-scale Motions in Turbulent Pipe Flow", *J. Fluid Mech.* **554**, pp. 521-542

Guala, M. et al., 2007, “An Experimental Investigation On Lagrangian Correlations of Small-scale Turbulence At Low Reynolds Number”, *J. Fluid Mech.*, **574**, pp. 405–427.

Gyr, A. and H.-W. Bewersdorff , 1989. “Change of Structures Close to The Wall of A Turbulent Flow in Drag Reducing Fluids.” *Structure of Turbulence and Drag Reduction, IUTAM Symposium Zurich/Switzerland 1989.* ed. A. Gyr, Berlin, Springer-Verlag.

Haidari, A. H. and C. R. Smith, 1994. “The Generation and Regeneration of Single Hairpin Vortices.” *J. Fluid Mech.* **277**, pp. 135-162.

Hamilton, J. M., J. Kim, et al., 1995. “Regeneration Mechanisms of Near-wall Turbulence Structures.” *J. Fluid Mech.* **287**, pp. 317-348.

Hammond, E. P., T. R. Bewley, et al., 1998. “Observed Mechanisms for Turbulence Attenuation and Enhancement in Opposition-Controlled Wall Bounded Flows.” *Phys. Fluids* **10**(9), pp. 2421-2423.

Han, T., and Patel, V.C. 1979, “Flow Separation On A Spheroid At Incidence.” *J. Fluid Mech.* **92**, 643 -657.

Head, M. R. and Bandyopadhyay, P, 1981, “New Aspects of Turbulent Boundary-Layer Structure”, *J. Fluid Mech.*, **107**, pp. 297-338.

Henderson, F., 1966, Open Channel Flow, Macmillan, New York

Henoeh, C. and J. Stace, 1995. "Experimental Investigation of A Salt water Turbulent Boundary Layer Modified by An Applied Streamwise Magnetohydrodynamic Body Force." *Phys. Fluids* **7**, pp. 1371.

Hermann, S.,1951, Boundary-Layer Theory, McGraw-Hill

Hoyt, J. W. 1989. "Drag Reduction by polymers and surfactants. Viscous Drag Reduction in Boundary Layers," *Progress in Astronautics and Aeronautics*. ed. D. M. Bushnell and J. N. Hefner, Washington DC., AIAA. pp. 413-429.

Hussain, A. K. M. F., 1986, "Coherent Structures and Turbulence", *J. Fluid Mech.*, **173**, pp. 303-356.

Hutchins, N. and Choi, K.-S., 2002, "Accurate Measurements of Local Skin Friction Coefficient using Hot-wire Anemometry," *Prog. Aero. Sci.*, **38**, pp. 421-446.

Hutchins, N. and Marusic, I., 2007, "Evidence of very long meandering features in the logarithmic region of turbulent boundary layers", *J. Fluid Mech.*, **579**, pp. 1-28.

Itoh, M., Tamano, S., and Yokota, K., 2005, “Velocity Measurement In Turbulent Boundary Layer of Drag-reducing Surfactant Solution”, *Physics of Fluids*, **17**

Iuso, G., Cicca, G. and Onorato, M. 2003. “Velocity Streak Structure Modifications Induced by Flow Manipulation”. *Phys. Fluids*, **15**, p.2602-2612.

Iwamoto, K., Fukagata, K. and Kasagi, N. et al., 2005, “Friction Drag Reduction Achievable By Near-wall Turbulence Manipulation At High Reynolds Numbers”, *Physics of Fluids*, **17**

Jang, P. S., Benney, D. J. & Gran, R. L. 1986, “On the Origin of Streamwise Vortices in a Turbulent Boundary Layer.” *J. Fluid Mech.* **169**, pp. 109–123.

Jeong, J., F. Hussain, et al., 1997. “Coherent structures near the wall in a turbulent channel flow.” *J. Fluid Mech.* **332**: 185-214.

Jiménez, J. and A. Pinelli, 1999. “The Autonomous Cycle of Near-wall Turbulence.” *J. Fluid Mech.* **389**: 335-359.

Jiménez, J., del Alamo, J. C. & Flores, O. 2004, “The Large Scale Dynamics of Near-wall Turbulence.” *J. Fluid Mech.* **505**, pp. 179–199.

Johansson, A. V., Alfredsson, P. H. and Eckelmann, H., 1986. "On the Evolution of Shear-layer Structures in Near-wall Turbulence." *Advance in Turbulence*, Mathieu and C.-B. G., Springer and Verlag.

Johansson, A. V., P. H. Alfredsson, et al. 1991. "Evolution and Dynamics of Shear-layer Structures in Near-wall Turbulence." *J. Fluid Mech.* **224**: 579-599.

Joshi, V. J. and Rempfer, D., 2007, "Energy Analysis of Turbulent Channel Flow Using Biorthogonal Wavelets", *Physics of Fluids*, **19**, pp. 1-12

Jukes, T, 2007. *Turbulent Drag Reduction Using Surface Plasma*. PhD Thesis, University of Nottingham

Jung, W. J., Mangiavacchi, N., and Akhavan, R., 1992, "Suppression of Turbulence in Wall-Bounded Flows by High Frequency Spanwise Oscillation", *Phys. Fluids A*, **4**, pp. 1605-1607.

Karniadakis, G. E., and Choi, K.-S., 2003, "Mechanisms on Transverse Motions in Turbulent Wall Flows," *Ann. Rev. Fluid Mech.*, **35**, pp. 45-62.

Kassinosa, S. C., Knaepen, B. and Carati, D., 2007, "The transport of a passive scalar in magnetohydrodynamic turbulence subjected to mean shear and frame rotation", *Physics of Fluids*, **19**

Kerho, M., 2002, "Active Reduction of Skin Friction Drag Using Low-Speed Streak Control (Invited)", *40th AIAA Aerospace Sciences Meeting & Exhibit*, 14-17 January 2002/ Reno, NV, pp 1-15

Keulegan, G.H., 1938 " Law of Turbulent Flow in Open Channels", *J. Res. Natl. Bur. Stand., Sect. A*, **21**, pp. 707-741

Kim, H. T., Kline, S. J. and Reynolds, W. C., 1971, "The Production of Turbulence Near a Smooth Wall in a Turbulent Boundary Layer", *J. Fluid Mech.*, **50**, No. 1, pp. 133-160.

Kim, J., 2005, "Physics of Wall Turbulence: A Perspective on Boundary-Layer Control", *2nd Int. Symp. on Seawater Drag Reduction*, 23-26 May, Busan, Korea.

Klebanoff, P. S., 1954, "Characteristics of Turbulence In a Boundary Layer with Zero Pressure Gradient", *NACA TN 3178*.

Kline, S. J., Reynolds, W. C., Schraub, F. A. and Runstadler, P. W., 1967, "The Structure of Turbulent Boundary Layers", *J. Fluid Mech.*, **30**, 4, pp. 741-773.

Kline, S. J., and Robinson, S. K., 1989a, "Quasi-Coherent Structures in the Turbulent Boundary Layer. Part I: Status Report on a Community-Wide Summary of the Data", *In Near Wall Turbulence. Proc. Zaric Meml. Conf. 1988*, eds. Kline, S. J. and Afgan, N. H., pp. 200-217.

Kline, S. J., and Robinson, S. K., 1989b, "Turbulent Boundary Layer Structure: Progress, Status, and Challenges", *Proc. 2nd IUTAM Symp. Struct. of Turbul. and Drag Reduct.*, Zurich, 1989.

Kline, S. J., 1991. "A Brief History of Boundary Layer Structures Research. Selfsustaining Mechanisms of Wall Turbulence," *Advances in fluid mechanics*. ed. R. L. Panton. Southampton, Computational Mechanics. **15**, pp. 1-12.

Kobayashia, H. "Large Eddy Simulation of Magnetohydrodynamic Turbulent Channel Flows With Local Subgrid-scale Model Based On Coherent Structures", *Physics of Fluids*, **18**

Kodama, Y., K. Sugiyama, et al. 2003. "The Degree and Mechanism of Skin Friction Reduction by Microbubbles." *Third International Symposium on Turbulence and Shear Flow Phenomena*, Sendai, Japan.

Konishi, Y. and Asai, M. 2004, "Experimental investigation of the instability of spanwise-periodic low-speed streaks", *Fluid Dynamics Research*, **34**, pp. 299–315

Kotas, T. J. 1977. "Streamline Pattern In A Confined Vortex Flow." *J. Mech. Eng. Sci.* **19**, 38-41

Kovasznay, L. S. G., 1970, "The Turbulent Boundary Layer", *Ann. Rev. Fluid. Mech.*, **2**, pp. 95-112.

Kovasznay, L. S. G., Kibens, V. & Blackwelder, R. F. 1970, "Large-scale Motion in The Intermittent Region of A Turbulent Boundary Layer." *J. Fluid Mech.* **41**, pp 283–325.

Kreplin, H. P. and Eckelmann, H., 1979. "Propagation of Perturbations In the Viscous Sublayer and Adjacent Wall Region." *J. Fluid Mech.*, **95**, pp. 305-322.

Kral, L.D. and Donova, J. F., 1996. "Numerical Simulation of Turbulence Control Using Electromagnetic Forces." *ASME Fluids Engineering Division Conference* **237**, pp. 319-329

Kramer, M. O., 1961, "The Dolphin's Secret", *J. Am. Soc. Nav. Engr.*, **73**, pp. 103-107.

Kunkel, G. J. and Marusic, I., 2006, "Study of the near-wall-turbulent region of the high-Reynolds-number boundary layer using an atmospheric flow", *J. Fluid Mech.*, **548**, pp. 375–402.

Laadhari, F., Skandaji, L., and Morel, R. 1994, “Turbulence Reduction in a Boundary Layer by a Local Spanwise Oscillating Surface”, *Phys. Fluids*, **6**, No. 10, pp. 3218-3220.

Landahl, M. T. 1975. “Wave Breakdown and Turbulence.” *SIAM J. Appl. Math.* **28**, pp. 735-736.

Laufer, J. & Narayanan, M. A. B. 1971, “Mean Period of The Turbulent Production Mechanism In A Boundary Layer.” *Phys. Fluids* **14**, pp. 182–183.

Lee, C., J. Kim, et al. 1998. “Suboptimal Control of Turbulent Channel flow For Drag Reduction.” *J. Fluid Mech.* **358**, pp. 245.

Lee, D. and Choi, H., 2001. “Magneto hydrodynamic Turbulent Flow in A Channel At Low Magnetic Reynolds Number”. *J. Fluid Mech.* **439**, pp. 367-394.

Legner, H. H. 1984. “A Simple Model For Gas Bubble Drag Reduction.” *Phys.Fluids* **27**(12), pp. 2788-2790.

Lekakisy, I, 1996, “Calibration and signal interpretation for single and multiple hot-wire /hot-film probes”, *Meas. Sci. Technol.* **7**, pp. 1313–1333.

Li, F.-C., Kawaguchi, Y., Segawa, T. and Hishida, K., 2004, “ Characteristics of Low-Speed Streaks and Vortex Structures in Drag-Reduced Turbulent Channel Flow Investigated by Stereoscopic PIV.” *Proceedings of IMECE'04: ASME International Mechanical Engineering Congress*, Anaheim, California.

Liberzon, A., Guala, M. and Kinzelbach, W. ea al., 2006, “On Turbulent Kinetic Energy Production And Dissipation In Dilute Polymer Solutions”, *Physics of Fluids*, **18**

Lim, J. and H. Choi, 1998. “Control of Streamwise Vortices With Uniform Magnetic Fluxes.” *Phys. Fluids* **10**(8), pp. 1997-2005.

Liu, Z.-C., Landreth, R. J., Adrian, T. J., and Hanratty, T. J., 1991, “High Resolution Measurement of Turbulent Structure in a Channel with Particle Image Velocimetry”, *Exp. In Fluids*, **10**, pp. 301-312.

Lu, S. S. and Willmarth, W. W., 1973, “Measurements of the Structure of the Reynolds Stress in a Turbulent Boundary Layer”, *J. Fluid Mech.*, **60**, 3, pp. 481-511.

MacPhail, D.C. 1940, “An Experimental Verification of the Isotropy of Turbulence Produced by a Grid,” *J.Ae.S.*, **8** pp. 73

Manca, O., Mastrullo R., and Mazzei, P., 1988, “Calibration of Hot-Wire Probes at Low Velocities in Air with Variable temperature”, *DANTEC Info.*, No. 6, pp. 6-8.

Mans, J. de Lange, H. C. and van Steenhoven, A. A., 2007, “Sinuous breakdown in a flat plate boundary layer exposed to free-stream turbulence”, *Physics of Fluids*, **19**. pp 1-4

Marie, L. and Daviaud, F. 2004, "Experimental Measurement of The Scale-by-scale Momentum Transport Budget In A Turbulent Shear Flow", *Physics of Fluids*, **16**, pp. 457-461.

Mathieu, J. and Scott, J. 2002, "An Introduction to Turbulent Flow", Cambridge University Press, pp. 230

Maxworthy, T., 1972, "The Structure And Stability Of Vortex Rings." *J. Fluid Mech.* **51**, 15-32.

Merkle, C. L., and Deutsch, S., 1989, "Drag Reduction in Liquid Boundary Layers by Gas Injection", In Bushnell, C. M., and Hefner, J. N., eds., *Viscous Drag Reduction in Boundary Layers*. Washington, DC: AIAA 203-261.

Merzkirch, W., 1987, Flow visualization, Academic Press, Inc.

Meng, J. C. S. and J. J. S. Uhlman, 1998. "Microbubble Formation and Splitting in A Turbulent Boundary Layer for Turbulence Production." *International Symposium on Seawater Drag Reduction, Newport, RI*.

Moin, P. and Kim, J., 1985, "The Structure of the Vorticity Field in Turbulent Channel Flow. Part I: Analysis of Instantaneous Fields and Statistical Correlations", *J. Fluid Mech.*, **155**, pp. 441-464.

Moser, R. D., Kim, J., and Mansour, N. N., 1999, “Direct Numerical Simulation of Turbulent Channel Flow up to $Re_\tau = 590$ ”, *Phys. Fluids.*, **11**, No.4, pp. 943 – 945.

Murlis, J., Tsai, H. M., and Bradshaw, P., 1982, “The Structure of Turbulent Boundary Layers at Low Reynolds Numbers”, *J. Fluid Mech.*, **122**, pp. 13-56.

Nagano, Y., and Tagawa, M., 1987, “Statistical Characteristics of Transfer Process In a Wall Turbulent Shear Flow,” *International symposia on transport phenomena*, Hemisphere Publishing, pp 275-288

Natrajan, V. K. and Christensen, K. T., 2006, “The role of coherent structures in subgrid-scale energy transfer within the log layer of wall turbulence”, *Physics of Fluids*, **18**

Natrajan, V. K., Wu, Y. and Christensen, T., 2007, “Spatial signatures of retrograde spanwise vortices in wall turbulence”, *J. Fluid Mech.*, **574**, pp. 155–167

Nezu, I., and Nakagawa, H., 1993, *Turbulence in open channel flows*, A. A. Balkema.

Nieuwstadt, F. T. M. and Dentoonder, J. M. J., 2001, “Drag Reduction By Additives: A Review.” In *Proc. Turbulence Structure and Modulation* (ed. Soldati, A. and Monti, R.). Springer.

Nosenchuck, D. M. and G. L. Brown, 1992. US patent: 5320309: Electro-magnetic device and method for boundary layer control. USA.

Nosenchuck, D. M. and G. L. Brown 1996. "Use of the Lorentz Force for Direct Boundary-layer Control." *XIXth international congress of theoretical and applied mechanics*, Kyoto, Japan.

O'Sullivan, P. L. and S. Biringgen 1997. "Direct Simulation of Low Reynolds Number Turbulent Channel Flow With EMHD Control." *28th AIAA Fluid Dynamics Conference, 4th AIAA Shear Flow Control Conference*.

O'Sullivan, P. L., 1998, "Direct Numerical Simulation of Low Reynolds Number Turbulent Channel Flow with EMHD Control", *Phys. Fluids*, **10**, No. 5, pp. 1169-1181.

Offen, G. R. and Kline S. J. 1973. "Combined Dye-Streak and Hydrogen-Bubble Visual Observations of A Turbulent Boundary Layer." *J. Fluid Mech.* **62**(2), pp. 223-239.

Offen, G. R. and Kline, S. J., 1975, "A Proposed Model of the Bursting Process in Turbulent Boundary Layers", *J. Fluid Mech.*, **70**, 2, pp. 209-228.

Orlandi, P. and Jiménez, J., 1994, "On the Generation of Turbulent Wall Friction", *Phys. Fluids.*, **6**, pp. 634-641.

Pang, J., and Choi, K.-S., 2004, "Turbulent Drag Reduction by Lorentz Force Oscillation", *Phys. Fluids*, **16**, No. 5, pp. L35-L38.

Pang, J., 2005, *Turbulence Control for Drag Reduction by Sspanwise Lorentz-Force Oscillation*, PhD thesis, University of Nottingham.

Paschkewitz, J. S., Dimitropoulos, D., and Hou, Y. X. et al., 2005, "An Experimental And Numerical Investigation of Drag Reduction In A Turbulent Boundary Layer Using A Rigid Rod-like Polymer", *Physics of Fluids*, **17**

Possdziech O. and Grundmaan, R., 2001. "Electromagnetic Control of Seawater Flow Around Circular Cylinders." *Eur. J. Mech. B-Fluids* **20**, pp. 255-274.

Prandtl, L., 1905, "On the Motion of a Fluid with Very Small Viscosity", *Verh. Int. Math. Kongr.*, 3rd, Heidelberg, 1904, pp. 484-91. Transl. 1928, NACA Memo No. 452.

Pullin, D. I., and Perry, A. E., 1980, "Some Flow Visualization Experiments On The Starting Vortex." *J. Fluid Mech.* **97**, 239-25

Quadrio, M. and S. Sibilla ,2000. "Numerical Simulation of Turbulent Flow In A Pipe Oscillating Around Its Axis." *J. Fluid Mech.* **424**, pp. 217.

Quadrio, M., Floryan, J. M. and Luchini, P., 2007, “Effect of streamwise-periodic wall transpiration on turbulent friction drag”, *J. Fluid Mech.*, **576**, pp. 425–444.

Raschi, W. and J. Elsom 1986. “Comments on The Structure and Development of The Drag Reduction-type Placoid Scale.” *Proceedings of the Second International Conference on Indo-Pacific Fishes.*, Ichthyological Society of Japan, Tokyo.

Rathnasingham, R., and Breuer, K. S., 2003, “Active Control of Turbulent Boundary Layers”, *J. Fluid Mech.*, **495**, pp. 209-233.

Rebbeck, H. and Choi, K., 2006, “A Wind-Tunnel Experiment On Real-time Opposition Control of Turbulence”, *Phys. Fluids*, **18**, pp. 1-13.

Renardy, M., 1995, “On the mechanism of drag reduction”, *J. Non-Newtonian Fluid Mech.*, **59**, pp.93-101

Ristenpart, W. D., Aksay, I. A., and Saville, D. A., 2007, “Electrohydrodynamic Flow Around A Colloidal Particle Near An Electrode With An Oscillating Potential”, *J. Fluid Mech.*, **575**, pp. 83–109

Robinson, S. K, 1991a, “Coherent Motions in the Turbulent Boundary Layer”, *Ann. Rev. Fluid. Mech.*, **23**, pp. 601-639.

Robinson, S. K., 1991b, “Kinematics of Turbulent Boundary Layer Structure”, *NASA TM* 103859.

Rossi, L., and Thibault, J.-P., 2002, “Investigation of wall normal electromagnetic actuator for seawater flow control”, *J. Turbulence*, **3**, 005.

Saville, A. M. and J. C. Mumford, 1988. “Manipulation of Turbulent Boundary Layers by Outer-layer Devices: Skin Friction and Flow-Visualisation Results.” *J. Fluid Mech.* **191**, pp. 389-418.

Saville, A. M., 1989. “Drag Reduction by Passive - A Review of Some Recent Developments.” *Structure of Turbulence and Drag Reduction, IUTAM Symposium Zurich/Switzerland 1989*. ed. A. Gyr, Berlin, Springer-Verlag, pp. 429-465.

Schlichting, H., 1979, *Boundary Layer Theory*, Mc-Graw Hill, 7th Ed., First published 1951.

Schoppa, W., and Hussain, F., 1998, “A Large-Scale Control Strategy for Drag Reduction in Turbulent Boundary Layers”, *Phys. Fluids*, **10**, No. 5, pp. 1049-1051.

Schoppa, W. and Hussain F., 2000. “Coherent Structure Dynamics in Near-Wall Turbulence.” *Fluid Dyn. Res.* **26**, pp 119-139.

Schoppa, W., and Hussain, F., 2002, “Coherent Structure Generation in Near-Wall Turbulence”, *J. Fluid Mech.*, **453**, pp. 57-108.

Shatrov, V. and Gerbeth, G., 2007, “Magnetohydrodynamic drag reduction and its efficiency”, *Physics of Fluids*, **19**

Sherman, D. M., 1998, *Manipulating Aerodynamic Boundary Layers Using an Electrohydrodynamic Effect Generated by a One Atmosphere Uniform Glow Discharge Plasma*, MS Thesis, University of Knoxville, TN.

Sherman, F. S., 1990, *Viscous Flow*, Int. Edition, McGraw Hill, Singapore.

Schlichting, H., 1951, *Boundary-Layer Theory*, McGraw-Hill.

Simpson, R. L., Chew, Y. T., and Shivaprasad, B. G., 1981, “ the Structure of a Separating Boundary Layer”, Part 2, “Higher Order Turbulent Results”, *J. Fluid Mech.*, **113**, pp. 53-73

Smith, C. R. and S. P. Schwartz, 1982. “Observations of Streamwise Rotation in The Near-wall Region of A Turbulent Boundary Layer.” *Phys. Fluids* **26**(3), pp. 641-652.

Smith, C. R. & Metzler, S. P. 1983, “The Characteristics of Low-speed Streaks in The Near-wall Region of A Turbulent Boundary Layer.” *J. Fluid Mech.* **129**, 27–54.

Smith, C. R. & Walker, J. D. A. 1994 Turbulent wall layer vortices. In *Fluid Vortices* (ed. S. Green). Springer.

Smith, C.R., and Walker, J. D. A., 1997, "Sustaining Mechanisms of Turbulent Boundary Layers: The Role of Vortex Development and Interactions," *Self-sustaining Mechanisms of Wall Turbulence*, ed. R. L. Panton, Computational Mechanics Publications, Boston, pp. 13-47.

Sreenivasan, K. R. 1988 "A Unified View of The Origin And Morphology of The Turbulent Boundary Layer Structure." *In Proc. IUTAM Symp. on Turbulence Management and Relaminarisation* (ed. H. W. Liepmann & R. Narasimha), Springer, pp. 37-61.

Tachie, F.M., Balachandar, R. and Bergstrom, D. J., 2001, "Open Channel Boundary Layer Relaxation Behind a Forward Facing Step at Low Reynolds Numbers", *J. Fluids Eng.*, **123**, pp. 539-544

Tachie, F.M., Balachandar, R. and Bergstrom, D. J., 2001, "Skin Friction Correlation in Open Channel Boundary Layers", *J. Fluids Eng.*, **123**, pp. 953-955

Tamilarasan, M. (2000). *The formation and use of compliant coatings for drag reduction in turbulent pipe flow*. PhD thesis, University of Nottingham.

Tennekes, H. and Lumley, J.L., 1997, *A First Course in Turbulence*, 16th printing, The MIT Press.

Tewari, S. S. and Jaluria Y., 1990, "Calibration of Constant-Temperature Hot-Wire Anemometers for Very Low Velocities in Air", *Rev. Sci. Instrum.*, **61**, No. 12, pp. 3834-3845.

Theodorsen, T., 1952, "Mechanism of Turbulence", *Proc. 2nd Midwestern Conf. Fluid Mech.*, 17-19 March, Ohio State University, Columbus, Ohio.

Thibault J.P. and Rossi L., "Electromagnetic Flow Control: Characteristic Numbers And Flow Regimes of A Wall-Normal Actuator." *J. Phys D: Appl. Phys.* **36**, pp 2559-2568

Thibault, J. -P. and Rossi, L., 2003, "Electromagnetic flow control: characteristic numbers and flow regimes of a wall-normal actuator", *J. Phys. D: Appl. Phys.* **36**, pp. 2559–2568

Tiederman, W. G., T. S. Luchik, et al., 1985. "Wall Layer Structure and Drag Reduction." *J. Fluid Mech.* **156**, pp. 419-437.

Tiederman, W. G., 1989. "The Effect of Dilute Polymer Solutions On Viscous Drag and Turbulence Structure." *Structure of Turbulence and Drag Reduction, IUTAM Symposium Zurich/Switzerland 1989*. A. Gyr. Berlin, Springer-Verlag.

Toh, S. and Itano, T., 2005, "Interaction Between A Large-scale Structure And Near-wall Structures In Channel Flow", *J. Fluid Mech.*, **524**, pp. 249–262.

Townsend, A. A. (1956). *The Structure of Turbulent Shear Flow*, Cambridge University Press.

Tsanis, I. K., 1987, "Calibration of Hot-Wire Anemometers at Very Low Velocities", *DANTEC Info.*, No. **4**, pp. 13-14.

Tsinober, A.B. and Shtern A.G. 1967. "Possibility of Increasing the Flow Stability In A Boundary Layer By Means of Crossed Electric And Magnetic Field." *Magneto-hydrodynamics*, 3(2), pp. 152-154.

Ueda, H., and Hinze, J. O., 1975, " Fine-structure Turbulence In The Wall Region of Turbulent Boundary Layer", *J. Fluid Mech.*, **67**, pp 125-144

Virk, P., 1975, "Drag Reduction Fundamentals", *AIChE J.*, **21**, pp.625-656.

Wallace, J. M., Eckelmann, H. and Brodkey, R. S., 1972, "The Wall Region in Turbulent Shear Flow", *J. Fluid Mech.*, **54**, No. 1, pp. 39-48.

Waleffe, F., Kim, J. & Hamilton, J. 1993 "On The Origin of Streaks In Turbulent Boundary Layers." *In Turbulent Shear Flows 8* (ed. F. Durst, R. Friedrich, B. E. Launder, F. W. Schmidt, U. Schumann & J. Whitelaw), Springer, pp. 37–49.

Waleffe, F. & Kim, J. 1997, “How Streamwise Rolls And Streaks Self-sustain In A Shear Flow.” *In Self-Sustaining Mechanism of Wall Turbulence (ed. R. L. Panton)*, Computational Mechanics Publication, Southampton. pp. 309–331.

Waleffe, F. 2003 “Homotopy of exact coherent structures in plane shear flows.” *Phys. Fluids*, **6**, pp.1517–1534.

Walsh, M. J., 1990, “Riblets”, In Bushnell, C. M., and Hefner, J. N., eds., *Viscous Drag Reduction in Boundary Layers*. Washington, DC: AIAA 203-261.

Warsop, C., 2004, “AEROMEMS-II: A European Research Effort to Develop MEMS Based Flow Control Technologies”, *2nd Flow Control Conference*, 28 June – 1 July, Portland, OR, AIAA 2004-2209.

Wassen, E., Kramer, F. et al. 2008. “Turbulent Drag Reduction by Oscillating Riblets”, AIAA 4th Flow Control Conference 23-26 June 2008, Seattle, Washington

Weier, T., G. Gerbeth, et al., 1998. “Experimental Study On Cylinder Wake Stabilization In An Electrolyte Solution By Means of Electromagnetic Force Localized On The Cylinder Surface.” *Experimental Thermal and Fluid Science* **16**, pp. 84-91.

Willmarth W. W., and Lu, S. S., 1972, "Structure of The Reynolds Stress Near The Wall", *J. Fluid Mech.*, **55**, No. 1, pp. 65-92.

Winter, K. G., 1977, "An Outline of Techniques Available for the Measurement of Skin Friction in Turbulent Boundary Layers", *Prog. Aero. Sci.*, **18**, pp. 1-57.

Xu, P. and Choi K. -S., 2008, "Boundary Layer Control for Drag Reduction", IUTAM Symposium on Flow Control and MEMS: Proceedings of the IUTAM Symposium, ed. Morrison, J. F., Lavoie, P. and Birch, D.M., Springer-Verlag New York.

Yang S.-Q and Dou, G., 2005, "Drag Reduction In A Flat-plate Boundary Layer Flow By Polymer Additives", *Physics of Fluids*, **17**

Yajnik, K. S. and M. Acharya, 1977. "Non-Equilibrium Effects In A Turbulent Boundary Layer Due to The Destruction of Large Eddies." *Structure and Mechanisms of Turbulence*, Berlin, Springer. **76**, pp. 249-260.

Yoon, H. S., El-Samni, O. A. and Chun, H. H., et al., 2006, "Drag Reduction In Turbulent Channel Flow With Periodically Arrayed Heating And Cooling Strips", *Physics of Fluids*, **18**

Zhao, H., Wu, J.-Z. and Luo, J.-S., 2004, "Turbulent drag reduction by travelling wave of flexible wall", *Fluid Dynamics Research*, **34**, pp.175–198

Zhou, J., Adrian, R. J., Balachandar, S. and Kendall, T. M., 1999, “Mechanisms for Generating Coherent Packets of Hairpin Vortices in Channel Flow”, *J. Fluid Mech.*, **387**, pp. 353-396.

Appendix I

This paper published in IUTAM Symposium on Flow Control and MEMS, J.F.Morrison et al. (Eds), 2008, Springer, pages 259-265

Boundary layer control for drag reduction by Lorentz Forcing

Peng Xu and Kwing-So Choi

School of Mechanical, Materials and Manufacture Engineering University of Nottingham, NG7 2RD, UK.; E-mail: kwing-so.choi@nottingham.ac.uk

Abstract. A study was carried out with an aim to better understand the drag reducing mechanisms by spanwise oscillation and spanwise travelling wave via Lorentz forcing flow control. A maximum 47% of flow drag reduction was achieved with $w^+ \approx 12.2$ when the Lorentz forcing spanwise oscillation was applied in a turbulent boundary layer. It was, however, shown that the spanwise travelling wave forcing can reduce or increase the skin friction drag depending on the operating conditions which offers a flexibility for flow control. A maximum 28.9% of drag reduction and 22.8% of drag increase have been achieved, respectively. Flow visualization indicated that the spanwise displacement of the streaky structures may play an important role in obtaining the drag reduction by spanwise travelling wave actuation.

Keywords: flow control; turbulent boundary layer; Lorentz force

1 Introduction

Electro-magnetic (Lorentz) force is a body force which is non-intrusive to the flow and allows many different types of control to be introduced such as streamwise force control [8], wall-normal blowing or suction [11], and spanwise oscillation [2,3,12]. Due to its benefits, flow control by Lorentz forcing (or called Electro-Magnetic Turbulence Control) has attracted many researchers' attention and has been extensively studied in the past decade.

Recent research showed that the turbulence regeneration cycle is associated with near-wall region [9], where one of the strategies for drag reduction is to modify or disturb any part of the near-wall activities [10]. The weakening of streamwise vortices [7] was successful in reducing skin friction drag. In the present paper two flow control schemes were introduced: spanwise oscillation and spanwise travelling wave via Lorentz forcing. The aim was to better understand the drag reducing mechanisms by Lorentz forcing. To achieve this, the velocity profiles and turbulent statistics with and without Lorentz forcing were obtained using hot-film anemometry. The flow visualizations were also performed.

2 Experiments

The experiments were carried out in a 7.3 meter long close-loop open-water channel with a working section of 600 mm by 300 mm where a 4.0 meter long test plate was placed horizontally. A trip device was placed just after the leading edge to make sure the flow in test section was fully turbulent. The freestream velocity was 0.1 m/s, and the Reynolds number was 388 based on the frictional velocity and boundary layer thickness. Tap water was made conductive by introducing electrolyte solution with a conductivity of 1.0 S/m through a wall slot 24 mm upstream of the electromagnetic (EM) actuator. Copper Sulphate solution was injected for velocity measurements, while Potassium Permanganate solution was used for flow visualization because of its dark red colour. Water temperature was controlled by a heat exchanger in the upstream tank and the temperature changing was within 0.1 °C throughout the measurements. Velocity signals were measured by the Dantec CTA hot-film anemometry with a single boundary-type sensor. The sensor was mounted in a vertical traverse gear with a step motor of 6 μm resolution. All the turbulent boundary layer profile measurements were made at the 7 mm downstream of the end of EM actuators where no electro-magnetic effect on hot-film sensor was detected.

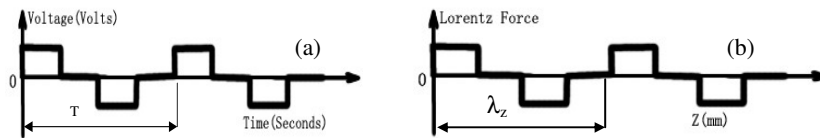


Fig. 1. Actuating signal to each electrode (a) for spanwise travelling wave control associated with Lorentz force (b).

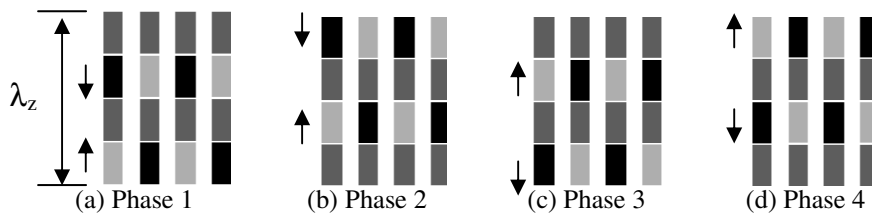


Fig. 2. (a)-(d) 4 phases of the travelling wave actuation. Black colour denotes positively activated electrodes; light grey denotes negatively activated and dark grey no-activated. Flow is from right to left.

A 0.25 mm thick Mylar sheet with etched copper laminate (0.017 mm thick) was laid flush with the surrounding test plate, below which permanent magnets (1.2T) were placed. The EM actuator covered streamwise distance of 300 mm ($x^+=1580$) and spanwise distance of 230 mm ($z^+=1214$). The penetration depth as defined by $\Delta^+=a^+/\pi$ was 7.6, where a^+ is the width of the electrode in wall units. Figure 1 (a) shows the square wave signal to each electrode, where the 'T' denotes an excitation period. A four-phase scheme was introduced here for the travelling wave excitation. The spatial distribution of the spanwise Lorentz force is shown in Figure 1 (b),

where the wave length λ_z is 495 wall units. Figures 2 (a)-(d) give an example of how the phase of the travelling wave being shifted.

3 Results

As shown in Figure 3, the logarithmic velocity profiles are shifted upward, indicating that the viscous sublayer is thickened by the spanwise oscillating Lorentz force; similar to [12]. This is also similar to the results for spanwise wall oscillation [4]. The turbulent intensity profiles showed significant reduction as well, not only in near-wall region but also in logarithmic region of the boundary layer. Meanwhile, both skewness and kurtosis of the streamwise velocity fluctuations were increased in the viscous sublayer and the buffer layer (not shown here). These increases in higher-moments are the consequence of a reduction in turbulence activities, agreeing well with the experiments carried out by Pang & Choi [12] and others on spanwise wall oscillation [1,5,13].

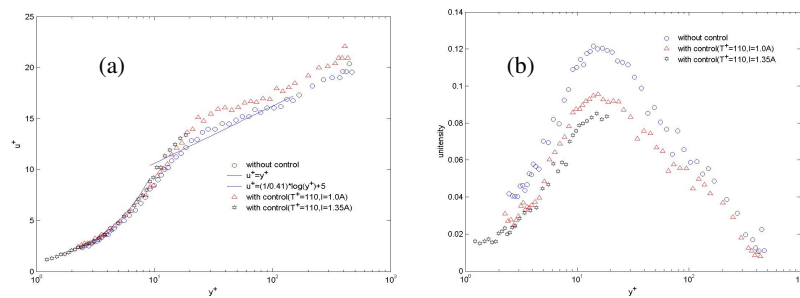


Fig. 3. (a) The logarithmic velocity profiles with and without spanwise oscillation actuation. (b) Turbulence intensity profiles.

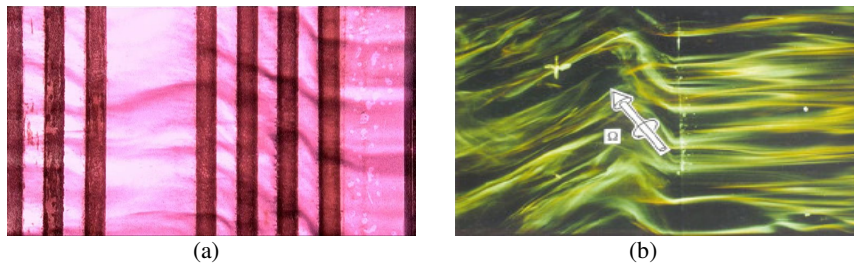


Fig. 4. (a) Visualization of near-wall streaky structures with Lorentz forcing spanwise oscillating actuation. Window area is $475 (x^+)$ by $382 (z^+)$ wall units. (b) Visualization of near-wall streaky structures with spanwise wall oscillation (Choi et al. 1998). Flow is right to left.

Figure 4 (a) shows the visualization picture of the near-wall streaky structures with Lorentz force oscillation. We can clearly see that the low-speed streaks are

twisted into the spanwise direction due to spanwise flow oscillation. These are very similar to those observed in spanwise wall oscillation (figure 4 (b)). Choi et al. [6] proposed that a negative spanwise vorticity is created in turbulent boundary layer due to the spanwise wall oscillation, which seems to apply to the Lorentz force flow oscillation equally. In our study, we have achieved a drag reduction up to 47% with a maximum spanwise velocity, w^+ , up to 12.2.

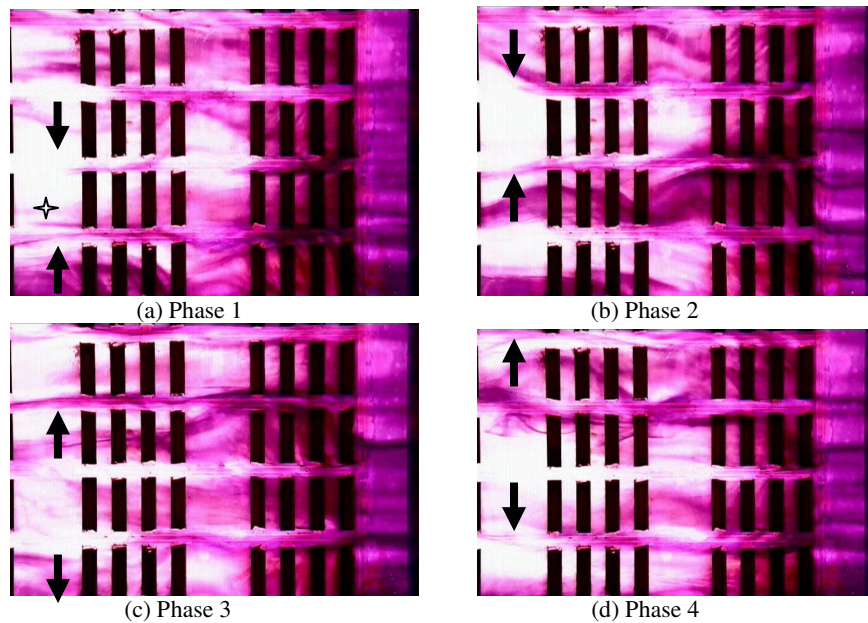


Fig. 5. Visualization of near-wall streaky structure with the Lorentz forcing travelling wave actuation Window size is $625 (x^+)$ by $500 (z^+)$ wall units. Flow is from right to left. Travelling wave direction is upward. Arrows show the activated rows of the electrodes with Lorentz forces. The star in (a) shows the spanwise position of z where the velocity measurement was carried out.

When the spanwise travelling wave forcing is applied, the logarithmic velocity profile is shifted upwards similar to that with spanwise flow oscillation. The turbulence intensity also shows a significant reduction across the entire region of the turbulent boundary layer (figures not shown here).

Figure 5 shows a series of flow visualization pictures, where the near-wall streaky structures are modified to give an appearance of ‘ribbons’, similar to [7]. As seen in figure 5, the low-speed streaks are twisted and propelled along the spanwise direction when the positive (upward direction in pictures) Lorentz force is imposed. If the force is strong enough, the streaky structures are able to travel out of the activated force region into the adjoining area. Then the streaks could not move further and cluster together to form ‘ribbons’ until the non-activated region becomes active. This spanwise motion of the streaky structures repeats across the entire section, where the spanwise displacement of the low-speed ‘ribbons’ can be up to the total width of the test sheet ($z^+ = 1214$ wall units). To achieve drag reductions,

we found that the spanwise displacement of low-speed ‘ribbons’ must be greater than 115 wall units (z^+). This almost compares to the spacing between low-speed streaks ($z^+ \sim 100$). Otherwise, drag increase is observed.

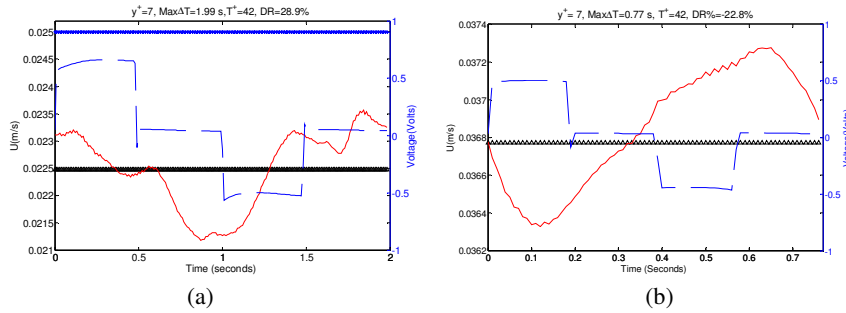


Fig. 6. Phase averaged streamwise velocity with spanwise travelling wave at $y^+=7$ at drag reducing condition (a) and at drag increasing condition (b). Triangles denote the local mean velocity; stars denote the mean velocity of no-control flow; solid lines denote the phase averaged velocity; dash lines denote the excitation signal.

The phase averaged streamwise velocity profiles at $y^+=7$ in one excitation period, as seen in figure 6, clearly show that the streamwise velocity of the turbulent boundary layer is modulated by the spanwise travelling wave actuation. High-speed region (velocity greater than the local mean velocity) and low-speed (velocity less than the local mean velocity) region appear alternately in one actuation cycle regardless of the amount of drag reduction. This confirms that the low-speed and high-speed ‘ribbons’ are not solely responsible for the drag reduction in spanwise travelling wave flow control by Lorentz forces. The phase averaged velocity profiles also shows that the period of the wave-form velocity is consistent with the excitation signal. Moreover, the phase averaged velocity in figure 6 (a) confirms the findings of flow visualization in figure 5. In figure 5 (a) (phase 1), some low-speed fluids have been able to move close to the position of the hot-film sensor, which can be seen from figure 6 (a) where the velocity is decreasing. At phase 2, the velocities have dropped down to the minimum, which supports the view in figure 5 (b) that the low-speed ‘ribbon’ is passing by the sensor. After that, figure 5 (c) and (d) show the high-speed region is approaching the sensor, which is affirmed by the increasing velocity in 6 (a). Please notice that the velocity measurement point is about 7 mm downstream the actuator and, here, the velocity signal lagged behind the input signal by about 0.3 seconds.

4 Conclusions

In this study, two turbulent flow control schemes were examined: spanwise oscillation and spanwise travelling wave via Lorentz forcing.

The maximum 47% of drag reduction has been achieved by spanwise flow oscillation at $w^+ \approx 12.2$. This shows a good agreement with the DNS results [2] and

our previous results [12]. The results of flow visualization show the streaky structures are periodically twisted into the spanwise direction by the oscillating Lorentz force, suggesting a similarity in the drag reduction mechanisms between the spanwise wall oscillation and Lorentz force oscillation. The mean velocity is reduced in the near-wall region and turbulent intensity decreases across the boundary layer, and both of the skewness and kurtosis are increased in the near-wall region ($y^+ < 10$).

The spanwise travelling wave actuation produces a drag reduction up to 28.9% and a maximum 22.8% of drag increase. When the drag reduction is achieved, the logarithmic velocity profile is shifted upward, indicating the thickening of the sublayer by the spanwise travelling wave. The turbulent intensity also reduces as described in spanwise oscillation.

Flow visualizations shows that the near-wall streaky structures are modified by the spanwise travelling wave actuation to form low-speed ‘ribbons’. Phase averaged streamwise velocity profiles, however, suggest that the low-speed ‘ribbons’ are not the sole reason for drag reduction. We found that the spanwise displacement of the low-speed ‘ribbons’ is also important to achieve drag reduction. In our experiments, drag reduction is achieved only when the low-speed ‘ribbons’ move more than 115 wall units in spanwise direction in one cycle of actuation sequence. When drag reduction is observed, the spanwise travelling wave appears to congregate the low-speed streaks to form ‘ribbons’, then propels them to move more than 115 wall units in spanwise direction.

References

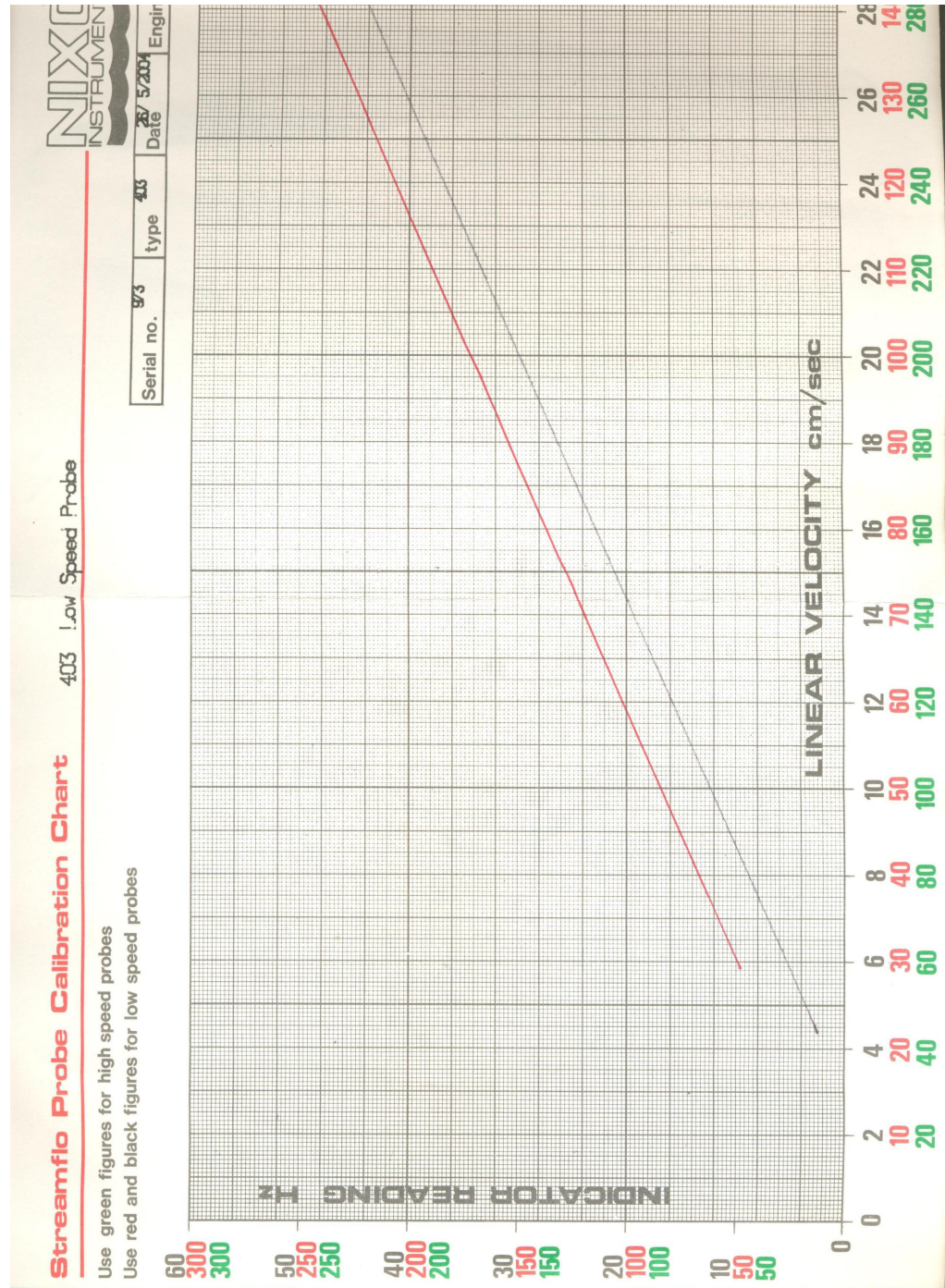
1. Baron, A. & Quadrio, M., Turbulent drag reduction by spanwise wall oscillation, *Appl. Sci. Res.*, **55** (1996) 311-326.
2. Berger, T. W., Kim, J., et al., Turbulent boundary layer control utilizing the Lorentz force, *Physics of Fluids*, **12** (2000) 631-649
3. Breuer, K.-S. Park, J., Henocho C., Actuation and control of a turbulent channel flow using Lorentz forces, *Phys. Fluids*, **16** (2004) 897-907
4. Choi, K.-S., Near-wall structure of turbulent boundary layer with spanwise-wall oscillation, *Phys. Fluids*, **14** (2002) 2530-2542
5. Choi, K.-S. & Clayton, B.R., The mechanism of turbulent drag reduction with wall oscillation, *Int. J. Heat and Fluid Flow*, **22** (2001) 1-9
6. Choi, K.-S. & DeBisschop, J.-R., et al., Turbulent boundary-layer control by means of spanwise wall oscillation, *AIAA Journal*, **36**(7) (1998) 1157-1163
7. Du, Y., Symeonidis, Y. & Karniadakis, G. E., Drag reduction in wall-bounded turbulence via a transverse travelling wave, *J. Fluid Mech.*, **457** (2002) 1-34
8. Henocho, C. & Stace, J., Experimental investigation of a salt water turbulent boundary layer modified by an applied streamwise Magnetohydrodynamic body force, *Physics of Fluids*, **7** (1995) 1371-1383
9. Jimnez, J. & Pinelli, A., The autonomous cycle of near-wall turbulence, *J. Fluid Mech.* **389** (1999) 335-359
10. Karniadakis, G.E. & Choi, K-S., Mechanisms on transverse motions in turbulent wall flows, *Ann. Rev. Fluid Mech.*, **35** (2003) 45-62

11. Nosenchuck, D. M., & Brown, G. L., Discrete spatial control of wall shear stress in a turbulent boundary layer, in *Near-wall Turbulent Flows*, So, R. M et al. (Eds), Elsevier, Amsterdam (1993) 689-698.
12. Pang, J. & Choi, K.-S., Turbulent drag reduction by Lorentz force oscillation, *Physics of Fluids*, **16** (2004) 35-38
13. Quadrio, M., & Sibila, S., Numerical simulation of turbulent flow in a pipe oscillation around its axis, *J. Fluid Mech.*, **424** (2000) 217-241
14. Schoppa, W. and Hussain F., A large-scale control strategy for drag reduction in turbulent boundary layers, *Phys. Fluids*, **10** (1998) 1049-1051

Appendix II

The Streamflo Probe Calibration Chart used in the study

The 403 Low Speed Probe is from NIXON Instrumentation. The figure below shows the scanned calibration chart.



Appendix III

The specifications of the temperature sensor used in the study

OMEGA series 700 Linear Response probes are fitted with precision 44018 linear thermistor elements rated to 100 °C. The data below is from 'the temperature handbook', OMEGA Engineering, Inc.

	°C	°F
* Linear Components Kit Model No.	44203	
Range	-30 to 50°C	-22 to 122°F
Thermistor Composite Model No.	44018	
Resistor Composite Model No.	44301	
Resistor Composite Values	R ₁ = 18,700 Ω, R ₂ = 35,250 Ω	
Thermistor Accuracy & Interchangeability	±0.15°C -30 to 100°C	±0.27°F -22 to +212°F
E ₀ Positive Slope	E _{out} = (+0.0067966 E _{in}) T +0.34893 E _{in}	E _{out} = (+0.00377588 E _{in}) T +0.228102 E _{in}
E ₀ Negative Slope	E _{out} = (-0.0067966 E _{in}) T +0.65107 E _{in}	E _{out} = (-0.00377588 E _{in}) T +0.771898 E _{in}
Resistance Mode	R _t = (-127.096) T +12175	R _t = (-70.608) T +14435
*E _{in} MAX.	3.0 Volts	
***I _T MAX.	475 μA	
***Load Resistance Minimum R.L.	10 MΩ	
Linearity Deviation	±0.16°C	±0.29°F